Lawrence Berkeley National Laboratory
Recent Work

Title
Surface and Interface Control in Nanoparticle Catalysis.

Permalink
https://escholarship.org/uc/item/5q23p874

Journal
Chemical reviews, 120(2)

ISSN
0009-2665

Authors
Xie, Chenlu
Niu, Zhiqiang
Kim, Dohyung
et al.

Publication Date
2020

DOI
10.1021/acs.chemrev.9b00220

Peer reviewed

Surface and Interface Control in Nanoparticle Catalysis

Chenlu Xie,[†, §] Zhiqiang Niu,[†, §] Dohyung Kim, [†, ‡, ⊥, §] Mufan Li,[⊥] and Peidong Yang[*,†, ‡, ⊥, ‖]

[†]Department of Chemistry, University of California, Berkeley, California 94720, United States

[‡]Department of Materials Science and Engineering, University of California, Berkeley, California 94720, United States

[⊥]Chemical Science Division, Lawrence Berkeley National Laboratory, Berkeley, California 94720, United States

[‖]Kavli Energy Nanoscience Institute, Berkeley, California 94720, United States

Abstract

The surface and interfaces of heterogeneous catalysts are essential to their performance as they are often considered to be active sites for catalytic reactions. With the development of nanoscience, the ability to tune surface and interface of nanostructures has provided a versatile tool for the development and optimization of a heterogeneous catalyst. In the review, we present the surface and interface control of nanoparticle catalysts in the context of oxygen reduction reaction (ORR), electrochemical CO_2 reduction reaction (CO_2 RR) and tandem catalysis in three sections. In the first section, we start with the activity of ORR on the nanoscale surface and then focus on the approaches to optimize the performance of Pt-based catalyst including using alloying, core-shell structure, and high surface area open structures. In the section of CO2 RR, where the surface composition of the catalysts plays a dominant role, we covered its reaction fundamentals and the performance of different nanosized metal catalysts. For tandem catalysis, where adjacent catalytic interfaces in a single nanostructure catalyze sequential reactions, we described its concept and principle, catalyst synthesis methodology and application in different reactions.

Contents

1. Introduction

Heterogeneous catalysis plays a central role in the chemical industry to produce fuels, fertilizers and fine chemicals that are vital to the modern civilization. The first clear realization of heterogeneous catalytic reactions between gases was demonstrated in 1817[1], where a hot platinum wire would become incandescent when putting in the mixture of coal gas and air. The platinum wire, well below the ignition temperature of the gaseous mixture, catalyzed the oxidation of coal gas and glow from the heat of the reaction. The size and surface area of the metal catalyst was soon found to be important to its catalytic performance,[2] where 'finely divided metal' could catalyze the reaction at a significantly lower temperature compared to the bulk counterpart. Since then, a variety of heterogeneous catalysts were discovered and optimized using empirical methods.

On the molecular level, the catalytic reaction takes place on the surface or interfaces of the solid catalyst, where reactants are adsorbed and subsequently converted to products that eventually desorbed from the catalyst surface. The pathway of the catalyzed reaction is governed by the geometric configuration and chemical bonding of substrate molecules on the surface, which could be controlled by the atomic and electronic structure of the surface or interface. In the past two decades, the development of nanoscience has fundamentally transformed the way that heterogeneous catalysts are designed. The ability to tune and characterize nanoparticles in nano-meter size regime has enabled direct manipulation of surfaces and interfaces of these catalysts and given rise to superior heterogeneous catalysts for electrochemical and thermal gas phase reactions.

The recent pursuit of clean energy has spurred the development of electrocatalyst for fuel cell application and carbon fixation, which extensively relies on the surface structure optimization of the catalyst. The first two sections of this review will cover the surface and interface control of the nanosized electrocatalysts for oxygen reduction reaction (ORR) and CO_2 reduction reaction (CO_2RR), respectively. For ORR reaction, the state-of-the-art electrocatalysts are Pt-based nanostructures, and catalysts with different surface composition, morphology and configuration will be discussed for their catalyst performance, which includes reaction overpotential, turnover frequency, and catalyst stability. The theoretical background, catalyst design principle and nanocrystal synthetic approach will also be discussed in this section. For CO_2 RR reaction, the section would first cover the fundamentals of CO_2 RR and the mechanisms that lead to different products. The performance matrix, including product distribution, reaction overpotential, catalyst activity, and stability, will be reviewed for metal nanocrystal of different elemental composition

and structures.

The ability to integrate well-defined nanosized objects into composite nanostructures provides unprecedented opportunities to form multiple catalytic interfaces with the elaborate spatial arrangement in a single nanostructured catalyst to carry out complex sequential reactions and exploit the synergistic effects between these catalytic interfaces to achieve high-value products. In the third section of the review, we describe the design principle, synthetic preparation and catalytic properties of such tandem catalysts. Specifically, we would cover the structure-performance relationships of heterogeneous catalysts with the emphasis on metal-oxide interfaces, and systematically review the methodologies to integrate different nanosized objects into nanostructures with control over their spatial arrangements. The final part of this section would cover examples of tandem catalysts and their working principles.
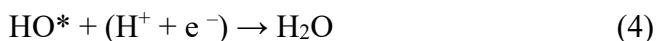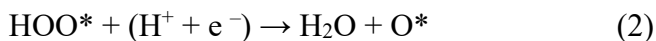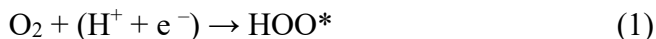
2. Oxygen reduction reaction

ORR is a reaction occurring at the cathodes in energy conversion/storage systems such as fuel cells and metal-air batteries. The sluggish kinetics of ORR comprises a major bottleneck of these energy devices. A high overpotential is required to drive the ORR at a reasonable rate. Tremendous research efforts have been dedicated to the development of cathode ORR catalysts that can lower the overpotential. Platinum (Pt)-based materials are the most practical catalysts so far for the low temperature proton exchange membrane fuel cells (PEMFCs) for transportation applications, although non-Pt catalysts have attracted increasing interest recently. Reducing the cathode Pt loading is of great importance to make PEMFC vehicles affordable to the masses. In the past decades, significant progress has been achieved in the development of low-Pt ORR electrocatalysts throughsurface and interface control at the nanoscopic scale. This section will focus on Pt-based ORR electrocatalysts. We start by outlining some theoretical considerations on the activity of Pt-based materials toward ORR. We then discuss the ORR activities on extended surface and how the knowledge acquired on extended surface is used to guide the development of nanostructured catalysts. Three categories of nanostructured catalysts are highlighted and discussed, including alloys, core-shell structures, and open architectures. Illustrative examples are used to provide a glimpse into how a material-by-design approach plays an important role in the development of nanostructured catalysts. This section concludes by discussing some design principles for active and durable Pt alloy catalysts. For more thorough understanding of this field, we refer the readers to a number of recent reviews.[3-9]

2.1. Theoretical studies

The ORR can proceed through either a two-electron pathway to generate hydrogen peroxide or a four-electron pathway leading to the full reduction of oxygen to water. The four-electron route is preferred for PEMFCs, not only due to its higher energy efficiency, but also because the hydroxy radicals derived from hydrogen peroxide can cause severe degradation of the perfluorinated sulfonic acid membranes. The experimental investigation of the molecular mechanism of ORR is difficult. Theoretical studies on extended Pt(111) surface suggest that an associative mechanism is more likely to dominate at high oxygen coverage. It includes four elementary steps, namely,

adsorption and protonation of oxygen to form HOO* (Equation 1), a second proton/electron transfer to the same oxygen atom followed by the dissociation of O–O bond (Equation 2), proton/electron transfer to the remaining oxygen atom (Equation 3) and a second proton/electron transfer to this oxygen atom to form water (Equation 4).

$$O_2 + (H^+ + e^-) \rightarrow HOO* \qquad\qquad (1)$$

$$HOO* + (H^+ + e^-) \rightarrow H_2O + O* \qquad\qquad (2)$$

$$O* + (H^+ + e^-) \rightarrow HO* \qquad\qquad (3)$$

$$HO* + (H^+ + e^-) \rightarrow H_2O \qquad\qquad (4)$$

The free energies of each intermediate (HOO*, O*, and HO*) have been calculated. The calculation shows that the intermediates' binding strength is linearly correlated across many different metals.[10] This is because they all bind to the surface through oxygen atom. The implication of this scaling relationship is that we can use only one variable to describe all the binding energies of the intermediates. The hydroxyl free energy (ΔG_{HO*}) is most frequently used as a descriptor to predict the ORR activity. The results are plotted in Figure 1a,[10] where the distance from a point to the equilibrium potential (the horizontal solid line) represents the overpotential to drive the ORR at high current density. This plot exhibits a volcano shape and an ideal catalyst should lie at the peak, at which point the overpotential is minimum. The notion behind this volcano plot is that the optimal catalyst should have optimum binding strength to the intermediates, neither too strongly nor too weakly, as firstly proposed by Sabatier a century ago.[11] For metals bind the oxygen-containing species too strongly, the activity is limited by the desorption of the products. On the other hand, for metals bind the oxygen too weakly, the activation of the reactants becomes problematic.

As depicted in Figure 1a, among the investigated metals, Pt(111) is close to the top of the volcano plot. Given that Pt(111) lies to the left of the peak, further weakening the binding of oxygen-containing intermediates on the surface can push its ORR activity higher. This has been achieved by altering the electronic structure of Pt by the way of alloying with non-precious transition metals. Figure 1b plots the calculated ORR activities of Pt$_3$M alloys as a function of the HO binding energy relative to platinum.[12] The plot shows nickel and cobalt are two metals that have optimal effect in tuning the binding energy of oxygen-containing species on Pt.
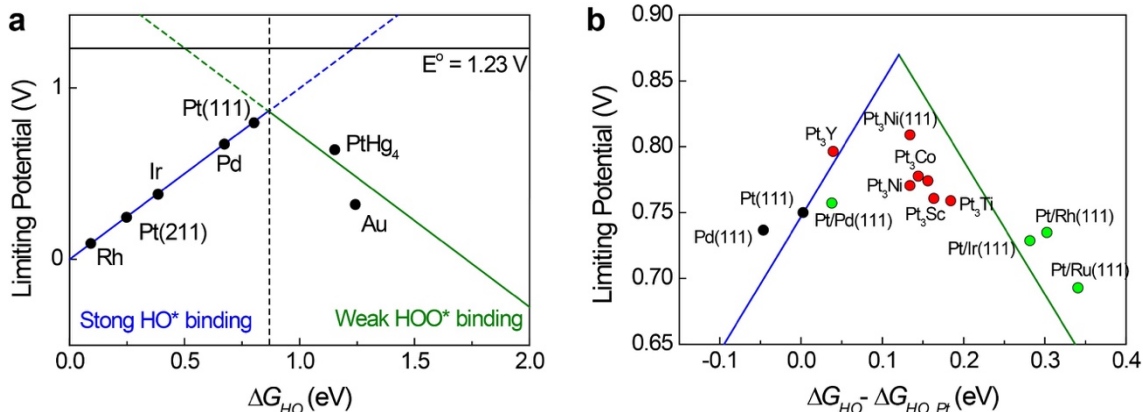
Figure 1. Trends in ORR limiting potentials plotted as a function of HO binding energy for monometallic surfaces (a) and Pt-based bimetallic surfaces (b). Blue line represents the strongly bound HO* region and the green line represents weakly bound HOO* region. The difference between the equilibrium potential of 1.23 V (black line) and the limiting potential is the theoretical overpotential. Reprinted with permission from ref [10]. Copyright 2018 American Chemical Society.

The d-band model, developed by Hammer and Nørskov,[13,14] has proven particularly helpful in understanding the alloying effects on the oxygen adsorption on Pt surface. The dissolution of non-precious metals is ubiquitous under PEMFC operation conditions, leaving a unique Pt-enriched surface with the alloying metals in sublayers. A compressive strain will be induced on surface Pt when the subsurface alloying metal is of smaller lattice constant than Pt. As a result, the d-band of surface Pt broadens due to enhanced wave-function overlap, and moves down in order to preserve its extent of d-band filling.[14] The downshift of the d-band center of surface Pt eventually leads to an increased occupation of the antibonding, and thus the destabilized Pt-oxygen interaction. The d-band model is also applied to explain the low ORR activity of undercoordinated surface sites (Figure 2).[15] Atoms on edge and corner are surrounded by less neighboring atoms, which causes a band narrowing and an upshift of the d-band center. The anti-bonding states will become emptier, leading to a stronger binding to oxygen-containing intermediates.

Figure 2. Projected densities of states (DOS) onto the d-states of different Pt surfaces with

decreasing atom density. Reprinted with permission from ref [15]. Copyright 2014 John Wiley & Sons.

2.2. ORR activity on extended surface

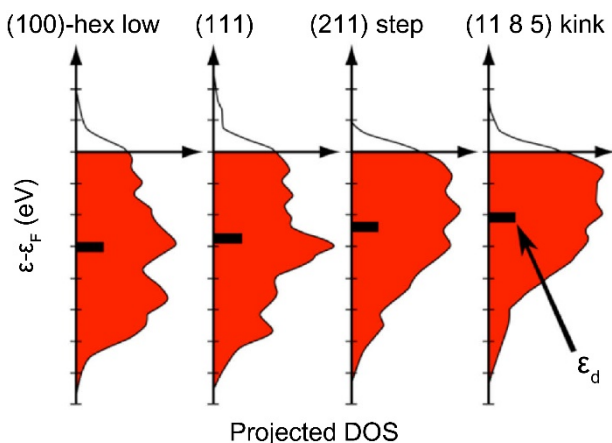Extended surface catalysts include two-dimensional single-crystalline or polycrystalline bulk surfaces as well as thin films. These surfaces afford a model system to investigate the effects of different structural parameters on the ORR activities, such as crystal facet, near-surface composition, surface segregation, etc. The results can be further compared with the theoretical predictions, providing valuable design principles for realistic nanoparticle ORR catalysts.

The ORR activities on single-crystalline Pt surfaces have been extensively studied. The ORR activity on low index Pt surface has been demonstrated to be in the order of Pt(100) < Pt(111) < Pt(110) in perchloric acid (HClO$_4$),[16] while in sulfuric acid (H$_2$SO$_4$) it follows the order of Pt(111) < Pt(110) < Pt(100).[17] The difference is attributed to the stronger adsorption of SO$_4^{2-}$ on Pt(111) than on Pt(100). High index Pt surfaces were also systematically investigated in acidic media.[18-22] It was found that the ORR activity grows with the increased density of step on the surface with (111) terrace,[18,20] while being independent on the step density with (100) terrace.[20] The fact that stepped surface is more catalytically active than Pt(111) is contradicted to theoretical predictions. This difference between the experimental and theoretical ORR activity remains elusive. A recent study introduces the concept of "generalized" coordination number as a geometric descriptor to predict the structure of optimal active sites.[23,24] The "generalized" coordination numbers of the active sites are calculated taking the second-nearest neighbors into consideration. According to this model, the concave sites at the step bottoms are more coordinated than Pt(111) and thus present higher activity.[24]
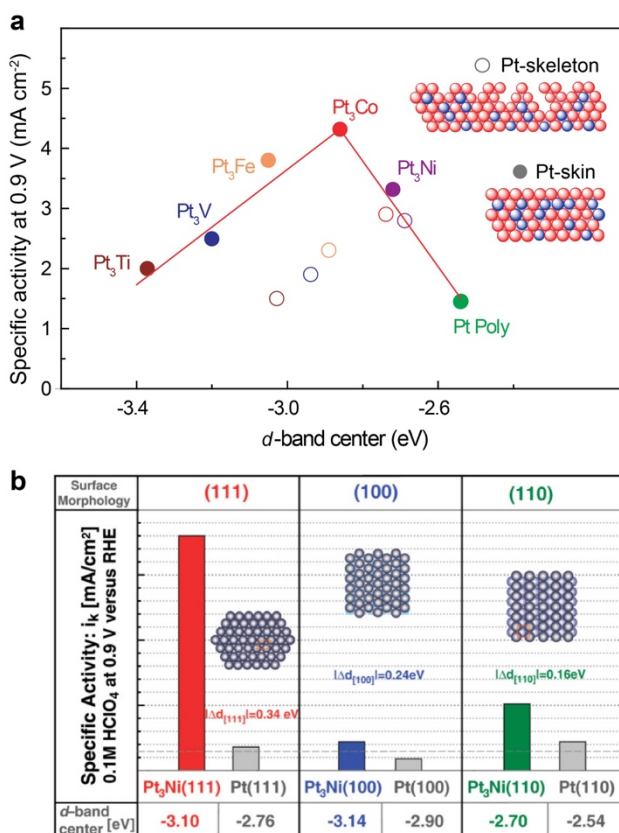
Figure 3. (a) Relationships between experimentally measured specific activity for the ORR on Pt₃M surfaces *versus* the d-band center position for the Pt-skin and Pt-skeleton surfaces. Reprinted with permission from ref.[25] Copyright 2007 Macmillan Publishers Limited. (b) Influence of the surface morphology and electronic surface properties on the kinetics of ORR. Reprinted with permission from ref.[26] Copyright 2007 the American Association for the Advancement of Science.

The effect of alloying was thoroughly examined on extended Pt-based alloy surfaces.[25,27] As mentioned in the previous section, the binding energy of oxygen-containing species on Pt(111) surface can be weakened by alloying with 3d-transition metals (3d-TMs). The measured ORR activity on polycrystalline Pt₃M alloy films is in line with theoretical predictions.[12] It shows that Pt₃Co has the highest ORR activity, followed by Pt₃Fe and Pt₃Ni (Figure 3a). In addition to 3d-TMs, rare earth metals (REMs) were identified as another type of alloying elements to enhance both the ORR activity and stability of Pt-based catalysts.[28] Experiments on polycrystalline surface[28-30] and thin films[31-33] have shown that the specific activities of Pt–REM alloys with yttrium (Y), gadolinium (Gd), samarium(Sm) and terbium (Tb) were enhanced by a factor of 5–10 over pure Pt. In light of the larger covalent radii of rare earth metals than Pt, a tensile strain was intuitively expected to be induced on the Pt–REM surface, which would lead to a stronger Pt-O interaction and thus higher overpotential for ORR. However, the extended X-ray absorption fine structure measurements (EXAFS) on Pt-Y catalysts indicate a lower Pt–Pt distance relative to pure Pt, namely, a compressive strain in Pt-Y.[34] Density functional theory (DFT) calculations suggest that the larger rare earth atoms can distort the closely packed structure of Pt, allowing more Pt

atoms to be accommodated onto the Pt overlayer than onto bulk Pt.[30,34]

Studies on extended surfaces have revealed that the near-surface structures of Pt-based alloys have profound influence on their ORR activities. Stamenkovic et al. prepared Pt_3M alloy surface under ultrahigh-vacuum through several sputtering/annealing cycles.[25] The composition of surface atomic layer was characterized by low-energy ion scattering (LEIS) and the electronic surface structure was studied by ultraviolet photoemission spectroscopy (UPS). While the as-sputtered Pt_3Fe surface had a surface composition the same to the bulk, the annealed Pt_3Fe surface presented a Pt enrichment on the topmost atomic layer and then a Pt depletion in the next two to three sublayers (Figure 3a). It was termed "Pt-skin".[12,25,35] The d-band center of the annealed Pt_3Fe with Pt-skin presented a downshift compared to the sputtered surface. Moreover, Fe dissolved from sputtered surface when in contact with acidic electrolyte, leaving a "Pt-skeleton" (Figure 3a), whereas the annealed surface with Pt-skin was quite stable under electrochemical environment. The electrocatalytic ORR activity on bulk Pt, Pt-skeleton and Pt-skin surfaces follows the order of Pt < Pt-skeleton < Pt-skin. In the meantime, the same group demonstrated a 10-fold activity enhancement of extended $Pt_3Ni(111)$–Pt-skin surface over Pt(111) (Figure 3b).[26] These results highlight the importance of near-surface composition and atomic structure in leveraging the activity of ORR catalysts.

2.3. From extended surface to nanoscale surface

The theoretical simulations and experimental studies on extended surfaces have outlined several key parameters that determine the ORR activity of Pt-based catalysts and provided some general principles for catalyst design. In order to achieve high utilization of precious Pt, the real-world catalysts are mostly tailored at the nanoscale. From the model extended surfaces to the real nanoscale surfaces, complexity increases. Particle size effects need to be considered before the knowledge acquired on extended surface can be used as design guidance for nanostructured catalysts.

2.3.1. Size effects

The properties of materials can change dramatically when scaling down their sizes. The first thing under consideration is the surface-to-volume ratio. The fraction of surface atoms, i.e. the ratio between surface atoms and the total atoms in a particle, increases exponentially as the particle size decreases to sub-10 nm scale.[36] Almost all the atoms are exposed at surface when a metal particle shrinks to one nanometer. Compared to atoms in the bulk, the surface atoms are under-coordinated and therefore are less stable. As a consequence, the melting point decreases with the decrease of particle's radius (Figure 4a).[37] For example, gold nanoparticles of 2 nm start melting at 800 K,[38,39] hundreds of degrees lower than the bulk form (1337 K). It is worth noting that the surface diffusion rate of metals roughly scales with melting point,[40,41] which often helps us evaluate the stability of nanostructures.
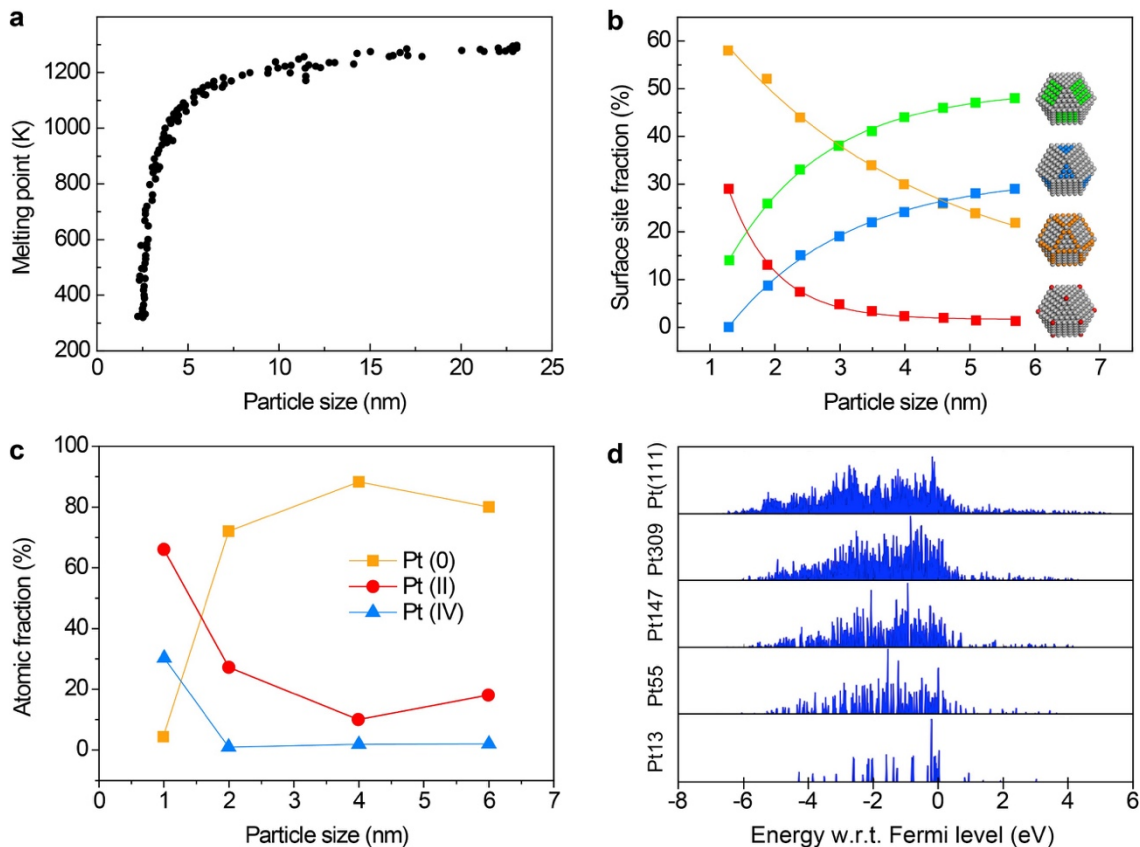
Figure 4. Size-dependent properties of metal nanoparticles. (a) Melting point of gold particles. Reprinted with permission from ref.[39] Copyright 1976 American Physical Society. (b) Percentages of different types of surface atoms (based on a cuboctahedron model). Reprinted with permission from ref.[42] Copyright 2012 American Chemical Society. (c) Oxidation state distribution of Pt as estimated from deconvolution of Pt 4f XPS peaks. Reprinted with permission from ref.[43] Copyright 2013 American Chemical Society. (d) Projected d-density of states for surface (111) platinum atoms averaged over all platinum atoms in the (111)-like face on clusters. Reprinted with permission from ref.[44] Copyright 2013 American Chemical Society.

The distribution of surface sites (e.g., terrace, steps, edges, corners, etc.) also changes with the particle size. As shown in Figure 4b,[42] the fraction of terrace atoms decreases continuously when decreasing the particle size. By contrast, the atoms at edges and corners, which have fewer direct neighbors than terrace atoms, gradually increase and become dominant when the size is approximately down to 2 nm.[45] Given that the decrease of coordination number can cause an upshift of the d-band center, the adsorption energies of oxygen-containing species on nanoparticles often exhibit a shift compared to their bulk counterparts. The O and HO adsorption energies on bulk Pt(111) and Pt nanoparticles have been compared using DFT. It was found the adsorption energies of O and HO change significantly by as much as 1 eV from bulk surface to 1 nm nanoparticle surface.[46] The stronger binding of oxygen-containing species on low-coordination sites leads to the size-dependent surface oxidation state. X-ray photoelectron spectroscopy (XPS) measurements of Pt nanoparticles have shown more oxidized Pt species on small particles than

large ones. For a particle with 1 nm in size, nearly 96% of Pt is in oxidized states (Figure 4c).[43] Meanwhile, it has been demonstrated that electrochemical reduction potentials of the surface oxide on Pt nanoparticles continuously shift towards lower potentials compared to the characteristic value for polycrystalline Pt foils as the particle size decreases.[47,48]

Another consequence of size effects is that alloys and phases not exist in bulk may become feasible at nanoscale. When the size of metallic particles decreases, the nonequilibrium phase can be kinetically trapped under ambient conditions or be stabilized as a result of the alteration of thermodynamic properties.[49-52] There are several examples of intrinsically-immiscible elements readily mix in finite particles,[53,54] such as Ag-Pt,[49] Ag-Co,[50] Rh-Ag and -Au,[55] Pd-Ru,[56] Au-Ni,[57] Pd-Pt,[58] Ag-Ni,[59] high-entropy-alloys,[51,60] and so on. In addition to these new solid solutions, the crystal structures of monometals could also be different in the nanometer region.[61] While bulk Au exclusively takes face-centered cubic (fcc) structure, hexagonal-close packed (hcp) structure is discovered in the nanostructure form.[62] Other examples include Rh,[62,63] Ru,[64] Ag,[65] Ni,[66,67] to name a few. These novel alloys and phases expand the material pool, and some have been proven to be potential ORR catalysts.[50]

The electronic structure of a metal changes accompanying the size reduction. An ultra-small nanoparticle could behave like a molecule instead of a metallic state (Figure 4d). Such metal–nonmetal transition occurs when the size of Pt is below 147 atoms (ca. 1.6 nm) according to DFT calculations.[44] The d-electron DOS of Pt clusters smaller than 1.6 nm is discrete, while a more continuous band of states is formed above 1.6 nm.[44] The molecule-like electronic state of Pt clusters exhibit stronger O adsorption energy than nanoparticles with larger sizes.[44,68]

2.3.2. Size dependent ORR activity and stability

The size-dependence of specific ORR activity (per unit surface area) has been a debate for a long time. Given that oxygenated species have stronger adsorption on low coordination sites that are populated in smaller nanoparticles, the specific ORR activity is expected to decrease as particle size decreases. This has been verified by many groups.[69-73] In contrast, other experimental results show negligible difference in specific activity.[74-76] Arenz et al. examined the influence of particle size on the ORR activity of Pt.[76] They found the ORR activities of Pt nanoparticles between 1 and 5 nm have very little variation. The contradictory observation of size-related ORR activity may come from the different catalyst preparation methods and activity evaluation protocols.

In fact, the study of the particle size effect on ORR activity requires the tight control over the size distribution of the investigated materials, while keeping the other structural parameters the same. Shao and Peles et al. carefully prepared carbon-supported Pt particles in the range of 1-5 nm using layer-by-layer growth by a Cu-UPD-Pt replacement technique, where UPD represents underpotential deposition.[72] The particle size distribution and particle dispersion on carbon support were well controlled. They have shown that the specific activity increases rapidly as the particle size grows to 2.2 nm and then reaches a plateau, while the mass activity increases from 1.3 nm to

2.2 nm, arrives at a summit at 2.2 nm, and then decreases as particle size further grows (Figure 5a). The reduced specific activity for Pt particles smaller than 2.2 nm is in good agreement with DFT calculations which suggest stronger Pt-O bond on low-coordination surface sites.[44,46]
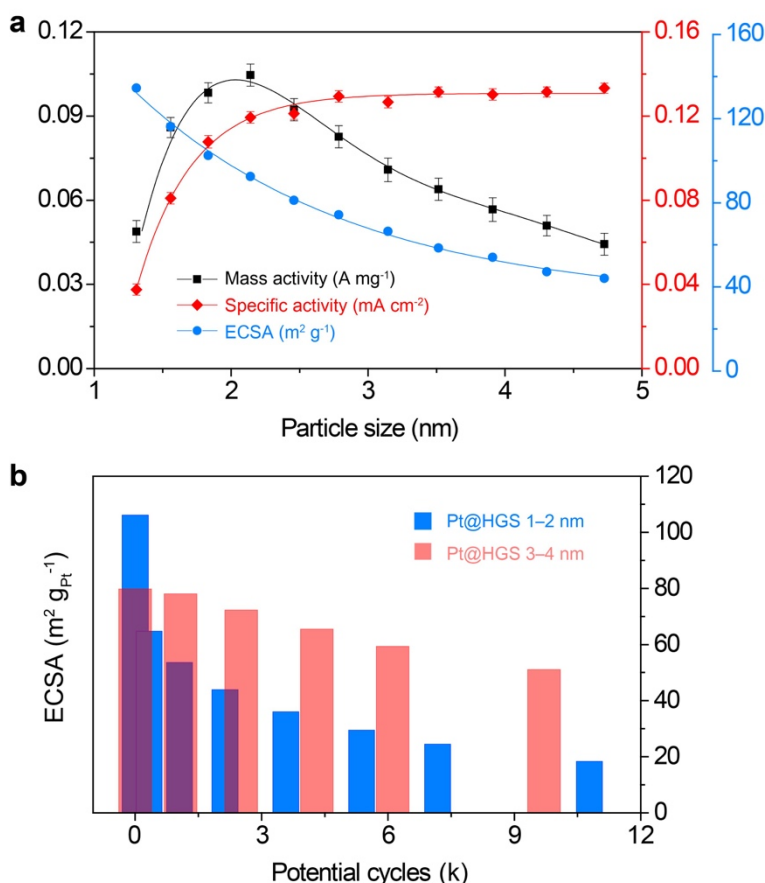
Figure 5. (a) Size-dependence of electrochemical active surface area (ECSA, blue circle), specific activity (red diamond), and mass activity (black square) of Pt/C. Reprinted with permission from ref.[72] Copyright 2011 American Chemical Society. (b) Degradation of ECSAs after representative potential cycles for Pt@HGS 1–2 nm and Pt@HGS 3–4 nm. Reprinted with permission from ref. [77] Copyright 2014 Beilstein-Institut.

Markovic et al. underlined the importance of using sufficiently well-defined materials to correlate particle size with ORR activity.[73] Uniform cuboctahedral Pt particles with sizes of 2.8 ± 0.4 nm, 4.1 ± 0.5 nm, 5.1 ± 0.4 nm, and 7.2 ± 0.6 were prepared using colloidal synthesis. By carefully controlling the particle dispersion on carbon and the electrochemical conditions, they have shown that the specific activity increases with increasing nanoparticle diameter, while the mass activity follows a volcano shape peaking at 4.1 nm. Their study also suggested the particle size effect is constantly evolving under moderate potential cycling, due to potential-induced Pt dissolution/redeposition and consequently a broadening of the particle size distribution.

Size-dependent stability of Pt-based ORR catalysts is another important issue.[78] Studies have shown that smaller nanoparticles suffer more severe Pt dissolution under fuel cell conditions.

Meier and Mayrhofer et al. compared the degradation of hollow graphitic sphere (HGS)-supported Pt catalysts with different particle sizes of 1–2 nm and 3–4 nm, respectively.[77] The electrochemically active surface areas (ECSAs) of the two materials were recorded during a stability test by imposing potential cycles between 0.4 and 1.4 V. After about 10000 degradation cycles, the Pt@HGS 1–2 nm lost 83% of its initial ECSA, whereas the Pt@HGS 3–4 nm lost only 34% (Figure 5b). In-depth analysis of CO-stripping features led to a conclusion that the ECSA loss is related to the dissolution of smallest nanoparticles in Pt@HGS 1–2 nm, which was also suggested by previous studies.[74,79] This conclusion was further confirmed by identical location transmission electron microscopy (TEM). The strong tendency to dissolution of Pt nanoparticles less than 2 nm can be explained by their higher faction of low-coordinated sites on surface as well as higher oxidation state. The dissolved Pt can be redeposited on larger particles, resulting in a growth of particle size. This process is known as Ostwald ripening. To circumvent catalyst degradation caused by Pt dissolution and Ostwald ripening, it is of primary importance to aim for larger particles (> 2nm) with great uniformity.

The investigation of the particle size effect of Pt alloys on ORR activity asks for more stringent requirement for the material control. Parameters such as composition, degree of alloying, and near-surface structure have to be taken into consideration. Stamenkovic et al. systematically studied the ORR activity of monodisperse Pt_3Co nanoparticles with average sizes of 3, 4.5, 6, and 9 nm.[80] The specific activities of Pt_3Co increase as the particle size grows larger. The cyclic voltammograms show that the smaller particles are oxidized at lower potentials, an indicator of stronger adsorption of oxygenated species. As a result of the balance between the specific surface area and activity, the maximum mass activity was established to be around 4.5 nm. Xia et al. finely controlled the edge length of Pt-Ni octahedral particles at a constant Pt/Ni atomic ratio around 2.4.[81] The specific ORR activities of these octahedra increased monotonically as the edge length increased from 6 to 12 nm, while the maximum mass activity was achieved at an edge length of 9 nm.

In contrast to the monotonic increase of the specific ORR activity with increasing particle size as demonstrated in pure Pt and Pt-rich alloys, an unusual volcano-shaped dependency of specific activity and stability on the particle size of Ni-rich $PtNi_3$ was established.[82] Strasser et al. prepared a series of uniform $PtNi_3$ nanoparticles with sizes of 3.2, 5.3, 6.7, 7.8, and 9.6 nm, respectively. It was found that the particles with sizes of 6.7 and 7.8 nm showed highest ORR specific activity and stability. A size-dependent Ni dissolution mechanism was suggested to play a more determining role than the surface coordination effect. These results highlight the complexity size-dependent activity and stability of bimetallic catalysts towards ORR.

2.4. Nanostructured Pt-based catalysts

The theoretical and experimental studies on extended model surface, together with the understanding of size-dependent ORR performance, have laid a foundation for the rational design of practical catalysts. Tremendous progress has been made in making high-activity ORR catalysts by controlling the surface and interface structures at the nanoscale. In this section, we will spotlight

some of the works according to three different catalyst categories, including alloys, core-shell structures, and open architectures.

2.4.1 Alloy nanoparticles

Pt-based alloys have attracted a lot of research interest in the development of cost-effective and high-performing ORR catalysts. The alloying elements not only reduce the amount of precious Pt but also enhance the catalytic activity of. However, mass production of fuel cell stacks requires further reduction of Pt loading. Many studies have been put forth to develop more active and stable alloy catalysts.

2.4.1.1. Composition control. The volcano relationship established for extended surface (Figure 1b, Figure 3a shows that Pt_3Ni and Pt_3Co are close to the optimal binding strength towards oxygen-containing species. Similar trend has been validated for high-surface-area nanoparticle catalysts. Stamenkovic et al. developed a general approach for the synthesis of monodisperse Pt_3M (M = Fe, Ni, Co) alloy nanoparticles with controlled particle size being constantly around 5 nm.[83] The ORR activity follows the order of $Pt_3Co > Pt_3Ni > Pt_3Fe$ (Figure 6a), with improvement factors of 2-3 against Pt/C. The same group also synthesized a series of Pt-Ni alloy particles of various Pt/Ni atomic ratios (that is, Pt_3Ni, PtNi, $PtNi_2$, and $PtNi_3$) using the same synthetic protocol.[84] The particle sizes were controlled to be about 5 nm for all compositions. The catalytic activities towards ORR exhibit a volcano-like dependence on the initial composition (Figure 6b). Among the four different alloy compositions, PtNi possesses the highest specific and mass activities. Post-mortem analysis has correlated the observed ORR trend with the remained Ni content and the thickness of Pt-skeleton structure. In another study, Strasser and co-workers developed a CO adsorption-assisted method to make homogeneous Pt-Ni alloys with sizes confined to 4 nm over a wide composition range from $Pt_{85}Ni_{15}$ to $Pt_{30}Ni_{70}$.[85] A monotonic dependence of the ORR activity on the initial Ni content was established (Figure 6c). The activity trend is coincident with the Ni content left in the particle after electrochemical activation and is further correlated with the associated lattice strain. The above-mentioned two studies both suggest that the Ni composition retained in the particle can serve as a descriptor for ORR activity.

In contrast to Pt–3d-TM, the compositional control of Pt–REM alloys is difficult because of REM element's extremely-high oxygen affinity and negative reduction potential. Chorkendorff and Stephens et al. developed the synthesis of size-selected (4, 5, 7, and 9 nm) Pt_xY nanoparticles by a gas aggregation technique.[86] The 9 nm Pt_xY displayed the highest mass activity (3.05 A mg_{Pt}^{-1}). The gas aggregation method was successfully extended to the synthesis of Pt_xGd nanoparticles, in which case the maximum mass activity was found to be 3.6 A mg_{Pt}^{-1} with 8 nm particle.[87] It should be noted that the crystal structures of both Pt_xY and Pt_xGd prepared by gas aggregation are lack of long-range order. Although some progress has been achieved in scalable synthesis of Pt–REM alloy nanoparticles,[88,89] the material control needs further improvement.
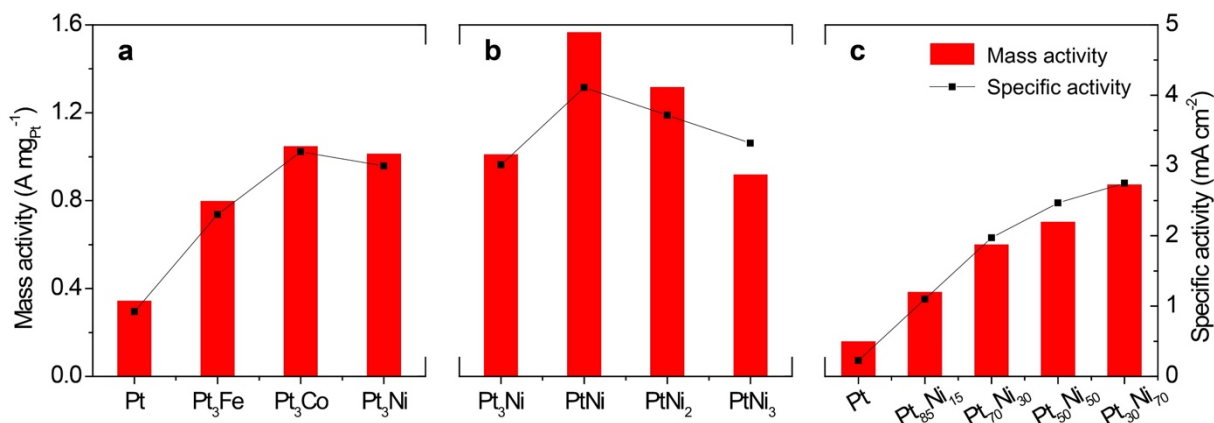
Figure 6. (a) The dependence of specific activity (black square) and mass activity (red bar) on the types of alloys with uniform sizes of 5 nm. Reprinted with permission from ref. [83] Copyright 2011 American Chemical Society. (b) The dependence of specific activity (black square) and mass activity (red bar) on the compositions of Pt-Ni alloys with uniform sizes of 5 nm. Reprinted with permission from ref.[84] Copyright 2011 Wiley-VCH Verlag GmbH & Co. KGaA, Weinheim. (c) The dependence of specific activity (black square) and mass activity (red bar) on the compositions of Pt-Ni alloys with uniform sizes of 4 nm. Reprinted with permission from ref. [85] Copyright 2014 American Chemical Society.

2.4.1.2. Shape control. Pt alloy nanocrystals enclosed by basal planes have been studied extensively. Cubic,[90-96] octahedral,[81,92,97-104] truncated octahedral,[92,102] tetrahedral,[95] and icosahedral[105] Pt alloys have been achieved thanks to the development of shape-controlled synthesis. Shape-directing agents are often employed to deliver the desired morphologies. It has been shown that the ORR activity increased monotonically with the fraction of (111) facets in weakly-adsorbing electrolyte ($HClO_4$),[102,103] which is consistent to what has been demonstrated on extended surfaces.

Octahedral Pt_3Ni particles, which are exclusively enclosed by (111) facets, represent a nanoparticulate replica of extended Pt_3Ni(111) surface, and thus have received enormous research interest. Indeed, the Pt_3Ni octahedra have reached significantly high specific activity when compared to commercial Pt/C. For instance, Xia et al. described the synthesis Pt-Ni octahedra of 6, 9, and 12 nm, respectively, using $W(CO)_6$ as a source of CO.[81] The 9 nm octahedra have a specific activity of 51-fold higher than that of the state-of-the-art Pt/C, together with a high mass activity of 3.3 A mg_{Pt}^{-1} at 0.9 V (all potentials are given *versus* reversible hydrogen electrode).[81,97] Figure 7a summarizes the mass activities of Pt-Ni octahedra as a function of ECSAs based on rotating disk electrode (RDE) measurement reported in literatures.[81,97,99,100,103,106-108] In general, the low ECSAs and poor stability of octahedral Pt_3Ni are two major problems that limits their performance in membrane electrode assemblies (MEAs). A sufficiently high ECSA is required for low-Pt PEMFC to warrant high-power performance.[109] The edge lengths of Pt-Ni octahedral particles are often around 10 nm,[92,97-99,103,110] with ECSAs below 50 m^2 g_{Pt}^{-1}. Recent studies have achieved Pt-Ni octahedra with edge lengths as small as 4 nm, and ECSA up to 67 m^2 g_{Pt}^{-1}.[100,108]

The morphology of octahedral Pt-Ni is not stable under electrochemical conditions. They evolve to rounded particles or concave structures after durability test.[73,100,111] Surface doping with a third metal such as Rh, Ga, and Mo has been shown to be effective in maintaining the octahedral shape in a long-term electrochemical measurement.[100,107,112] Mo has been demonstrated to suppress the dissolution of Ni in acidic media.[113] In Mo-doped Pt_3Ni octahedra, DFT calculations suggested that there is a strong tendency for Mo to segregate onto vertex sites of octahedra, stabilizing both Ni and Pt atoms through the formation of relatively strong Mo–Pt and Mo–Ni bonds.[100] A recent study by Cho and co-workers have systematically compared the morphological and compositional evolutions of Pt-Ni octahedra with and without Ga modification (Figure 7b).[107] It revealed that the majority of Pt-Ni particles incorporated with < 2 at. % of Ga maintained their octahedral shape after 30k cycles, while the Pt-Ni counterparts became spherical after only 4k cycles. The distribution of Pt, Ni, and Ga throughout the surface of Ga-doped Pt-Ni octahedra remained nearly the same up to 12k cycles, and then a Pt-rich surface was recorded after 30k cycles. The Ni content in Ga-doped Pt-Ni octahedra were kept above 30 at. % throughout the entire stability test. In contrast, the Ni content in Pt-Ni octahedra decreased to 10 at. % after 30k cycles.
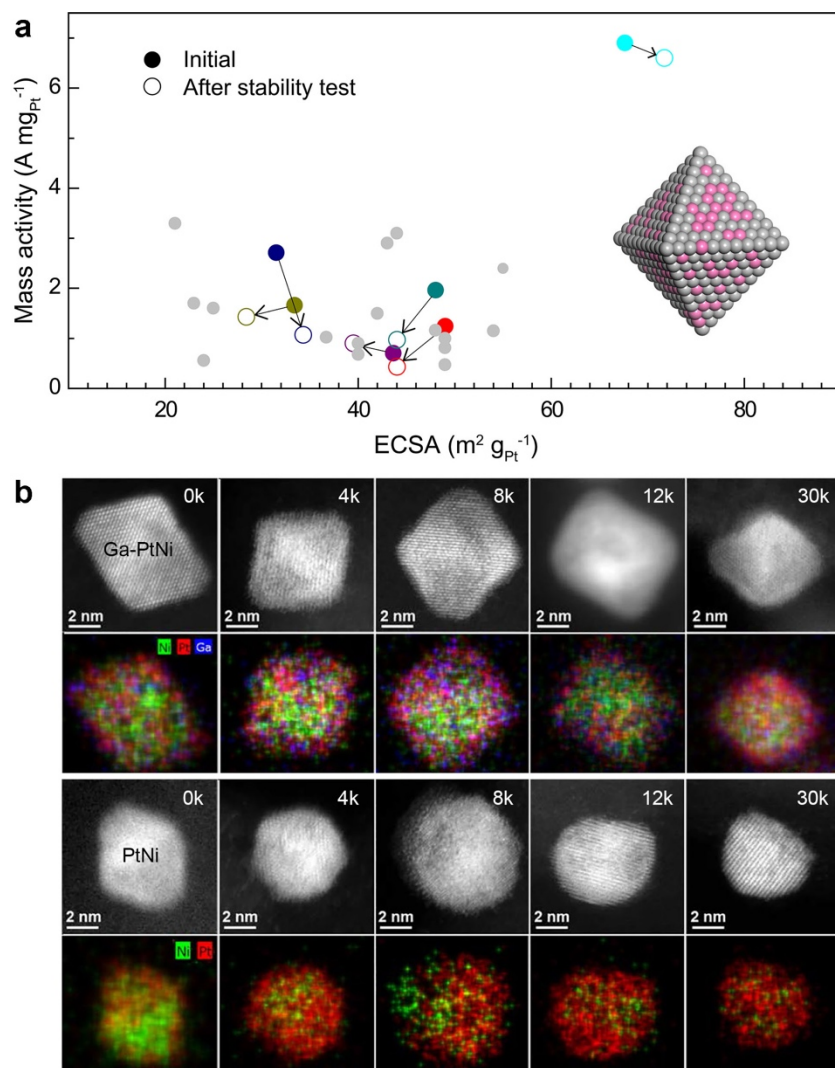
Figure 7. (a) Mass activity at 0.9 V as a function of ECSA for Pt-Ni octahedral particles reported in literatures. [81,97,99,100,103,106-108] Solid and open circles represent initial and final mass activities, respectively. (b) HAADF-STEM and EDX elemental mapping images of Ga-doped Pt-Ni octahedra and Pt-Ni octahedra during stability tests. Reprinted with permission from ref.[107] Copyright 2018 American Chemical Society.

In addition to octahedra, one-dimensional (1-D) nanostructures have also attracted a lot of attention. Compared with nanoparticles, 1-D structural motif is less vulnerable to aggregation[114-116] They have been demonstrated to have less ECSA loss than conventional nanoparticles during durability test.[114-116] Moreover, the 1-D nanostructures can form inter-connected and conductive networks, which greatly reduce the thickness of catalyst layer in MEA by eliminating carbon support.[117-120] Templates are often used in the preparation of 1-D Pt alloys.[121] Transition metal nanowires such as Ag,[120] Cu,[122-124] and Ni[125,126] are the most popular templates. Pt can be deposited onto the metal nanowires via galvanic replacement, a process that Pt ions are reduced at the

expense of the oxidation and dissolution of the less-noble transition metals. Although galvanic replacement allows the access of 1-D Pt alloys with great efficiency and versatility, the products are often characterized by ill-defined surfaces and interfaces.[120,122-126] Alternatively, 1-D Pt alloys have also been made via template-free colloidal synthesis.[127-130] Huang et al. described a general method for the production of Pt-M (M = Ni, Fe, Co, Rh) alloy nanowires (Figure 8a,b).[131,132] The as-made Pt-Ni nanowire exhibit a specific activity of 9.2 mA cm^{-2} and a mass activity of 4.15 A mg$_{Pt}^{-1}$ at 0.9 V. Duan et al. reported jagged Pt nanowires made by electrochemical dealloying of Pt-Ni alloy nanowires.[133] The jagged nanowires exhibit a remarkably high specific activity of 11.5 mA cm^{-2} and a mass activity of 13.6 A mg$_{Pt}^{-1}$ at 0.9 V (Figure 8c–f).
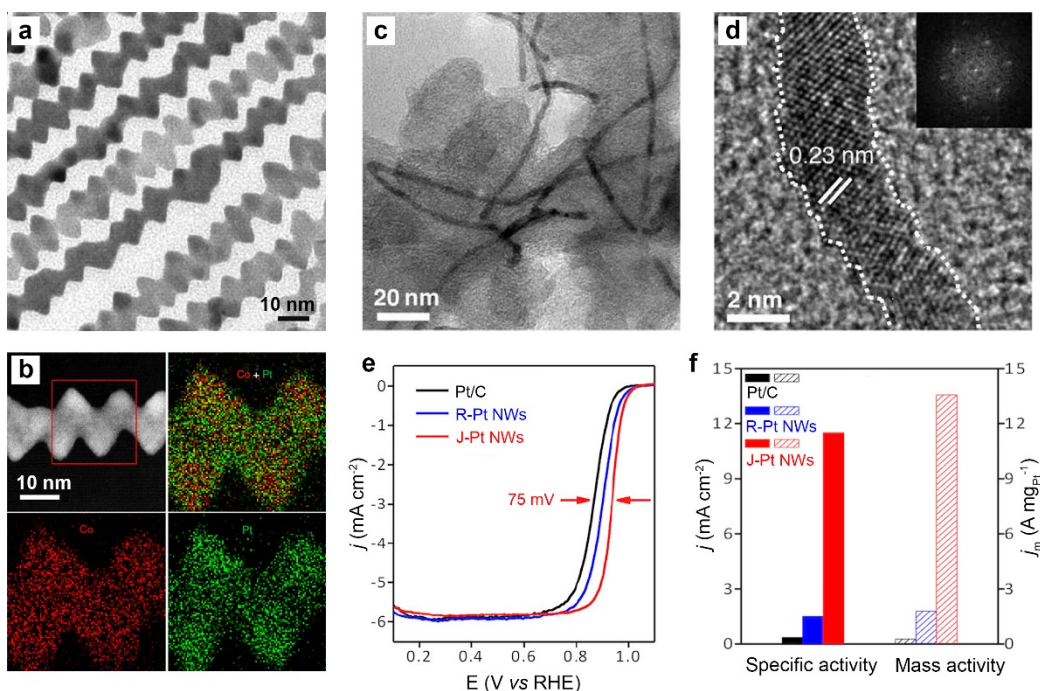
Figure 8. TEM image (a) and HAADF-STEM and EDX elemental mapping images (b) of hierarchical Pt-Co nanowires. Reprinted with permission from ref.[132] Copyright 2016 Macmillan Publishers Limited. TEM image (c), HRTEM image (d), ORR polarization curves (e), and the specific activities and mass activities (f) of jagged Pt nanowires. Reprinted with permission from ref.[133] Copyright 2016 the American Association for the Advancement of Science.

2.4.1.3. Phase control. Ordering and segregation are two processes observed in binary alloy systems. They are in relation to the electronic structures of electrocatalysts. Ordering of a random alloy leads to an intermetallic compound with defined stoichiometry and long-range order in crystal structure. In contrast, phase segregation results in enrichment of constituent atoms at a microscopic region. The two processes are determined by the interplay between lattice mismatch, mixing enthalpy and surface energies of each elements.
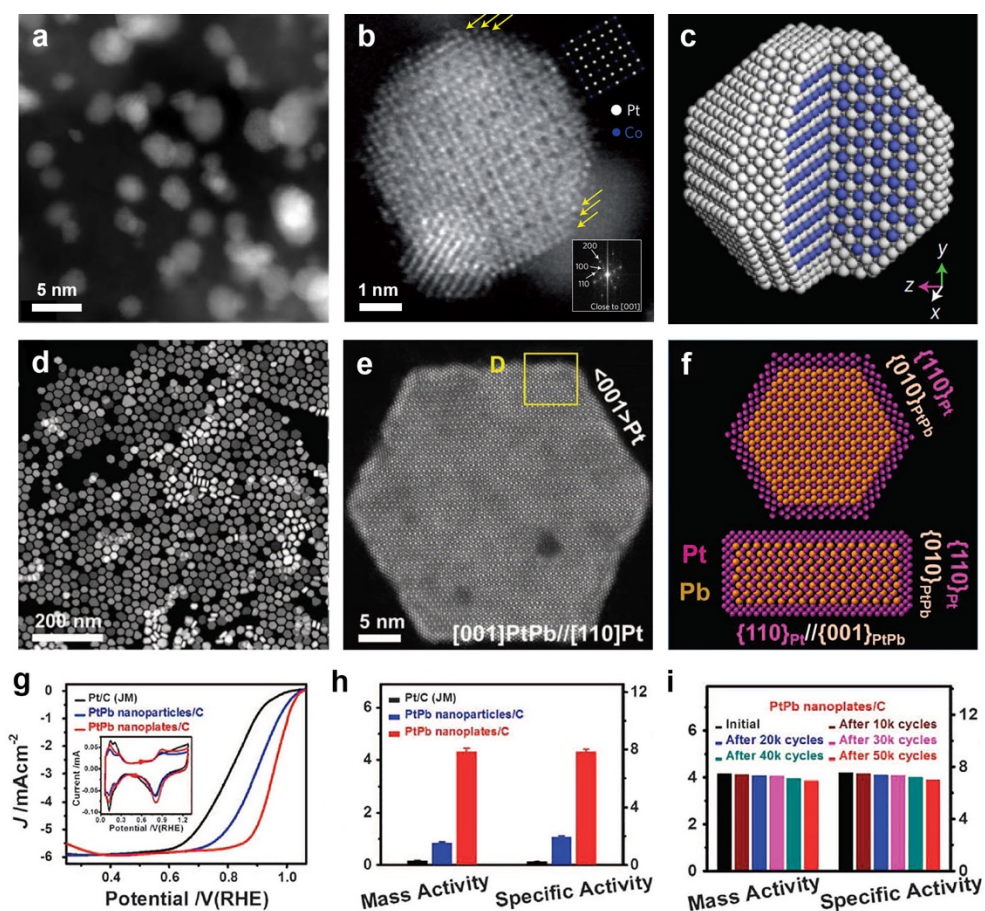
Figure 9. HAADF-STEM images (a, b) and the structure model (c) of Pt_3Co intermetallic nanoparticles with a 2-3 atomic-layer-thick Pt shell. Reprinted with permission from ref.[134] Copyright 2013 Macmillan Publishers Limited. HAADF-STEM images (d, e), structure model (f), ORR polarization curves (g), specific activities and mass activities (h), and the stability (i) of PtPb intermetallic nanoparticles with a 4 atomic-layer-thick Pt shell. Reprinted with permission from ref.[135] Copyright 2016 the American Association for the Advancement of Science.

Intermetallics (or ordered alloys) have been a long-standing research topic in search of active and durable ORR catalysts. The disorder-order transformation of Pt-M usually takes place at high temperatures. To prevent particle sintering during thermal annealing, pristine Pt-M particles were often coated by protective shells such as metal oxides,[136,137] carbon,[138] molten salts,[123,139] and so on. A variety of Pt intermetallics (Pt-Fe,[136,138-140] Pt-Co,[134] Pt-Cu,[141] Pt-Cr,[142] Pt-Ni,[139,143] Pt-Pb[135,144,145]) have been achieved and investigated for ORR. In a study of Pt_3Co particles, Abruña et al. annealed Pt_3Co particles at different temperatures. Atomic-resolution electron microscopic analysis of the particles annealed at 700 °C (Pt_3Co-700) suggests a unique structure composed of an ordered Pt_3Co core and a 2-3 atomic-layer-thick Pt shell (Figure 9a).[134] The Pt shell over the intermetallic core has a 0.8% smaller lattice constant than Pt_3Co random alloy, and thus exhibits a specific activity of 1.1 mA cm^{-2} at 0.9 V, over 3-fold increase compared with Pt_3Co alloy and Pt/C.

19

More importantly, the Pt shell and the ordered Pt_3Co core make these nanoparticles very stable, as evidenced by a minimal activity loss after 5000 potential cycles. A recent study by Huang et al. disclosed that ordered PtPb nanoplates take a similar core-shell structure with four atomic-layer-thick Pt shell on intermetallic PtPb core (Figure 9b).[135] The PtPb nanoplates have a specific activity of 7.8 mA cm^{-2} and a mass activity of 4.3 A mg$_{Pt}^{-1}$ at 0.9 V, with negligible activity decay after 50000 potential cycles. Tensile strains on Pt(110) were proposed to account for the enhanced ORR activity.

Surface segregation plays a pivotal role in determining the catalytic and chemical properties of alloys. As mentioned earlier, a "Pt-skin" structure has been established on $Pt_3Ni(111)$ by thermal treatment of Pt_3Ni in ultra-high vacuum (UHV).[26] The annealed $Pt_3Ni(111)$ surface shows an oscillating compositional profile, with the outermost layer being comprised of pure Pt and the subsurface layer being enriched by Ni compared with the bulk composition. The extended $Pt_3Ni(111)$–Pt-skin shows 90 times higher specific activity than the state-of-the-art Pt/C catalysts .[26] This exceptional activity have encouraged a pursuit of the Pt-skin structure on nanoparticles.[146-149] Stamenkovic et al. have demonstrated that the adsorption properties of the Pt-skin structures are significantly altered compared with monometallic Pt.[150] The study shows that the adsorption of underpotentially deposited hydrogen (H_{upd}) is suppressed on Pt-skin surface (measured as charge) while the surface coverage of CO_{ad} is not affected. As a result, the ratio between the charges of CO stripping (Q_{CO}) and H_{upd} ($2Q_H$) is approximately 1.5 on Pt-skin surfaces. The $Q_{CO}/2Q_H$ ratio has been used as an easy way to identify the formation of the Pt-skin structure. To replicate the Pt-skin structures on nanoparticles, post-synthesis thermal treatment has been proven to be a necessary step. The resultant surface structure and composition of Pt-M alloys are dependent on the annealing temperatures and atmospheres. Cuenya and co-workers studied the segregation and alloying phenomena of PtNi nanoparticles by annealing them from room temperature to 650 °C under vacuum, H_2, and O_2 environments, respectively. [151] Annealing in O_2 causes an enhanced Ni surface segregation at all temperatures. By contrast, in H_2 and vacuum, Ni segregates on surface only at low temperature region (< 270 °C), while Pt diffuses towards the surface at higher temperatures.

2.4.2. Core-shell nanoparticles

Core-shell nanoparticles constitute an important type of ORR catalysts. The core-shell nanoparticles are composed of catalytically active Pt shell on less expensive cores to enhance Pt utilization. The core materials not only serve as structure templates but also modify the d-band of the Pt shell. A rich variety of options are available to the core materials, such as late transition metals (Ni,[125,152] Co,[153] Pd[154]), intermetallics and alloys (CuAu,[155] PdFe,[156] PdCu,[157] PdCo[158], AgPd,[159] AuPd,[160]), early transition metal carbides,[161] nitride,[162,163] metal oxide,[164] and so on. The core-shell catalysts have been achieved by different approaches.

2.4.2.1. Seeded epitaxial growth. Seeded epitaxial growth refers to the oriented overgrowth of thin layers of catalytically active Pt on faceted crystalline seeds. Seeded epitaxial growth in

solution-phase has great potential for scalable manufacturing of core-shell ORR catalysts with well-defined shell thickness and crystal orientation. The growth starts from heterogeneous nucleation of Pt on a secondary metal surface, followed by continuous Pt addition on the nucleation sites, and ends up with complete wetting of the seed through surface migration of Pt adatoms. Undesired homogeneous nucleation of Pt is usually circumvented by keeping the precursor concentration at a low level. To this end, syringe pump is frequently employed so that the precursor is successively introduced into the growth solution over a period of time. The diffusion rate of Pt adatoms is another key factor that affects the growth modes. Xia and co-workers have examined the role of surface diffusion in seeded growth.[165] It has been shown that the diffusion rate of surface adatoms can be maneuvered by changing the growth temperature. At a low temperature, wherein surface diffusion is sluggish, island structures formed on seed surface due to localized hetero-nucleation and growth. In contrast, a conformal and smooth shell formed at an elevated temperature thanks to thermally promoted surface diffusion. A third issue in relation to epitaxial overgrowth is the galvanic replacement reaction of Pt with metal seeds, which will lead to porous structures and ill-defined interface.[166] Therefore, the difference in redox potential has to be considered when choosing the core materials. The lattice mismatch between Pt and the core materials is non-negligible. The degree of lattice mismatch together with the number of atomic layers of Pt determine the magnitude of surface strain and thus the d-band of Pt. It is challenging to synthesize conformal epitaxial-structures when there is a large difference between the lattice constants of core and shell materials. For this reason, the choice of core materials is limited to a small group of metals when Pt is taken as shell.[167] It is interesting to see conformal core-shell structures can be made using block copolymer as templates, even for two materials with significant lattice mismatches.[168,169]

Palladium has been intensively used as a substrate for the deposition of Pt. It is because of the availability of a rich variety of well-defined Pd nanocrystals and the small lattice mismatch between Pd and Pt.[167] Epitaxial Pd@Pt core-shell particles in shapes of cube,[170,171] octahedron,[172] decahedron,[173] icosahedron,[174] and plate[175] have been successfully made. The number of Pt atomic layers can be tuned by controlling the volume of the precursor solution injected (Figure 10a–h).[170,172,174] It offers a viable approach to optimize the surface strain and the corresponding ORR activity. Highest specific ORR activities of Pd@Pt are all achieved by depositing 2–3 monolayers of Pt on Pd seeds.[170,172,174] Among different morphologies, icosahedral Pd@Pt$_{2.7ML}$ presents the best specific activity of 1.36 mA cm^{-2} and mass activity of 0.64 A mg$_{Pt}^{-1}$ at 0.9 V. The high performing icosahedral Pd@Pt was attributed to the highly-strained and (111)-enclosed Pd seeds.[174] Compared with single-crystal seeds (i.e., cube and octahedron), 20-fold twinned icosahedral Pd seed could result in a corrugated Pt shell which is beneficial to ORR.[174] Core-shell ORR catalysts made by conformal and epitaxial deposition have also been demonstrated for Pt$_3$Ni@Pt,[176] Ag@Pt,[177] Pd@Pt$_3$Ni,[178] PdCu B2@PtCu,[157] and so on.

In spite of the above-mentioned progress, there is a strong impetus to expand the seeds from noble metals and their alloys to 3d-TM (e.g., Fe, Co, Ni, and Cu), not only for cost reduction but also because of the beneficial effects of 3d-M in improving the ORR activity of Pt. Unfortunately,

conformal and epitaxial deposition of Pt on 3d-TM has limited success.[179] This is because the reduction potentials of 3d-M are much lower than that of Pt, and thereby galvanic replacement would be involved. Eventually, the well-ordered surface structures in seeds would be destructed during the redox process, forming ill-defined Pt shell and core/shell interface. Our group recently demonstrated a successful case of epitaxial deposition of a conformal and ultrathin Au shell on (100) surface of Cu nanowires.[166] The reduction potential of Au precursor is reduced by modifying the ligand environment, such that the growth pathway is switched from galvanic replacement to epitaxial overgrowth. It would be interesting to investigate whether this method can be extended to epitaxial deposition of Pt on Cu and other 3d-TMs.
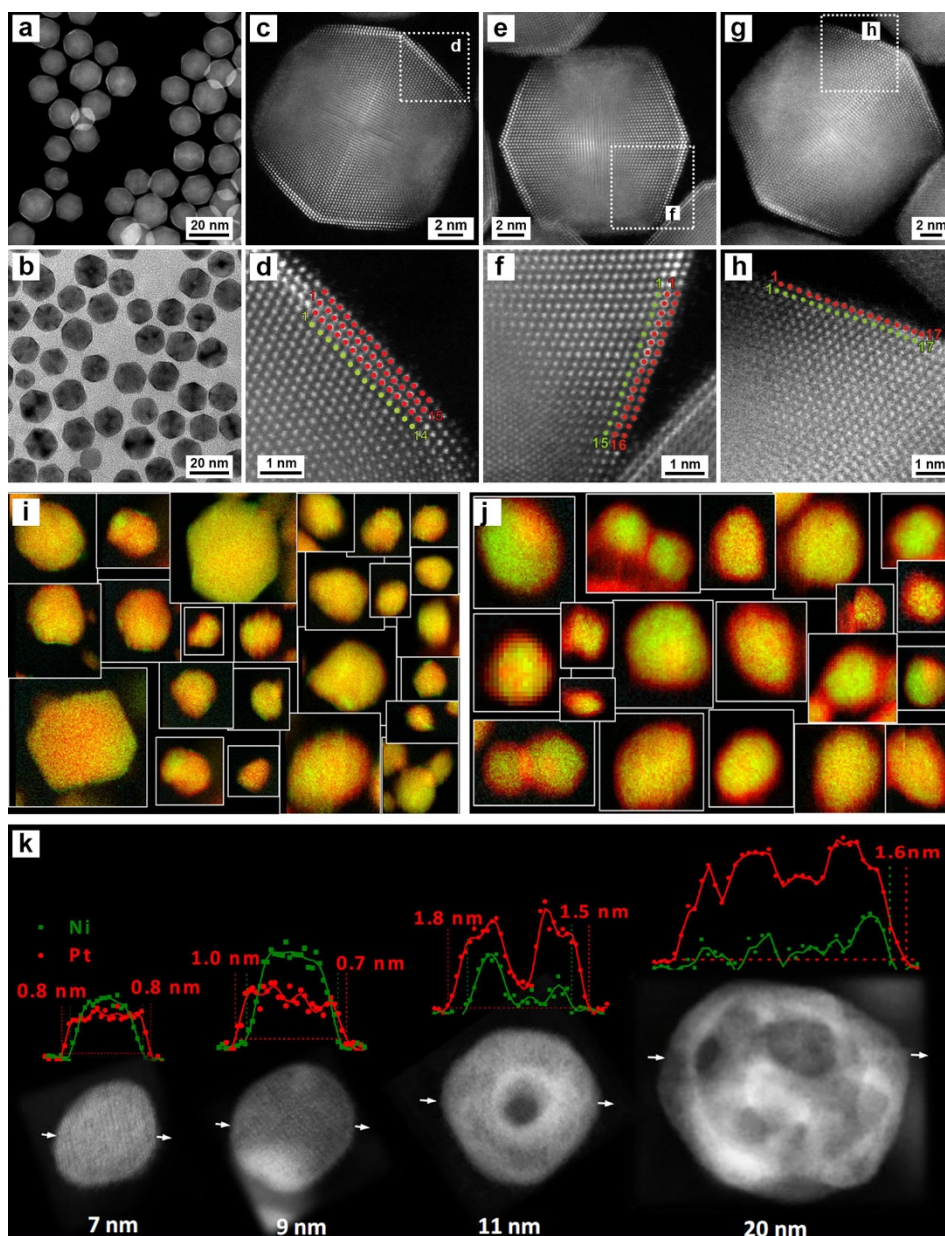
Figure 10. HAADT-STEM (a) and TEM (b) images of epitaxial Pd@Pt$_{2.7ML}$ icosahedra core-shell particles. HAADF-STEM images of Pd@Pt icosahedra with tunable Pt shell thickness of 2.7 (c,d), 2 (e,f), 0.7 (g,h) monolayers. Reprinted with permission from ref.[174] Copyright 2015 Macmillan Publishers Limited. Collage of EELS spectroscopic images of Pt-Co nanoparticles after heat treatment (I) and then after dealloying (J) to realize core-shell particles. Reprinted with permission from ref.[180] Copyright 2011 American Chemical Society. (k) HAADF-STEM images and the corresponded EELS line profiles of PtNi$_3$ particles with different sizes after 10000 cycles of stability test. Reprinted with permission from ref.[181] Copyright 2014 Springer Nature.

2.4.2.2. Dealloying. Electrochemical dealloying of Pt-poor alloy nanoparticles has been demonstrated to be a versatile route for the preparation of core-shell electrocatalysts.[181-184] PtM$_3$ alloys (PtCu$_3$) was introduced by Strasser and co-workers in 2007.[185] When subjected to electrochemical corrosion, the less noble metal in Pt-poor alloys is selectively removed, leaving a Pt-rich shell and Pt-poor core (Figure 10i, j). A broad range of core-shell nanoparticles has been made by dealloying PtM$_3$ precursors (M = Fe, Co, Ni, V, Cu, Mn, Ag) which are made by high-temperature annealing.[182,185-190] The ORR activity of the dealloyed PtM$_3$ (made at 800 °C) follows a sequence of M = Ag < Pt < V ~ Mn < Fe < Co < Ni, roughly proportional to the atomic radius of M. This trend can be explained by the surface strain induced by the core-shell geometry: Pt-poor core with smaller lattice parameter results in a higher degree of compressive strain in Pt-rich shell, which in turn leads to a weaker Pt–O bond compared with pure Pt. Since dealloyed PtNi$_3$ has shown the highest ORR specific activity,[185,190] the particle size effect of PtNi$_3$ was investigated in more detail. To address this, PtNi$_3$ particles with a size distribution of 3 to 25 nm were employed.[191] The compositional and morphological change of dealloyed PtNi$_3$ before and after electrochemical stability test were studied by electron energy loss spectroscopy (EELS) and scanning tunneling electron microscopy (STEM), respectively. It was found smaller nanoparticles (7 and 9 nm) remain solid core-shell structures and retain substantial amount of Ni up to 60 at% after 10000 potential cycles, whereas the larger particles (11 nm and 20 nm) evolve to nanoporous structures and lose a large portion of the initial Ni content (Figure 10k). In correspondence with the size-dependent structural and compositional evolution, both the ORR activity and stability of smaller dealloyed PtNi$_3$ (3–12 nm) are better than the larger one (3–25 nm).[191] With these insights, size-controlled PtNi$_3$ (about 5 nm) was developed, deployed in MEA, and tested under realistic automotive fuel cell conditions.[192] The activity and durability of this new fuel cell catalyst have met and exceeded the U.S. Department of Energy (DOE) 2020 targets.

2.4.2.3. Cu$_{upd}$-mediated electrodeposition. Adzic et al. have developed a Cu$_{upd}$-mediated electrodeposition method for the preparation of Pt monolayer (ML) catalysts. In this method, a monolayer of Cu is electrochemically coated on a core by UPD, and then Pt$_{ML}$ is deposited through galvanic replacement of the Cu monolayer by Pt. The Pt$_{ML}$ catalysts have a 100% utilization of precious Pt. Moreover, the properties of the top Pt$_{ML}$ can be finely tuned by 1) using different core materials with tunable compositions and shapes and 2) controlling the number of Pt atomic layers.

The ORR activity of Pt$_{ML}$ have been systematically investigated on substrates of Pd, Ru, Au,

Ir, and Rh.[193] Among these underlying substrates, Pd(111) shows best promoting effect on ORR activity due to a downshift of the d-band center of Pt_{ML} on Pd. The catalytic benefits of the Pd substrate can be further increased by alloying with Fe, Co, and Ni.[193-197] Adzic et al. also investigated the shape effect for Pt_{ML} catalyst by comparing tetrahedral and spherical Pd substrates.[198] Their results suggest that the tetrahedral $Pd@Pt_{ML}$ features more surface contraction compared with spherical $Pd@Pt_{ML}$, and thus delivers a higher ORR activity. Improved ORR stability has been demonstrated by introducing Au into the Pt_{ML} core-shell catalysts. For example, a core-shell catalyst comprising Pt_{ML} on Pd_9Au alloy core was developed.[160] The $Pd_9Au@Pt_{ML}$ core-shell catalyst has a minimal degradation in ORR activity after 100000 potential cycles between 0.6 and 1.0 V. In situ X-ray absorption spectroscopy demonstrates a retarded Pd oxidation after the Au incorporation.

An advantage of Cu_{upd}-mediated electrodeposition is that the number of Pt atomic layers can be accurately controlled by repeating the deposition cycles. It affords a material basis for comparing the shell thickness effect on oxygen reduction. Adzic et al. varied the thickness of Pt monolayers on both Pd and Pd_3Co cores.[194] ORR measurements show that the specific activity doesn't change when varying the thickness of Pt from 1 to 3 layers. However, a thickness-dependent ORR activity was established on Ru core.[199] The specific activity decreases in the order of $Ru@Pt_{2ML} > Ru@Pt_{3ML} > Pt/C > Ru@Pt_{1ML}$. DFT calculations show that Pt overlayers on Ru destabilize oxygenated species with respect to pure Pt. However, the destabilization is too strong in the case of one single Pt overlayer, such that O−O bond breaking becomes rate limiting.

2.4.3. Open architectures

Highly open nanostructures are emerging as a new class of ORR catalysts. Mesoporous structures, nanocages, and nanoframes are three representatives. These open architectures can be considered as well-ordered assemblies of small nanoparticles in three-dimensional patterns. Open structures not only afford sufficient surface areas and active sites, but also bring benefits to durability by circumventing particle agglomeration and Ostwald ripening.[77] Open architectures have demonstrated promising ORR activity and stability measured by RDE technique,[200,201] although their performance in MEA requires further investigation.

2.4.3.1 Mesoporous structures. Different to convex nanoparticles, mesoporous structures are with negative curvature. Their surface is rich of concave sites. These concave sites are potentially more active than Pt(111) terrace sites according to the descriptor based on conceptual "generalized" coordination number ($\overline{CN}$).[23,24] In the work of Calle-Vallejo et al., a coordination-activity plot is established, showing that optimal surface sites should possess a $\overline{CN} \approx 8.3$.[23,24] While Pt(111) terrace sites have a $\overline{CN}$ of 7.5, creating small cavities on Pt(111) will increase the $\overline{CN}$ and approach the optimal value for ORR. Another difference between nanoparticles and mesoporous structures is that the electric double layers (EDLs) within a pore channel may overlap when the pore size is down to the scale comparable to the thickness of EDL, and thereby altering the local

electric field.[202-204] Chung and Kim et al. have shown that the electrochemically effective surface area of mesoporous Pt electrode is controlled by ionic strength.[203] They found the inner surface of the pore becomes more easily accessible when increasing the concentration of supporting electrolyte to an extent that the electric field in the pores no longer overlap. Last but not least, it should be noted that the residence time of reactants near inner surface may be prolonged due to the confined space in pores and channels, leading to an enhanced conversion.
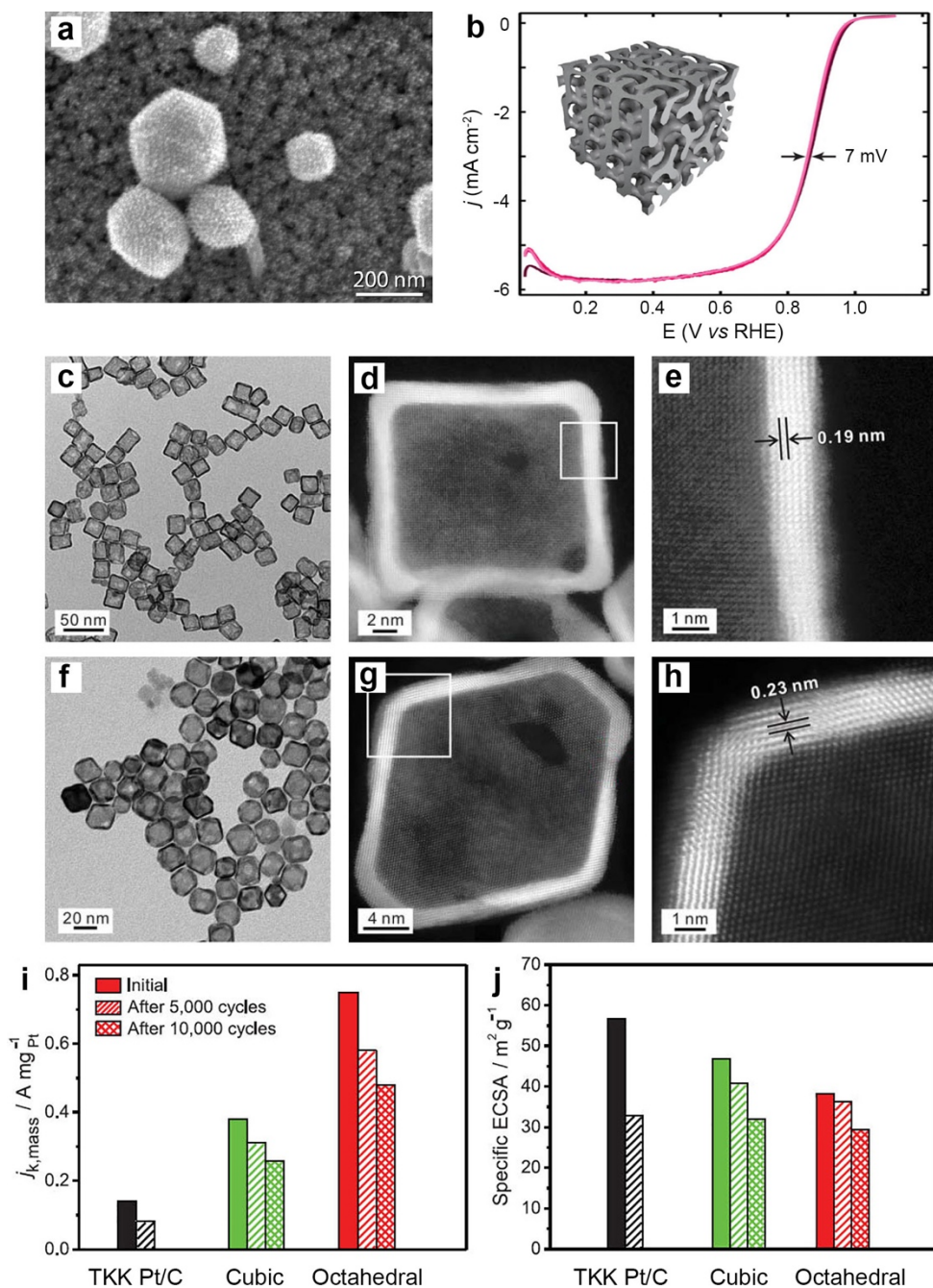
Figure 11. SEM image (a) and ORR polarization curves before and after 10k potential cycles (b) for mesoporous Pt. Reprinted with permission from ref.[205] Copyright 2012 American Chemical Society. TEM images (c) and HAADF-STEM images (d, e) of cubic nanocages. TEM images (f) and HAADF-STEM images (g, h) of octahedral nanocages. Mass activities (i) and ECSAs (j) of Pt nanocages before and after ADT. Reprinted with permission from ref.[201] Copyright 2015 the American Association for the Advancement of Science.

Templates are frequently employed to synthesize mesoporous Pt electrocatalysts. Electrochemical or chemical reduction of Pt salts in structure-directing templates will transfer the long-range orders from the templates to Pt. Lyotropic liquid crystals were used as structure-directing media to synthesize mesoporous Pt for the first time in 1997 by Attard and co-workers.[206,207] The liquid-crystal template method was then extended to the synthesis of Pt alloys, such as PtRu,[208] PtNi,[208] and PtAu,[209] by Yamauchi and co-workers. Mesoporous silica is another popular template. Jaramillo et al. reported a mesoporous Pt thin film as active and stable ORR catalyst.[205] The mesoporous Pt thin film possesses a double gyroid morphology (Figure 11a), which presents higher diffusivity compared with other mesoporous structures. An extra benefit of this self-supported extended mesoporous film is the elimination of carbon support in device application. It could reduce the thickness of catalyst layer and thus reduce the mass transfer resistance. A specific activity of 0.31 mA cm^{-2} was achieved on the mesoporous Pt film, on par with commercial Pt/C. The mesoporous Pt film is significantly more stable (Figure 11b) than commercial Pt/C as revealed by accelerated durability test (ADT). The enhanced stability was ascribed to the smaller fraction of under-coordinated Pt sites on the surface of mesoporous network than small nanoparticles. With silica templates, Yamauchi et al. also demonstrated that the size of mesoporous Pt can be controlled by varying the reduction time.[210] Joo and Yim et al. have achieved mesoporous Pt alloys with Ni, Fe, Co, and Cu using spherical mesoporous silica nanoparticles as templates.[211] Among these alloys, mesoporous PtNi contained an intermetallic phase. It exhibited an initial mass activity of 0.11 A mg$_{Pt}$$^{-1}$ (RDE), and the mass activity increased by 75% after 50000 ADT cycles. The intermetallic mesoporous PtNi was further evaluated in MEA. The beginning-of-life (BOL) and end-of-life (EOL) (after 5000 ADT cycles) mass activities were 1.34 A mg$_{Pt}$$^{-1}$ and ca. 0.78 A mg$_{Pt}$$^{-1}$, respectively, exceeding the DOE technical targets. The outstanding durability of mesoporous ORR catalysts was also manifested in ternary Au-Pd-Pt by Ding and co-workers.[212] A ultrathin Pt-Pd shell was deposited on nanoporous Au membrane. An initial mass activity of 1.14 A mg$_{Pt}$$^{-1}$ was obtained at 0.9 V. The activity increased to 1.47 A mg$_{Pt}$$^{-1}$ after 30000 potential cycles and kept stable over a further 70000 cycles.

2.4.3.2. Nanocages. Nanocages are hollow nanostructures enclosed by oriented surfaces. In comparison to mesoporous structure, nanocages are characterized by their larger cavities and well-controlled surface structures.[213] Nanocage can be considered as two-dimensional nanosheet folding in three-dimensional space. It offers favorable extended surface for oxygen reduction while holds a higher ECSA than conventional thin films.[117] Theoretically, the inner surface of nanocages is accessible because the existence of holes and openings in surrounding walls. Nanocages, similar to mesoporous structures,[205] are less susceptible to particle agglomeration because of their pre-

sintered architecture. However, defective sites residing at holes and openings may trigger the dissolution of Pt, thus breeding uncertainty about their long-term stability.

Nanocages can be prepared through galvanic replacement of Pt salts with faceted nanocrystals that are made of a less noble metal. A key challenge is to make galvanic replacement proceed in a controllable fashion. Xia et al. described a synthetic protocol for Pt-Ag alloy nanocages with controllable surface quality through galvanic replacement pathway.[214] Alternatively, nanocages can be achieved by selective etching method. The conformal and epitaxial M@Pt core-shell structures can be converted to nanocages by selectively removing the metallic core without destructing the well-defined shell structures.[213] Xia et al. described the synthesis and selective etching of cubic and octahedral Pd@Pt core-shell particles (Figure 11c–h).[201] The resultant cubic and octahedral nanocages have ECSAs of 46.8 and 38.2 m^2 g_{Pt}^{-1}, respectively. The ECSAs of the nanocages are quite close to those of the parent Pd@Pt core-shell particles.[170,172] The similar ECSAs between nanocages and core-shell particles suggests that O_2 diffusion to interior surface remains problematic. The octahedral nanocages have a specific activity of 1.98 mA cm^{-2} and a mass activity of 0.75 A mg_{Pt}^{-1} at 0.9 V (Figure 11i, j), both higher than the values for parent Pd@Pt core-shell octahedra.[172] The selective etching method has been extended to prepare other (111) facet-bound nanocages, such as decahedra,[173] icosahedra,[215] plates,[175] and tubes.[216]

2.4.3.3 Nanoframes. With a high level of morphological complexity, nanoframes are open structures with three-dimensional accessibility. The complex morphologies of nanoframes are found to derive from the compositional segregation in pristine bimetallic nanocrystals. By using aberration-corrected scanning transmission electron microscopy (AC-STEM) and EELS, Strasser et al. reported a compositional segregation phenomenon within octahedral Pt_xNi_{1-x} (x = 0.4, 0.5, 0.6) particles.[217] The pristine $PtNi_{0.6}$ octahedra are comprised of Pt-rich skeleton along the edges and corners, whereas Ni atoms enrich in (111) facets. Under electrochemical conditions, the Ni-rich Pt-Ni particle first evolve to concave octahedra after 25 potential cycles and then become hexapods after 4 000 potential cycles. This morphological degradation pathway is caused by a preferential leaching of Ni-rich (111) facets. Later, the same group revealed that the growth trajectory of Pt-Ni octahedra takes a reverse process.[218] It has been shown that a Pt-rich phase develops into hexapods at the early stage of the growth, followed by a deposition of Ni phase at the concave hexapod surface. The growth trajectory accounts for the compositional segregation observed in the octahedral Pt-Ni nanoparticles and determines their degradation pathway in ORR electrocatalysis.

Nanoframe catalysts have been realized in several bimetallic systems by dealloying the compositionally segregated particles, such as Pt-Ni,[219-224] Pt-Co,[225] Pt-Cu,[226-229] Pt-Ni-Cu,[230] and Rh-Cu.[231] Recently, Xia et al. developed a site-selected deposition and etching approach to make Rh nanoframe.[232] In the synthesis, Pd nanocubes with truncations at corners and edges were employed as seeds for the deposition of Rh. The surface of Pd nanocubes are bound by six (100) facets which are strongly capped by bromide ions. As a result, Rh atoms could only deposit at the corners and edges of Pd nanocubes to form a core-frame structure. Given that Rh is more resistant

to oxidative corrosion than Pd, the Pd-Rh core-frame structures are transformed to Rh nanoframe after selectively etching Pd. The site-selected deposition approach was also applied to the preparation of Au nanoframes employing Ag decahedra as seeds.[233]

Our group recently discovered a compositional heterogeneity within $PtNi_3$ rhombic dodecahedra.[200] According to energy dispersive X-ray spectroscopy (EDX), Pt enriches at the edges of the rhombic dodecahedron, whereas Ni is enclosed inside. Selective removal of the Ni-rich phase left a Pt_3Ni rhombic dodecahedral nanoframe with the 24 edges intact (Figure 12a). The three-dimensional open architecture of the Pt_3Ni nanoframes allows O_2 to approach the catalytically active surface from any direction. In addition, the nanoframe is able to confine ionic liquidto increase the O_2 concentration near catalyst surface. A Pt-skin structure can be introduced to the Pt_3Ni nanoframe by carefully controlling the annealing atmosphere and temperature. All these beneficial effects lead to a 36-fold enhancement in mass activity and a 22-fold enhancement in specific activity compared with the state-of-the-art Pt/C catalyst (Figure 12b).
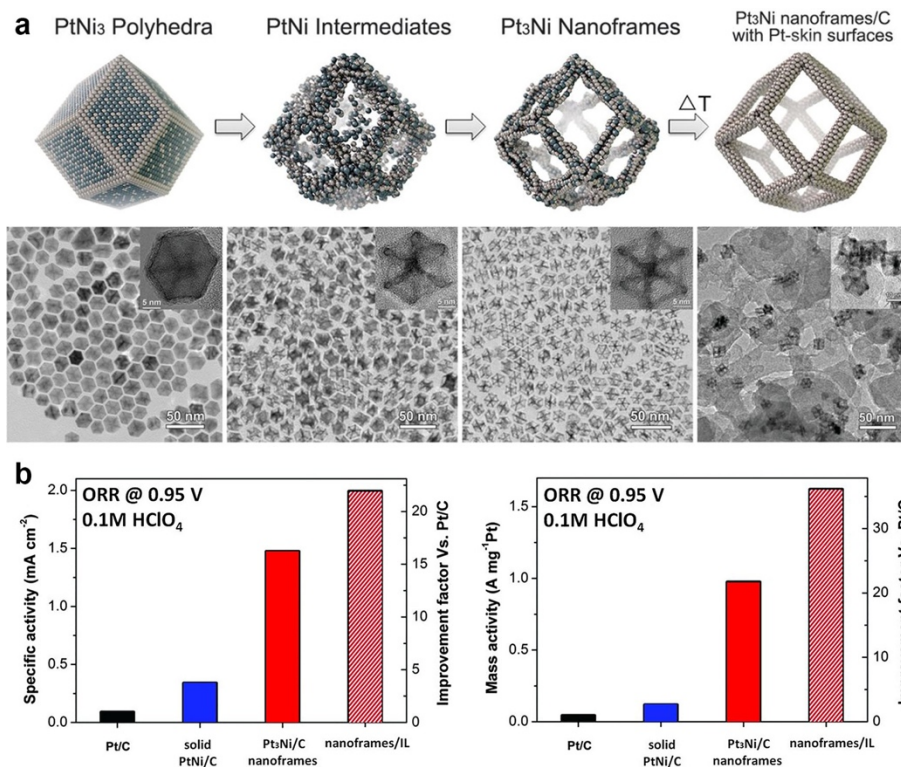
Figure 12. (a) Schematic illustrations and corresponding TEM images of the samples obtained at four representative stages during the evolution process from segregated $PtNi_3$ polyhedra to Pt_3Ni nanoframes. (b) Specific activities and mass activities measured at 0.95 V, and improvement factors *versus* Pt/C catalysts. Reprinted with permission from ref.[200] Copyright 2014 the American Association for the Advancement of Science.

In situ X-ray absorption spectroscopy (XAS) was used to compare the atomic surface structure of Pt_3Ni rhombic dodecahedral nanoframes with and without Pt-skin.[234] As previously mentioned, The $ECSA_{COad}/ECSA_{Hupd}$ ratio is an indicator of Pt-skin formation. We have shown

the nanoframes with Pt-skin have an $ECSA_{COad}/ECSA_{Hupd}$ ratio of 1.5 because of the weaker binding of H_{upd} to the Pt-skin surface, whereas the nanoframes without Pt-skin, which are less active for ORR, only exhibit a ratio of 1.0.[200] They are termed as $Pt_3Ni(1.0)$ and $Pt_3Ni(1.5)$, respectively. Before subjected to electrochemical environment, the $Pt_3Ni(1.0)$ showed a higher oxidation state of Ni, while the $Pt_3Ni(1.5)$ demonstrated a higher portion of Pt on its surface. Upon exposure to acidic electrolyte and potential cycling, both catalysts exhibited Pt surface enrichment due to the dissolution of surface Ni. However, $Pt_3Ni(1.5)$ showed a higher degree of Pt surface segregation, leading to better protection of Ni from oxidation.

We also investigated the growth mechanism of rhombic dodecahedron by a quasi-*in situ* sampling at a lower growth temperature to capture critical growth stages.[235] It was found that the growth of $PtNi_3$ rhombic dodecahedra starts from the anisotropic overgrowth of Pt-rich phase on faceted nanocrystals along <111> and <200> directions, which results in Pt-rich branch structures. High resolution transmission electron microscopy (HRTEM) revealed that there are plenty of steps between the arms of the growing branches. These steps could serve as Ni deposition sites and the space between the arms is eventually filled out by Ni-rich phase to form a complete rhombic dodecahedron. In this primary rhombic dodecahedron, Pt segregates on the 14 axes, forming a Pt-rich tetradecapod embedded in a Ni-rich shell. With longer growth time, the Pt-rich phase selectively migrates outwards from the 14 axes to the 24 edges, becoming a Pt-rich frame enclosing a Ni-rich interior phase. The outward migration of Pt can be attributed to the relaxation of internal strain caused by larger atomic radius of Pt than Ni. Meanwhile, the lower surface energy of Ni(110) than Pt(110) rationalizes the Pt segregation onto 24 edges rather than on surface.[236] Thereafter, Pt continues to enrich on the edges as reflected by the increased edge thickness and Pt/Ni atomic ratio. The complete growth trajectory is depicted in Figure 13a, b. Several factors have been identified as crucial to the formation of $PtNi_3$ rhombic dodecahedron: the comparison of reduction potential of the two metal precursors, the anisotropic overgrowth on faceted seeds, step-induced metal deposition, and the directional migration of atoms within a shaped nanocrystal. All these insights can be used for rational design of new ORR catalysts.

As an example of how the mechanistic understanding of $PtNi_3$ rhombic dodecahedron could inspire catalyst innovations, we have developed a new architecture called excavated nanoframe.[237] We discovered that at the stage of step-induced deposition, preferential deposition of Pt occurred when the Ni feeding was reduced. As a result, more Pt was deposited between Pt-rich branches and connected Pt-rich branches into Pt-rich sheets. Ni eventually filled up in the concave space bounded by the branches and sheets so as to form a rhombic dodecahedron. Excavated nanoframes were obtained by post-synthesis Ni corrosion that retain not only Pt-rich edges, but also Pt-rich sheets in between (Figure 13c). The resultant excavated nanoframe is more active than the hollow nanoframe towards ORR, because the two-dimensional sheets within the frame have higher Ni composition and more neighboring atoms. A specific activity of 1.35 mA cm^{-2} and a mass activity of ca. 0.64 A mg$_{Pt}^{-1}$ were achieved at 0.95 V, which are about 10 and 6 times higher than that of commercial Pt/C, respectively.
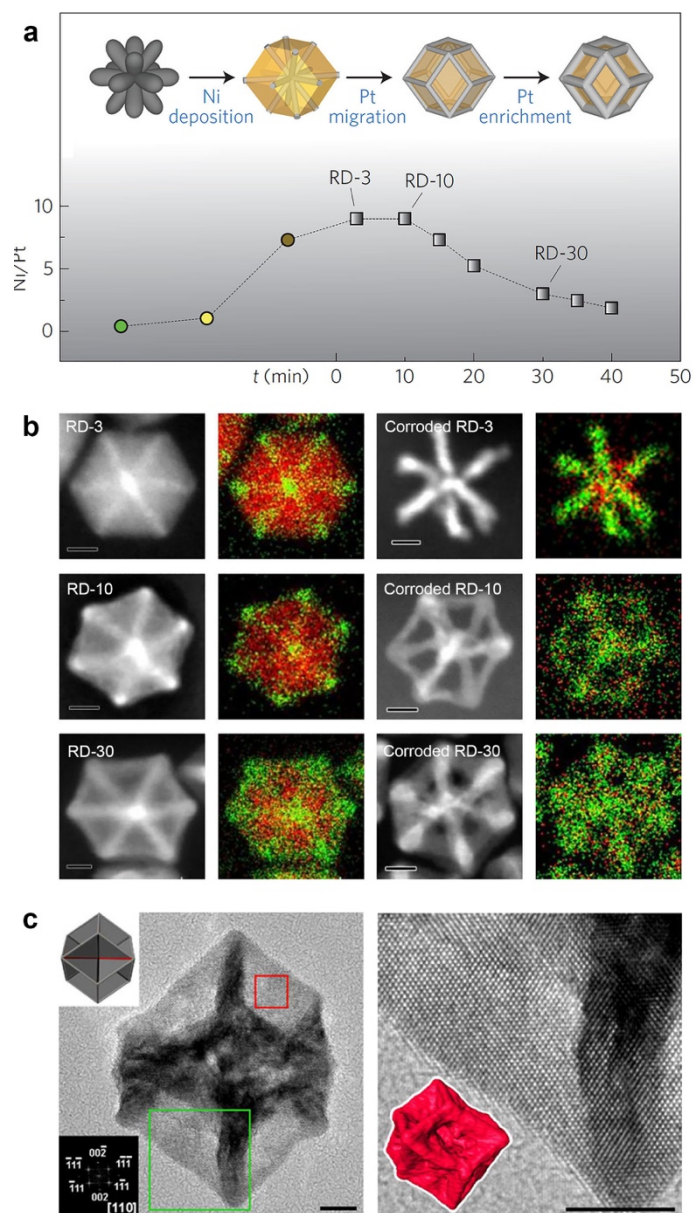
Figure 13. (a) Schematic illustration of the complete growth process of a Pt–Ni rhombic dodecahedron. The composition plot indicates that Ni content in the products increases first and then decreases. (b) STEM–EDX analysis of segregation and migration of Pt in Pt–Ni rhombic dodecahedra. Scale bar: 6 nm. Reprinted with permission from ref. [235] Copyright 2016 Macmillan Publishers Limited. (c) HRTEM images of excavated nanoframe oriented in ⟨110⟩ direction. Scale bar: 5 nm. Reprinted with permission from ref [237]. Copyright 2017 American Chemical Society.

Although the structure design and controlled synthesis is of paramount importance in tailoring the activity and stability of ORR electrocatalysts, post-synthesis treatment has been demonstrated of equal significance.[106,174,192,238-242] We compared three different procedures of post-synthesis treatment in order to gain more insights into how catalyst processing can affect the ORR activity

and stability of the nanoframe catalysts. In the three procedures, we changed the chemical corrosion extents of the Ni-rich phase in PtNi$_3$ rhombic dodecahedra, namely, non-corrosion, mild corrosion by acetic acid, and violent corrosion by nitric acid. After being loaded on carbon support, these three samples were submitted to electrochemical activation until reaching a stable cyclic voltammogram profiles. During the electrochemical activation, the unstable Ni species would be further swept off. By comparing the evolutions of the ECSAs, specific activities, mass activities, and Ni compositions of the three samples over 30000 ADT cycles, we established a trade-off relationship between the ORR activity and stability. The non-corroded sample exhibited the highest initial ORR activities by retaining more Ni content in the particle, but its ORR activity declined rapidly. The sample corroded by nitric acid presented lowest initial activity but kept very stable throughout the ADT tests. This is because a stable Pt$_3$Ni composition was achieved right after the nitric acid treatment. Lastly, acetic acid corrosion delivered nanoframes with performance in between. The variations of composition, elemental distribution, and morphology were characterized using TEM, high-angle annular dark-field scanning transmission electron microscopy (HAAD-STEM), EDX, and powder X-ray diffraction (XRD). Based on these information, the Ni content in the catalysts was thought to be a key factor that affecting the resultant ORR activity and stability. The initial Ni contents are a major contributor to the different initial ORR activities. However, high Ni content (larger than 25% in this case) couldn't be maintained in long-term potential cycles. The electrochemical Ni dissolution would trigger a series of structural changes which led to catalyst deactivation. The understanding of the deactivation of nanoframe catalysts will bring benefits to accomplish balanced ORR performance for the catalysts with complex architectures.

2.5. Catalyst design in a nutshell

After surveying the concepts and research milestones for both extended surfaces and nanostructured catalysts, it is time to discuss some guidelines for designing active and durable Pt-based catalysts. In the first place, a good ORR catalyst should bear as less as low-coordination surface sites, such as those on the edges and corners of a nanoparticle. The low-coordination surface sites would have such strong Pt–O bond that the sites are "poisoned" by oxygen-containing species. Moreover, the low-coordination sites are more susceptible to Pt dissolution under fuel cell conditions,[243] causing serious ECSA loss and activity degradation. The fraction of edge and corner sites would increase dramatically when particle size is below a critical value.[244] In this sense, increasing particle size will provide great gain in specific activity and stability, as supported by several experimental studies.[72,73,77,78] However, the requirement of high Pt utilization in practical application necessitates an upper limit for the particle size in order to achieve sufficiently high ECSA and mass activity. An average size in the range of 3–5 nm might be a reasonable target for nanoparticle catalyst design to reconcile mass activity and durability.

Innovations on catalysts' architectures can break the size limitation for nanoparticles. Considerably high ECSAs have been achieved for shaped core-shell structures and open structures,

while their global dimensions are way beyond 5 nm. For instance, the ECSA of 20 nm Pt_3Ni nanoframes with edge thickness of 2 nm was measured to be 67.2 m^2 g_{Pt}^{-1}, nearly two times as high as that of 5 nm nanoparticles (33.8 m^2 g_{Pt}^{-1}).[200] Architecture innovation makes it possible to replicate "extended surface" to nanoscale by projecting single-crystalline or polycrystalline nanosheets in three-dimensions.[125,237] As thus, the coordination of surface atoms can be tailored by controlling the surface orientation. Moreover, compared with small nanoparticles, architectures with larger dimensions have lower surface curvature and thus reduced surface energy. Additionally, interconnected architectures are less susceptible to agglomeration.

Finding a balanced amount of 3d-TM in a Pt alloy is crucial for both activity and durability. By leveraging strain effects and ligand effects, a high initial content of 3d-TM usually boosts BOL activity.[85,192,245] However, 3d-TM is vulnerable to corrosion under fuel cell conditions. The EOL atomic ratio of 3d-TM is often below 25%. Massive 3d-TM leaching may cause severe catalyst destruction[245] and will contaminate membrane and ionomer. Core-shell structure comes to the forefront of catalyst design to retain as much as 3d-TM content. Core-shell structures attained through dealloying process, galvanic replacement reaction, or epitaxial deposition may lead to different catalysts' behaviors. Epitaxial deposition on 3d-TM holds the key for better control over the shell structure and interface structure. The dynamic diffusion of 3d-TM in core-shell structures upon exposure to heat, moisture, adsorbed molecules, and acid requires carefulness when performing a series of post-synthesis treatments.

Incorporation of a third metal into Pt alloys provides an opportunity to forge more stable catalysts. The foreign metal takes effect under different mechanisms. The first example is Au, which was introduced into Pt alloy catalysts in forms of dopant,[246] interlayer,[152] core material,[212] or surface cluster.[247] The stabilizing effects of Au was attributed to its high nobility, which raised the oxidation potential of neighboring Pt. The second mechanism is selective site-blocking. Introducing a foreign meal (such as Mo) which preferentially segregates on low-coordination sites can shield these undesired sites from forming Pt–O bond and dissolution.[100] Lastly, metals with low surface diffusivity (such as Ir) were employed to alleviate the morphological instability of complex nanostructures.[40] We think all the three approaches will be more frequently engaged in future catalyst design.

3. Electrochemical reduction of carbon dioxide

3.1. Fundamentals of CO_2 electroreduction

Electrochemical reduction of CO_2 can result in a wide range of products, from simple products such as carbon monoxide or formate to more complex molecules like *n*-propanol. So far, more than 16 products have been identified[248,249] and they can be categorized by their number of carbon atoms or the number of electron transfers required to produce them (Figure 14). C_1 compounds are most profoundly studied, in terms of acquiring the capability to produce them and gaining the understanding of the reactions involved. The difficulty associated with forming C-C

bonds by electrochemical methods has prevented much progress for other higher-order products. Facilitating multiple electron transfers (beyond two electrons) along the reaction pathway poses another difficulty, as it requires optimizing the interactions of a large number of intermediates along the reaction pathway.[250] However, there has been some progress in forming multicarbon products (C_2-C_3),[251-253] such as ethylene and ethanol, and there is still a considerable amount of research effort to better elucidate the mechanistic pathways to these products.
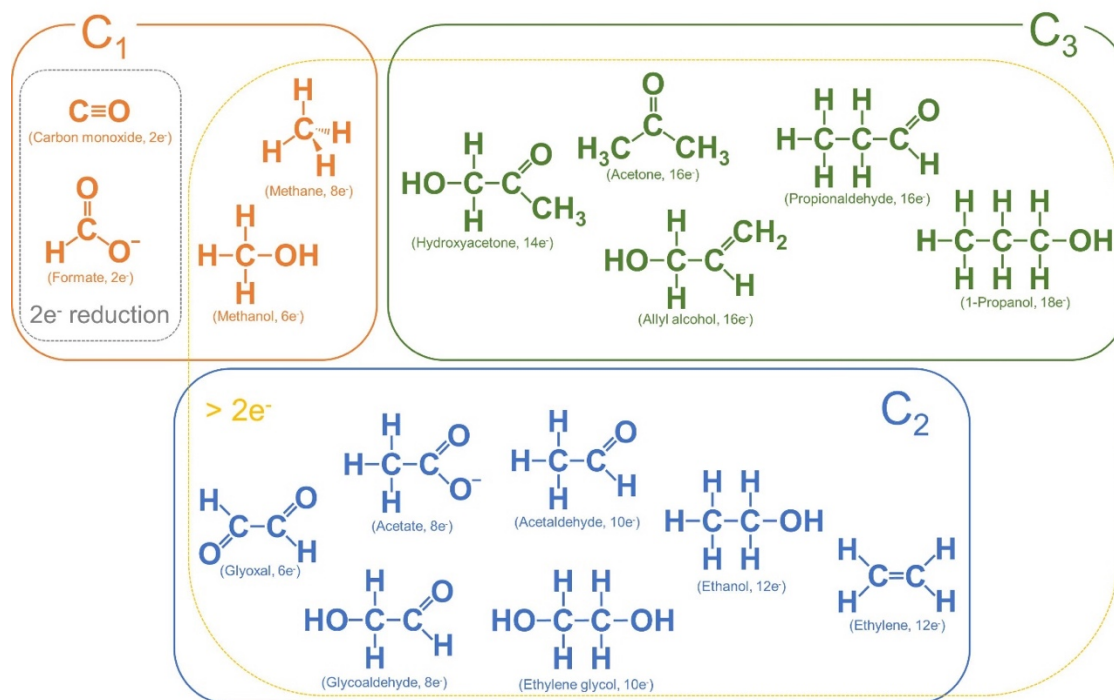
Figure 14. Various products formed by electrochemical reduction of carbon dioxide in aqueous media. Electron numbers in the parenthesis indicate the number of electrons required to generate the products from CO_2.

In order to produce any useful products from CO_2, the thermodynamic requirements for its conversion to the product molecules need to be understood. Table 1 lists the standard reduction potentials of the products. In the reference scale of the reversible hydrogen electrode (RHE), which is a thermodynamic reference point for protons being reduced to hydrogen gas, the standard reduction potentials of most of the products lie close to 0V (vs. RHE, unless stated otherwise). To be more precise, the majority of them are actually above 0V, which means that the energy input needed to produce these products should be less than that required for H_2 formation. Considering the vast amount of previous research efforts in water electrolysis, recycling carbon dioxide seems, in the face of climate change, not only desirable but also technically feasible.

C1				C2			
Carbon monoxide	Formate	Methanol	Methane	Glyoxal	Glycoaldehyde	Acetate	Acetaldehyde
-0.11 V	-0.02 V	0.03 V	0.17 V	-0.16 V	-0.03 V	0.14 V	0.05 V

C2			C3				
Ethylene glycol	Ethanol	Ethylene	Hydroxyacetone	Acetone	Allyl alcohol	Propionaldehyde	1-Propanol
0.20 V	0.08 V	0.07 V	0.46 V	0.10 V	0.05 V	0.09 V	0.10 V

Table 1. Standard reduction potentials of products derived from carbon dioxide. Potentials are referenced to the reversible hydrogen electrode (*i.e.* V vs. RHE).

However, most often, the potentials applied to generate these products are far more negative than their standard reduction potentials. Overpotentials have been more than a couple hundred millivolts to almost a volt just to see the onset of product formation. This clearly implies that there are large kinetic barriers that need to be overcome for electrochemical CO_2 transformation. Moreover, not only the sluggish reaction kinetics limit the energy efficiency of the reaction, but it allows the H_2 gas formation from the reduction of water to take place more readily. This eventually results in H_2 consuming for a large fraction of the charge being passed to the electrodes. While there have been some efforts to replace water with other non-aqueous media that also have a higher capacity for dissolved CO_2 concentration,[254] the requirement of proton supply to the carbon dioxide transformation pathway makes the H_2 forming side reaction inevitable.

Understanding the CO_2 reduction reaction pathways is critical in overcoming the kinetic barriers and avoiding the competing H_2 evolution reaction. Moreover, it will provide the means to control the formation of various CO_2 reduced products generated simultaneously, so that a certain desired product can be selectively gained. While the mechanisms still being studied, there is a consensus on the certain pathways and intermediates deemed important. The following sections describe the current state of understanding for converting CO_2 to C_1 and C_{2+} products.

3.1.1. Mechanistic pathways to C1 products

The pathways to two-electron reduction C_1 products (carbon monoxide and formate) are better understood than other products involving multielectron transfers ($> 2e^-$) and the formation of C-C bonds. Figure 15a shows the pathway to CO formation. The first intermediate suggested is the $*CO_2^{\bullet-}$ (* denotes an active site) formed by a single electron transfer (ET) to CO_2. The sluggish

reaction kinetics for CO_2 reduction requiring high overpotentials are considered due to this first step of CO_2 activation that has a standard reduction potential of -1.9 V vs. NHE (Normal hydrogen electrode).[249] While this may be an equilibrium potential between CO_2 and $CO_2^{\bullet-}$, it illustrates the difficulty in forming $*CO_2^{\bullet-}$ which is an adsorbed intermediate. Electrokinetic studies have also suggested the $*CO_2^{\bullet-}$ formation step as a rate-determining step (RDS) for CO_2-to-CO conversion. Polycrystalline foils of gold and silver have exhibited Tafel slopes of ~120mV/dec, which indicates a single electron transfer rate-limiting step.[255-259] Therefore, having a catalytic surface that can better stabilize $*CO_2^{\bullet-}$ would facilitate the reaction moving forward and the subsequent electron and proton transfers would lead to $*CO$ that can readily desorb as a product.
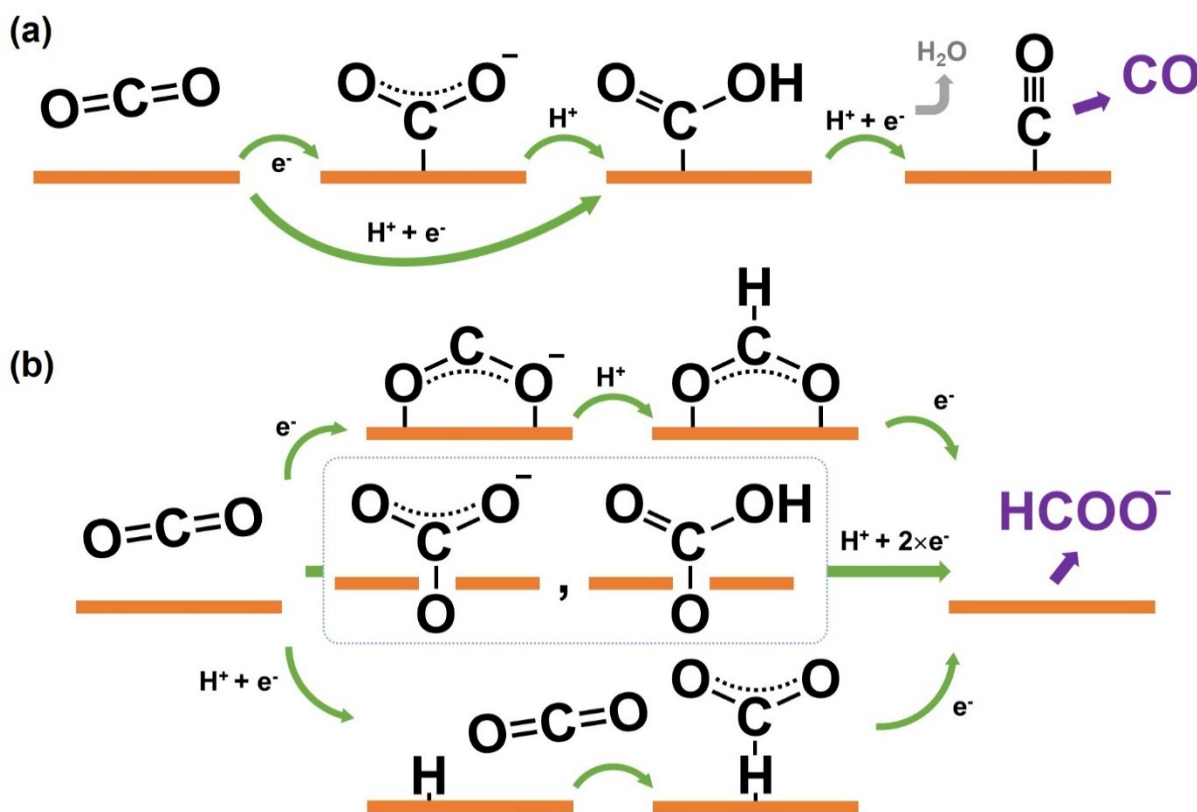
Figure 15. Mechanistic pathways to (a) CO and (b) $HCOO^-$ formation. The intermediates shown inside the blue dotted box in (b) are the ones proposed to exist on oxidized metal surfaces acting as a catalyst for formate.

However, there have been reports that suggest a different first step reaction in the pathway to CO.[260,261] The first elementary reaction proposed for CO production on silver surfaces is the concerted-proton electron transfer (CPET) to CO_2 to directly form $*COOH$.[260] Increased CO formation rates on bulk Ag surfaces by the increased concentration of bicarbonate (HCO_3^-), which can act as a proton donor, supports the proposed step. In contrast, it has been shown that CO

formation rates on polycrystalline gold surfaces are not affected by the proton donor concentration.[262,263] Moreover, CPET for CO_2-to-*COOH as a RDS still results in a Tafel slope around 118mV/dec.[256,259,260] A recent study using an *operando* IR spectroscopic technique on Ag films has shown surface bound intermediates of COOH at low overpotential regions further supporting the CPET pathway to CO.[261] *$CO_2^{\bullet-}$ was observed at more negative potentials suggesting the accessibility of the rate-determining ET pathway dependent on the potential applied. Therefore, it may be possible that the reaction mechanisms for CO_2-to-CO conversion differ based on the type of surface used.

Formate producing pathway is more complex.[264] While it may share the same first intermediate with CO on surfaces that produce both,[265] other intermediates have been suggested on catalyst surfaces that are rather selective for formate. Specifically, CO_2 is suggested to bind to the catalyst surface through oxygen atoms (Figure 15b). It was shown theoretically that there is a strong correlation between the HCOO⁻ activity and OCHO binding energy to the catalyst surface, instead of that of the COOH.[266,267] Moreover, Tafel slopes on tin foils suggests a chemical rate-determining step (most likely protonation) after a reversible single electron transfer.[268] This may mean that the proton (PT) and electron transfer (ET) steps are separated, with the first electron transfer occurring to form a *$OCO^{\bullet-}$.

But the necessity of surface oxides for formate production[268] and only the partial reduction of the oxidized tin at the catalytically relevant potentials[269,270] suggest a different mechanism. *In situ* attenuated total reflectance infrared spectroscopy (ATR-IR) on tin electrodes have identified tin-carbonate species as an active intermediate for formate production.[270] Spectroscopic observation of metal-carbonate species on some of the *p*-block elements, such as tin and indium,[270-272] rather suggests an alternative mechanism for CO_2 binding to produce formate, where CO_2 binds to the surface through an oxygen atom originating from the surface (Figure 15b).

It seems that not all *p*-block metals behave identically for CO_2 conversion to formate. Formate activity measured on oxide-derived Pb supports a reaction pathway in which the RDS is the first ET to form *$CO_2^{\bullet-}$.[273] Moreover, it is proposed that the metastable Pb oxides are the active species for CO_2 reduction while being inactive for H_2 evolution, which accounts for the significant suppression of the H_2 activity obtained from oxide-derived Pb. However, the catalytic role of metastable Pb oxides is ambiguous. Metastable Pb oxides have been observed during *in-situ* ATR-IR.[272] However, the lack of metal-carbonate signals on Pb, in contrast to Sn and In, suggests a different mechanism for the production of formate that may not involve Pb oxides. Moreover, because of the enhanced formate production on both types of Pb surfaces, which are the oxide-etched and anodized, the catalytic role of metallic sites and the metastable oxides in Pb seems to require further investigation. A more in-depth study on bismuth surfaces is required as well, where so far metallic bismuth sites are proposed to be active for formate production.[272]

Outside the *p*-block metals, palladium is often considered as an element for HCOO⁻ production. However, it is also well utilized for CO formation and the relevant potential regions for the production of each are clearly separated. It is due to the fact that the hydrogen absorption

properties of Pd make it unique for formate production, allowing it to generate formate very close to its thermodynamic equilibrium potential with unit selectivity.[274] Electrohydrogenation mechanism is proposed for Pd where the surface hydride (PdH) interacts with CO_2 leading to the bond formation between H and C (Figure 15b). While other possibilities may not be ruled out, this mechanism is suggested based upon the catalytic behavior of palladium hydrides formed from H_2 gas to chemically hydrogenate CO_2.[274]
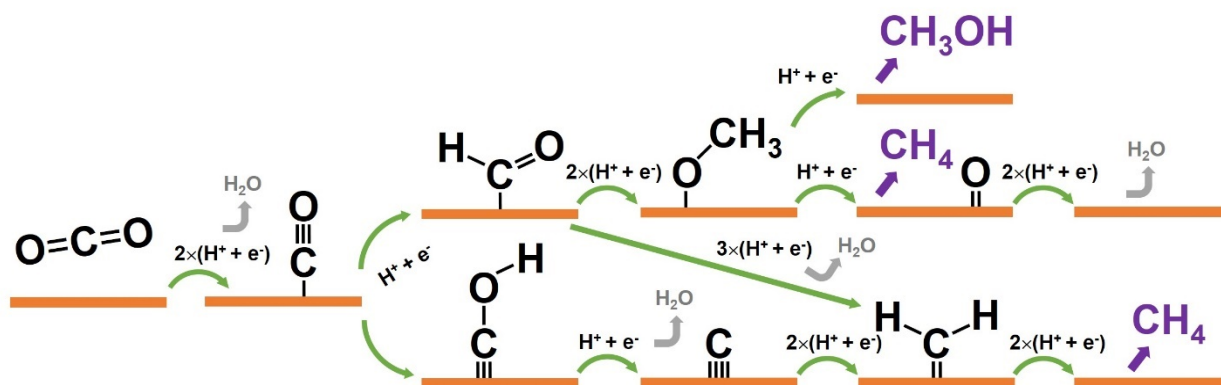

Figure 16. Mechanistic pathways to methane and methanol formation.

Among the C_1 products, the formation of methane is less understood due to the fact that it requires 8 electron and proton transfers with a large number of individual reaction steps (Figure 16). While it is widely accepted that the CH_4 is produced from an adsorbed CO intermediate, the mechanistic pathways down the *CO are less clear. Understanding the CH_4 formation has largely been driven by theory,[275-278] which has suggested a few possible reaction mechanisms and tried to explain the CH_4 activity trend found for various transition metals.[279] Elementary steps have been studied on model Cu surfaces since copper is the only known element that can produce appreciable amounts of methane.[249,280]

The main question is at which stage does the oxygen dissociate from *CO to be left with only C-H bonds. This question is closely related to the first protonation pathway to the adsorbed carbonyl (Figure 16). Density functional theory calculation performed on a model Cu surface has predicted a pathway that involves a *CHO intermediate.[275] From the adsorbed formyl, subsequent proton and electron transfers occur on the carbon atom to form a methoxy (*OCH$_3$) intermediate and dissociation of the oxygen atom occur together with the final step of CH_4 formation (Figure 16). Earlier experimental works have also suggested *CHO as a key intermediate from the observation of electrochemical conversion of formaldehyde to methane.[281-283] However, methanol is the dominant product for formaldehyde reduction on copper surfaces and methanol (as a methoxy intermediate) cannot be further electrochemically reduced to methane.[283] In addition, CO_2 electroreduction on copper exhibits negligible amounts of methanol as a product.[248] All of these observations suggest that a different type of intermediate from *CHO should be present along the pathway to methane.

The other possible configuration that could result from protonating an adsorbed carbonyl is the *COH. By considering the kinetics of each elementary step, a high barrier for *OCH$_3$ to CH$_4$ was identified which should favor methanol formation from *OCH$_3$.[276] Instead, *CO to *COH is considered as the first step to CH$_4$ which subsequently produces *C and *CH$_2$ along the reaction pathway (Figure 16).[276,282] Therefore, a distinction could be made between the two pathways for methanol (involving *CHO) and methane (*COH). Furthermore, it was shown that the energetic barrier to a transition state leading to *COH was much lower to that of *CHO which could explain the high selectivity to methane over methanol on copper surfaces.[276]

One possibility that should not be neglected is the formyl (*CHO, or formaldehyde (HCHO)) to carbene (*CH$_2$) transition.[281-283] While electroreduction of formaldehyde mostly results in methanol, small amounts of methane have been observed. Therefore, a pathway involving *CHO to CH$_4$ may exist[277] and occur simultaneously with the *COH pathway during the electrochemical reduction of CO$_2$ (Figure 16). Mechanistic studies have supported this idea by suggesting the formation of *CHOH and the subsequent release of water to lead to *CH$_2$ by multiple protonation steps.[277,278]

3.1.2. Mechanistic pathways to C$_{2+}$ products

Understanding how C-C bonds form is of critical importance in electroreduction of CO$_2$ to facilitate the formation of multicarbon products. So far, the mechanistic pathways to C$_3$ products are not well known. Among the C$_2$ products, ethylene is by far the most well-studied product as it can reach up to reasonably high faradaic efficiency (FE) of 50 ~ 60% using certain catalyst materials. Similar to methane, mechanistic studies for CO$_2$ to ethylene conversion have been conducted using copper surfaces because of their unique capability to allow C$_2$-C$_3$ product formation which is absent in most of the other materials.
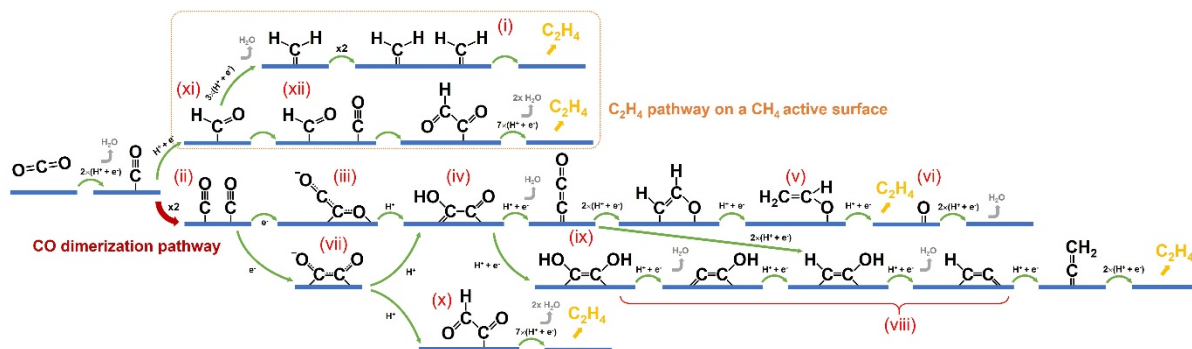

Figure 17. Mechanistic pathways to ethylene formation.

Earlier studies that observed C$_2$H$_4$ formation on copper electrodes have proposed reaction schemes that involve the (i) coupling of carbenes (*CH$_2$), as shown in Figure 17.[282,284,285] The same

dimerization reaction was considered for the reduction of carbon monoxide (CO) to C_2H_4 on copper.[286] However, an alternate C-C bond formation pathway by the dimerization of *CO has been proposed as well.[287] It is based on a number of experimental observations, such as the difference in the Tafel behavior of CH_4 and C_2H_4 and the C_2H_4 formation occurring at more positive bias compared to that for CH_4, suggesting a distinct intermediate from *CH_2 that leads to C_2H_4. By the electrokinetic studies indicating a single electron transfer RDS without any pH dependence, electron transfer coupled (ii) CO dimerization to *$C_2O_2^-$ was proposed (Figure 17).[287]

Experimental works of CO electroreduction on various types of copper surfaces have supported the existence of both pathways. By directly reducing CO, which is known as a major intermediate for CO_2 reduction to hydrocarbons, on single crystal copper surfaces of (111) and (100), it was shown that two separate pathways exist for C_2H_4.[288] The catalytic pathway to C_2H_4 observed for both surfaces seemed to share a common intermediate with that to CH_4. However, an additional pathway existed for Cu(100) at less negative potentials with a high ratio for C_2H_4/CH_4. This pathway was suggested to be associated with the CO dimerization mechanism. Furthermore, CO reduction experiments on a Cu(110) surface which resulted in a similar activity trend as observed for Cu(111) confirmed that the CO dimerization pathway may only exist for Cu(100) type surfaces.[289]

Theoretical studies have supported the CO dimerization pathway. Using the computational hydrogen electrode model to consider the thermodynamic stability of various intermediates, (iv) *CO-COH was identified as a stable intermediate after CO dimerization.[290] Furthermore, it was shown that this ($H^+ + e^-$) transfer step is decoupled with a RDS of a single electron transfer to *CO + *CO (or CO(g)) to form *$C_2O_2^-$. The stable adsorption geometry of the *$C_2O_2^-$ was suggested in a way that carbon and oxygen atoms bind to the copper surface in a (iii) bridging mode (Figure 17). Along the reaction pathway to C_2H_4, (v) intermediates *OCH_2CH_2 and *$OCHCH_2$ have been suggested in the later stages which match well with the experimental observation of ethylene oxide reduction to ethylene on copper surfaces.[283,289,290] Based on the experimental and theoretical results, the mechanistic pathway to C_2H_4 was proposed as shown in Figure 17 (vi) leaves an oxygen atom at the surface to be reduced to water.[252,290]

Recently, a more rigorous approach was applied to CO reduction on Cu(100) by using ab initio molecular metadynamics simulations (AIMμD) with layers of the explicit solvent to better describe the solid-electrolyte interface.[277] The pathway proposed in this work contains (vii) *$C_2O_2^-$ dimer bound to the surface by two carbon atoms and also (viii) other intermediates in the same manner throughout the reaction, where both oxygens dissociate early during the process (Figure 17). The previously considered (ix) *CCO intermediate was suggested to contribute minorly in C_2H_4 formation by being reduced to *CH-COH.
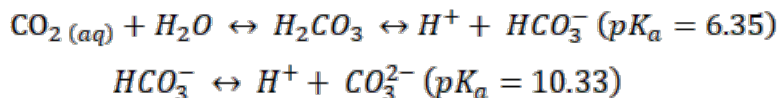
Alternative pathways after *CO dimerization have been proposed as well. It mainly differs by the protonation site on a *$C_2O_2^-$ to result in a (x) *COCHO as shown in Figure 17.[291-293] The likelihood of (x) *COCHO formation over (iv) *COCOH has been supported by the higher stability of *COCHO estimated by theory and the formation of glyoxal as a minor product.[292]

Furthermore, instead of the *CH$_2$, (xi) *CHO is suggested as a shared intermediate for both CH$_4$ and C$_2$H$_4$ so that C$_2$H$_4$ formation still follows through the pathway involving *COCHO (xii) by the interaction of *CO and *CHO.[277,292,293] However, spectroscopic observations of CO reduction on copper surfaces have supported the presence of (iv) *COCOH. *In situ* Fourier transform infrared spectroscopy (FTIR) was used to detect (iv) *COCOH, which was further supported by DFT calculations.[294] Including the other C$_2$ products that may share some of the reaction steps and intermediates,[277,292] the C$_2$ products formation pathway needs further investigation to elucidate the mechanisms and gain the capabilities for selective product generation.

3.1.3. Other environmental factors

Electrochemical environment factors play significant roles in CO$_2$ electroreduction. While CO$_2$ reduction studies have been mostly conducted in aqueous electrolyte solutions around the neutral pH,[249] there have been some efforts to utilize non-aqueous solvents. The main advantages of using non-aqueous electrolytes are the increased solubility of dissolved carbon dioxide and the suppression of H$_2$ evolution.[249] For instance, CO$_2$ saturation levels in acetonitrile and dimethylformamide are 279mM and 199mM, respectively. Compared against the CO$_2$ solubility in water (33mM), these solvents have about 6 to 8 times the capacity for CO$_2$. The characteristic activity and product distribution of electrocatalysts significantly differs from their catalytic behaviors in aqueous media. Products such as CO, formate and oxalic acid have been observed on various metal electrodes in organic solvents.[249]

When utilizing aqueous electrolytes, CO$_2$ equilibrium dynamics and the resulting buffering capability need to be considered. Dissolved carbon dioxide establishes a dynamic equilibrium between carbonic acid, bicarbonate, and carbonate.[249]

$$CO_{2\,(aq)} + H_2O \leftrightarrow H_2CO_3 \leftrightarrow H^+ + HCO_3^- \ (pK_a = 6.35)$$

$$HCO_3^- \leftrightarrow H^+ + CO_3^{2-} \ (pK_a = 10.33)$$

Carbonic acid (H$_2$CO$_3$) formed from dissolved carbon dioxide deprotonates to bicarbonate with a pK$_a$ of 6.35. Then, bicarbonate equilibrates with carbonate with a pK$_a$ of 10.33. The pH values of a saturated bicarbonate electrolyte under 1 atm CO$_2$ range from 6 to 8 depending on the bicarbonate concentration.[287] Furthermore, while the active species participating in the reaction is considered as the dissolved CO$_2$ molecules (*i.e.* CO$_{2(aq)}$), CO$_2$ can also be supplied from the equilibrium reaction with bicarbonate which has been spectroscopically observed.[295,296]

However, near the electrode surface, pH drifts away from the equilibrium value in the bulk. This is due to the proton consumption (or hydroxide formation) occurring simultaneously with every charge consumed for the reduction reactions. Therefore, the local pH near the electrode shifts to higher values compared against the bulk pH and the extent of the shift is determined by the bicarbonate concentration (and its corresponding buffering capacity), the rate of charge consumption, and the mass transfer kinetics.[287,297,298] Furthermore, as concentrations of CO$_2$ and the stability of reaction intermediates are affected by pH, local pH variations need to be taken into account in the development of electrocatalysts. For instance, the high local pH translating to a lack

of proton donors can reduce the competition against HER and thereby improving the selectivity of C_1 products such as CO. It has also been observed with a variety of Cu-based catalysts that the high local pH tends to facilitate C_{2+} formation.[299-302] One of the reasons for the observed improvement in C_{2+} selectivity under basic pH conditions is due to the formation of C_{2+} products being pH-independent so that the other products that are pH-dependent tends to be suppressed at a selected bias relative to RHE.[298,303] However, there have been also suggestions that the increased OH concentrations could lead to a stabilization of the C-C intermediate.[301] Nevertheless, all these studies illustrate the importance incorporating the pH effects into a catalytic system design for CO_2RR.

Electrolyte salt used and its concentration can affect the CO_2 reduction activity/selectivity. The choice of the anion influences the reaction by its buffering capacity in maintaining the local pH close to equilibrium and capability to act as a proton donor.[249,262] Therefore, product distributions for the CO_2 reduction products and the faradaic efficiency for HER which is a competing reaction all varies depending on its type and concentration.

Cationic species also influence the reaction at the surface of a catalyst which is observed as a shift in the current density and production distribution.[249] As the cation size becomes larger (*i.e.* from Li^+ to Cs^+ among alkali metal ions) CO_2 reduction reactions are favored on metal surfaces.[304-306] One explanation provided for this effect is the decreasing pK_a for cation hydrolysis with increasing cation size which leads to a higher buffering capacity near the electrode.[306] It is suggested that larger cations with increased buffer capacity keep the pH relatively lower and as a result the local CO_2 concentration higher, providing a favorable environment for CO_2 reduction.[306,307] In addition, cations have been suggested to play crucial roles in stabilizing surface intermediates. It has been shown that certain intermediates, such as *COOH, *CHO, and *C_2O_2, can be stabilized by either the co-adsorbed cation[308] or the electric field induced by the solvated cation in the vicinity of the catalyst surface.[309,310] In terms of intermediate stabilization, cation-dependent activity was attributed to the varying cation concentration at the outer Helmholtz plane (OHP) with larger cations reaching higher concentrations due to their stronger driving force to be at the OHP.[310]

Temperature and pressure can also influence the catalytic behavior observed on the electrodes. These two factors mainly alter the concentration of dissolved CO_2 in the electrolyte solution, where low temperatures and high CO_2 pressures favor higher CO_2 concentrations in a saturated solution.[287,311,312] Increased CO_2 concentration allows higher selectivity for CO_2 reduced products with even metals that mainly perform HER.[249]

Another important aspect to consider is the effect of impurity metal ions in the solution that can adversely interfere with the CO_2 catalytic reaction.[249] Small concentrations of metal impurities, such as lead or iron, can form adsorbed monolayers under reductive bias and this type of surface contamination can lead to the enhancement of hydrogen evolution against CO_2 reduction. It has been also shown that anodic stripping of impurity metals can recover the CO_2 electrocatalytic activity and the need of pre-electrolysis of electrolyte solutions has been emphasized.[313] Metal

impurity deposition can also be avoided by extracting metal impurities from electrolyte solutions by other means.[314,315] Another possible reason for catalyst deactivation is the poisoning caused by reaction intermediates. Some studies have suggested carbon-based contaminants or adsorbed organic species to cause deactivation.[282,284,316]

3.2. Catalyst materials for CO₂ electroreduction

Various materials have been tested as electrocatalysts for CO_2 reduction. A broad distinction can be made by the state of the materials, which are homogeneous and heterogeneous catalysts. There have been many efforts to utilize metal containing molecular complexes as homogeneous CO_2 electrocatalysts.[317] More recently, owing to the advances in nanomaterial synthesis, various kinds of heterogeneous CO_2 electrocatalysts have appeared.[253] Here, we focus on the materials used for heterogeneous CO_2 electrocatalysis.

Their classification can be made by the products formed (Figure 18).[249,254,318] A large number of metals have been tested and among them, copper is the only element capable of generating a useful amount of products in need of more than two electron transfers (> 2e⁻), such as the hydrocarbons and multicarbon oxygenates. Some studies have shown that other metals can form these complex products, albeit in trace amounts.[279] Thus, other metals are usually categorized based on their major CO_2 reduced product, either CO or formate. CO formation is favored on metals such as gold and silver, while formate production has been largely observed on metals like lead, tin, and bismuth. For metals traditionally well explored for H_2 evolution, such as nickel or platinum, H_2 formation dominates even under CO_2 reduction conditions, making them essentially not much useful as CO_2 electrocatalysts.

Figure 18. Metals classified by their major products for CO_2 electroreduction. Four groups are identified: H_2 (red), formic acid (yellow), CO (blue) and beyond CO* (cyan) that is hydrocarbons and multicarbon oxygenates. Reprinted with permission from ref.[318] Copyright 2017 Wiley-VCH Verlag GmbH & Co. KGaA,Weinheim.

The activity trend observed among various metals has been explained by their characteristic interaction strength towards the CO_2 reduction intermediates. Specifically, the binding energy of CO to the surface is used as a guide to interpreting their catalytic behavior.[319-321] The explanation

is that metals such as gold or silver that bind CO weakly favor CO as a product, while metals such as platinum or nickel that bind CO strongly is poisoned by the bound CO and mostly generates H_2 gas. Copper is unique in terms of having the optimum binding strength for *CO which allows further electron and proton transfer steps to produce higher order products. A thorough analysis of the reaction products observed from transition metal surfaces could also correlate the methane/methanol formation activity to their CO binding strength.[279] Metals with stronger CO binding (*i.e.* Cu, Ni, Pt, and Fe) were shown to exhibit more positive onset potentials for both products compared to that of the metals with weak CO binding (*i.e.* Au, Ag, and Zn). Though the methane/methanol faradaic efficiency may be low on those strong CO binding metals besides copper, the work has shown that CO binding strength is an important parameter in CO_2 electroreduction.

For multielectron reactions that involve a larger number of intermediates, the binding energy of each individual intermediate needs to be considered to better understand and manipulate the reaction pathway. The ideal case would be a complete control of the interaction strength for each intermediate so that the entire reaction pathway has negligible energy barriers and mostly downhill pathways. However, this is not easy to achieve on a catalytic surface composed of a single element due to what is so called the scaling relations.[319,321] It is a linear scaling trend observed for binding energies of a larger number of intermediates that share a common surface binding motif. For instance, a metal surface with a strong affinity for a CO adsorbate also has strong interactions (and higher binding energies) for *COOH and *CHO. With this constraint, it is very difficult for a single element surface to have the optimum interaction strength for all the intermediates observed along the reaction pathway, where, for some intermediates, a weaker interaction may be desirable.

In order to break away from the scaling relationship and add more degrees of freedom to the energetics of intermediates, additional modes of binding need to be introduced on the catalyst surface to either stabilize or destabilize certain intermediates. Decoupling the binding energies of multiple intermediates in this manner is feasible, as certain intermediates have the potential of allowing additional binding modes due to their molecular configuration, such as having an oxygen atom situated close to the catalyst surface. Therefore, catalyst modification strategies such as metal alloying and surface functionalization using molecular promoters have been proposed that may facilitate specific interactions to certain intermediates.[319]

Besides the metal-based electrocatalysts, materials purely composed of organic elements, such as the carbon-based materials, have proven their potential to be effective catalysts for CO_2 electroreduction. In contrast to the catalytic inertness of pure carbon electrodes, nitrogen-doped carbon materials have exhibited activities towards various C_1 and C_2 products depending on how these materials are treated.[322-326] Furthermore, certain metallic elements in the form of single atoms have proven to be active for CO_2 reduction, which are actually not favored as CO_2 electrocatalysts in an ensemble form.[179,327] While the potential of these catalysts bring additional opportunities to the search of highly efficient and robust CO_2 electrocatalysts, we limit our discussion to metallic nanocatalysts for the scope of this review.

3.2.1. Gold and Silver-based nanoparticle catalysts for CO production

Nanostructured materials tend to exhibit enhanced catalytic activity due to the presence of unique active sites on their surfaces which are absent in bulk materials.[328] This approach can be applied to gold and silver to promote CO_2 conversion to CO. Enhanced CO_2-to-CO conversion was observed using gold nanoparticles as electrocatalysts and changes in activity by the systematic variation of their size was studied to illustrate the favorable surface configurations for CO_2 activation.[329,330] Monodisperse gold nanoparticles that range from 4 to 10 nm in size were tested under identical conditions which resulted in the 8 nm Au NPs exhibiting the highest CO FE across a range of potentials (Figure 19a).[329] By studying the relative fraction of the various adsorption sites present on the Au NPs of varying size, it was shown that the Au NPs which exhibit high CO selectivity possess the optimal density of CO_2 active edge sites (Figure 19b). Free energy calculations of the reaction pathways to CO formation illustrates that these edge sites provide low energy barriers to *COOH,[329] which is the critical step to CO_2 activation. Therefore, the enhancement of CO_2 reduction activity observed from Au NPs as electrocatalysts can be attributed to them having a large density of active sites capable of providing low energetic pathways to the formation of relevant intermediates, most likely the first few steps of CO_2 activation.
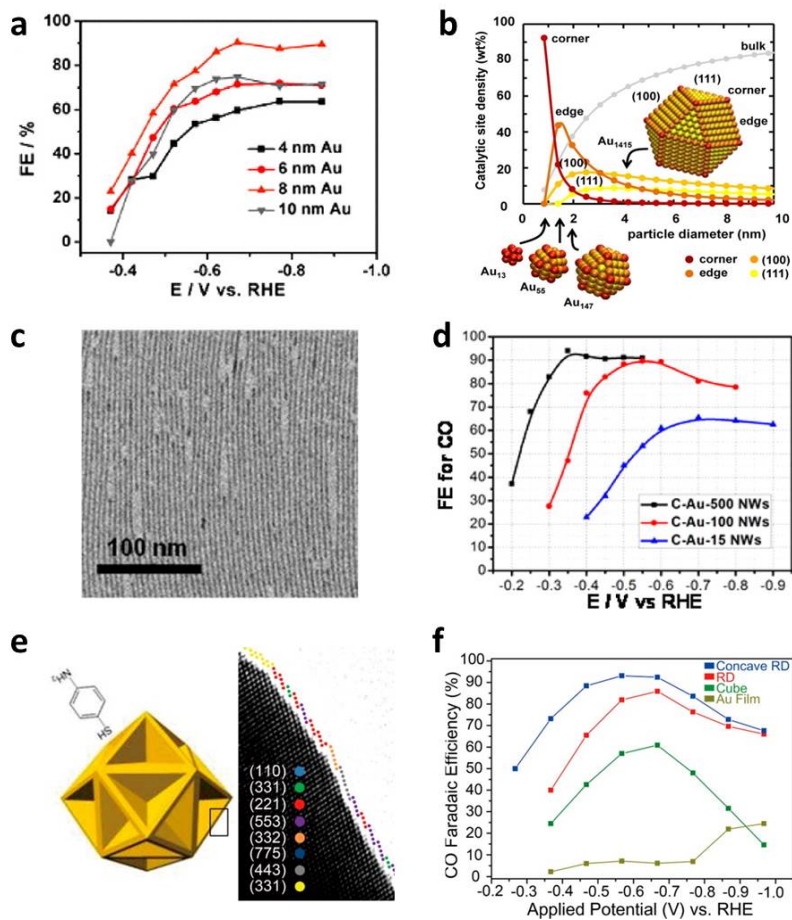
Figure 19. Size and shape-dependent catalytic activity of gold nanoparticles for CO_2 electroreduction. (a) Size-dependent CO FE of gold nanoparticles. (b) Density of adsorption sites (yellow, light orange, dark orange, or red symbols for (111), (001), edge, or corner on-top sites, respectively) on a closed-shell cuboctahedral Au cluster. (a) and (b) reproduced from ref.[329] Copyright 2013 American Chemical Society. (c) TEM image of 2nm width Au NWs. (d) CO FE of Au NWs with different lengths that are 500, 100, and 15nm, respectively. (c) and (d) reproduced from ref.[331] Copyright 2014 American Chemical Society. (e) Concave rhombic dodecahedral Au NPs with multiple high-index facets. (f) CO FE of concave rhombic dodecahedral Au NPs compared against other Au NPs. (e) and (f) reproduced from ref [332]. Copyright 2015 American Chemical Society.

In this aspect, nanomaterials of other morphologies can be beneficial as well. Depending on their shape, the relative distribution of the active sites can be controlled by maximizing the density of CO_2 active sites to non-active sites (*i.e.* H_2 active). This was demonstrated by using ultrathin Au nanowires as CO_2 electrocatalysts with 2 nm width which exhibits a high abundance of active edge sites due to their morphology leading to significant improvements in CO FE close to its thermodynamic potentials (Figure 19c and d).[331] A similar effect was also observed with concave rhombic dodecahedron Au NPs (Figure 19e and f) which are enclosed by a large fraction of high index crystal surfaces, such as (331) and (221), favorable for CO_2 electroreduction.[332]

Metal nanoparticles can be shrunk down to very small sizes of just a few nanometers, which are so-called the metal clusters, that exhibit distinct crystal symmetry compared to its bulk counterpart. Because of their unique structure, gold clusters have been utilized as CO_2 electrocatalysts.[333-335] Au_{25} clusters exhibit an onset of CO formation not far from the thermodynamic potential and close to unit selectivity around -1V.[81] Furthermore, it was shown that the charge state of the Au_{25} clusters is important for their activity with the negatively charged Au_{25} cluster being able to better stabilize CO_2.[334] First-principles calculation has shown that dethiolated gold sites on the clusters are the key active sites that can reduce the overpotentials associated with intermediate stabilization.[336] In this regard, the morphology of the Au_{25} cluster turns out to be important in being able to provide active sites on their surface, from a recent demonstration of Au_{25} nanospheres exhibiting a higher CO FE and production rate compared to Au_{25} nanorods.[337] With the added benefit of their significant mass activity (measured in terms of CO produced or CO_2 consumed per gram of material), renewable electricity powered devices have been demonstrated for their potential application to large-scale CO_2 conversion systems.[335]

The size and shape-dependent catalytic properties of Ag nanoparticles have been studied as well. Size-dependent CO_2 reduction activity of Ag nanoparticles in ionic liquids have shown that the highest CO selectivity is observed from 5nm particles.[338] While there was an increase in the CO activity from bulk to smaller nanoparticles, it declined after reaching below 5nm. This volcano type trend was attributed to the optimum binding strength of intermediates at the surface of 5nm particles. Furthermore, triangular Ag nanoplates have been shown to exhibit improved CO faradic efficiency (96.8% at -0.86 V vs. RHE compared against Ag NPs with 65.4%) with a very positive onset (-0.21V) potential[339] which was explained by the Ag nanoplates having a larger population of CO_2 active sites compared to the Ag NPs, similar to the effects observed for various shapes of gold nanocatalysts.[329,331]

As electrocatalytic reactions occur at the interface between the solid material and the liquid media containing the reactants, surface functionalization of nanoparticles can result in the enhancements of their catalytic activity. Various types of interface have been created by surrounding the nanoparticles with specific polymers or attaching molecular enhancers to the nanoparticle surfaces.[340-343] For instance, although the exact mechanism is unclear, it has been shown that embedding the Au clusters or nanoparticles to a binder that contains sulfonate end groups (*e.g.* Nafion) promotes their CO selectivity.[340] Au and Ag nanoparticles have also been modified on the surface with specific functional groups, such as thiols[341,344] and carbenes,[342] that enhanced the stability of major intermediates leading to CO formation.
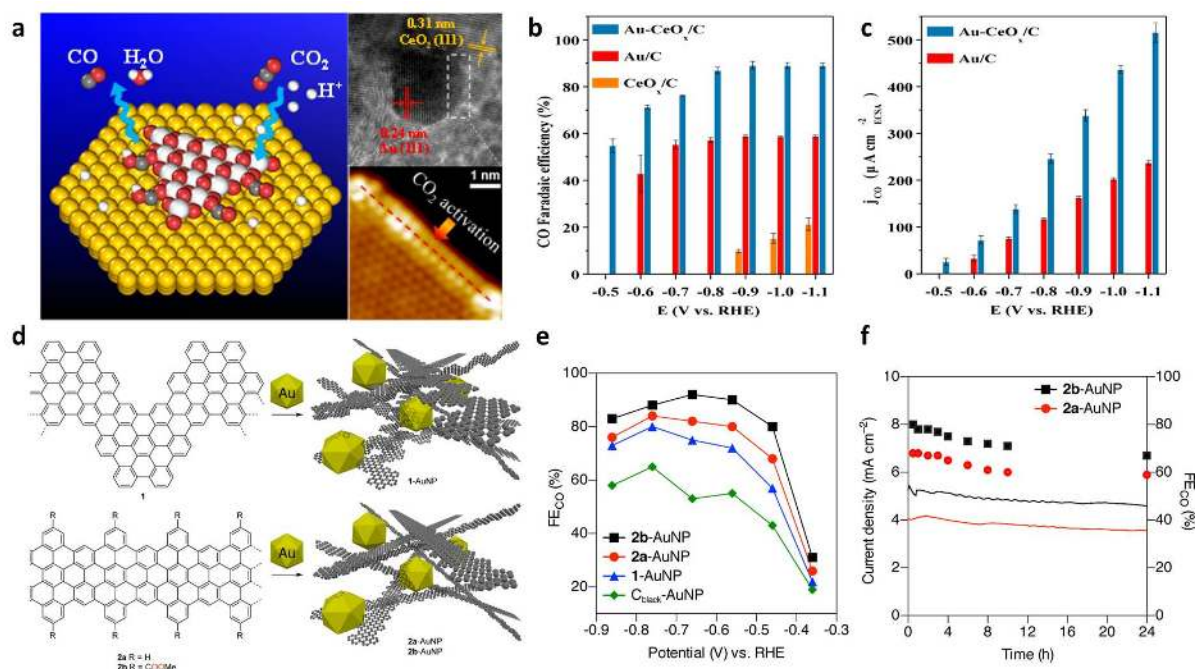
Figure 20. Enhanced catalytic properties arising from NP-support interactions. (a) Au-CeO$_x$ catalyst with its interface suitable for CO$_2$ activation. (b) Faradaic efficiency and (c) specific activity for CO production over Au/C, CeO$_x$/C and Au−CeO$_x$/C catalysts in CO$_2$-saturated 0.1M KHCO$_3$ solution. (a-c) reproduced from ref [345]. Copyright 2017 American Chemical Society. (d) Design of GNR-Au NP composite materials. Chevron (1) and cove (2a and 2b) GNRs synthesized from molecular precursors are used. (e) CO FE by 1-AuNP (blue triangles), 2a-AuNP (red circles), 2b-AuNP (black squares), and C$_{black}$-AuNP (green diamonds) composite electrodes. (f) Total current density and CO FE for 2a-AuNP (red line) and 2b-AuNP (black line) over 24 h. Both show little change between 10 and 24 h of fixed potential electrolysis at −0.47 V vs RHE. (d-f) reproduced from ref [346]. Copyright 2017 American Chemical Society.

Apart from inducing certain surface properties to the nanoparticles to be used as catalysts, their catalytic behavior can also be altered by the type of support used (Figure 20). This approach has been demonstrated with nanoparticles on various oxide and carbon-based supports for CO$_2$-to-CO conversion.[345-348] Au NPs on CeO$_x$ exhibited a 30% increase in the CO FE (~90% at -0.89V) and 2.2 times increase in the CO specific activity compared to those of the Au NPs on C (Figure 20b and c).[345] The enhanced catalytic property was attributed to the strong adsorption of CO$_2$ and stabilization of the *COOH intermediate at the Au-CeOx interface (Figure 20a) demonstrating the potential of metal-oxide interface engineering for CO$_2$ electrocatalysis. However, it is possible that the catalytic property of the supported NPs may be altered across their entire surface by the metal-support interactions. For Au/TiC, spectroscopic investigations combined with DFT calculations showed that modifications to the electronic structures of Au (*i.e. sp-* and *d-*bands) by the charge transfer from the underlying support may be responsible for its improved activity.[347] Compared to commonly used carbon supports, the use of graphene nanoribbons has promoted CO$_2$

electroreduction as well. It was shown that loading Au NPs on graphene nanoribbons led to improvements in the activity/selectivity for CO production (Figure 20d).[346] Tunability of graphene nanoribbons allowed various modifications of the support that positively shifted the Au NP activity (Figure 20e). Furthermore, the strong interactions between the metal NPs and the graphene support prevented deactivation of the catalyst caused by nanoparticle aggregation and sintering (Figure 20f). While the exact mechanism of catalytic enhancement by the various supports needs further investigation, positive demonstrations of the approach allow additional parameters to be tuned in the design of CO_2 electrocatalysts.

Besides the colloidal nanoparticle electrocatalysts, oxide-derived nanostructured surfaces of gold and silver foils have proven to be effective for selective CO production.[255,349,350] This method was first demonstrated with gold oxide films made by electrochemical treatments of gold foils.[255] Gold oxide films were reduced under cathodic bias to form oxide-derived Au NPs which exhibit marked improvements in the CO formation activity compared to the polycrystalline gold electrodes. CO FE reaches > 90% with only 200mV of overpotential applied at which polycrystalline gold foils are not active.[255] It was further shown that the enhanced catalytic behavior resulted from the increased stabilization of $*CO_2^{\bullet-}$, shifting the RDS to the next protonation step instead of the initial ET to CO_2. Similar effects were shown with the oxide-derived nanostructures of Ag formed by electrochemical methods[350] and oxygen plasma treatments.[349]

However, there have been various ideas as to the nature of the active sites for these oxide-derived metallic nanostructures. One hypothesis for their enhanced catalytic behavior is the creation of high density grain boundaries by the reduction of oxides to metals which can act as the active sites.[351,352] Grain boundary densities on the surface of Au NPs were quantitatively correlated with their CO_2-to-CO version activity to show that the grain boundary surface terminations are the highly CO_2 active sites.[351] Recently, direct probing of the increased local activity at the grain boundaries of polycrystalline gold electrodes using scanning electrochemical cell microscopy further supported this idea.[352] DFT calculations have helped to understand the role of grain boundaries at which the broken symmetry of gold atoms tends to better stabilize the *COOH intermediate.[353,354] On the other hand, there have been some claims that there are residual oxides even under cathodic bias that promotes the catalytic activity of the oxide-derived Ag nanostructures.[349,355,356] Moreover, the high surface area characteristic of these oxide-derived nanostructures allows modification of the local environment conditions near the electrode surface, such as shifting the pH and blocking the flow of certain reactants by limited mass transfer, that are favorable to CO_2 electroreduction.[350,357,358] Therefore, the study of oxide-derived metallic nanostructures as CO_2 electrocatalysts requires a careful consideration of all the possible factors that could contribute to the observed catalytic activity in order to better elucidate the nature of active sites on these surfaces.[352]

Nanostructuring of bulk surfaces have resulted in the promotion of CO activity as well.[256,260,357-360] Similar to the nanoparticles used as catalysts, nanostructured bulk surfaces contain catalytically active sites that can better stabilize the important intermediates, such as the

highly curved surfaces exposing the low coordination surfaces.[256,260] Furthermore, nanostructured tips have shown to provide strong electric fields that could allow higher concentration of CO_2 near catalytic surfaces for higher catalytic turnover as demonstrated with the Au nanoneedles for CO production.[360] However, often times, as the method of nanostructuring bulk surfaces induce other structural characteristics at various length scales, the catalytic effects of all the features are combined together to result in an enhanced output. For instance, it has been shown that high surface area porous architectures can inhibit H_2 evolution (and enhance CO selectivity) by the diffusional gradients created within the structure for the proton donors.[357,358] In addition, nanostructured bulk electrodes can enhance CO_2 mass transport by the facile release of the gas bubbles created on their surface, promoting higher current density for the CO_2 reduced products.[361] In this regard, understanding the catalytic effects of individual structural parameters and combining them in a synergistic manner seem of paramount importance for CO_2 electrocatalysis.

3.2.2. Nanomaterials of *p*-block elements for formate production

CO_2 electroreduction to formate can be observed by using elements such as Hg, Pb, Sn, and In.[249] Majority of these elements fall under the category of the *p*-block elements and their nanoparticle or nanostructured forms have been demonstrated as active catalysts for CO_2-to-formate conversion.

Among these elements, Sn has been studied the most in various forms. Demonstration of formate production using Sn cathodes dates back to the early 1980s.[362] While some theoretical works have shown that the high formate activity of Sn originates from its optimum binding strength towards a *OCHO intermediate,[266] identification of the Sn oxides as the active species[264,268-270] has led to the development of Sn oxide nanomaterials as catalysts. SnO_2 nanoparticles of varying size loaded onto carbon black and graphene supports (Figure 21a) were studied for their size-dependent activity, where 5nm particles exhibited the highest formate FE (Figure 21b).[363] The tendency of smaller SnO_2 nanoparticles being more active has also been observed by the interconnected SnO_2 NPs (< 5nm) that significantly suppressed hydrogen evolution and promoted formate production.[364]
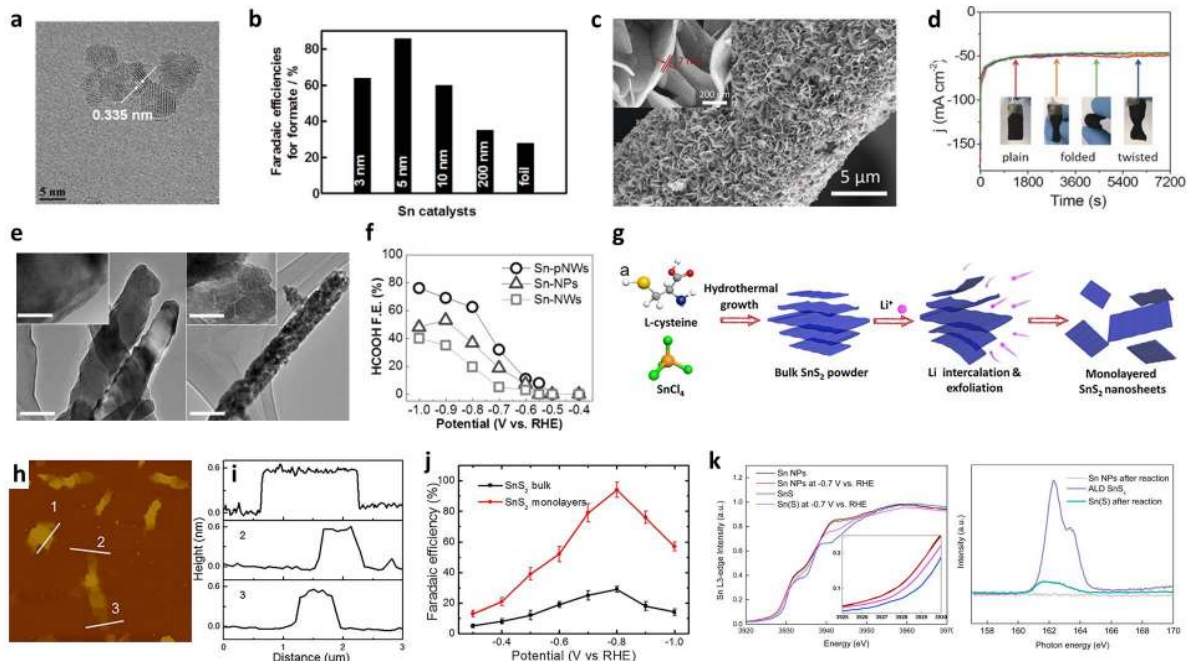
Figure 21. Sn oxide and sulfide nanomaterial electrocatalysts for formate production. (a) High-resolution TEM image showing SnO_2 NPs on graphene. (b) Particle size dependence of faradaic efficiencies for CO_2 reduction to formate on SnO_2 NPs. (a) and (b) reproduced from ref [363]. Copyright 2014 American Chemical Society. (c) SEM image of SnO_2 nanosheets on carbon cloth. (d) i–t curves of the SnO_2/CC electrode at -1.6 V vs. Ag/AgCl after folding or twisting 10 times. (c) and (d) reproduced from ref [365]. Copyright 2017 Wiley-VCH Verlag GmbH & Co. KGaA, Weinheim. (e) TEM images of the SnO_2 NWs (Sn-NWs, left) and the porous SnO_2 NWs (Sn-pNWs, right). (f) Formate FE vs. potential of Sn-pNWs, Sn-NWs, and Sn-NPs (commercial SnO_2 NPs). (e) and (f) reproduced from ref [366]. Copyright 2017 Wiley-VCH Verlag GmbH & Co. KGaA, Weinheim. (g) Schematic illustrating the synthesis of SnS_2 monolayers. AFM image (h) and the corresponding height profiles (i) of SnS_2 monolayers. (j) Formate FE at various potentials for the SnS_2 monolayers. (g-j) reproduced from ref [367]. Copyright 2018 Elsevier Inc. (k) *In situ* Sn L_3-edge XANES spectra of the SnS compared against Sn NPs (Left) and XPS spectra of both at the S 2p position (Right). (k) reproduced from ref [368]. Copyright 2017 Elsevier Inc.

Various morphologies of Sn oxides have also shown to be promising for CO_2 electroreduction. SnO_2 nanosheets grown on carbon cloth (Figure 21c) exhibited formate FE of 87% at moderate overpotentials (880mV) with a high current density of 50mA cm^{-2}, which was enabled by the high density of sheets grown on individual carbon fibers providing a large surface area.[365] In addition, due to the flexibility of the carbon cloth support, the electrode demonstrated its structural robustness by the unaltered current outputs followed by multiple twisting and folding cycles (Figure 21d). SnO_2 nanowires have been studied as well where the induced structural porosity by further chemical treatments boosted the selectivity of the original SnO_2 NWs above that of the commercially available SnO_2 NPs (Figure 21e and f).[366] The use of nanoscale SnO_2 as a CO_2 electrocatalyst has proven successful in other types of structures, such as the nanourchins and

nanofibers.[369,370]

The origin of catalytic enhancement observed in SnO_2-based nanomaterials remains unclear. While there are some proposed hypotheses, such as the high density of grain boundaries present on these nanomaterials,[364,366] a more suitable explanation that could apply broadly to the SnO_2-based catalysts would be the presence of oxidized Sn under reductive bias conditions to perform as the active site,[272,371] as stated earlier. In this regard, tin sulfide catalysts have shown to exhibit high catalytic activity towards formate.[367,368,372] Single-layered SnS_2 nanosheets made by the exfoliation of bulk SnS_2 powder (Figure 21g-j) exhibited formate FE above 90% at -0.8V with long-term stability (~80 hrs).[367] Catalytic activity compared against the bulk SnS_2 powder hinted towards better stabilization of the *HCOO intermediate. The enhanced stabilization of *HCOO may be due to the incomplete reduction to metallic Sn as shown from the *in-situ* experiments of ALD grown SnS_x.[368] X-ray Absorption Near Edge Structure (XANES) measured *in-situ* showed that Sn maintains a higher oxidation state than the zero metallic state under bias, while XPS confirms the presence of remaining sulfur afterwards (Figure 21k). Together with the oxides, these set of oxidized Sn nanomaterial catalysts illustrate the importance of higher valence states of Sn for CO_2-to-formate conversion.

However, metallic Sn in the form of quantum sheets has been shown to be highly active for formate.[373] Oxidation of Sn was prevented by confining the metal in between the graphene layers, which was clearly proven by X-ray absorption spectroscopy (XAS). The enhanced activity towards formate could be attributed to a multitude of factors that include the lowered coordination environment of Sn on the surface of quantum sheets, which is similar to exposing a higher density of stepped surfaces or high index facets on the nanoparticles. This example illustrates that metallic Sn can be active for CO_2 reduction with a unique surface atomic construction that can better stabilize the intermediates to formate. Also, in this regard, it was shown that certain facets of Sn (*e.g.* Sn(200)) enhances the adsorption of $CO_2^{\bullet-}$ and HCO_2 by the strong responses recorded in the Fourier-transformed alternating current voltammetry.[374]
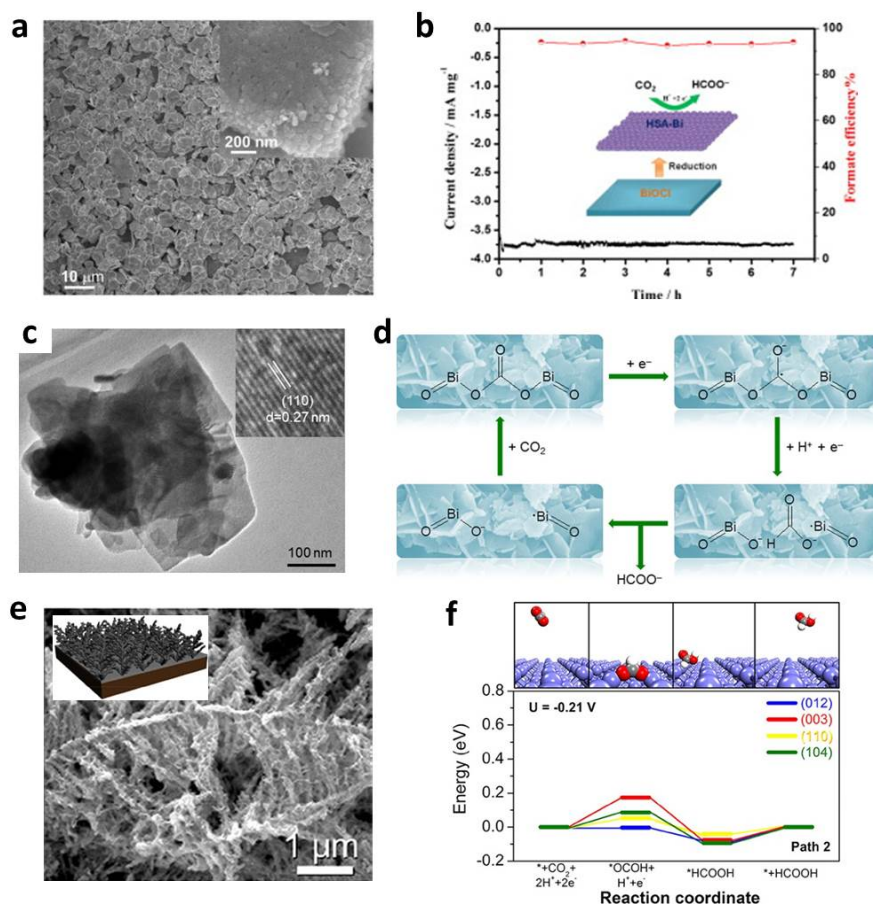
Figure 22. Bi nanocatalysts for CO_2 electroreduction. (a) Bi nanosheets electrochemically reduced from BiOCl nanosheets. (b) Long-term formate production from BiOCl-derived nanosheets. (a) and (b) reproduced from ref [375]. Copyright 2014 Elsevier B.V. (c) TEM image of $Bi_2O_2CO_3$ nanosheets. (d) Proposed mechanism for the reduction of CO_2 to formate on the $Bi_2O_2CO_3$ nanosheets. (c) and (d) reproduced from ref [376]. Copyright 2017 American Chemical Society. (e) SEM image of the Bi dendrite catalyst. (f) CO_2-to-formate reaction pathway via the *OCOH intermediate for various Bi planes of (003), (012), (110), and (104). (e) and (f) reproduced from ref [377]. Copyright 2017 American Chemical Society.

The approach with other elements has been similar as well. Nanomaterials derived from oxidized bismuth have been shown to be catalytically superior for formate production to the pristine metallic Bi. Bi nanosheets that are derived from various sources, including bismuth oxides and sulfides, exhibited high formate FE (80~90%) at lowered overpotentials (Figure 22).[375,376,378] For instance, single crystalline BiOCl nanosheets made by hydrothermal synthesis[379] could be used as CO_2 electrocatalysts, where their reduced form produced formate up to 92% FE (Figure 22a and b).[375] $Bi_2O_2CO_3$ nanosheets (Figure 22c) were able to reduce the overpotentials required for selective formate production by approximately 300mV compared to its metallic counterpart.[376] The

enhanced catalytic activity was attributed to the structure of $Bi_2O_2CO_3$ which already bears a carbonate group that may take part in the reaction pathway as an intermediate (Figure 22d). While this mechanism has been proposed based on the observation of adsorbed carbonate as an intermediate on metals such as tin and indium,[270,271] it remains uncertain as to whether the carbonate pathway can be considered as a general mechanism for formate production on p-block elements. A study using BiO_x nanoparticles showed that under reductive bias conditions the bismuth oxides are reduced to metallic bismuth which is quite different from the behavior observed with tin oxides that retain their oxidized states.[380] Therefore, it is plausible that the oxide-derived bismuth catalysts are active due to the surface structures of metallic bismuth that are formed from the phase transition process.

In this regard, nanostructuring of Bi has proven to be an effective strategy for formate production. Bi dendrites (Figure 22e) synthesized by electrodeposition was shown to exhibit high formate FE (> 90%) with long term stability (> 10 hrs).[377,381] Their favorable catalytic behavior was attributed to the high-index planes exposed on their surface that can better stabilize the *OCOH intermediate (Figure 22f).[377] However, alternative explanations can been provided for the nanostructured Bi catalysts, such as the high electric fields at nanostructured corners[382] or the porosity effects limiting H_2 evolution,[357,358] and further efforts are needed to deconvolute the various effects that span over multiple length scales.

Lead is another element that seems unclear as to the nature of active sites for formate production. A study using lead oxide found that its H_2 evolution activity was suppressed by 2 - 3 orders of magnitude compared to that of the pristine Pb foil.[273] It concluded that a metastable Pb oxide layer exists at the surface of the Pb oxide catalyst that mainly blocks proton reduction while still promoting a slow CO_2 reduction and accounting for its high formate selectivity. However, a theoretical work has found that the lead exhibits a strong affinity for oxygen that leads to a more stable formation of *OCHO compared against *H resulting in its high formate selectivity.[383]

While various nanoparticle forms of p-block elements have proven successful in promoting CO_2 conversion to formate, their catalytic origin tends to vary depending on the element used and for some elements, our understandings are still quite limited.[272] Fundamental studies in this regard should be further pursued to elucidate their underlying mechanism. The insights learned can be incorporated into nanoparticle catalysts to facilitate high rates of selective formate production.

3.2.3. Palladium-based nanomaterials for CO and formate production

Pd tends to be a unique element capable of producing both CO and formate, whereas most of the other elements known to be active for the 2-electron reduced products favor the formation of just one of the two. This bifunctionality of Pd is due to the formation Pd hydrides in electrolytic conditions that promote formate production by the interaction of CO_2 and *H.[274,384,385] Since the PdH_x are accessed near the thermodynamic potential for H_2 evolution, high formate FE can be attained while H_2 FE is limited (Figure 23).[386,387] Beyond certain potentials, metallic Pd surfaces

develop which promote CO formation instead. Therefore, the structural factors of catalysts taken into consideration may vary depending on the product desired.
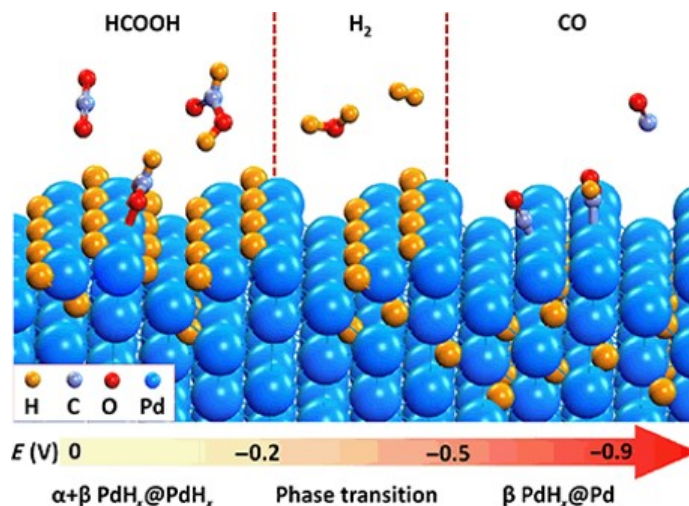
Figure 23. Phase transformation of Pd at negative potentials during electrochemical CO_2 reduction. Reproduced from ref [387]. Copyright 2017 Tsinghua University Press and Springer-Verlag Berlin Heidelberg.

As CO_2-to-$HCOO^-$ conversion seems to be facilitated by the catalytically active Pd hydrides, the tendency of their formation from the starting Pd structure should be considered for the design of formate producing catalysts.[388,389] Study of Pd NPs showed that NPs are generally more active for formate compared to bulk Pd substrates (Figure 24a and b).[388] This is due to the fact that it is more difficult to fully convert the bulk Pd to PdH_x from its low surface/volume ratio.[274,388] Furthermore, there existed a size-dependent selectivity trend towards formate within the Pd NPs (Figure 24b) where 6.5nm NPs exhibited the highest formate FE close to 98%.[388] This trend could be rationalized by the higher H_2 activity observed from smaller Pd NPs with increased density of low-coordinate surfaces. Therefore, promoting the formation of PdH_x should be considered at the same time together with suppressing H_2 evolution in the development of formate selective Pd electrocatalysts.
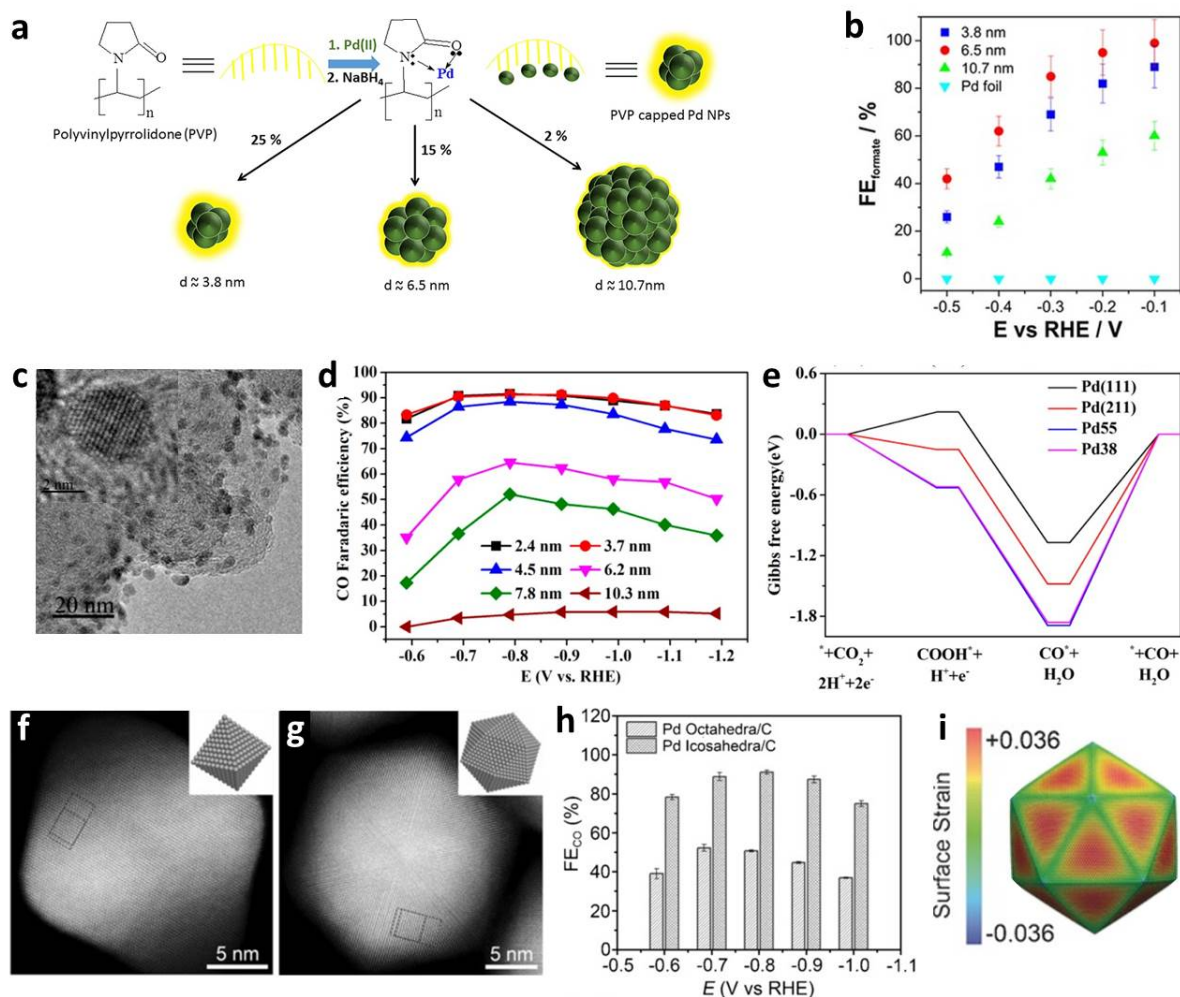
Figure 24. Pd nanoparticle catalysts for CO_2 electroreduction to CO and formate. (a) Schematic of Pd NP synthesis. (b) Formate FEs of Pd NPs of various size. (a) and (b) reproduced from ref [388]. Copyright 2017 Wiley-VCH Verlag GmbH & Co. KGaA, Weinheim. (c) TEM image of 3.7nm Pd NPs on carbon support. Inset is a HRTEM image of a Pd NP. (d) CO FEs of Pd NPs (e) Free energy diagrams for CO_2 reduction to CO on various Pd surfaces. (c-e) reproduced from ref [390]. Copyright 2015 American Chemical Society. HAADF-STEM images of a Pd octahedron (f) and Pd icosahedron (g). (h) CO FEs of Pd octahedra and icosahedra. (i) Surface strain fields of a Pd icosahedron. (f-i) reproduced from ref [391]. Copyright 2017 Wiley-VCH Verlag GmbH & Co. KGaA,Weinheim.

At more negative biases beyond the formate producing regime, the surface of Pd catalysts turn into metallic Pd that can be active for CO_2-to-CO conversion.[387] The structure-activity correlation of Pd nanoparticles for CO production has been studied as well.[390,391] As shown in Figure 24d, highest CO FE was observed for the smaller Pd NPs (2-4nm).[390] The observed trend was attributed to the strong stabilization of the *COOH intermediate on the corner and edge sites that are more

prevalent on the smaller NPs (Figure 24e), similar to the activity trends explained for the other noble metal NPs.[329,390] Strengthening the adsorption of the *COOH intermediate can be achieved by other methods, such as the strain engineering of NP surfaces. Shape dependent activity of Pd NPs showed that Pd icosahedra are more selective towards CO compared to the Pd octahedra (Figure 24h).[391] It was shown that the surface of an icosahedron are under tensile stress (Figure 24i) which results in an upward shift of the d-band and a corresponding increase in *COOH stabilization.

While the dual nature of Pd is attractive for the versatile use of the element, it has some drawbacks. The main issue is that the formate producing Pd hydrides can be poisoned by CO limiting their use.[274] In this regard, there have been efforts to increase the catalytic stability of these materials by suppressing CO formation.[392,393] Further efforts in preventing deactivation and increasing catalytic turnover for formate production and lowering overpotentials for CO formation are expected by studying Pd nanoparticles as CO_2 electrocatalysts.

3.2.4. Copper-based nanomaterials for higher order products

Under the classification of metals as CO_2 electrocatalysts, copper is so far the only element capable of producing higher order compounds that require more than two electron transfers as major products.[249,254] Therefore, many of the efforts in CO_2 electroreduction have been based on using Cu as a catalyst: understanding how it is active for CO_2 conversion[252,275,276,281-283,287,288,290,291,293,394,395] and developing ways to boost its catalytic efficiency. While copper has the potential to be active for higher order products, its activity/selectivity towards these products tends to be governed by the structural factors of catalysts. Cu-based nanomaterials have been shown to provide the structural configurations and catalytic motifs for promoting their formation.
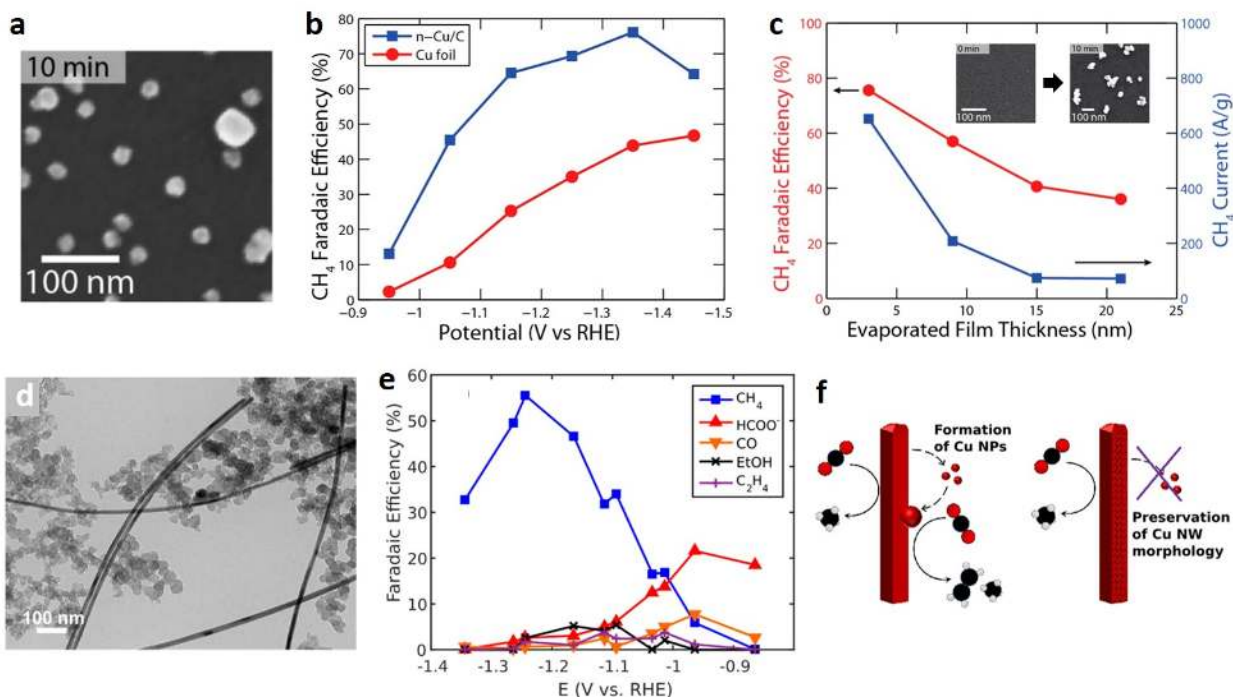
Figure 25. Cu NP and NW electrocatalysts for selective CH_4 formation. (a) SEM image of the ~25nm Cu NPs on glassy carbon (n-Cu/C) formed after polarization for 10 min at −1.25 V under CO_2 electroreduction conditions. (b) CH_4 FEs of n-Cu/C and copper foil. (c) CH_4 FE and mass activity as a function of evaporated copper film thickness. Inset shows a 3 nm copper film turning into Cu NPs after polarization at −1.25 V for 10 min. (a-c) reproduced from ref [396]. Copyright 2014 American Chemical Society. (d) TEM micrograph of Cu NWs loaded on carbon black. (e) Products of CO_2 reduction using Cu NWs, showing the prevalence of CH_4 over other products. (f) Scheme showing the onset of C_2H_4 followed by the disintegration of Cu NWs to small NPs. By preserving the Cu NW morphology (right), high CH_4 selectivity can be maintained. (d-f) reproduced from ref [397]. Copyright 2017 American Chemical Society.

Methane is a frequently observed C_1 product that needs multiple electron transfers (> 2e⁻). Its formation on bulk Cu foil has been observed with selectivity up to 40% at potentials more negative than -1V.[248] With regards to its selective formation, Cu-based nanocatalysts have proven to be effective.[396,397] In one study, it was shown that ~25nm Cu NPs dispersed on glassy carbon support exhibited ~80% CH_4 FE, which was about twice larger than that of Cu foil (Figure 25a and b).[396] Furthermore, regardless of the starting Cu structure, as long as the amount of Cu supported on glassy carbon was controlled, high CH_4 selectivities could be obtained by forming similarly sized Cu NPs during electrolysis (Figure 25c). This suggests that the CH_4 active Cu NPs are formed as the thermodynamically favorable structures under operational conditions and the deepened understanding of these structures would aid in the design of CH_4 selective catalysts. However, in the case of Cu NWs, it was shown that the initial structure is the active entity for CH_4 with FEs at 50 ~ 60% (Figure 25d-f).[397] Under biased conditions, the Cu NWs electrochemically disintegrated into smaller NPs that resulted in a mix of CH_4 and C_2H_4. While these works improved on the

possibility of CO_2 conversion to CH_4, it still remains uncertain as to the nature of active sites and ways to reduce the overpotentials required which is quite high at this point making the overall process energetically inefficient.

Multicarbon products (C_{2+}) that result from coupling of carbons are often viewed as in competition to methane. This may be due to the fact that mechanistic pathways diverge after the common intermediate *CO, so that the more it is used for methane the less available it becomes towards multicarbons.[252] Therefore, in order to obtain C_{2+} products, catalyst structures need to be tuned to promote the reaction pathways that involve C-C coupling. In terms of the effects of Cu surfaces, single crystal studies have shown that certain Cu facets, such as the (100) and stepped (100) surfaces, favor ethylene over methane.[398,399] The favored production of ethylene (and other C_{2+} products) on (100) type surfaces has been explained by the lower energy barrier towards the dimerization of the *CO intermediate compared to that of the other Cu surfaces.[294,400-402]

Owing to this structure sensitivity of C_{2+} products, nanoparticles bearing (100) surfaces have been utilized for the selective conversion of CO_2 to multicarbons. Electrochemical cycling of Cu foils in aqueous halide solutions results in a high density of nanoscale cubes that are active for ethylene (Figure 26a and b).[403] Detailed study of this potential cycling method in the presence of halide ions has shown that Cu foil oxidizes to Cu halide nanocubes during the positive scan that further converts to Cu_2O nanocubes (Figure 26c).[404] It seems that the Cu_2O nanocubes can act as good electrocatalysts for CO_2 to multicarbons, as demonstrated in other works as well.[405]
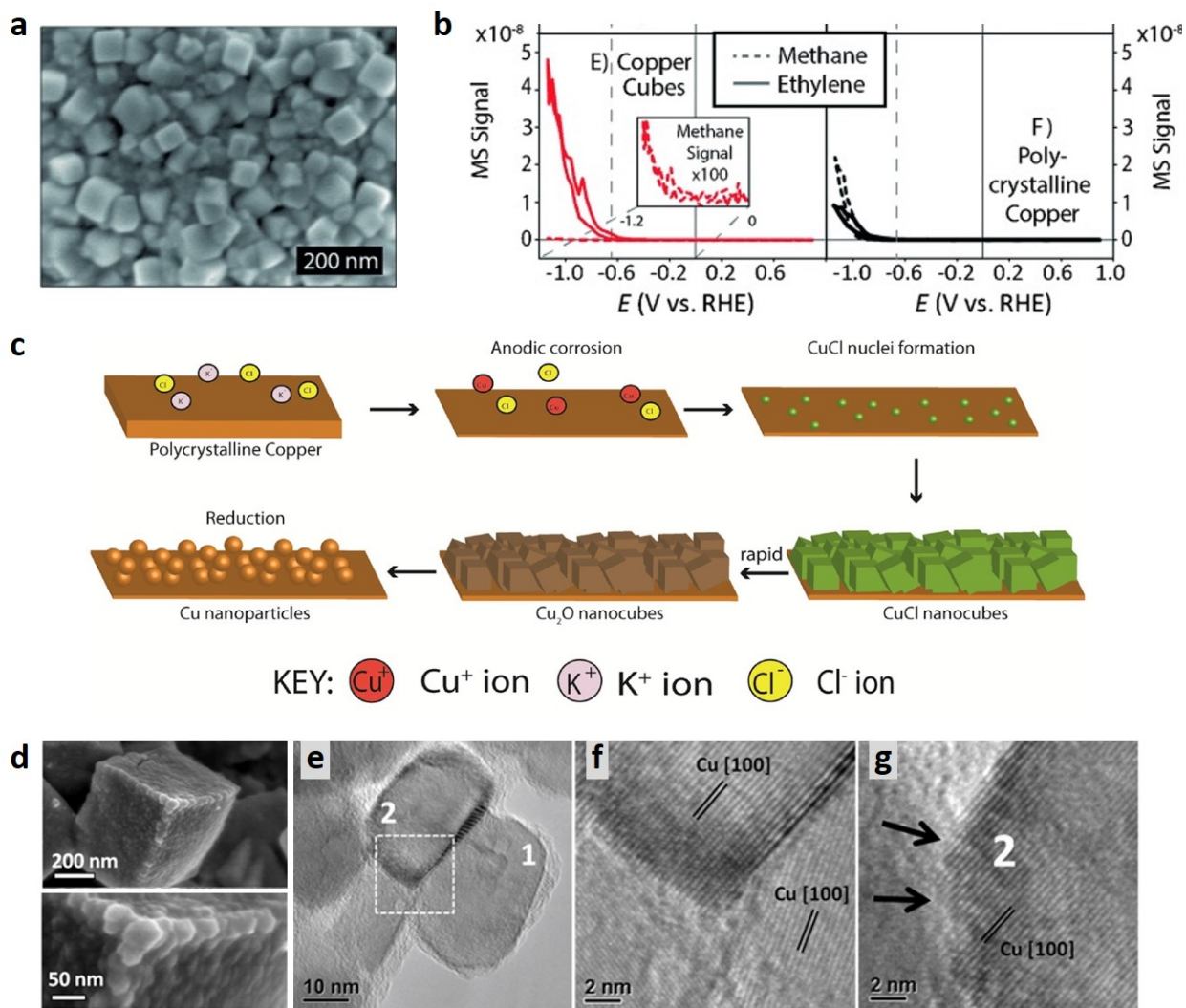
Figure 26. Cu_2O nanocubes as CO_2 electrocatalysts. (a) SEM image of copper nanocube surface formed by cycling a polycrystalline electrode in KCl. (b) Methane (dashed) and ethylene (solid) formation measured by OLEMS on the copper nanocube surface and polycrystalline copper. (a) and (b) reproduced from ref [403]. Copyright 2015 Wiley-VCH Verlag GmbH & Co. KGaA,Weinheim. (c) Schematic illustrating the formation of copper halide and copper oxide nanocubes. (c) reproduced from ref [404]. Copyright 2016 Wiley-VCH Verlag GmbH & Co. KGaA,Weinheim. (d) SEM image of halide-derived copper cubes after CO_2 electroreduction. (e-g) HRTEM images of the halide-derived copper cubes after CO_2 electroreduction. (d-g) reproduced from ref [405]. Copyright 2015 The Royal Society of Chemistry.

In this regard, the phase stability of Cu_2O under reductive bias conditions should be considered. Under CO_2 reduction conditions, metallic Cu is the thermodynamically favored phase.[406] Therefore, the structures that are derived from Cu_2O nanocubes are the truly active catalysts for C_{2+} products and the question remain as to what those are. Characterization of the Cu_2O nanocubes

after electrolysis shows aggregates of small Cu NPs (Figure 26). Some studies have suggested that the small Cu NPs derived from the oxide cubes are mainly composed of (100) facets (Figure 26d-g).[405] However, due to the fact that the surfaces of these catalysts contain interconnected small NPs, other explanations for the active sites, such as the grain boundary terminations, have been proposed.[404] The catalytic relevance of the claim involving the high density of grain boundaries as active sites for the C_{2+} products is further supported by works that use bulk copper oxides as CO_2 electrocatalysts.[407-409] Cu oxides made by a multitude of approaches that include thermal oxidation,[407] oxygen plasma,[410] chemical growth,[411,412] and electrochemical deposition[413-416] have proven to be useful as an electrocatalyst for CO_2 conversion to C_{2+} products. One of the claims that have been used to explain their favored selectivity towards the C_{2+} products is the presence of high density of grain boundaries on the oxide-derived Cu surfaces.[352,417]

Other works have emphasized the role subsurface oxygen in oxide-derived copper for CO_2 electroreduction.[418-421] Studies of Cu_2O nanocubes as CO_2 electrocatalysts have shown the presence of residual subsurface oxygen on the Cu_2O-derived Cu NPs.[418,419] In the near surface regions of the Cu_2O-derived Cu NPs where there was a lack of crystallinity, oxidized Cu atoms could be detected by EELS indicating the presence of oxygen atoms (Figure 27). The local O concentration in those regions approximate to about a 20 at% which is not as high as the Cu_2O phase but still substantial compared to a pristine Cu metal. Positron annihilation spectroscopy (PAS) was performed to further support the presence of oxygen in the amorphous layers, eventually leading to a conclusion that the oxide derived Cu NPs may contain an amorphous Cu outerlayer with oxygen atoms included at its subsurface. The energetic stability of subsurface O atoms in Cu has been discussed by theory[420] and experimental techniques such as ambient pressure X-ray photoelectron spectroscopy on single crystal Cu surfaces have further supported the idea.[421]
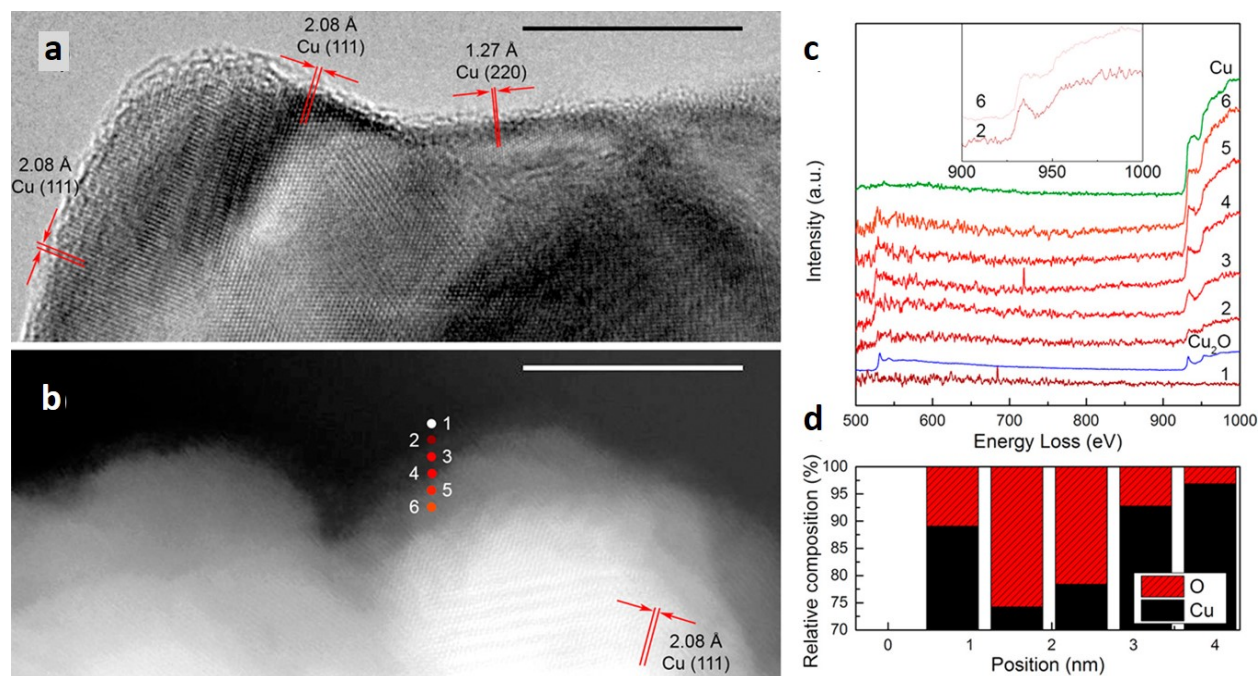
Figure 27. Presence of subsurface oxygen on reduced Cu_2O nanocubes. (a) HRTEM and (b) STEM ADF image of reduced Cu_2O nanocubes. Scale bars are 10 nm. (c) STEM EEL spectra acquired at the points indicated in (b). Reference spectra for Cu_2O and Cu are shown in blue and green, respectively. (d) Quantitative analysis of the STEM EEL spectra. Figure reproduced from ref [418]. Copyright 2017 American Chemical Society.

With regards to the residual oxygen, various works have suggested similar ideas of the retained oxidized Cu phase (*i.e.* the presence of Cu(I) states) under reductive conditions as critical for the high multicarbon activity,[410,415,422,423] despite not as specific as the hypothesis of subsurface oxygens. For instance, by treating the Cu foils with oxygen plasma, it was shown that the superior activity for multicarbons resulting from the treatment may originate from the stable copper oxide species on the surface (Figure 28).[410] *Operando* spectroscopic techniques have been employed as well to show that oxidized Cu phase may be catalytically relevant for C_{2+} products formation.[415,423] A similar approach has been demonstrated with copper nitride nanoparticles which had a better advantage of retaining the oxidized copper states during electrochemical operation, leading to higher selectivity for multicarbon formation with prolonged catalytic stability (Figure 28).[424]

Figure 28. The presence of oxidized copper states contributing to multicarbon formation. (a) EDS elemental maps, HRTEM, and SAED analysis of Cu foils treated with oxygen plasma. The images labeled 'after reaction' are used catalysts for CO_2RR for 1h at −0.91 V vs. RHE. Scale bars are 300 nm (top row, left three); 20 nm (top row, right); 200 nm (bottom row). (b) Summary o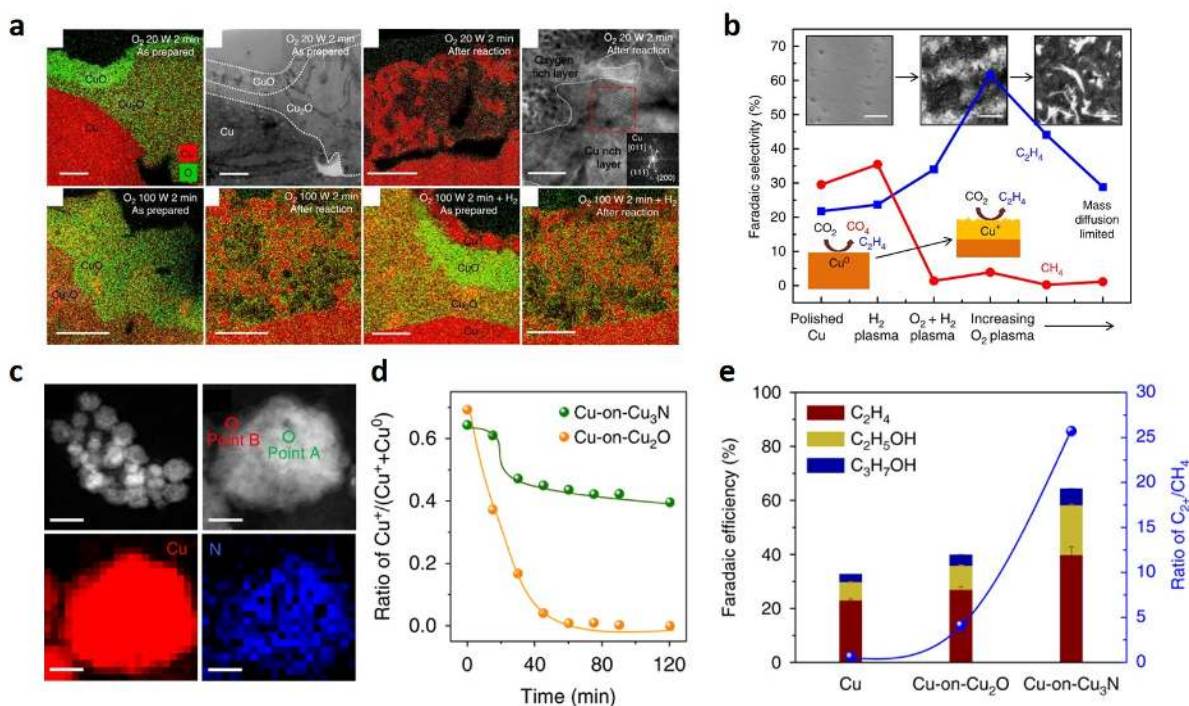f hydrocarbon selectivity of plasma-treated Cu foils. (a-b) reproduced from ref [410]. Copyright 2016 Macmillan Publishers Limited. (c) HADDF-STEM images and STEM-EELS elemental maps of the Cu-on-Cu_3N catalyst. Scale bars are 50 nm (top, left) and 10 nm (top, right and bottom row). (d) Ratio of Cu^+ relative to the reaction time at −0.95 V vs. RHE. (e) Comparison of faradaic efficiency for C_{2+} and the ratio of C_{2+}/CH_4 at −0.95 V vs. RHE on Cu, Cu-on-Cu_2O, and Cu-on-Cu_3N. (c-e) reproduced from ref [424]. Copyright 2016 Macmillan Publishers Limited.

However, there have been observations that suggest the opposite: metallic Cu being the active material of the oxide-derived Cu catalyst for CO_2 electroreduction. *In Situ* X-ray Absorption Spectroscopy of Cu(I) oxide and Cu(II) carbonate/hydroxide used as catalysts has shown that the active state of the material is metallic Cu with little relevance of their activity to the starting oxidation state.[425] Furthermore, another study that tested various oxide-derived Cu catalysts revealed that the their high surface area obtained from the oxidation treatment is critical for their high C_{2+} selectivity. The high surface area of oxide-derived catalysts brought sufficiently high current density that caused a shift to a higher pH near the catalyst surface and promoted C_{2+} formation.[426] In this regard, electrolyzers with gas-diffusion electrodes and basic electrolytes (*i.e.* KOH) have shown to be effective for selectively converting CO_2 to ethylene. By combining the effects of high concentration of CO_2 near the vicinity of the electrode and basicity of electrolytes towards intermediate stabilization, C_2H_4 FE close to 70% has been demonstrated.[427] These observations rather suggest that oxides may not be closely relevant to the C_{2+} product activity of

Cu catalysts. There is the possibility that the oxides that have been observed for some of the oxide-derived Cu materials may reside in the bulk of the material and be still present under electrochemical conditions. Furthermore, the formation of oxides from metallic copper after electrochemical operation may happen rapidly from other sources besides air exposure, such as the aqueous electrolyte.[428]

In this regard, controlling the structure of metallic Cu nanocatalysts has received considerable attention. Owing to the favored selectivity towards C_{2+} products on Cu (100) type surfaces,[398,399] colloidally synthesized Cu nanocubes have been tested as CO_2 electrocatalysts.[429] Among the Cu nanocubes of various edge length (20 to 60nm), the cubes of intermediate size (44nm) exhibited the highest selectivity towards the CO_2 reduced products (FE_{CO2RR} = 80%) and ethylene (FE_{C2H4} = 41%). This trend of peak C_{2+} selectivity in the intermediate size regime was explained by the optimal balance of the relative population of plane and edge atoms. However, how this results in an enhanced C_{2+} activity remains unclear. There have been also attempts to tune the structure of copper catalysts at larger scales, such as the construction of dendrites and porous scaffolds, that have promoted multicarbon formation.[430-433] The promotional effects seem to originate from the environmental conditions caused by the structures, such as the local pH effects, as they lack structural preciseness down to atomic scales. As the C_{2+} products tend to be promoted by various approaches that span over large length scales, it seems important to precisely understand the impact of individual effects and combine them together to create synergistic outcomes.

Another important aspect of nanocatalysts is their reconstruction under operation. It has been shown that copper may be susceptible to structural changes under CO_2 electrochemical conditions (Figure 29), which can even be directly observed using techniques such as ECSTM.[434,435] Moreover, a recent work has shown that the structural transformation occurring under electrochemical conditions can actually be beneficial for C_{2+} forming catalysis.[436] Fusion of densely arranged spherical Cu NPs during electrolysis resulted in an array of nanoscale Cu cubes that could drive CO_2 to C_{2+} products at surprisingly low overpotentials (Figure 29). It was shown that the rather counter intuitive approach of allowing the NPs to fuse was actually beneficial for promoting C_{2+} formation. While still a lot remains to be understood with regards to how the transformation occurs and whether it can be precisely controlled, the work clearly brought to attention the importance of structural changes occurring for electrocatalysts under operation.
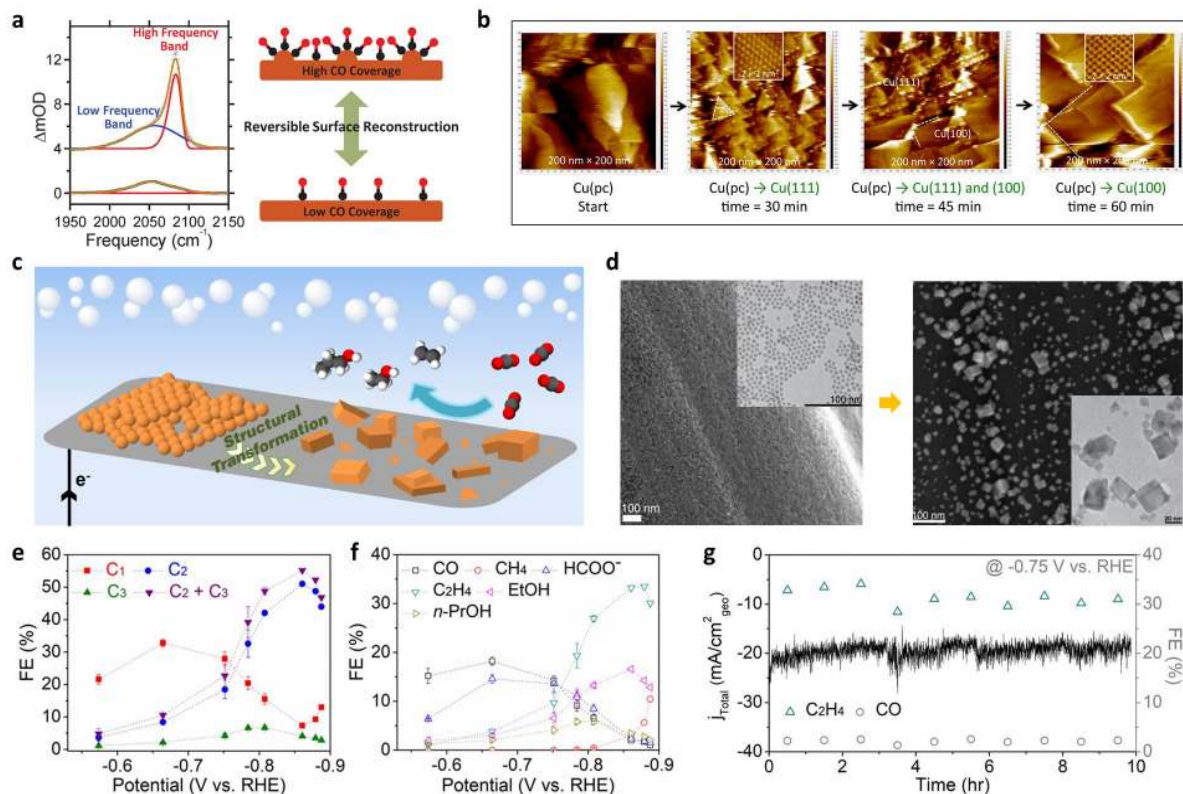
Figure 29. Dynamic structural evolution of copper during electrocatalysis. (a) IR spectrum in the CO stretch region under high (above) and low (below) overpotentials applied to Cu foil electrodes. (a) reproduced from ref [434]. Copyright 2017 American Chemical Society. (b) *Operando* electrochemical scanning tunneling microscopy of a polycrystalline copper electrode, Cu(pc), held at -0.9V vs. SHE in 0.1M KOH. (b) reproduced from ref [435]. Copyright 2016 Elsevier B.V. (c) Schematic illustrating the transformation process of Cu NP ensembles to an active catalyst for C_2–C_3 product formation. (d) SEM and TEM images showing the structural changes of the Cu NP ensembles during CO_2 electroreduction. FE of C_1, C_2, and C_3 products (e) and the major products (f) at various potentials for the transformed Cu NPs. Electrochemical tests were conducted using 0.1M KHCO$_3$ solution at 1atm CO_2. (g) Long-term electrolysis at −0.75V vs. RHE with gas products measured every hour. Electrochemical tests were conducted using 0.1M CsHCO$_3$ solution at 1atm CO_2. (c-g) reproduced from ref [436]. Copyright 2017 National Academy of Sciences.

Among the C_{2+} products, ethylene tends to be by far the majority observed. There have been some efforts to produce other multicarbon products that include ethane, ethanol and *n*-propanol. Studies using copper single crystals have shown that stepped terraces of Cu(100) and (110) are more selective towards multicarbon oxygenates.[398,399,437,438] In this regard, agglomerated Cu nanocrystals (~15nm size) exhibited high activity for *n*-propanol with its FEs reaching close 10% and their activity was attributed to the high density of defective sites at the nanocrystal junctions.[439]

A rather surprising result has been observed as well from using Cu NPs on nitrogen doped carbon nanospikes to produce ethanol at FE of 60% at -1.2V with speculations on the synergistic interactions between the Cu NP and the carbon material.[440] Furthermore, copper sulfide NPs have been shown to be capable of boosting formate and multicarbon alcohols formation.[441,442] Engineering macroscopic structures of copper can also steer the products in between the various multicarbons, such as between ethylene and ethane by altering the retention times of the intermediates within its structure.[443]

While copper-based nanomaterials have provided improvements with multicarbon production from CO_2, the molecular mechanism of how they are produced remains elusive. Along the same line, the exact nature of the required catalytic motifs to promote multielectron transfers and C-C coupling remains to be identified. Continued efforts in the study of Cu nanocatalysts for CO_2 electroreduction may shed light into these major questions and bring the technology to a level closer to practical applications.

3.3. Other elemental systems for CO_2 electroreduction

Besides the elements discussed above that fall under the major category, other various elemental systems have proven to be useful as CO_2 electrocatalysts. For instance, molybdenum electrodes have been observed to produce methanol at low overpotentials, albeit at slow rates.[444] While less studied than the other CO forming catalysts, Zn-based catalysts can reach high selectivity for CO.[445] Among a multitude of examples, nanomaterials of transition metal chalcogenides and cobalt oxides are discussed which are active for CO and formate, respectively.

Transition metal dichalcogenides can function as an active catalyst for CO_2-to-CO conversion in ionic liquids. After the first identification of molybdenum disulphide as a promising alternative CO catalyst for noble metals,[446] a range of metal dichalcogenide 2D nanoflakes have been explored as catalysts.[447] Among the explored, WSe_2 nanoflakes exhibited the highest activity for CO with overpotentials as low as 54mV (Figure 30a-c), which was attributed to their low work function and strong binding energies toward CO_2 reduction intermediates. Furthermore, it was shown that the CO_2 electrocatalytic property of transition metal dichalcogenides could be tuned by using dopant atoms, as demonstrated with Nb doping on vertically aligned MoS_2 that resulted in an increased activity (Figure 30d-f).[448]
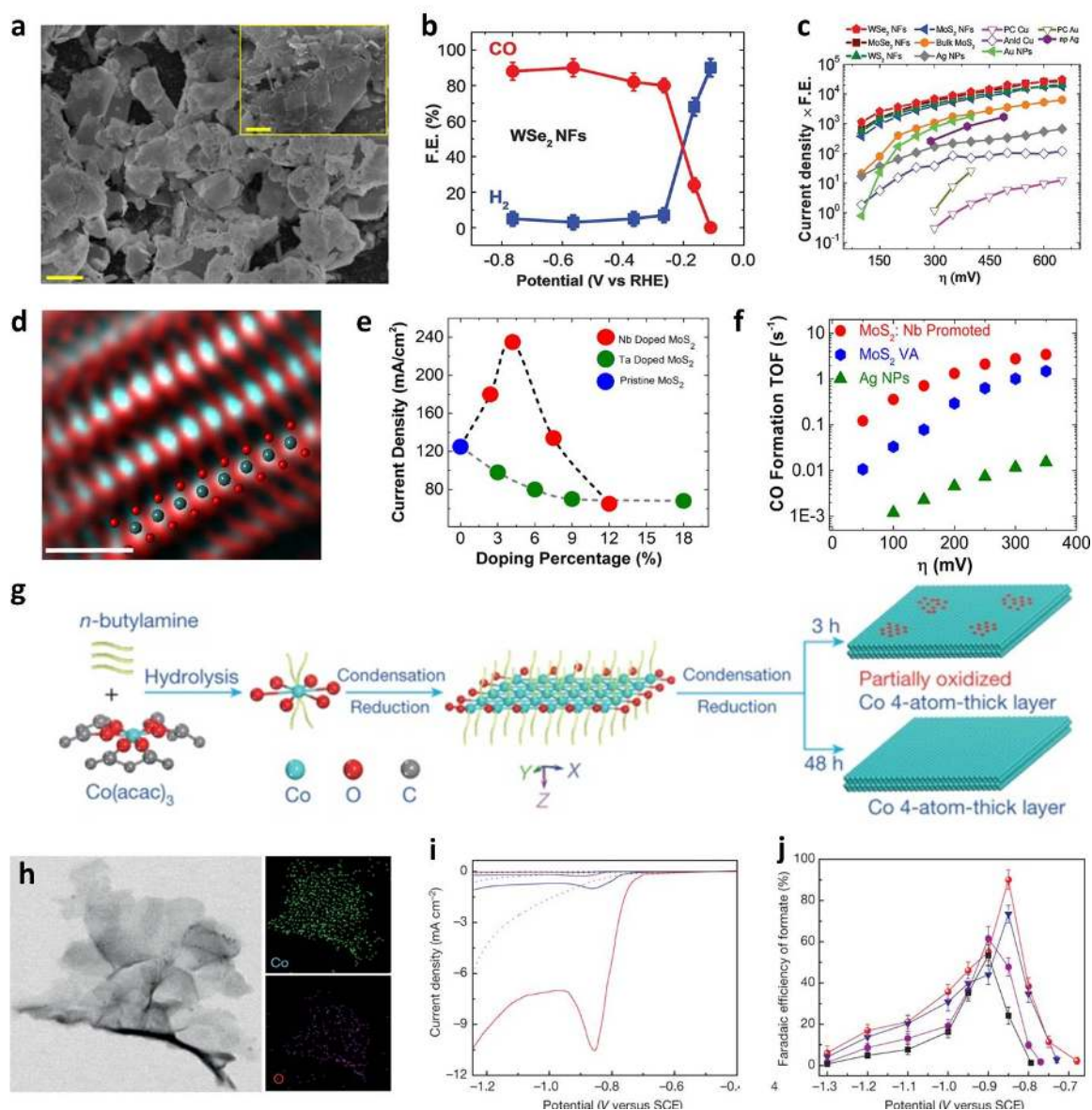
Figure 30. Transition metal dichalcogenides and cobalt oxides as CO_2 electrocatalysts. (a) SEM image of WSe_2 nanoflakes (scale bar, 2 μm and 200 nm in the inset). (b) CO and H_2 FE at different applied potentials for WSe_2 NFs. (c) Overview of different catalysts' activity. (a-c) reproduced from ref [447]. Copyright 2016 the American Association for the Advancement of Science. (d) RGB image of Nb doped vertically aligned MoS_2 nanosheets, which is constructed from HAADF and annular bright-field images. (e) Current density as a function of dopant percentage for Nb-doped and Ta-doped MoS_2 nanosheets. (f) CO TOF for Nb-doped MoS_2 nanosheets, pure MoS_2 nanosheets (MoS_2 VA), and Ag NPs. (d-f) reproduced from ref [448]. Copyright 2017 American Chemical Society. (g) Schematic of the synthesis process of partially oxidized Co 4-atom-thick layers. (h) TEM image and elemental mapping of the Co 4-atom-thick layers. (i) Linear sweep voltammetric curves in a CO_2-saturated (solid line) and N_2-saturated (dashed line) 0.1M Na_2SO_4 aqueous solution. (j) Faradaic efficiencies of formate at each given potential. Data are shown for

partially oxidized Co 4-atom-thick layers (red), Co 4-atom-thick layers (blue), partially oxidized bulk Co (violet) and bulk Co (black). (g-j) reproduced from ref [449]. Copyright 2016 Macmillan Publishers Limited.

With cobalt being moderately selective for formate at low overpotentials, it was shown that atomically thin oxidized cobalt layers can boost the formate FE up to 90% and increase the catalytic activity by 5- to 10-folds compared against the metallic counterparts (Figure 30g-j).[449] When comparing Co_3O_4 catalysts of varying thicknesses, the thinnest layers exhibited the highest formate selectivity/activity.[450] Besides the high electronic conductivity of the thin Co_3O_4 layers,[450] it was shown that the oxygen vacancies present on the catalyst material could reduce the energy barrier towards the rate determining pronation step to form the *HCOO intermediate.[451]

3.4. Multimetallic nanomaterials as CO_2 electrocatalysts

Use of multiple element systems as catalysts offers several distinct advantages over the single element counterparts. First of all, fine tuning of the catalyst properties, such as its electronic structure, in between the discrete values observed from single elements becomes possible. This opens up the possibility of attaining catalyst structures with optimum characteristics for driving catalytic reactions that may not be accessible otherwise.[321] In addition, it may allow the decoupling the interactions between the catalyst surface and various intermediates beyond the limits of scaling relations.[319] This is particularly important for multi-electron reactions which involve a large number of intermediates. Very often optimization of the adsorption energy for each individual intermediate is required which is difficult to achieve on a surface composed of a single element. In this regard, multimetallic nanomaterials have been studied as CO_2 electrocatalysts with a focus on how the inclusion of a second element to the system affects their catalytic properties.[452]
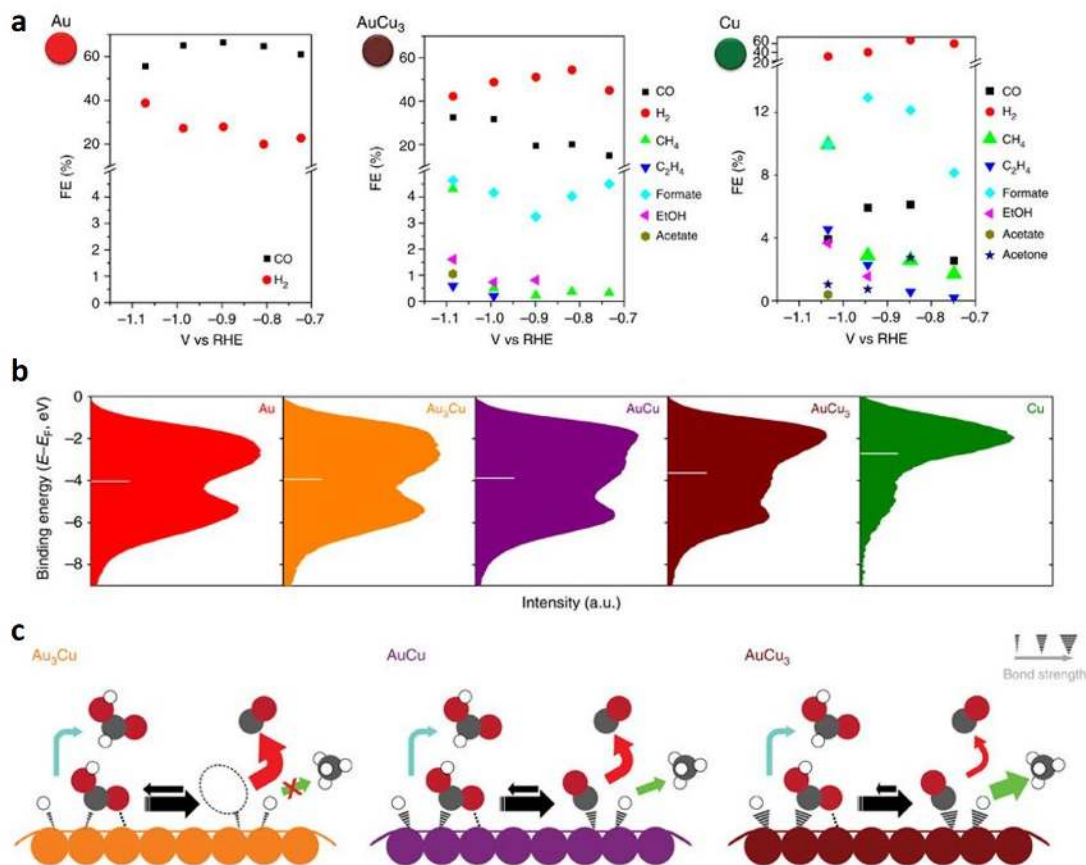
Figure 31. Composition-dependent activity of AuCu alloy nanoparticles. (a) FE of the CO_2 reduced products formed from the AuCu alloy nanoparticles. (b) Surface valence band photoemission spectra of Au–Cu bimetallic nanoparticles. (c) Schematic showing the proposed mechanism for CO_2 reduction on the catalyst surface of AuCu alloy nanoparticles. Filled circles with grey is C, red is O and white is H. The relative intermediate binding strength is indicated by the stroke weight (on the top right corner). Additional binding between the COOH and the catalyst surface is presented as a dotted line. Arrows between the adsorbed COOH and adsorbed CO is to show the difference in probability of having COOH adsorbed on different types of surfaces. Colored arrows indicate the pathway to each product: red for CO, blue for formate and green for hydrocarbons. Larger arrows indicate higher turnover. (a-c) reproduced from ref [453]. Copyright 2014 Macmillan Publishers Limited.

The attempt to systematically study the effects of catalyst composition on its CO_2 electrocatalytic behavior was first made by using the gold-copper alloy nanoparticles.[453] It was shown that by changing the composition of the NPs, the product distribution shifted accordingly such that the Cu-rich NPs favored more of the higher-order products like methane and ethylene (Figure 31a). This trend was attributed to the shift in the electronic structure of the NPs which governed the binding strength of intermediates (Figure 31b and c).[454] Similar trends in the shift of catalytic

selectivity have been observed in other elemental systems, such as Au-Pt,[455] and Cu-Pd.[456]

While electronic structures of catalysts have profound effects on the catalytic reactions, they are an average representation of surfaces where the local geometric configuration of active sites can also play significant roles.[453] In this regard, the distribution of both elements in the system and the precise configuration of surface atoms become important. For bimetallic systems of certain elemental combinations, there may exist thermodynamically favorable intermetallic phases exhibiting distinct catalytic properties. The CO_2 electrocatalytic property of intermetallic phases has been explored using Au-Cu[457] and Cu-Pd[458] nanoparticles, where a distinct shift in the catalytic activity was observed (Figure 32). Atomic-level investigations on the ordered AuCu NPs showed that the transition to an intermetallic phase accompanies surface-enrichment of a more noble element (Figure 32g), which is the cause for the activity to change. Even without intentionally causing an element redistribution, it may occur naturally by the dynamic evolution of catalyst materials in electrochemical media. This phenomenon has been observed with the Cu-In alloys where the system eventually converts to a Cu-rich core and a In hydroxide shell that is favorable for CO production.[459,460] The noble metal rich core and an oxide shell has been demonstrated in NP systems of Pd-Sn,[461] Ag-Sn,[462] and Cu-Sn[463] as well, where the tin oxide shells have promoted CO and formate production depending on its configuration and the underlying element. In addition, an interface between the two elemental nanostructures have also been investigated for promoting CO_2 conversion such as the Cu-In[460] and Bi-Sn.[464] Overall, a rich library of CO_2 catalyst materials has been studied for the multielemental systems from not just the change of composition, but the various mixing patterns of a combination of elements and phases.
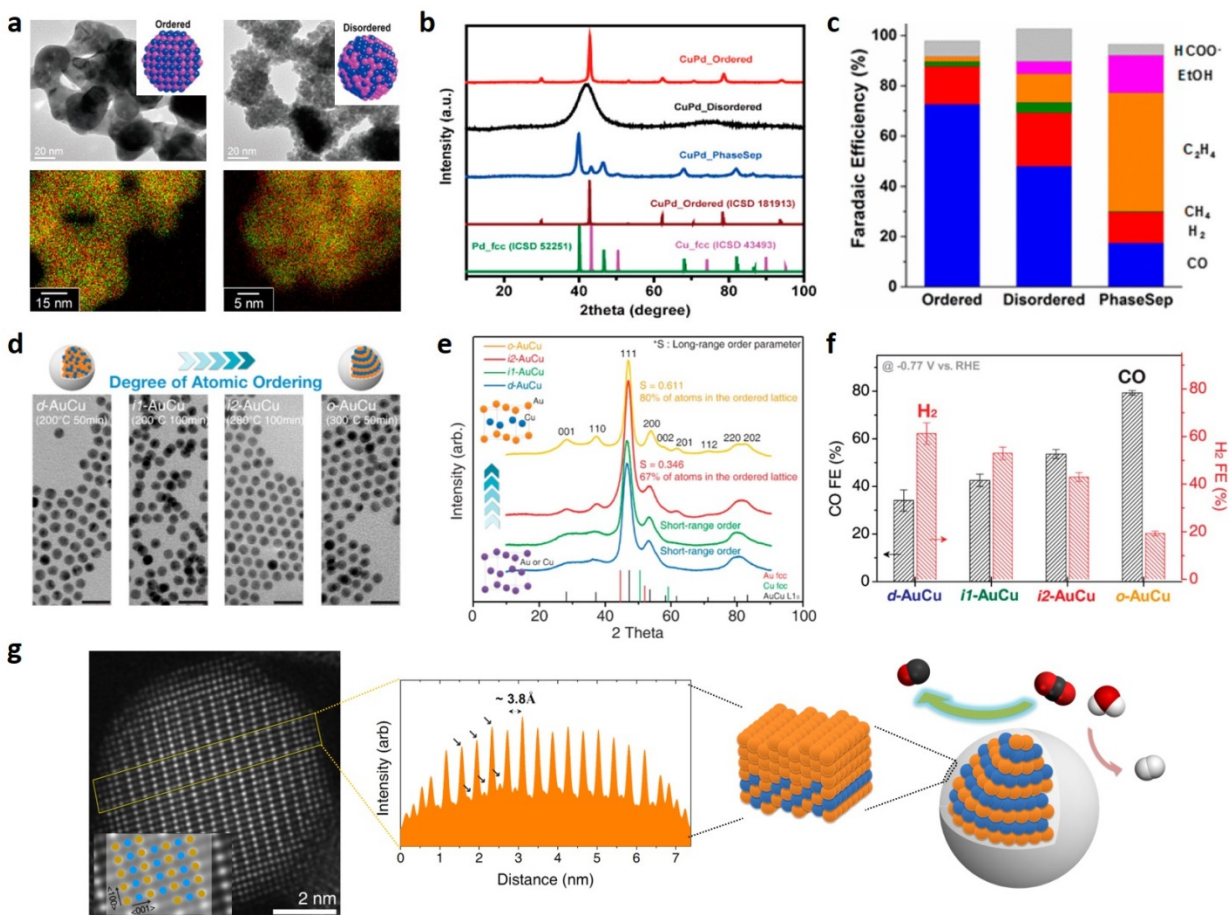
Figure 32. Catalytic activity of intermetallic nanoparticles. (a) TEM images and EDS maps of ordered and disordered CuPd nanoparticles. (b) XRD patterns of CuPd nanoparticles. (c) Production distributions of CuPd nanoparticles. (a-c) reproduced from ref [458]. Copyright 2017 American Chemical Society. (d) TEM images of AuCu bimetallic NPs synthesized at various conditions allowing for systematic tuning of the degree of ordering. Scale bar, 20 nm. (e) XRD of AuCu bimetallic NPs. (f) Electrochemical CO_2 reduction activities of AuCu bimetallic NPs. (g) Structural investigation of ordered AuCu NP (*o*-AuCu) at atomic resolution. Aberration-corrected HAADF-STEM image of *o*-AuCu and a magnified STEM image of the center of the particle as inset. Shown is the overlapping schematic of the structure projection. Atoms in orange and blue color represent gold and copper, respectively. Intensity profile across the particle measured from the yellow box. The distance between the strong intensities matches with the separation between gold atoms. Arrows indicate alternating high and low intensities, which represent gold and copper atoms, respectively. A schematic of a particle shows a gold-enriched outer layer of a few atom thickness that is responsible for the enhanced CO_2 conversion. (d-g) reproduced from ref [457]. Copyright 2017 American Chemical Society.

While most of the binary systems have been used towards promoting 2-electron reduced products

of CO and formate, a few selection of the element combinations have resulted in the formation of multicarbons. So far, the most studied is the Ag-Cu system which has been effective for shifting the selectivity towards multicarbon oxygenates.[465-467] There have been a number of explanations regarding its catalytic origin. One of the hypotheses is related to the phase immiscibility of the Ag-Cu system, which states that the CO (or the *CO) produced at the Ag phase translates to the Cu phase to promote ethanol formation.[465,467,468] This idea has been tested with microfabricated Ag-Cu electrodes where the distance between the two phases and their relative portion were systematically controlled.[467] With the approach, an increase in the multicarbon oxygenate/ethylene ratio was observed up to ~2.4 compared against 0.6 of pure Cu and the enhanced oxygenates selectivity was attributed to the increased *CO on Cu by the high local CO concentrations created from the nearby Ag. On the other hand, a work that monitored the state of the Ag-Cu alloy catalysts during CO_2 electroreduction has instead proposed that the inclusion of Ag atoms in a Cu-rich alloy phase results in a compressive strain of the Cu surface that enhances CO binding relative to H and O to promote multicarbon oxygenates.[466] The oxygenates promoting effect, especially the carbonyl and carboxylate containing products, of Ag-Cu systems has been demonstrated with mixtures of small Ag and Cu nanoparticle mixtures in a polymer film that gave 21% FE for acetate.[469] Furthermore, besides the Ag-Cu system, there have been other element combinations that have resulted in multicarbon products albeit at low FEs.[470] It is expected that increasing efforts in this direction may bring catalysts that could facilitate complex products formation beside the copper-based catalysts heavily invested so far.

4. Nanostructured materials for tandem catalysis

4.1. Introduction to tandem catalysis

Transformation of simple building blocks into complex molecules is the essence of the modern chemical industry, where fine chemicals, polymers, and pharmaceuticals are produced from vastly available feedstocks such as fossil fuels and other natural resources. Millennia before the modern era, chemical transformations toward complexity have already played central roles in the origin of life. Biological organisms, with all its complex molecules such as proteins and sugars, are essentially built from simple reagents such as CO_2 and H_2O through multi-step reactions catalyzed by enzymes. While many of these catalytic reactions have to be carried out step by step, some of them are deliberately coupled spatially and temporally.[471] For example, in photosynthesis, bicarbonate transported into carboxysomes are converted to CO_2 by carbonic anhydrase and subsequently take part in the Calvin cycle catalyzed by RuBisCO.[472,473] The carboxysomes, a bacteria microcompartment, confines the CO_2 releases in the dehydration reaction and prevent its loss to the cytoplasm, thus creating a favorable local environment for the CO_2 fixation reaction.[474] Another example is the sequential reduction of carboxylic acids into alcohols in the confined space of metabolosomes, where the toxic and unstable aldehyde intermediates produced in the initial carboxylic acid reduction is consumed *in situ* by the subsequent reduction reactions to give alcohols.[475,476]

These multi-enzymes catalyzed reactions in nature are inspiring examples for the development of inorganic catalysts for coupled multi-step reactions.[477,478] Tandem catalysis, where sequential reactions are coupled and catalyzed by a single nanostructured catalyst with multiple active sites, presents a number of opportunities to improve chemical transformations. It eliminates the steps for intermediates separation, purification, and transportation which is especially beneficial in situations where the reaction intermediates (product of the first reaction) are thermally unstable or toxic. In addition, by coupling multiple reactions, tandem catalysis could alter the thermodynamic landscape of the individual reactions and achieve superior performance. The most straightforward effect in this perspective is the shifting of chemical equilibrium, where the second reaction would consume the products from the first reaction and shift the equilibrium of the first reaction to forward direction via Le' Chatelier's principle and thus improve the productivity. On the microscopic level, co-existence of reactant, intermediates, and products of multiple sequential reactions could result in the synergy between different chemical reactions. One typical case is the reaction intermediates of the first reaction could directly transfer to the catalytic sites of the second reaction, which would effectively change the reactant of the subsequent reaction and thus lead to altered reactivity. These synergistic effects on the microscopic level could lead to greatly improved activity and selectivity of individual reactions and thus facilitate the overall chemical conversion.

In this chapter, we would discuss the principle and application of tandem catalysis, and also summarize the synthetic approaches to produce such catalysts. Herein we would limit our discussion on nanostructured inorganic heterogeneous catalysts and mostly focus on gas phase thermal reactions. For homogeneous tandem catalysis using molecular catalysts, the scientific considerations are largely different and they have been summarized in various review articles.[479-481]

4.2. Principles and Considerations on the design of tandem catalysis

Conceptually, the strategy of tandem catalysis seems straightforward and could be generally applied to most sequential reactions, where multiple well-optimized catalytic sites can be simply mixed. However, several factors need to be evaluated for the feasibility and rational design of tandem catalysts.

The primary and most obvious consideration is the compatibility of the coupled reactions. The chemical species of each step would need to be compatible. This is simple to understand as exposing the reagent of one reaction to the catalyst and reactant of another reaction could lead to undesirable side reactions or degradation of the catalyst. The reaction condition, including temperature, pressure and chemical environment, also need to be compatible. Also, the optimum conditions for each reaction are often not identical, so a compromise needs to be made to achieve overall optimal reactivity and selectivity. In general, the starting point of the tandem catalysis design is to identify the range of conditions where both of the coupled reactions are thermodynamically favorable. The search for the optimum condition within this range would often focus on reaction kinetics. In this process, the tuning of temperature, pressure, reactants

stoichiometry, or catalytic active sites would affect the kinetics of all the reaction steps. Thus, optimization of the overall tandem reaction would be much more complicated than individual single step reaction.

In the design of tandem catalysis, surface and interface of nanostructures play crucial roles. Catalytic gas phase reaction mostly take place on the surface of the catalysts, and the catalytic active sites often reside on metal-oxide interfaces. The optimization of single-step reactions would then involves tuning of the surface and interface of heterogeneous catalysts, which have attracted tremendous research efforts in the past decades.[482-484] For instance, the surface to volume ratio and numbers of surface unsaturated sites, which are tunable by particle size, would determine the overall amount of catalytic active sites.[483] The composition and structure of the catalyst surface are often controlled by the phase and exposed facet of the particles, which could determine the reaction product distribution by affecting the adsorption configuration of substrates.[484,485]

In tandem catalysis, integration of the catalysts for two or more reactions create more interfaces, which can affect the catalyst characteristic for both reactions and also the transport of reaction intermediates between the two catalysts. For example, in the tandem catalytic system where Fischer-Tropsch (F-T) synthesis and hydrocracking reaction are coupled, cobalt nanoparticles (catalysts for F-T synthesis) are integrated with zeolites (catalysts for cracking). Interfacing cobalt nanoparticles with zeolite would affect the reducibility of cobalt resulting in a modulated activity and selectivity of the first step (i.e. F-T synthesis) and thus lead to a different product distribution of the overall tandem reaction.[486,487] In addition, the spatial allocation of the different components also plays a central role, especially on intermediates transport. The intimacy of these distinct sites has been reported to affect the product distribution significantly,[488,489] and we will discuss this with detailed reaction examples in the following sections.

For coupled reactions, the favorable condition ranges for the individual reactions need to overlap, thus limiting the choices of catalysts for each reaction. Moreover, in the catalyst synthesis process, the integrity of each catalytic component needs to be maintained without aggregation or severe surface reconstruction (e.g., alloy formation during integration of two distinct metal catalyst).[490] This is especially important for high surface area catalysts employing porous oxides, which usually need harsh conditions to fabricate. In addition, the optimization of the tandem catalysts requires precise control of the ratio and spatial location of different catalytic active sites. These requirements make the preparation of nanostructured tandem catalysts a formidable synthetic challenge and require a comprehensive understanding of the synthesis and integration of a variety of nanomaterials. In the next section, we will aim to provide a toolbox for achieving the synthesis of tandem catalysts with the emphasize on the methods of integration of nanoscale objects into well-defined nanostructures with controlled interfaces. And we will then discuss the application of tandem catalysis and their corresponding surface and interface control in the third section.

4.3. Synthetic Design of Nanostructured Tandem Catalysts

In principle, the integration of multiple catalytic active sites can be achieved by sequentially depositing the constituents of each active sites. The most straightforward way to realize such structure is by depositing these components layer-by-layer. Such deposition is essentially two-dimensional, where the size of the layer is macroscopic, same as the size of the catalyst. This layer-by-layer deposition is often carried out by physical deposition of materials or conformal chemical growth, which is simple and highly generalizable. The catalysts prepared in this way is structurally well-defined and suitable for fundamental study, but suffers from the low surface area, limited thermal stability and cannot be used for large scale industrial processes. The alternative way for preparing tandem catalyst is seeded growth, where each catalytic component is chemically grown on each other in a three-dimensional (3D) manner and essentially produce a powder form, high surface area catalyst. This process often involves an oxide support to serve as the substrate ('seed') for other catalytic components. Such three-dimensional catalysts are often synthetically challenging but can have high surface area and stability, and can be scaled-up for industrial processes. In the next section, we describe these two strategies of tandem catalysis synthesis separately as a toolbox for catalysts synthetic design.

4.3.1 Integration of Catalytic Components using Layer-by-Layer Deposition

The attempt to construct a tandem catalyst with controlled construction of all interfaces was first made by Yang et al. with the Langmuir-Blodgett (LB) method. [488,491] A monolayer of Pt cubes and CeO_2 cubes were assemble by LB method and then deposited on the silica substrate sequentially, forming a nanocrystal bilayer structure CeO_2-Pt-SiO_2 with two distinct interfaces Pt/CeO_2 and Pt/SiO_2 (Figure 33). Ultraviolet/ozone treatment was used to remove the capping agents of the nanocubes, creating clean metal-metal oxide interfaces. The vertical clefts between the nanocrystals ensured the access of gas molecules to catalytic interfaces. The tandem ethylene hydroformylation with methanol was carried out on this bilayer catalyst to produce propanal with very high selectivity. This concept represents a powerful approach towards designing complex nanostructure with well-defined interfaces for tandem catalysis and could be expanded to other catalyst systems.[492]
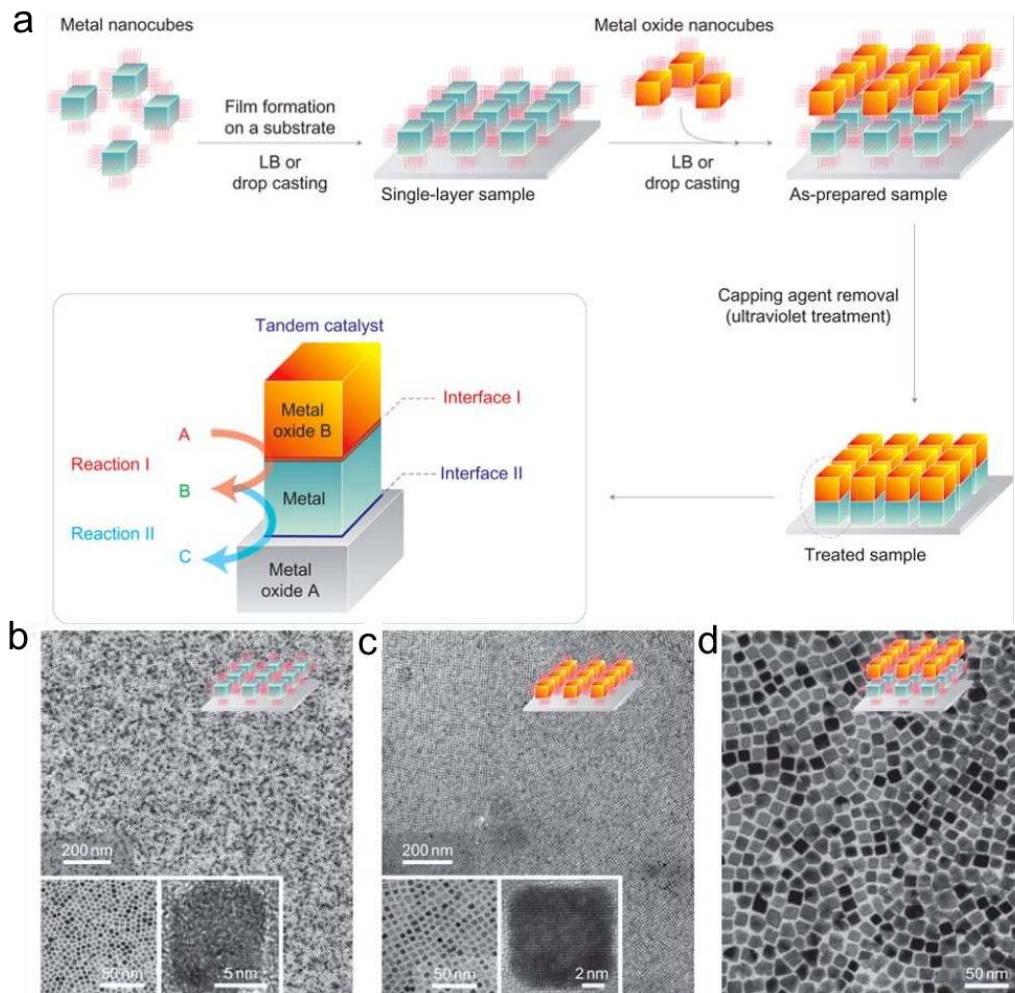
Figure 33. Assembly process for nanocrystal bilayer tandem catalyst synthesis. (a) Detailed assembling procedure. TEM images of (b) monolayer of Pt nanocubes prepared by the LB technique, (c) monolayers of CeO_2 nanocube prepared by drop casting, (d) CeO_2 nanocube monolayer on a Pt monolayer. The inset figures are the TEM images of higher magnification (left) and HRTEM images of a single nanocrystal (right).[488] Reprinted with permission from ref [488]. Copyright 2011 Macmillan Publishers Limited.

Atomic layer deposition (ALD) is another promising approach to fabricate tandem catalysts with well-defined structure.[493-496] ALD is a technique where thin layers of inorganic materials are grown on the substrate via a sequence of self-limiting chemical reactions. Due to its self-limiting character, ALD allows precise control of the thickness of the films (or size of particles) of a variety of materials with excellent conformity, uniformity, and controllable composition. Therefore, it is possible to construct complex nanostructure with multiple well-defined interfaces via ALD by depositing multilayer of metal or oxides on the substrate. Through alternative overcoating of oxides and metal nanoparticles, catalysts with multiple metal-metal oxide interfaces can be achieved, such as $ZnO/Pt/Al_2O_3$,[497] $Al_2O_3/Cu/SiO_2$,[498] $Fe_2O_3/Pt/Al_2O_3$,[499,500] etc (Figure 34a-c). However, in this case, there is no channel for the reactants molecules to access the active sites of

the bottom layers. In order to create pores for gas diffusion, high-temperature treatments in air or hydrogen are generally used by inducing densification and/or crystallization of the ALD layers.[493,498] Furthermore, Qin et al. developed a template-assisted ALD overcoating method to prepare the tandem catalyst with a tube-in-tube structure. For example, such tandem catalyst with Ni/Al$_2$O$_3$ and Pt/TiO$_2$ interfaces were fabricated by sequentially depositing an Al$_2$O$_3$ layer, Ni nanoparticles, a sacrificial layer (polyimide layer here), Pt nanoparticles and a TiO$_2$ layer on a carbon nanofiber template, followed by O$_2$ calcination and H$_2$/Ar reduction (Figure 34d-f). By removing the sacrificial layer, nanoscopic open space between the two interfaces could be obtained and the distance between the interfaces can be tuned by the thickness of the sacrificial layer.[501] Another example using a similar method is the CoO$_x$/TiO$_2$/Pt tubular catalyst in which two types of metals nanoparticles were separately located on the inner and outer surface of the TiO$_2$ nanotube (Figure 34g).[502] This ALD based approach could realize controllable assembling of many types of metal-oxide interface in a tandem catalyst.
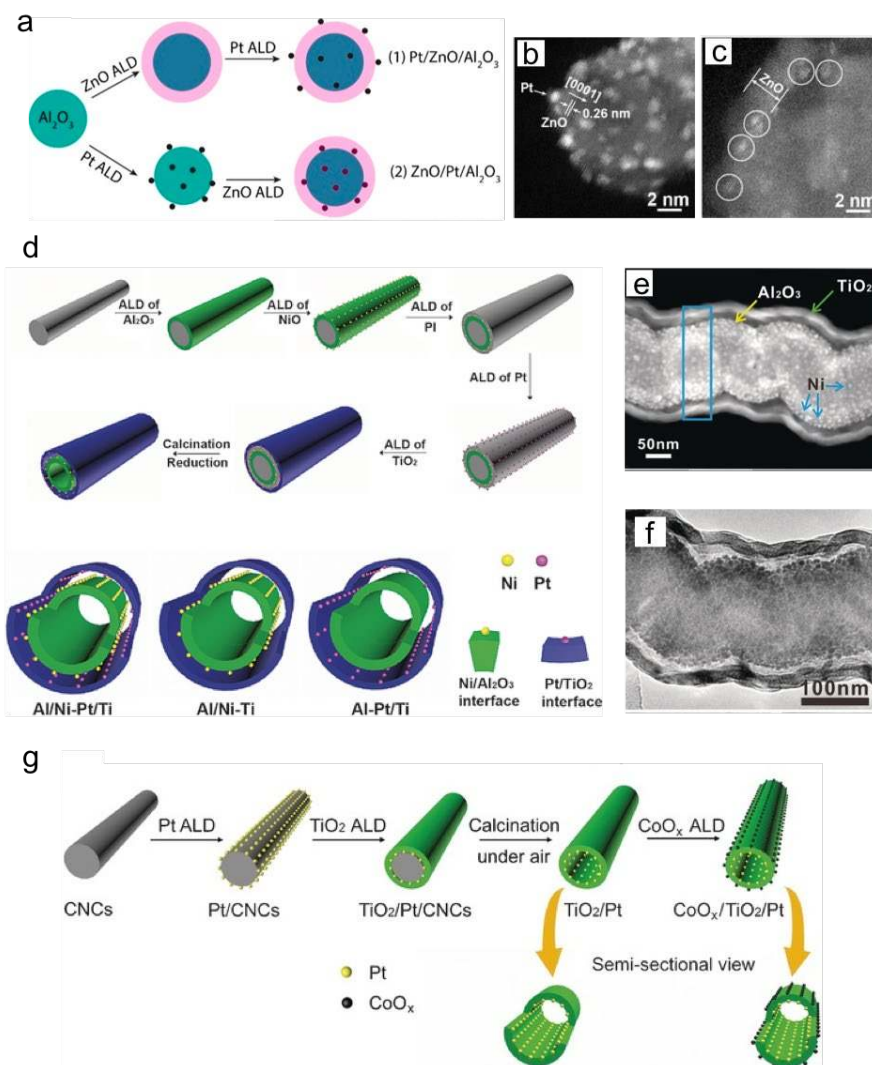
Figure 34. Complex nanostructure with multiple metal-oxide interfaces prepared by ALD. (a) Preparation of Pt/ZnO/Al$_2$O$_3$ and ZnO/Pt/Al$_2$O$_3$ catalysts with inverse spatial arrangement. Aberration-corrected HAADF-STEM images of (b) Pt/ZnO/Al$_2$O$_3$ and (c) ZnO/Pt/Al$_2$O$_3$.[497] (a)-(c) reprinted with permission from ref [497]. Copyright 2016 American Chemical Society. (d) Schematic illustrating the synthesis of the tandem catalyst with Ni/Al$_2$O$_3$ and Pt/TiO$_2$ interfaces and their semi-sectional views. HAADF-STEM image (e) and TEM image (f) of the Al/Ni-Pt/Ti catalyst.[501] (d-f) reprinted with permission from ref [501]. Copyright 2016 Wiley-VCH Verlag GmbH & Co. KGaA, Weinheim. (g) Schematic illustration of the synthesis process for TiO$_2$/Pt and spatially separated CoO$_x$/TiO$_2$/Pt catalyst by template-assisted ALD.[502] Reprinted with permission from ref [502]. Copyright 2016 Wiley-VCH Verlag GmbH & Co. KGaA, Weinheim.

The layer by layer deposition method is very versatile and can deposit various materials with almost no compatibility issues. The distance of each interface or catalytic sites could be well-controlled by particles size or film thickness. Ideally, this approach could be utilized to construct any tandem catalysts with good structural control over surfaces and interfaces, and thus suitable for conducting fundamental studies on tandem catalysis. However, the surface area of obtained catalysts is limited and the structural integrity of the catalysts can be compromised relatively easily during reactions and other high-temperature processes. For practical application of tandem catalysis, 'three dimensional (3D)' catalysts are required.

4.3.2 Integration of Catalytic Components by Sequential Growth

Three-dimensional, powder forms catalyst can be prepared by sequentially growing different nanomaterials on seed nanocrystals where metal and oxides nanoparticles could be coupled together to yield diversified nanostructures with well-defined, catalytically active interfaces.[503,504] This method is highly versatile, as the spatial arrangement of nanoscopic building blocks can be simply controlled by the sequence of growth and the morphology and coverage of each building block can be controlled by the growth condition. The sequential growth method for catalyst preparation, solely based on wet chemical processes, can be readily scaled up to industrial scale. Catalysts prepared in this method can also have high surface area and stability when porous oxides are incorporated in the nanostructure for gas accessibility and structural reinforcement purpose.

Based on their architecture, the basic nanostructures employed for the tandem catalyst can be divided into three categories: metal decorated oxides composite nanostructure, metal-oxides heterostructure and core-shell nanostructure (Figure 35).[503] These nanostructures can be further integrated to give more complexed catalytic structures. In the seeded growth process, uniform coverage of the secondary component on the seed during the growth favors the formation of the core-shell nanostructure, while the nucleation and growth of secondary component on specific sites on the seed yield the other two hybrid nanostructures. This is generally driven by the lattice mismatch or the interfacial energy between metal and the oxides. Thus, both the structure of the seed and the condition of the growth determines the structure of the final product. Since the

secondary components are chemically grown on the seeds, the interfacial metal-oxide interactions are generally strong.

Metal decorated oxides composite nanostructure

Metal-oxides heterostructure

Core-Shell nanostructure

Figure 35. Schematic of metal-oxide hybrid structure with different architecture.[503] Reprinted with permission from ref [503]. Copyright 2018 Macmillan Publishers Limited.

The metal decorated oxides composite nanostructure could be prepared by metal nanoparticles deposition on the surface of metal oxides. The shape of the metal oxides nanocrystal is tunable by the growth condition, including spherical nanoparticles,[505,506] nanocubes,[507] nanorods etc.[508-510] In a typical synthetic procedure, the pre-synthesized metal oxides nanocrystal (CeO_2, SiO_2, TiO_2, Al_2O_3, zeolites, etc), is mixed with metal precursor solution. Heterogeneous nucleation of the metal nanoparticle by reduction or decomposition of the precursors on oxides nanocrystals would give the product nanostructures. The size of the metal nanoparticles could be controlled by the types of reducing agent, reaction temperature, types and amounts of surfactants, etc. For instance, Au/TiO_2 composite nanoparticles have been prepared using $HAuCl_4$ as Au precursor, ascorbic acid as reducing agent and PVP as the stabilizer. The monodispersed TiO_2 nanospheres were employed as support for the Au nucleation and growth (Figure 36).[505] In this case, the size of Au nanoparticles were controlled by the reduction times. The metal decorated oxides composite nanostructures are simple to prepare and can incorporate a wide range of metal nanoparticles and oxide supports. The other two architectures can be perceived as more elaborately controlled metal-oxide composite structures that have more well-defined interfaces and spatial arrangement of building blocks.
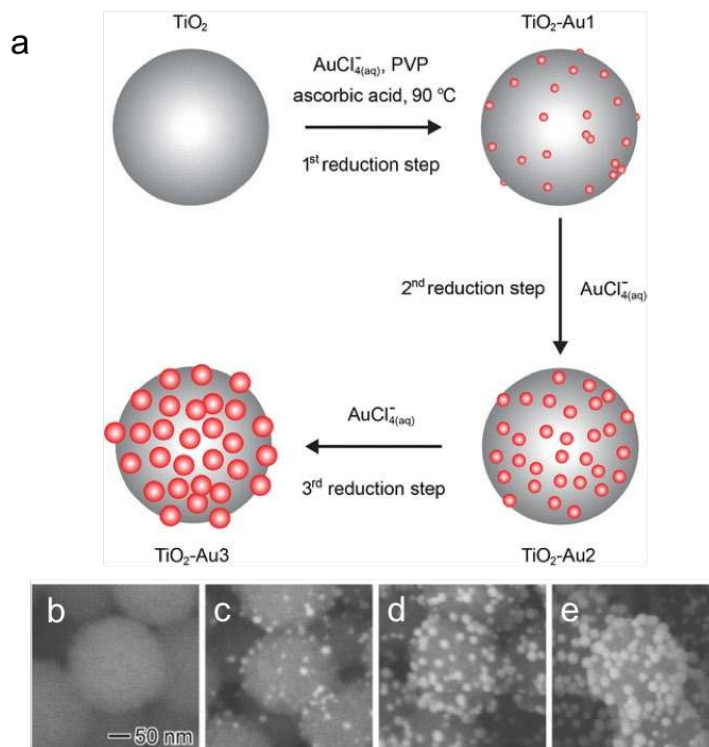
Figure 36. (a) Synthesis of TiO$_2$ colloidal spheres decorated with Au nanoparticles having controlled sizes distribution images of (b) TiO$_2$ spheres and TiO$_2$-Au particles obtained after the (c) first ,(d) second, and (e) third reduction steps.[505] Reprinted with permission from ref [505]. Copyright 2013 American Chemical Society.

In the case of the metal-oxide heterostructure, they are usually fabricated by aligning two dissimilar components together at a small junction. The common architectures include dumbbell-like heterostructure,[511-513] nanodimer,[514,515] hierarchical heterostructure and so on[516-520]. In these structures, the ratio between the metal and oxides as well as their spatial arrangement is well defined. Additionally, the seeded growth process to produce such well-defined structures are often epitaxial, leading to almost atomically well-defined interfaces.   For example, Sun et al. successfully demonstrated the synthesis of Au-Fe$_3$O$_4$ dumbbell-like nanoparticles through the epitaxial growth of iron oxides on the pre-synthesized Au seed, the size of the nanoparticles could be tuned from 2-8 nm for Au and 4-20 nm for Fe$_3$O$_4$ (Figure 37a-d).[511] Li et al. have fabricated the Au-ZnO heterostructures with a novel hexagonal pyramid-like structure via a similar method, where Au nanocrystals performed as seeds, and ZnO pyramid nanoparticles epitaxial grew over it (Figure 37e-f).[517] Pre-synthesized metal oxides can also serve as the seeds for metal nanoparticles nucleation and growth. For example, Xu et al. utilized the as-prepared Fe$_3$O$_4$ nanoparticles as seeds to construct the Ag-Fe$_3$O$_4$ nanodimer. In this system, the surface Fe(II) sites act as the catalytic center for the reduction of Ag$^+$ and the nucleation of Ag particles (Figure 38a-d).[515] This seed mediated method has been generalized to many catalyst system, including Pt-Fe$_3$O$_4$,[521,522] Au-TiO$_2$,[523] Co-TiO$_2$,[524] AuPd-Fe$_x$O$_y$, etc.[525] In addition, the heterostructure can also be prepared by mixing both metal oxide and metal precursor in a surfactant-mediated thermal

reduction/decomposition reaction. For instance, the linear and branched Au-ZnO hybrid structures can be obtained by using different surfactants in a one-pot synthesis (Figure 38e-g).[518,519]
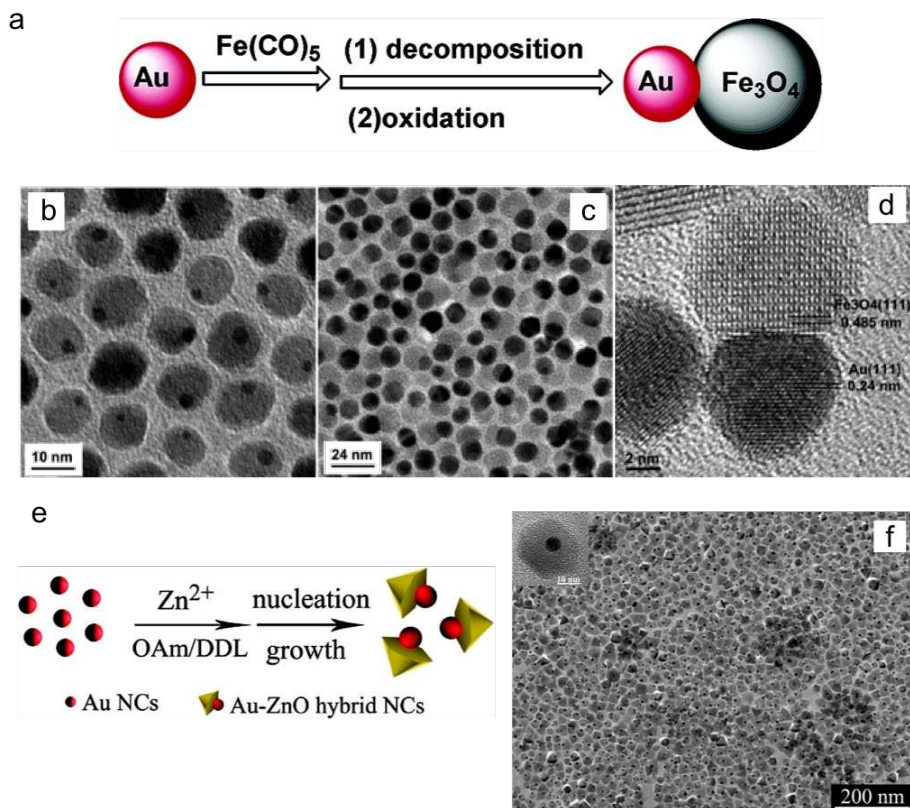
Figure 37. (a) Schematic of synthesis procedure of Au-Fe$_3$O$_4$ dumbbell-like structure. TEM image of (b) the 3-14 nm Au-Fe$_3$O$_4$ particles, (c) the 8-14 nm Au-Fe$_3$O$_4$ particles and (d) HR-TEM image of one 8-12 nm Au-Fe$_3$O$_4$ particle.[511] Reprinted with permission from ref [511]. Copyright 2005 American Chemical Society. (e) Schematic illustration of the formation of the Au-ZnO hybrid NPs and (f) TEM image of the Au-ZnO nanopyramids. The inset shows a single Au-ZnO nanoparticle.[517] Reprinted with permission from ref [517]. Copyright 2011 American Chemical Society.
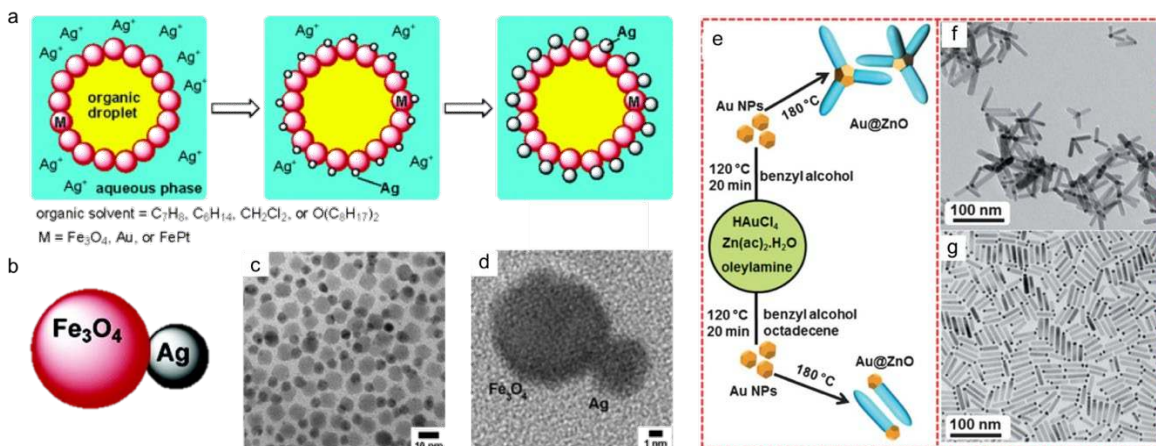
Figure 38. (a) Synthetic procedure of Fe$_3$O$_4$-Ag heterostructure using Fe$_3$O$_4$ nanopartices as seeds. Schematic (b) and TEM images (c, d) of as-synthesized Fe$_3$O$_4$-Ag.[515] Reprinted with permission from ref [515]. Copyright 2005 American Chemical Society. (e) Schematic representation of the synthesis of linear and branched Au@ZnO hybrid nanocrystals. Overview TEM image of (e) branched and (g) linear Au@ZnO hybrid nanocrystals.[518] Reprinted with permission from ref [518]. Copyright 2013 The Royal Society of Chemistry.

For the core-shell nanostructure, it is synthesized by growing a shell or multilayer of shells on seed nanocrystals.[526-528] The core-shell configuration would prevent the core nanoparticles from sintering and aggregation and provide high thermal stability especially during reactions at high temperature. Compared with the other metal-oxide hybrid structure, the preparation of core-shell nanostructure is more complex due to the conformal and uniform coating of the oxides on the core nanoparticles. Moreover, the shell needs to be porous for the diffusion of substrate molecules. Mesoporous silica and titanium oxides are commonly used for the shell coating in a sol-gel process, where silicon or titanium precursor undergoes rapid hydrolysis to produce metal hydroxide solution, followed by polycondensation, gelation, drying and crystallization process.[528,529] For example, Yang et al. reported the preparation of Pt/mesoporous silica core-shell (Pt@mSiO$_2$) nanoparticles (Figure 39a-b).[528] Pt nanocubes were prepared using tetradecyltrimethylammonum bromide (TTAB) as the capping agent and tetraethyl orthosilicate (TEOS) was used as a silica precursor. TTAB surfactants would form micelles in aqueous solution due to their amphipathic nature, so they performed as structure-directing templates for silicates polymerization. After removing TTAB, the mesoporous silica shell was formed. The thickness of the mesoporous oxides shell could be tuned by the reaction time, pH, solvent, etc, from several nanometers (2-5nm) to several hundred nanometers. The pore size of the oxides is also tunable and highly depends on the type of templates used to direct the growth of structure. The similar synthetic process could be applied for the hydrophobic nanocrystal core. For instance, Hyeon et al. synthesized the Fe$_3$O$_4$@mSiO$_2$ nanoparticles, wherein the inside Fe$_3$O$_4$ nanocrystals are capped by oleic acid and are hydrophobic (Figure 39c-i). In this case, cetyltrimethylammonium bromide (CTAB) was added, serving not only as the stabilizing surfactant for the transfer of hydrophobic Fe$_3$O$_4$ nanocrystals to the aqueous phase.[530] In addition, zeolites are also used to encapsulate the metal nanoparticles,

which has well-defined microporous structure and tunable acid sites (Figure 40).[531,532] This is usually more challenging due to the complexity of zeolite synthesis and low encapsulation efficiency. The commonly reported methods are via post-synthetic treatments such as ion exchange or wet impregnation, and the resulted metal nanoparticles were located both inside the zeolite cavities and on the external surface.[533-535] Many efforts are devoted to improve the encapsulation efficiency or develop new synthetic strategy.[531,536-539] Recently, Xu et al. reported a cationic polymer-assisted method to encapsulate Pt nanoparticles into MFI zeolites (Figure 40).[532] They utilized the cationic polymer (polydiallydimethylammonium chloride) as lining agent to bind the anionic Pt precursor ($PtCl_6^{2-}$) to the zeolite crystallization domains via electrostatic interactions, thus yield catalysts with >90% Pt nanoparticles encapsulated in the zeolite matrix.
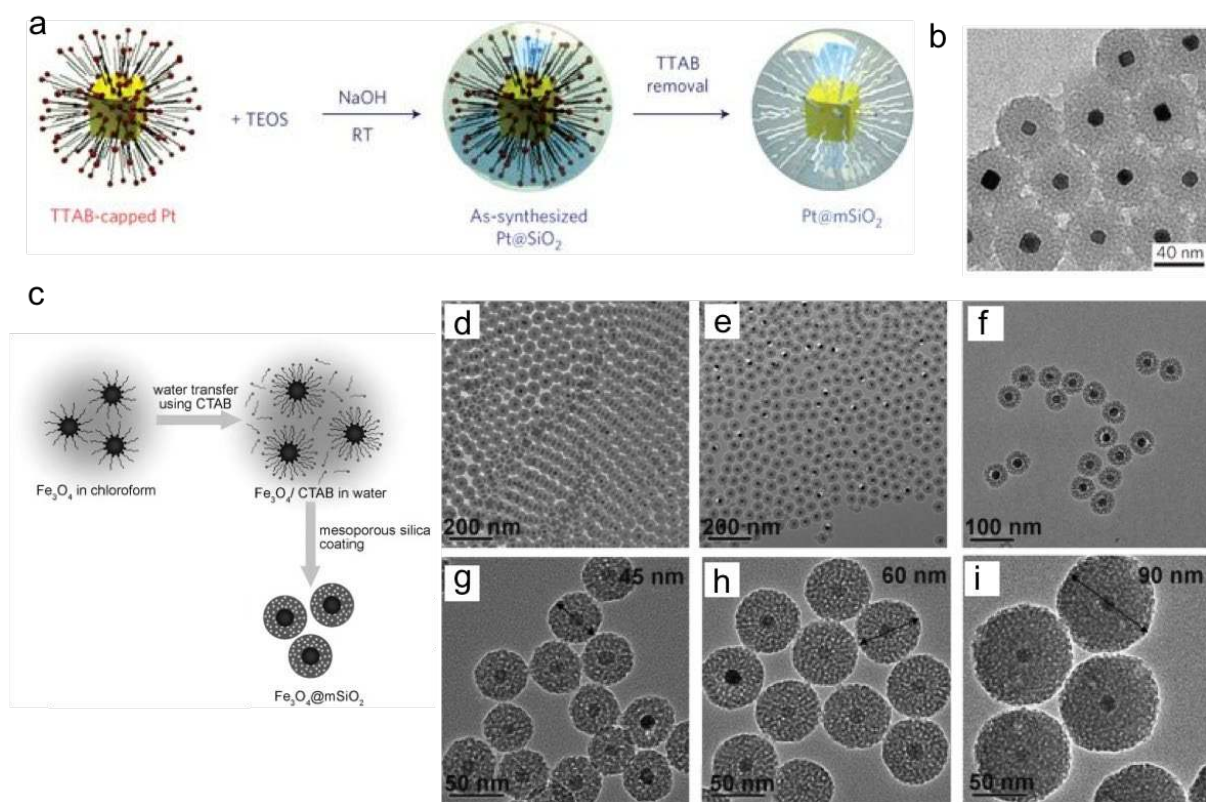
Figure 39. Preparation procedure of mesoporous silica coating. (a) Schematic representation of the synthesis of hydrophilic Pt@mSiO$_2$ nanoparticles. (b) Representative TEM image of the as-synthesized Pt@mSiO$_2$.[528] Reprinted with permission from ref [528]. Copyright 2008 Macmillan Publishers Limited. (c) Schematic illustration of the synthetic procedure for hydrophobic magnetite nanocrystal /mesoporous silica core–shell nanoparticles. TEM images of (d) 53 nm Fe$_3$O$_4$@mSiO$_2$ with 15 nm core. e, f) 45 nm Fe$_3$O$_4$@ mSiO$_2$ with 22 nm core. TEM images of Fe$_3$O$_4$@mSiO$_2$ with difference size of (g) 45 nm, (h) 60 nm and (i) 90 nm.[530] Reprinted with permission from ref [530]. Copyright 2008 Wiley-VCH Verlag GmbH & Co. KGaA, Weinheim.
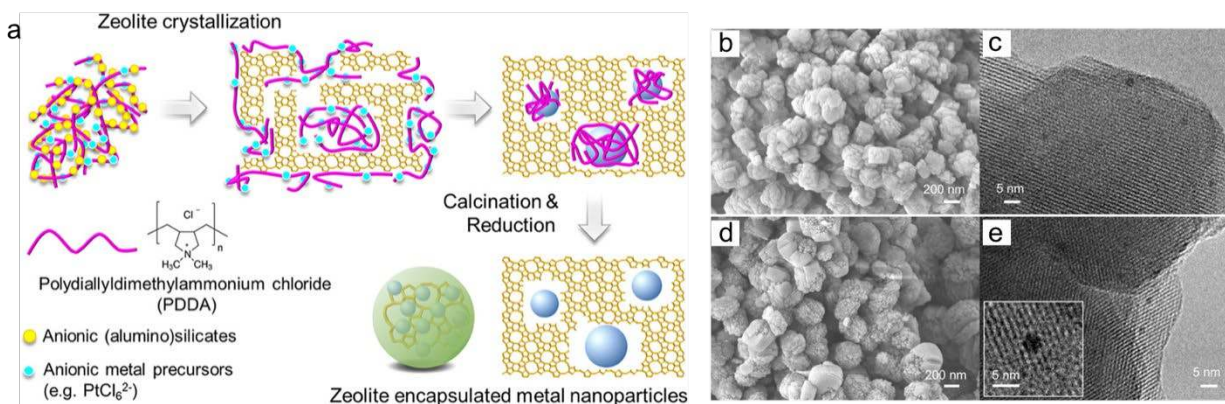
Figure 40. (a) Schematic of the strategy for encapsulating Pt nanoparticles into zeolite matrices. Representative SEM images of (b) Pt@Si-MFI and (c) Pt@HZSM-5, and high-resolution TEM images of (d) Pt@Si-MFI and (e) Pt@HZSM-5.[532] Reprinted with permission from ref [532]. Copyright 2018 American Chemical Society.

Among the three architectures, metal decorated oxide composite nanostructure is most versatile with almost no limitation on the scope of oxides and metals. Each component in this type of structures is individually tunable, enabling reliable fine-tuning of the final nanostructures. Several tandem reactions were reported with this architecture, especially with zeolites as the oxides in CO and CO_2 hydrogenation reactions,[540,558] which will be discussed in details in the next section.

Compared to metal decorated oxide composite nanostructure, metal-oxide heterojunction has additional requirements on the structure of the final product, where the metal and oxide are often combined in a one-to-one ratio (or other well-defined ratio). While the selection of materials are more limited for metal-oxide heterojunction comparing to metal decorated oxide composite nanostructure, its structure and metal-oxide interfaces are more well-defined. Although metal-oxide heterojunctions have not yet been used for tandem catalysis, future catalyst development can greatly benefit from their atomically well-defined interfaces and uniform morphologies.

The core-shell structure would give higher thermal stability due to the encapsulation of the shell. Additionally, the confinement effect of the shell could have an effect on the product distribution and yield potentially through modulation of local intermediates concentration.[542] Coating a shell on the metal-oxides heterostructure or metal decorated oxide composite structure is a convenient way to construct the catalyst with dual interfaces for tandem reactions. For example, Yang et al. report the CeO_2-Pt@mSiO_2 tandem catalyst with a core-shell configuration, which features both Pt/CeO_2 and Pt/SiO_2 functional interfaces (Figure 41a-d).[543] Loading a second metal on the shell yield a new metal-oxide interface as exemplified by the CeO_2-Pt@mSiO_2-Co catalyst with two new interfaces Pt/CeO_2 and Co/SiO_2 (Figure 41e).[544] This synthetic protocol offers a highly generalizable method to integrate different metal-oxide interfaces in a controllable way.
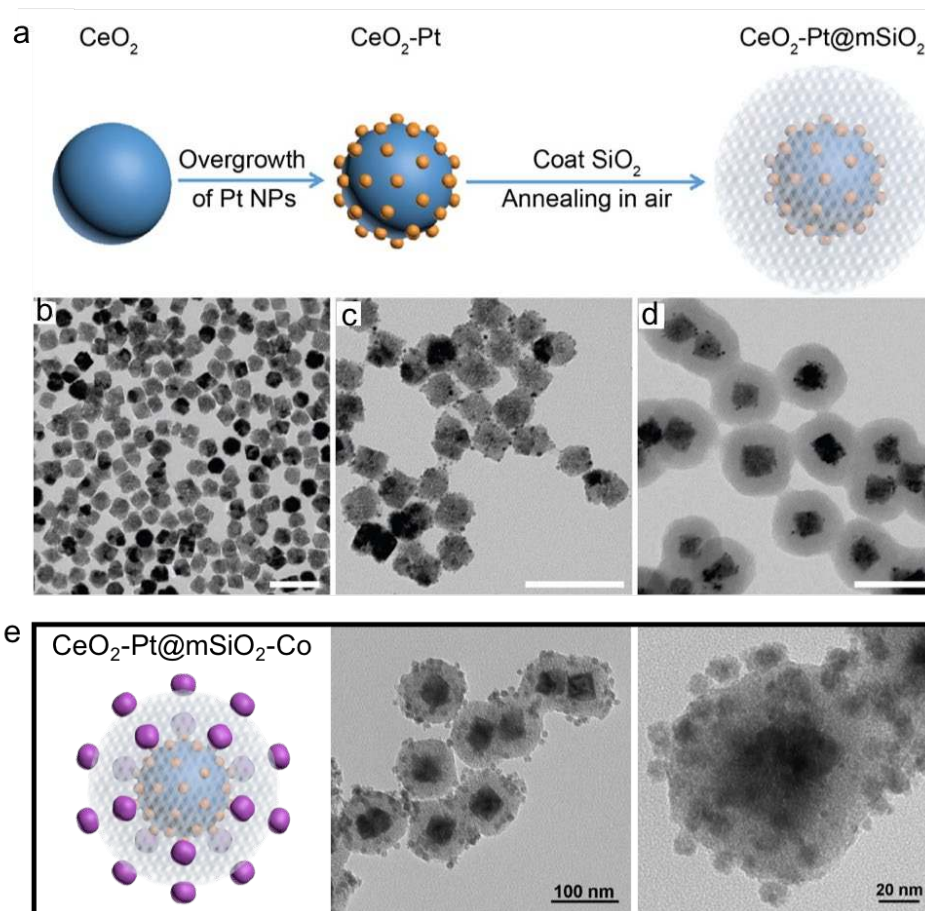
Figure 41. Fabrication of the complex nanostructure with multiple well-defined interface using metal-oxide hybrid structure as building blocks. (a) Synthesis of the tandem catalyst $CeO_2-Pt@mSiO_2$. (b) TEM image of well-dispersed CeO_2 nanoparticles. (c) TEM image of CeO_2-Pt nanoparticles synthesized the overgrowth of Pt. (d) TEM image of core−shell $CeO_2-Pt@mSiO_2$ nanoparticles. Scale bar: 100 nm.[543] Reprinted with permission from ref [543]. Copyright 2016 American Chemical Society. (e). Synthesis of $CeO_2-Pt@mSiO_2-Co$ by loading monodispersed cobalt nanoparticle onto the silica shell and representative TEM images of the structure.[544] Reprinted with permission from ref [544]. Copyright 2017 American Chemical Society.

4.4. Application of tandem catalysis

4.4.1 Olefin Hydroformylation.

Hydroformylation of olefins is an important industrial process to produce aldehydes from olefins, CO and hydrogen. The reaction is mainly carried out with homogenous catalysts, such as Rh-based or Co-based molecular complex.[545] Recently, substantial efforts have been devoted to developing heterogeneous catalysts since it is easier for product separation and catalyst recycling. Rh- and Pt-based nanocrystals are mainly studied but they give low aldehyde selectivity due to the dominance

of competitive olefin hydrogenation reactions.[546-551] Yang et al. for the first time demonstrated that tandem catalysis is a plausible approach to overcome the low selectivity of aldehyde, where ethylene hydroformylation was performed with CO and H_2 *in situ* produced from methanol decomposition over a bilayer tandem catalyst CeO_2-Pt-SiO_2 (Figure 42).[488] A high selectivity toward propanal (up to 94%) was achieved via the tandem hydroformylation process with ethylene and methanol, and selectivity of ethane, the product of the competing reaction (i.e. ethylene hydrogenation), is almost negligible. Control experiments over the single interface catalysts (e.g. Pt-CeO_2 and Pt-SiO_2 catalysts) indicated that Pt-CeO_2 interface catalyzes the methanol decomposition to yield CO and H_2, and that Pt-SiO_2 interface catalyzes the following ethylene hydroformylation. The co-existence of both Pt-CeO_2 and Pt-SiO_2 interfaces and their spatial arrangements are key to the product distribution. If the position of the Pt layer and CeO_2 layer were switched, which yields the Pt-CeO_2-SiO_2 bilayer catalyst with only one metal-oxide interface (i.e. Pt-CeO_2), no formation of propanal was observed. Moreover, the physical mixture of Pt-CeO_2 and Pt-SiO_2 catalysts in different proportions always give ethane as the dominant product and the propanal formation was negligible.
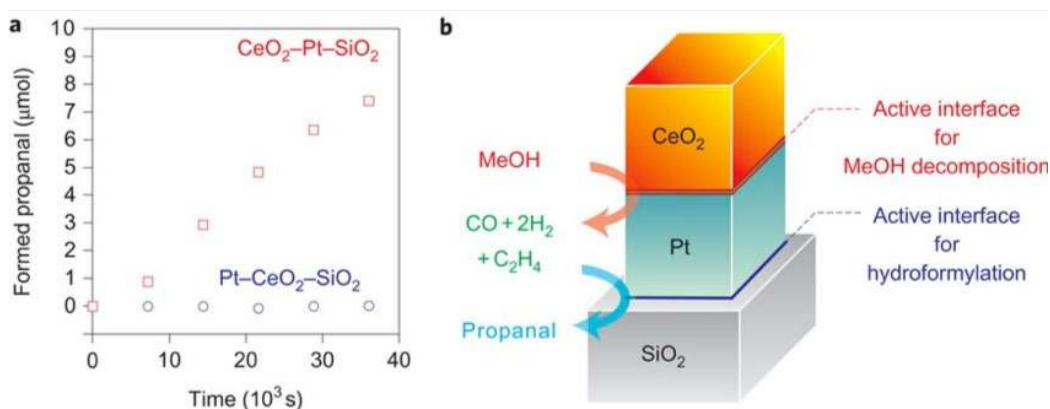
Figure 42. Tandem hydroformylation on the bilayer catalyst CeO_2-Pt-SiO_2. (a). Propanal produced as a function of reaction time over CeO_2-Pt-SiO_2 and Pt-CeO_2-SiO_2 bilayer from ethylene and methanol. (b). Illustration of the CeO_2-Pt-SiO_2 tandem catalyst.[488] Reprinted with permission from ref [488]. Copyright 2011 Macmillan Publishers Limited.

A thorough mechanism study was carried out by the same research group on the three dimensional tandem catalyst CeO_2-Pt@miSO$_2$, which has the same catalytic interfaces and consists of a CeO_2-Pt core and a mesoporous shell (Figure 43a).[543] This core/shell configuration would further provide thermal stability and enhance active-site accessibility. Their studies reveal that the presence of ethylene for the hydroformylation step slows down the initial methanol decomposition, preventing the accumulation of CO and H_2 and thus favoring propanal formation (Figure 43b, c). The selectivity is also promoted by the fact that reaction intermediates produced from methanol decomposition are poised to directly undergo hydroformylation upon migration from one catalytic interface to another(Figure 43d). This synergistic effect between the two sequential reactions and the corresponding altered reaction pathway, compared to the single-step reaction, constitute the key advantage of this tandem catalysis.
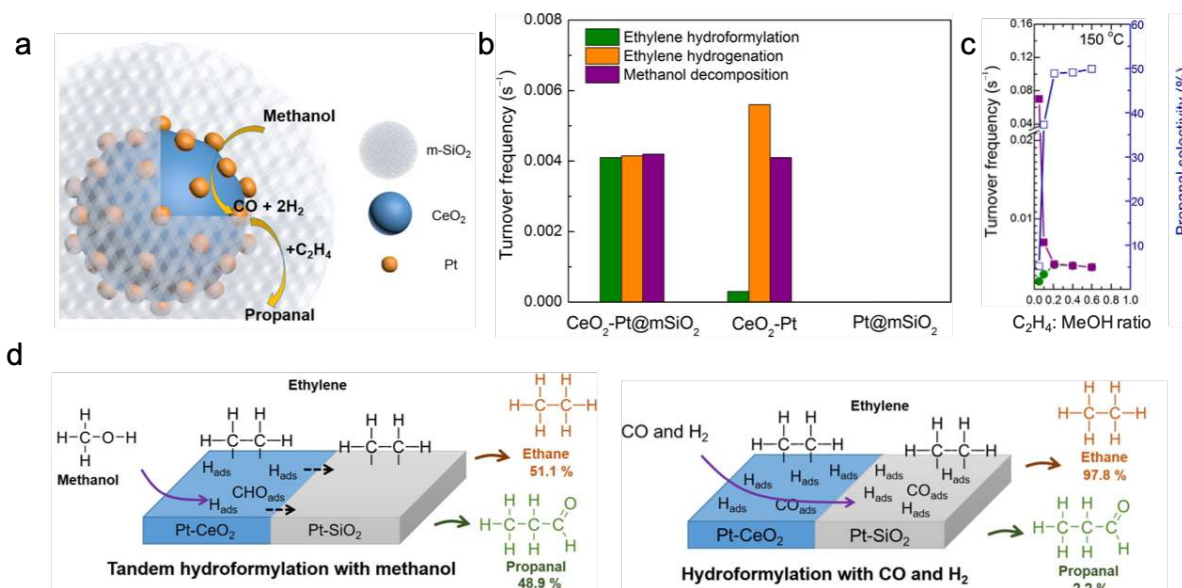
Figure 43. Tandem ethylene hydroformylation on CeO_2-Pt@$mSiO_2$ catalysts with core-shell configuration. (a). Schematic of the tandem catalyst and the sequential reactions. (b) Ethylene hydroformylation with methanol carried out at 150°C over CeO_2−Pt@$mSiO_2$ and single interface catalysts CeO_2−Pt and Pt@$mSiO_2$ (c) Inhibiting effect of ethylene on the methanol decomposition. The addition of ethylene slows down the methanol decomposition (i.e. lower turnover frequency), but promote propanal selectivity. (d). Proposed reaction pathway for the tandem hydroformylation.[543] Reprinted with permission from ref [543]. Copyright 2016 American Chemical Society.

4.4.2 Fischer-Tropsch synthesis

F-T synthesis is a very important technology to produce fuels and chemicals from CO and hydrogen.[552-554] Typically, F-T synthesis contains the dissociation of CO and H_2 to form CH_x and coupling of CH_x to C_nH_m products. The coupling of CH_x is usually uncontrollable, and thus give a broad distribution of hydrocarbons, following the well-recognized Anderson-Schulz-Flory (ASF) distribution.[554] According to this distribution, the maximum selectivity of the products in a specific carbon range is limited. For instance, the C_2-C_4 hydrocarbons(including both paraffins and olefins) selectivity would not exceed 58%, and the selectivity of gasoline (C_5-C_{11}) and diesel (C_{10}-C_{20}) is limited to 45% and 39%, respectively. Subsequent steps of hydrocracking or hydro-refining are needed to further improve the liquid fuel selectivity.[555-557] In this context, studies have shown that tandem catalysis offers a promising means to circumvent selectivity boundaries set by the ASF distribution for the F-T synthesis.

The production of liquid fuels such as gasoline and diesel could be maximized by integrating F-T synthesis and zeolite-based hydrocracking in a tandem system, to simplify and intensify the syngas to liquid technology. This could be achieved by fabricating the active F-T metal nanoparticles and acidic zeolites together, and there are two main types of architectures highlighted

in the recent studies: metal nanoparticles decorated on zeolites and metal nanoparticle/zeolite core-shell structure.[487,540,558] Tsubaki et al. reported an H-beta zeolite coated Co/Al$_2$O$_3$ core-shell catalyst for the tandem system.[540] The Co/Al$_2$O$_3$ catalyzes the F-T synthesis while the zeolite membrane catalyzes the hydrocarbons cracking and isomerization to give 60-70% selectivity of C$_5$-C$_{12}$ hydrocarbons with a ratio of iso-paraffin to n-paraffins of about 2.34 (Figure 44a-d). Tsubaki et al. also prepared the composite catalysts Co/zeolite Y, where Co nanoparticles are supported by the zeolites Y. This catalyst produces up to 74% C$_5$-C$_{11}$ hydrocarbons.[558] The pore size and acidic properties of the zeolites are revealed to have a significant impact on the final product distribution. With strong Brønsted acidity in the zeolites, over-cracking of heavy hydrocarbons might happen and lead to a low selectivity to liquid fuel (C$_{5-20}$) but high selectivity to methane and C$_2$-C$_4$. With mild Bronsted acidity, higher selectivity of liquid fuels would be obtained (Figure 44e-h).[558] Also, they found that the mesopores of the zeolite Y exhibited higher selectivity of heavier hydrocarbons than micropores.
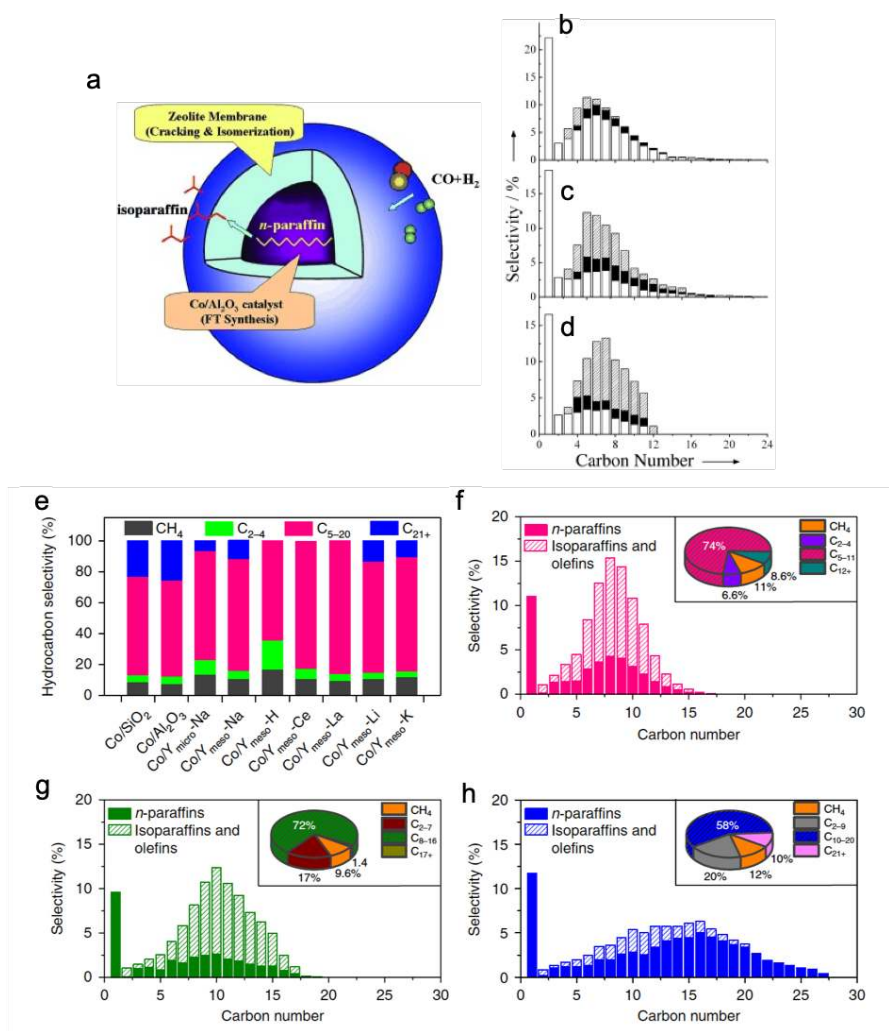

Figure 44. (a). Schematic of the H-beta zeolite coated Co/Al$_2$O$_3$ core-shell catalyst. Product distribution for (b) conventional Co/Al$_2$O$_3$, (c) the physical mixture of Co/Al$_2$O$_3$ and beta-zeolite,

and (d) the zeolite-coated Co/Al_2O_3 catalyst. □=n-paraffin, ▪=olefin, hatched=iso-paraffin.[540] Reprinted with permission from ref [540]. Copyright 2007 Wiley-VCH Verlag GmbH & Co. KGaA, Weinheim. (e) The hydrocarbons selectivity of F-T synthesis over the conventional Co catalyst and composite catalyst containing zeolites Y. The selectivity can be tuned by the acid properties of the zeolites. Detailed produce distribution of zeolite Y with different acidity: (f) Co/Y_{meso}-Ce (g) Co/Y_{meso}-La, (h) Co/Y_{meso}-K.[558] Reprinted with permission from ref [558]. Copyright 2018 Macmillan Publishers Limited.

In addition, lower olefins can also be produced using tandem catalysis with a high selectivity that breaks the limit of ASF distribution.[489,559,560] Bao et.al reported a process that produces C_2-C_4 olefin with a selectivity of 80%, by combining the active component for CO/H_2 activation (i.e. $ZnCrO_x$ here) and the component for C-C coupling (i.e. MSAPO).[489] The $ZnCrO_x$ activate syngas to a ketene intermediate, which was subsequently converted to olefins in the confined zeolite pores. The product selectivity of the tandem reactions highly depends on the ease of migration of the first reaction products or intermediates to the active sites of the second reaction,[561,562] which could be controlled by the proximity of the different active components. A closer proximity would favor the production of lower olefins. Only 23% of C_2-C_4 olefin selectivity is obtained when MSAPO was packed below the $ZnCrO_x$ and separated by a layer of inert quartz wool (Figure 45a). Reducing the intermediate transport distance by packing $ZnCrO_x$ and MSAPO in an alternate sequence, a relative higher C_2-C_4 olefin selectivity (65%) was achieved. Further shortening the distance between the two active components by well-mixing lead to more enhanced C_2-C_4 selectivity (80%). Wang et al. also demonstrated the selective conversion of syngas to C_2-C_4 olefins using a similar strategy (Figure 45b-c).[560] The Zn-Zr binary oxides, as the methanol synthesis component from syngas, were coupled with zeolites SAPO-34 which is active for methanol to olefin catalyst, and C_2-C_4 selectivity was reached up to 70%. A similar proximity effect was observed as well. Moreover, the selection of catalytic component for maximizing the activity of each reaction step and the thermodynamic coupling of the two sequential reactions are crucial to the final reaction properties. Methanol is typically produced from syngas at 473-573K, while the C-C coupling is favored at a higher temperature, for instance, 673K-723K is the optimal temperature for SAPO-34 to produce C_2-C_4 olefins. Zn-Zr binary oxides were able to produce methanol as a major product in a higher temperature range from 523K to 673K, compared to other methanol synthesis catalyst such as conventional Cu-Zn-Al oxides. As a result, selecting Zn-Zr binary oxides as the first methanol synthesis catalyst enable the selective formation of the C_2-C_4 olefins in the second step at its optimized temperature (e.g. 673K). The coupling of these two reactions could also thermodynamically drive the conversion of syngas, where the CO conversion is seven-times higher over Zn-Zr/SAPO-34 than it was over Zn-Zr oxides alone.
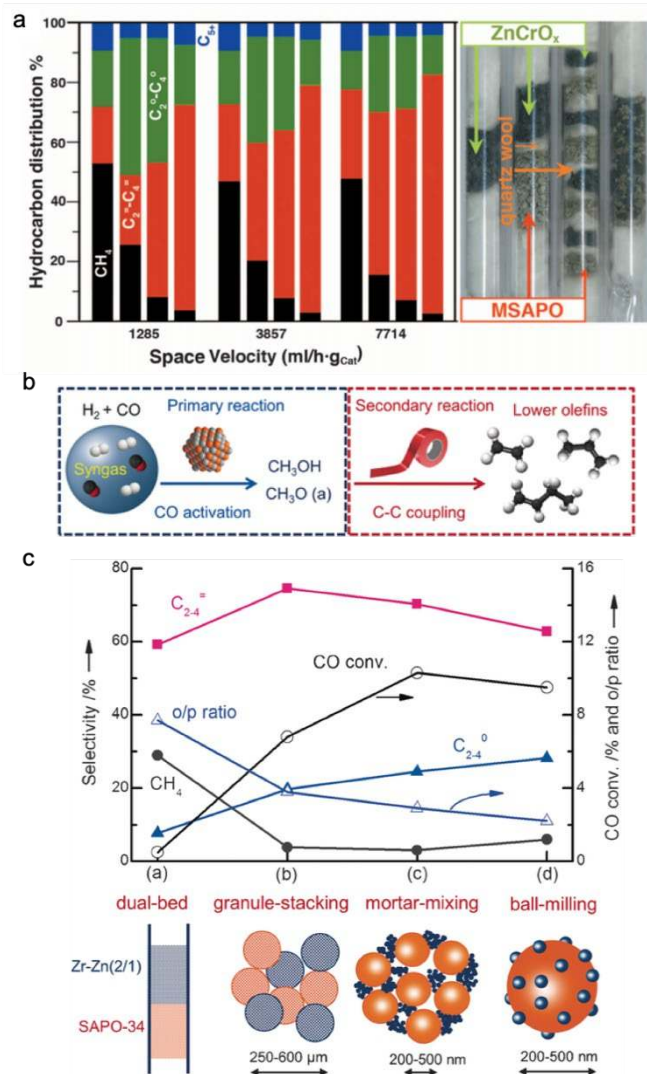
Figure 45. (a) Catalytic performance of ZnCrOₓ/MSAPO for F-T synthesis. Detailed product distribution over the catalysts with different active sites proximity as a function of space velocity. The picture on the right represents Mode 1 to 4 from left to right: Mode 1, ZnCrOₓ only; Mode 2: MSAPO packed below ZnCrOₓ, separated with quartz wool; Mode 3, ZnCrOₓ and MSAPO are packed alternatively and separated by quartz wool. Mode 4: Well-mixed ZnCrOₓ and MSAPO.[489] Reprinted with permission from ref [489]. Copyright 2016 the American Association for the Advancement of Science. (b) Conversion of syngas to lower olefins by the integration of active components for methanol production (Zr-Zn oxides) and subsequent C-C coupling (SAPO-34). (c) The effect of proximity between two components on the final product distribution.[560] Reprinted with permission from ref [560]. Copyright 2016 Wiley-VCH Verlag GmbH & Co. KGaA, Weinheim.

2.3.3 CO₂ hydrogenation

Transformation of CO_2 into value-added chemicals has been a long-standing objective due to the emerging environmental issues and rising energy demands. In this regards, CO_2 hydrogenation provides an attractive approach.[177,563] So far, great progress have been made to produce various C1 chemicals, including CO,[564,565] methane,[566,567] methanol,[568-570] and formic acid.[571] Of particular interest is the transformation of CO_2 to hydrocarbon with two or more carbons, such as lower olefins ($C_2^=$-$C_4^=$), gasoline (C_5-C_{11}) and liquefied petroleum gas (C_3^0-C_4^0). They are key intermediates in the chemical industry or can be used as fuels. However, converting CO_2 to these C_{2+} products is still challenging through one-step reaction due to the high C-C coupling barrier. Tandem catalysis is an attractive strategy for this purpose, and generally, there are two main pathways to produce long-chain hydrocarbons from CO_2 and hydrogen (Figure 46).
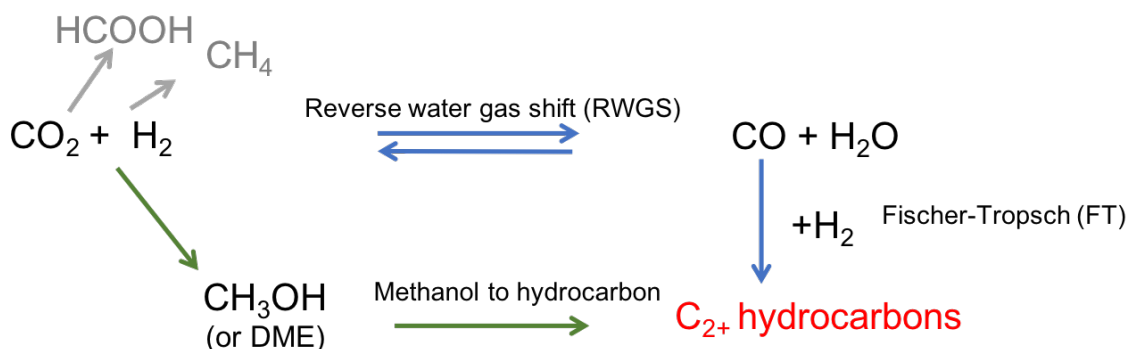
Figure 46. Schematic of the two possible reaction pathway for CO_2 hydrogenation via tandem catalysis.

The first route is via CO intermediates, where CO_2 is converted to CO through reverse water gas shift (RWGS) reaction and followed by the F-T synthesis to produce C_{2+} hydrocarbons.[544,572,573] Yang et al. developed a core-shell nanostructured catalyst CeO_2-Pt@$mSiO_2$-Co for the production of C_2-C_4 hydrocarbons(Figure 47a,b).[544] The RWGS reaction is conducted over a CeO_2/Pt interface and the formed CO subsequently reacts with H_2 through FTS process on the neighboring Co/$mSiO_2$ interfaces. A selectivity of 60% towards C_2-C_4 hydrocarbons was obtained, while CO and CH_4 are the primary products for Pt/CeO_2 catalyst and Co/$mSiO_2$ catalyst, respectively. Moreover, high selectivity toward gasoline-range hydrocarbons (C_5-C_{11}) was also achieved from CO_2 via RWGS reaction and the F-T synthesis. Sun and co-workers reported a catalyst comprised of Na-Fe_3O_4 and nanocrystalline HZSM-5, which displays the selectivity of C_5-C_{11} hydrocarbons with 78% as well as low CH_4 and CO selectivity (Figure 47c, d).[573,574] It was observed that CO_2 was initially reduced to CO via RWGS on Fe_3O_4 sites followed by subsequent hydrogenation of CO to α-olefins via F-T synthesis on *in situ* formed Fe_2C_5 sites, and C_5-C_{11} hydrocarbons were then formed via the zeolite acid-catalyzed oligomerization, isomerization, and aromatization.
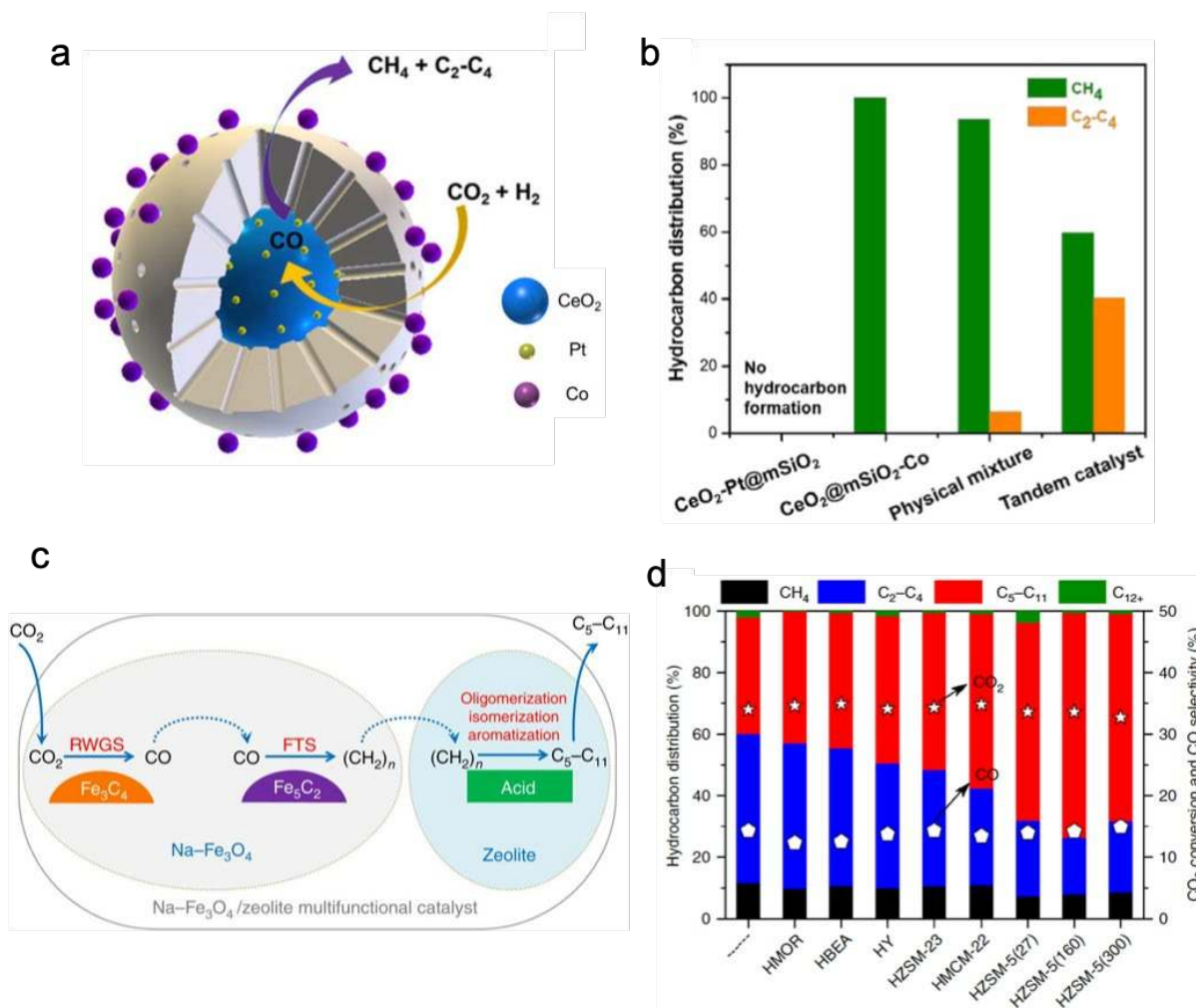
Figure 47. Tandem CO_2 hydrogenation via CO intermediates. (a) Schematic of CeO_2-Pt@mSiO_2-Co tandem catalyst for CO_2 hydrogenation and (b) the catalytic performance of single-interface catalysts CeO_2−Pt@mSiO_2 and CeO_2@mSiO_2−Co, physical mixture catalyst and the tandem catalyst.[544] Reprinted with permission from ref [544]. Copyright 2017 American Chemical Society. (c) Reaction scheme and (d) catalytic performance for CO_2 hydrogenation to gasoline-range hydrocarbons over Na–Fe_3O_4/Zeolite.[574]. Reprinted with permission from ref [574]. Copyright 2017 Macmillan Publishers Limited.

The second route combines the CO_2 hydrogenation to methanol and the subsequent methanol-to-hydrocarbons process (including the methanol-to-olefin (MTO), methanol-to-propene(MTP) and methanol-to-gasoline (MTG) process) on the acidic sites.[568-570,572,575-578] For examples, Sun et al. developed a bifunctional catalyst containing partially reducible metal oxides (In_2O_3) and HZSM-5 zeolite that yields a high selectivity to C_{5+} hydrocarbons (78.6%) (Figure 48a, b).[177] The In_2O_3 activate CO_2 and H_2 to methanol and C-C coupling subsequently occurs inside zeolite pore to produce hydrocarbons.[570] In another example, Li et al. showed a tandem catalyst ZnZrO/SAPO

fabricated with a ZnO-ZrO$_2$ nanoparticles and a Zn-modified SAPO-34 zeolite, that can achieve a selectivity for C$_2$-C$_4$ olefins as high as 80-90% among hydrocarbon products (Figure 48c, d).[579] The ZnO-ZrO$_2$ nanoparticles generate methanol from CO$_2$ hydrogenation and the SAPO is responsible for the methanol to lower olefins conversion. The excellent selectivity was attributed to the collaborative coupling of the two reactions. According to the results from *in situ* diffuse reflectance infrared Fourier transform spectroscopy (DRIFTS) and chemical trapping-mass spectrometry, it could conclude that the CH$_x$O species (mainly surface CH$_3$O, CHO species, and gas-phase CH$_3$OH) are derived first on the surface of ZnZrO via CO$_2$ and then possibly transfer onto SAPO zeolite where these species are converted to hydrocarbons. Moreover, aromatics can also be produced via the combination of Zn or Zr oxides and H-ZSM-5 in a single catalyst.[580,581]
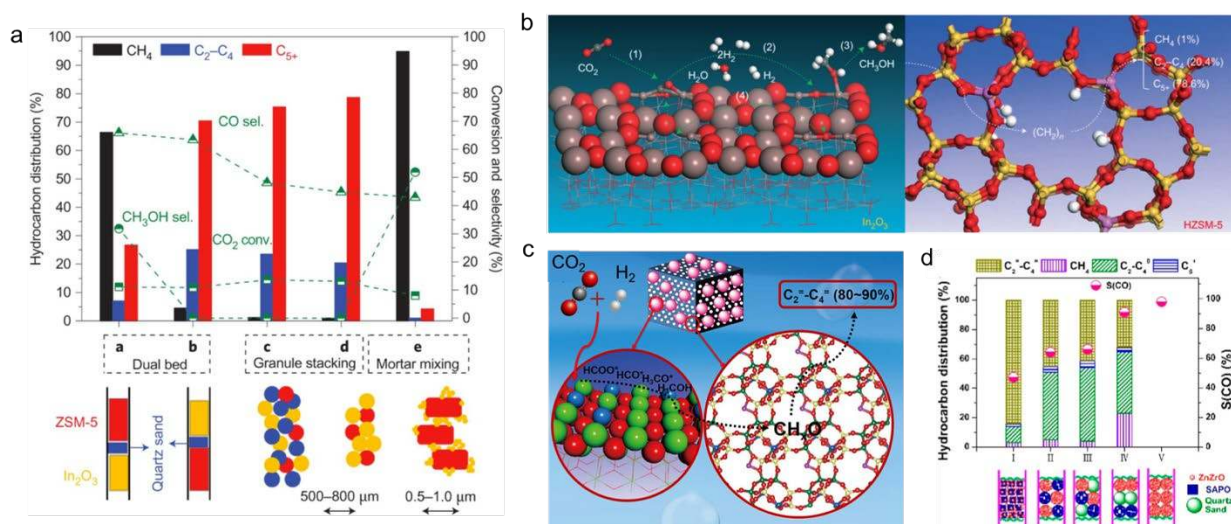
Figure 48. Tandem CO$_2$ hydrogenation via methanol intermediates. (a) CO$_2$ hydrogenation on In$_2$O$_3$/H-ZSM-5 catalyst with different integration manner, which gives different proximity between the two active components and (b) its molecular-level mechanism.[177] Reprinted with permission from ref [177]. Copyright 2017 Macmillan Publishers Limited. (c) Schematic for the proposed reaction mechanism of tandem reaction on the catalyst, ZnZrO$_x$/SAPO and (d) Catalytic performance over ZnZrO$_x$/SAPO, integrated catalyst components ZnZrO$_x$ and SAPO with different proximity.[579] Reprinted with permission from ref [579]. Copyright 2017 American Chemical Society.

Similarly, the proximity of different active sites is also of great importance in the tandem CO$_2$ hydrogenation. For example, in the case of In$_2$O$_3$/H-ZSM-5 to yield C$_{5+}$ hydrocarbons, when the In$_2$O$_3$ and H-ZSM-5 particles are well-mixed, which has closer proximity compared to the dual-bed configuration, the C$_{5+}$ selectivity enhanced and the undesirable water gas shift reaction and CH$_4$ production were suppressed. This proximity effect was observed in other systems, such as ZnZrO$_x$/H-ZSM-5 system. Moreover, it is worth noting that the very close contact between the catalytic sites might weak the synergistic effect in some case.[561] In the case of In$_2$O$_3$/H-ZSM-5, the very close contact of the two components lead to the deactivation of C-C coupling sites. As a result, a lower selectivity of C$_{5+}$ was observed.[177]

In addition to the proximity, the spatial arrangements of different catalytic sites are important to the catalytic performance. When the different active sites are mixed and randomly distributed in the catalyst, it results in a low chance that the products or intermediates desorbed from the first interface to be involved in the second reaction. A well-defined core/shell configuration would be beneficial in this case. The products of the first reaction have to be reacted on the second active sites before diffusing out of the shell. For example, in the case of CeO_2-Pt@$mSiO_2$-Co catalyst, it was observed that the physical mixture of Pt/CeO_2 and Co/$mSiO_2$ catalysts mainly produce methane but only a small number of C_2-C_4 hydrocarbons.[544] This high C_2−C_4 hydrocarbons selectivity is attributed to the unique spatial arrangement of two metal-oxide interfaces, which creates local environments conducive for multistep reactions that a physical mixture fails to achieve.

2.3.4 Electro- and Photo- and Biochemical Reactions

Heterogeneous tandem catalysis is not limited to thermal gas-phase reactions but can also be applied to electrochemical, photochemical and biochemical reactions in solutions.[582-587] For sequential electrochemical reactions, the molecules can be reduced/oxidized multiple times over different electrocatalysts to selectively yield products otherwise difficult to achieve. For example, Jaramillo et al. reported an electrocatalyst composed of gold nanoparticles on a polycrystalline copper foil (Au/Cu) that is highly active and selective for CO_2 reductions to alcohols with C-C bonds.[587] At low overpotentials, the rate of CO_2 reduction on Au/Cu to >2e- products is more than 100 times faster than on Cu (Figure 49a). Moreover, Au/Cu favors the production of C_{2+} alcohol at low overpotentials compared to pure Au or Cu (Figure 49b, c). It is suggested that the trends in alcohol production originate from a tandem catalysis mechanism, where gold nanoparticles reduce CO_2 to CO near the copper surface, driving a high CO coverage, which then undergo selective C-C coupling over the copper surface and produce C_{2+} alcohols.
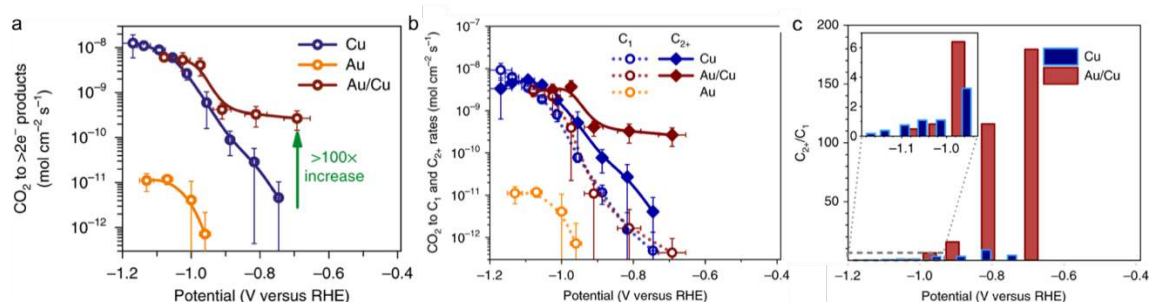
Figure 49. Improved C_{2+} alcohol production on an Au/Cu catalyst via a tandem reaction pathway. (a). Rate of CO_2 reduction to > 2e- products. (b). Rate of CO_2 reduction to C_1 and C_{2+} products on the copper, gold and Au/Cu electrodes. (c). Potential dependence of the molar ration of C_{2+} to C_1 products.[587] Reprinted with permission from ref[587]. Copyright 2018 Macmillan Publishers Limited.

Photocatalytic reaction could also be incorporated in tandem catalysis, which is especially beneficial when the intermediates are difficult to separate or store. A good example is

photocatalytic H_2 production coupled with hydrogenation or hydrodehalogenation.[582] Decorating Cu_2O cubes with Pd nanocatalysts could result in a tandem catalytic system for the hydrodehalogenation of polychlorinated biphenyls (PCBs) to produce biphenyl in an aqueous solution with light (Figure 50a).[582] In this tandem catalytic system, the Cu_2O produce H_2 via photocatalysis that is subsequently activated on the Pd surface to drive hydrodehalogenation. Substituting external H_2 source with *in situ* photogenerated H_2 eliminates the need for H_2 transportation and storage and reduces the carbon footprint of the hydrodehalogenation reactions.

The photoreductive catalysts can also be coupled to biological organisms to power enzyme-catalyzed reduction reactions.[583,584,586] For example, bacterium *Moorella thermoacetica* photosensitized with CdS nanoparticles could reduce CO_2 to acetic acid (Figure 50b).[588] Moreover, the *Moorella thermoacetica*-CdS structure can be paired with photoactive TiO_2 (Figure 50c). As such, the photooxidation and photoreduction occur at two distinct light-harvesters and generate O_2 in tandem with CO_2 reduction.[589]
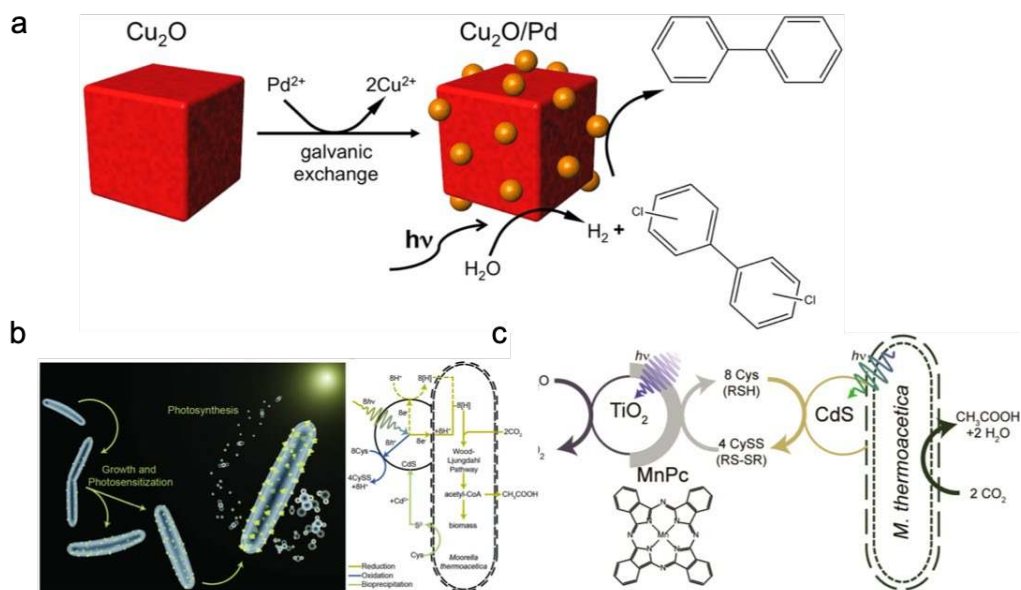
Figure 50. Tandem catalysis in photocatalytic reactions and biocatalysis (a) Fabrication and activity of Cu_2O/Pd tandem catalysts for light-driven hydrodehalogenation.[582] Reproduced with permission from ref [582]. Copyright 2014 American Chemical Society. (b) Schematic of M. thermoacetica–CdS hybrid system.[588] Reproduced with permission from ref [588]. Copyright 2016 The American Association for the Advancement of Science. (c) Schematic of the M. thermoacetica–CdS/TiO_2–MnPc tandem system. Illumination of M. thermoacetica–CdS drives the reduction of CO_2 into acetic acid, coupled to the oxidation of Cys to CySS. Co-illumination of TiO_2–MnPc drives the reduction of CySS back into Cys, coupled to oxidation of water to H_2O.[589] Reproduced with permission from ref [589]. Copyright 2016 American Chemical Society.

4.5. Summary

Tandem catalysis, where sequential reactions are coupled and carried out on a single nanostructured catalyst with multiple active sites, directly converts simple molecules into complex products. By eliminating the steps for intermediates separation, purification, and transportation, tandem catalysis benefits the reactions involving toxic or unstable intermediates. Moreover, the thermodynamic landscape of the coupled reactions in tandem catalysis is different from the individual reactions, which could achieve increased reaction selectivity and yield. This altered thermodynamic landscape could originate from a simple shifted in chemical equilibrium or complex synergy between the coupled reactions. The prerequisite of tandem reaction systems is the compatibility assessment of the two individual reactions, especially identifying the temperature and pressure range where both reactions are thermodynamically favorable and ensuring the chemical compatibility of the reactants and intermediates of both reactions. The optimization of tandem catalysis processes is complex due to the coupling between two reactions, and tuning any single factor would affect multiple elementary reactions in the system.

Tandem catalysis also poses a synthetic challenge that requires precise control of the composition, morphology and interfacial structure of the nanostructured catalyst to incorporate the active sites for both reactions and enable the synergy between the coupled reactions. In section two we provided a toolbox that summarized the synthetic approaches to integrate multiple nanoscopic materials into ordered structures, which are categorized as layer-by-layer deposition and seeded secondary growth. This versatile toolbox would help mitigate the compatibility issues in synthesizing highly well-defined nanostructured catalysts with high precision. Tandem catalysis has been applied in thermal gas-phase reactions such as olefin hydroformylation, Fischer-Tropsch synthesis and CO_2 hydrogenation as well as the integration of bio- and photo- catalytic reactions.

Although considerable achievements have been made in tandem catalysis, it is still a vastly open field with great potential and opportunities. While the current efforts are majorly focused on the discovery of new tandem catalyst for certain target reaction, the library of modular catalytic components with well-characterized catalytic activity, well-understood reaction environment compatibility and well-established synthetic accessibility is yet to emerge. With the development of such library, modular catalytic components can be rationally assembled into nanostructured catalysts with desirable performance. Also, many of the demonstrated tandem catalysts are the physical mixture of different active components, going towards well-defined nanostructures could further establish structure-properties relationships and improve the catalysts. Moreover, future research on the synergy between the sequential reactions, such as determining the key reaction intermediates and their transport, the modulation of one reaction by the other, and the dynamic evolution of the different catalytic components will also open up new opportunities. *In situ* characterization methods will also help understand the reaction mechanism by revealing the structural properties of the catalysts as well as identifying the configuration of key intermediates. These understanding will give rise to new tandem reaction systems with unprecedented product distributions that will revolutionize the roadmaps of chemical synthesis. From a practical point of view, conversion of CO_2 into value-added products and fuels can profoundly benefit from tandem catalysis as these reactions intrinsically involve sequential reduction reactions, which are also

essential reactions for establishing a carbon-neutral economy. The future development of tandem catalysis could give more complex, higher-value products from simple feedstocks, such as the production of bioactive amino acids and hydrocarbons directly from small gas molecules for agricultural and biomedical applications.

5. Summary and outlooks

The extensive research on nanoscience has given rise to abilities to synthesis nanomaterials with precisely controlled composition, morphology, and structures. These materials have been widely used for heterogeneous catalysis, where substrate molecules in liquid or gas phase adsorb and react on their surfaces. The interfaces between constituents of a composite nanostructure profoundly affect the properties of these constituents, thus indirectly tuning their reactivity as heterogeneous catalysts. In the first section of this review, we discuss nanoscopic catalyst for electrochemical oxygen reduction reactions, where the effect of surface and interface on catalytic reactivity is most direct and obvious. As platinum plays a central role in this reaction, a major effort in ORR catalyst development is to enhance the density of platinum atoms on the surface of a metal alloy catalyst and maximize the nanoparticle surface area. The second part of the review focus on electrochemical CO_2 reduction catalyst, which is a reaction closely related to a carbon-neutral economy and strongly rely on nanoscopic heterogeneous catalysts. In CO_2 RR, the surface composition of the catalyst is a deterministic factor to the product distribution, and it is worth noting that the promising copper catalyst for producing hydrocarbons and alcohols greatly benefit from surface structural engineering such as oxide-derived synthetic methods. In the final section of the review, we cover tandem catalysis as an elegant approach for synthesizing complex molecules from simple building blocks by coupling sequential reactions on a single nanostructured catalyst. There are numerous examples of metal-oxide interfaces being crucial to the activity of gas-phase catalysts, and these interfaces would need to be further integrated in a precise way to catalyze coupled sequential reactions. In summary, the surfaces and interfaces are the keys to heterogeneous catalysts, and the synthetic control and in-depth characterization of these surfaces and interfaces will remain a vital task for the development of heterogeneous catalysis.

The interface and surface control of nanoparticle catalysis is close related to the blossoming interest in clean energy, which is relevant to the fuel cell (ORR), carbon fixation (CO_2RR) and fossil fuel industry (tandem catalysis). For ORR, remarkable progress has been made to understand and improve the Pt-based materials in terms of activity and durability; For CO_2 reduction, a variety of metal nanocrystals could produce CO, formate, hydrocarbons or alcohols; For tandem catalysis, simple molecules derived from fossil resources can be processed into fuels and other high value products. While the pursuit for discovering more efficient and stable catalysts is always ongoing, *in situ* and operando techniques, such as *in situ* XRD, X-ray absorption and TEM, could enable the direct observation of catalyst structure evolution under reaction condition. These observations would help to understand the actual catalytic active sites and provide guidance for rational catalyst

design. The combination of synthetic exploration, rational catalyst optimization, and in-depth catalyst characterization will be the key to achieve next-generation nanomaterials based catalysts.

AUTHOR INFORMATION

Corresponding Author

*E-mail: p_yang@berkeley.edu.

Author Contributions

§C.X., Z.N. and D.K. contributed equally to this work.

Notes

The authors declare no competing financial interest.

Biographies

Chenlu Xie received her B.S. in chemistry from University of Science and Technology of China in 2013. In 2018, she completed her Ph.D. in chemistry at University of California, Berkeley under the supervision of Prof. Peidong Yang. She is currently a postdoctoral scholar in Department of Mechanical Engineering at Stanford University. Her research interests include tandem catalysis and electrocatalysis for energy and environmental applications.

Zhiqiang Niu received his B.S. (2007) and Ph.D. (2012) in chemistry from Peking University and Tsinghua University, respectively. He worked as a postdoctoral fellow in department of physics at Tsinghua University from 2012 to 2014. Then he joined Prof. Peidong Yang's group as a postdoctoral fellow in college of chemistry at University of California, Berkeley. During his stay in Berkeley, he also worked in California Research Alliance (CARA) with BASF. His research interests include wet-chemical synthesis of nanostructures, low-Pt PEMFC catalysts, and heterogeneous catalysis for organic synthesis.

Dohyung Kim received his Ph.D. in Materials Science and Engineering from the University of California, Berkeley in 2018. His Ph.D. research focused on the development of nanoparticle catalysts for electrochemical transformations of carbon dioxide under the supervision of Prof. Peidong Yang. Currently, he is a postdoctoral scholar at the Department of Chemical Engineering, Stanford University.

Mufan Li received his B.S. in chemistry from Nanjing University in 2012. And he received his Ph.D. from University of California, Los Angeles under the supervision of Prof. Xiangfeng Duan in 2017. He currently works as a postdoctoral researcher at the University of California, Berkeley in the group of Prof. Peidong Yang. His research focuses on metallic nanomaterials for energy related electro-chemical studies.

Prof. Peidong Yang received a B.S. in chemistry from University of Science and Technology of China in 1993 and a Ph.D. in chemistry from Harvard University in 1997. He did postdoctoral research at University of California, Santa Barbara before joining the faculty in the Department of Chemistry at the University of California, Berkeley in 1999. He is currently professor in the Department of Chemistry, Materials Science and Engineering and a senior faculty scientist at the Lawrence Berkeley National Laboratory. He is S. K. and Angela Chan Distinguished Chair Professor in Energy. He is the director for California Research Alliance by BASF and the Kavli Energy Nanoscience Institute.

Reference

(1)   Davy, H. VIII. Some new experiments and observations on the combustion of gaseous mixtures, with an account of a method of preserving a continued light in mixtures of inflammable gases and air without flame. *Philosophical Transactions of the Royal Society of London* **1817,** *107*, 77-85.

(2)   Davy, E.; Babington, F. VI. On some combinations of platinum. *Philosophical Transactions of the Royal Society of London* **1820,** *110*, 108-125.

(3)   Gasteiger, H. A.; Kocha, S. S.; Sompalli, B.; Wagner, F. T. Activity benchmarks and requirements for Pt, Pt-alloy, and non-Pt oxygen reduction catalysts for PEMFCs. *Appl. Catal., B* **2005,** *56*, 9-35.

(4)   Borup, R.; Meyers, J.; Pivovar, B.; Kim, Y. S.; Mukundan, R.; Garland, N.; Myers, D.; Wilson, M.; Garzon, F.; Wood, D. Scientific aspects of polymer electrolyte fuel cell durability and degradation. *Chem. Rev.* **2007,** *107*, 3904-3951.

(5)   Debe, M. K. Electrocatalyst approaches and challenges for automotive fuel cells. *Nature* **2012,** *486*, 43-51.

(6)   Stephens, I. E.; Bondarenko, A. S.; Grønbjerg, U.; Rossmeisl, J.; Chorkendorff, I. Understanding the electrocatalysis of oxygen reduction on platinum and its alloys. *Energy Environ. Sci.* **2012,** *5*, 6744-6762.

(7)   Wang, Y.-J.; Zhao, N.; Fang, B.; Li, H.; Bi, X. T.; Wang, H. Carbon-supported Pt-based alloy electrocatalysts for the oxygen reduction reaction in polymer electrolyte membrane fuel cells: particle size, shape, and composition manipulation and their impact to activity. *Chem. Rev.* **2015,** *115*, 3433-3467.

(8)   Shao, M.; Chang, Q.; Dodelet, J.-P.; Chenitz, R. Recent advances in electrocatalysts for oxygen reduction reaction. *Chem. Rev* **2016,** *116*, 3594-3657.

(9)   Seh, Z. W.; Kibsgaard, J.; Dickens, C. F.; Chorkendorff, I.; Nørskov, J. K.; Jaramillo, T. F. Combining theory and experiment in electrocatalysis: Insights into materials design. *Science* **2017,** *355*, eaad4998.

(10)   Kulkarni, A.; Siahrostami, S.; Patel, A.; Norskov, J. K. Understanding Catalytic Activity Trends in the Oxygen Reduction Reaction. *Chem. Rev.* **2018,** *118*, 2302-2312.

(11)   Sabatier, P. La catalyse en chimie organique (Berange, Paris, 1920). *La catalyse en chimie organique (Berange, Paris, 1920)* **2014**.

(12)   Stamenkovic, V.; Mun, B. S.; Mayrhofer, K. J. J.; Ross, P. N.; Markovic, N. M.; Rossmeisl, J.; Greeley, J.; Norskov, J. K. Changing the activity of electrocatalysts for oxygen reduction by tuning the surface electronic structure. *Angew. Chem., Int. Ed.* **2006,** *45*, 2897-2901.

(13)   Hammer, B.; Norskov, J. Why gold is the noblest of all the metals. *Nature* **1995,** *376*, 238-240.

(14)   Hammer, B.; Nørskov, J. K. Theoretical surface science and catalysis—calculations and concepts. *Adv. Catal.* **2000,** *45*, 71-129.

(15)   Jens, K.; Studt, F.; Abild-Pedersen, F.; Bligaard, T. *Fundamental concepts in heterogeneous catalysis*; John Wiley & Sons, 2014.

(16)   Markovic, N.; Gasteiger, H.; Ross, P. N. Kinetics of oxygen reduction on Pt (hkl) electrodes: implications for the crystallite size effect with supported Pt electrocatalysts. *J. Electrochem. Soc.* **1997**, *144*, 1591-1597.

(17)   Markovic, N. M.; Gasteiger, H. A.; Ross Jr, P. N. Oxygen reduction on platinum low-index single-crystal surfaces in sulfuric acid solution: rotating ring-Pt (hkl) disk studies. *J. Phys. Chem.* **1995**, *99*, 3411-3415.

(18)   Gómez-Marín, A. M.; Feliu, J. M. Oxygen reduction on nanostructured platinum surfaces in acidic media: Promoting effect of surface steps and ideal response of Pt (1 1 1). *Catal. Today* **2015**, *244*, 172-176.

(19)   Hitotsuyanagi, A.; Nakamura, M.; Hoshi, N. Structural effects on the activity for the oxygen reduction reaction on n (1 1 1)–(1 0 0) series of Pt: correlation with the oxide film formation. *Electrochim. Acta* **2012**, *82*, 512-516.

(20)   Hoshi, N.; Nakamura, M.; Hitotsuyanagi, A. Active sites for the oxygen reduction reaction on the high index planes of Pt. *Electrochim. Acta* **2013**, *112*, 899-904.

(21)   Kuzume, A.; Herrero, E.; Feliu, J. M. Oxygen reduction on stepped platinum surfaces in acidic media. *J. Electroanal. Chem.* **2007**, *599*, 333-343.

(22)   Maciá, M. D.; Campiña, J. M.; Herrero, E.; Feliu, J. M. On the kinetics of oxygen reduction on platinum stepped surfaces in acidic media. *J. Electroanal. Chem.* **2004**, *564*, 141-150.

(23)   Calle-Vallejo, F.; Tymoczko, J.; Colic, V.; Vu, Q. H.; Pohl, M. D.; Morgenstern, K.; Loffreda, D.; Sautet, P.; Schuhmann, W.; Bandarenka, A. S. Finding optimal surface sites on heterogeneous catalysts by counting nearest neighbors. *Science* **2015**, *350*, 185-189.

(24)   Calle-Vallejo, F.; Pohl, M. D.; Reinisch, D.; Loffreda, D.; Sautet, P.; Bandarenka, A. S. Why conclusions from platinum model surfaces do not necessarily lead to enhanced nanoparticle catalysts for the oxygen reduction reaction. *Chem. Sci.* **2017**, *8*, 2283-2289.

(25)   Stamenkovic, V. R.; Mun, B. S.; Arenz, M.; Mayrhofer, K. J. J.; Lucas, C. A.; Wang, G. F.; Ross, P. N.; Markovic, N. M. Trends in electrocatalysis on extended and nanoscale Pt-bimetallic alloy surfaces. *Nat. Mater.* **2007**, *6*, 241-247.

(26)   Stamenkovic, V. R.; Fowler, B.; Mun, B. S.; Wang, G.; Ross, P. N.; Lucas, C. A.; Marković, N. M. Improved oxygen reduction activity on Pt3Ni (111) via increased surface site availability. *Science* **2007**, *315*, 493-497.

(27)   van der Vliet, D. F.; Wang, C.; Tripkovic, D.; Strmcnik, D.; Zhang, X. F.; Debe, M. K.; Atanasoski, R. T.; Markovic, N. M.; Stamenkovic, V. R. Mesostructured thin films as electrocatalysts with tunable composition and surface morphology. *Nat. Mater.* **2012**, *11*, 1051-1058.

(28)   Greeley, J.; Stephens, I.; Bondarenko, A.; Johansson, T. P.; Hansen, H. A.; Jaramillo, T.; Rossmeisl, J.; Chorkendorff, I.; Nørskov, J. K. Alloys of platinum and early transition metals as oxygen reduction electrocatalysts. *Nat. Chem.* **2009**, *1*, 552-556.

(29)   Escudero-Escribano, M.; Malacrida, P.; Hansen, M. H.; Vej-Hansen, U. G.; Velázquez-Palenzuela, A.; Tripkovic, V.; Schiøtz, J.; Rossmeisl, J.; Stephens, I. E.; Chorkendorff, I. Tuning the activity of Pt alloy electrocatalysts by means of the lanthanide contraction. *Science* **2016**, *352*, 73-76.

(30)   Escudero-Escribano, M.; Verdaguer-Casadevall, A.; Malacrida, P.; Grønbjerg, U.; Knudsen, B. P.; Jepsen, A. K.; Rossmeisl, J.; Stephens, I. E.; Chorkendorff, I. Pt5Gd as a highly active and stable catalyst for oxygen electroreduction. *J. Am. Chem. Soc.* **2012**, *134*, 16476-16479.

(31)   Lindahl, N.; Zamburlini, E.; Feng, L.; Grönbeck, H.; Escudero-Escribano, M.; Stephens, I. E.; Chorkendorff, I.; Langhammer, C.; Wickman, B. High Specific and Mass Activity for the Oxygen Reduction Reaction for Thin Film Catalysts of Sputtered Pt3Y. *Adv. Mater. Interfaces* **2017**, *4,* 170031.

(32)   Hwang, S. J.; Kim, S.-K.; Lee, J.-G.; Lee, S.-C.; Jang, J. H.; Kim, P.; Lim, T.-H.; Sung, Y.-E.; Yoo, S. J. Role of electronic perturbation in stability and activity of Pt-based alloy nanocatalysts for oxygen reduction. *J. Am. Chem. Soc.* **2012**, *134*, 19508-19511.

(33)   Yoo, S. J.; Kim, S.-K.; Jeon, T.-Y.; Hwang, S. J.; Lee, J.-G.; Lee, S.-C.; Lee, K.-S.; Cho, Y.-H.; Sung, Y.-E.; Lim, T.-H. Enhanced stability and activity of Pt–Y alloy catalysts for electrocatalytic oxygen reduction. *Chem. Commun.* **2011**, *47*, 11414-11416.

(34)   Hernandez-Fernandez, P.; Masini, F.; McCarthy, D. N.; Strebel, C. E.; Friebel, D.; Deiana, D.; Malacrida, P.; Nierhoff, A.; Bodin, A.; Wise, A. M. Mass-selected nanoparticles of Pt x Y as model catalysts for oxygen electroreduction. *Nat. Chem.* **2014**, *6*, 732-738.

(35)   Stamenkovic, V. R.; Mun, B. S.; Mayrhofer, K. J.; Ross, P. N.; Markovic, N. M. Effect of surface composition on electronic structure, stability, and electrocatalytic properties of Pt-transition metal alloys: Pt-skin versus Pt-skeleton surfaces. *J. Am. Chem. Soc.* **2006**, *128*, 8813-8819.

(36)   van Helden, P.; Ciobica, I. M.; Coetzer, R. L. J. The size-dependent site composition of FCC cobalt nanocrystals. *Catal. Today* **2016**, *261*, 48-59.

(37)   Lai, S.; Guo, J.; Petrova, V.; Ramanath, G.; Allen, L. Size-dependent melting properties of small tin particles: nanocalorimetric measurements. *Phys. Rev. Lett.* **1996,** *77*, 99-102.

(38)   Font, F.; Myers, T. Spherically symmetric nanoparticle melting with a variable phase change temperature. *J. Nanopart. Res.* **2013,** *15*, 2086.

(39)   Buffat, P.; Borel, J. P. Size effect on the melting temperature of gold particles. *Phys. Rev. A* **1976,** *13*, 2287-2298.

(40)   Li, Y.; Hart, J. L.; Taheri, M. L.; Snyder, J. D. Morphological Instability in Topologically Complex, Three-Dimensional Electrocatalytic Nanostructures. *ACS Catal.* **2017,** *7*, 7995-8005.

(41)   Alonso, C.; Salvarezza, R.; Vara, J.; Arvia, A.; Vazquez, L.; Bartolome, A.; Baro, A. The Evaluation of Surface Diffusion Coefficients of Gold and Platinum Atoms at Electrochemical Interfaces from Combined STM-SEM Imaging and Electrochemical Techniques. *J. Electrochem. Soc.* **1990,** *137*, 2161-2166.

(42)   Yuan, Y.; Yan, N.; Dyson, P. J. Advances in the Rational Design of Rhodium Nanoparticle Catalysts: Control via Manipulation of the Nanoparticle Core and Stabilizer. *ACS Catal.* **2012,** *2*, 1057-1069.

(43)   Wang, H.; Wang, Y.; Zhu, Z.; Sapi, A.; An, K.; Kennedy, G.; Michalak, W. D.; Somorjai, G. A. Influence of size-induced oxidation state of platinum nanoparticles on selectivity and activity in catalytic methanol oxidation in the gas phase. *Nano Lett.* **2013,** *13*, 2976-2979.

(44)   Li, L.; Larsen, A. H.; Romero, N. A.; Morozov, V. A.; Glinsvad, C.; Abild-Pedersen, F.; Greeley, J.; Jacobsen, K. W.; Nørskov, J. K. Investigation of Catalytic Finite-Size-Effects of Platinum Metal Clusters. *J. Phys. Chem. Lett.* **2013,** *4*, 222-226.

(45)   Janssens, T. V.; Clausen, B. S.; Hvolbæk, B.; Falsig, H.; Christensen, C. H.; Bligaard, T.; Nørskov, J. K. Insights into the reactivity of supported Au nanoparticles: combining theory and experiments. *Top. Catal.* **2007,** *44*, 15.

(46)   Han, B.; Miranda, C.; Ceder, G. Effect of particle size and surface structure on adsorption of O and OH on platinum nanoparticles: A first-principles study. *Phys. Rev. B* **2008,** *77*, 075410.

(47)   Maillard, F.; Schreier, S.; Hanzlik, M.; Savinova, E.; Weinkauf, S.; Stimming, U. Influence of particle agglomeration on the catalytic activity of carbon-supported Pt nanoparticles in CO monolayer oxidation. *Phys. Chem. Chem. Phys.* **2005,** *7*, 385-393.

(48)   Roduner, E. Size matters: why nanomaterials are different. *Chem. Soc. Rev.* **2006,** *35*, 583-592.

(49)   Aslam, U.; Linic, S. Kinetic trapping of immiscible metal atoms into bimetallic nanoparticles through plasmonic visible light-mediated reduction of a bimetallic oxide precursor: case study of Ag–Pt nanoparticle synthesis. *Chem. Mater.* **2016,** *28*, 8289-8295.

(50)   Holewinski, A.; Idrobo, J.-C.; Linic, S. High-performance Ag–Co alloy catalysts for electrochemical oxygen reduction. *Nat. Chem.* **2014,** *6*, 828-941.

(51)   Yao, Y.; Huang, Z.; Xie, P.; Lacey, S. D.; Jacob, R. J.; Xie, H.; Chen, F.; Nie, A.; Pu, T.; Rehwoldt, M. Carbothermal shock synthesis of high-entropy-alloy nanoparticles. *Science* **2018,** *359*, 1489-1494.

(52)   Huang, J. L.; Li, Z.; Duan, H. H.; Cheng, Z. Y.; Li, Y. D.; Zhu, J.; Yu, R. Formation of hexagonal-close packed (hcp) rhodium as a size effect. *J. Am. Chem. Soc.* **2017,** *139*, 575-578.

(53)   Liu, J.; Jiao, M.; Lu, L.; Barkholtz, H. M.; Li, Y.; Wang, Y.; Jiang, L.; Wu, Z.; Liu, D.-j.; Zhuang, L.et al. High performance platinum single atom electrocatalyst for oxygen reduction reaction. *Nat. Commun.* **2017,** *8*, 15938.

(54)   Ferrando, R.; Jellinek, J.; Johnston, R. L. Nanoalloys: from theory to applications of alloy clusters and nanoparticles. *Chem. Rev.* **2008,** *108*, 845-910.

(55)   García, S.; Zhang, L.; Piburn, G. W.; Henkelman, G.; Humphrey, S. M. Microwave synthesis of classically immiscible rhodium–silver and rhodium–gold alloy nanoparticles: Highly active hydrogenation catalysts. *ACS Nano* **2014,** *8*, 11512-11521.

(56)   Kusada, K.; Kobayashi, H.; Ikeda, R.; Kubota, Y.; Takata, M.; Toh, S.; Yamamoto, T.; Matsumura, S.; Sumi, N.; Sato, K. Solid solution alloy nanoparticles of immiscible Pd and Ru elements neighboring on Rh: changeover of the thermodynamic behavior for hydrogen storage and enhanced CO-oxidizing ability. *J. Am. Chem. Soc.* **2014,** *136*, 1864-1871.

(57)   Molenbroek, A. M.; Nørskov, J. K.; Clausen, B. S. Structure and Reactivity of Ni− Au Nanoparticle Catalysts. *J. Phys. Chem. B* **2001,** *105*, 5450-5458.

(58)   Kobayashi, H.; Yamauchi, M.; Kitagawa, H.; Kubota, Y.; Kato, K.; Takata, M. Atomic-level Pd− Pt alloying and largely enhanced hydrogen-storage capacity in bimetallic nanoparticles reconstructed from core/shell structure by a process of hydrogen absorption/desorption. *J. Am. Chem. Soc.* **2010,** *132*, 5576-5577.

(59)   Zhang, Z.; Nenoff, T. M.; Huang, J. Y.; Berry, D. T.; Provencio, P. P. Room temperature synthesis of thermally immiscible Ag− Ni nanoalloys. *J. Phys. Chem. C* **2009,** *113*, 1155-1159.

(60) J.-W., Y.; S.-K., C.; S.-J., L.; J.-Y., G.; T.-S., C.; T.-T., S.; C.-H., T.; S.-Y., C. Nanostructured High-Entropy Alloys with Multiple Principal Elements: Novel Alloy Design Concepts and Outcomes. *Adv. Eng. Mater.* **2004,** *6*, 299-303.

(61) Cheng, H.; Yang, N.; Lu, Q.; Zhang, Z.; Zhang, H. Syntheses and Properties of Metal Nanomaterials with Novel Crystal Phases. *Adv. Mater.* **2018**, 1707189.

(62) Huang, X.; Li, S.; Huang, Y.; Wu, S.; Zhou, X.; Li, S.; Gan, C. L.; Boey, F.; Mirkin, C. A.; Zhang, H. Synthesis of hexagonal close-packed gold nanostructures. *Nat. Commun.* **2011,** *2*, 292.

(63) Duan, H.; Yan, N.; Yu, R.; Chang, C.-R.; Zhou, G.; Hu, H.-S.; Rong, H.; Niu, Z.; Mao, J.; Asakura, H. Ultrathin rhodium nanosheets. *Nat. Commun.* **2014,** *5*, 3093.

(64) Kusada, K.; Kobayashi, H.; Yamamoto, T.; Matsumura, S.; Sumi, N.; Sato, K.; Nagaoka, K.; Kubota, Y.; Kitagawa, H. Discovery of face-centered-cubic ruthenium nanoparticles: facile size-controlled synthesis using the chemical reduction method. *J. Am. Chem. Soc.* **2013,** *135*, 5493-5496.

(65) Huang, T.-K.; Cheng, T.-H.; Yen, M.-Y.; Hsiao, W.-H.; Wang, L.-S.; Chen, F.-R.; Kai, J.-J.; Lee, C.-Y.; Chiu, H.-T. Growth of Cu Nanobelt and Ag Belt-Like Materials by Surfactant-Assisted Galvanic Reductions. *Langmuir* **2007,** *23*, 5722-5726.

(66) Kim, C.; Kim, C.; Lee, K.; Lee, H. Shaped Ni nanoparticles with an unconventional hcp crystalline structure. *Chem. Commun.* **2014,** *50*, 6353-6356.

(67) Leng, Y.; Wang, Y.; Li, X.; Liu, T.; Takahashhi, S. Controlled synthesis of triangular and hexagonal Ni nanosheets and their size-dependent properties. *Nanotechnology* **2006,** *17*, 4834.

(68) Li, L.; Abild-Pedersen, F.; Greeley, J.; Nørskov, J. K. Surface tension effects on the reactivity of metal nanoparticles. *J. Phys. Chem. Lett.* **2015,** *6*, 3797-3801.

(69) Perez-Alonso, F. J.; McCarthy, D. N.; Nierhoff, A.; Hernandez-Fernandez, P.; Strebel, C.; Stephens, I. E.; Nielsen, J. H.; Chorkendorff, I. The effect of size on the oxygen electroreduction activity of mass-selected platinum nanoparticles. *Angew. Chem., Int. Ed.* **2012,** *124*, 4719-4721.

(70) Loukrakpam, R.; Luo, J.; He, T.; Chen, Y.; Xu, Z.; Njoki, P. N.; Wanjala, B. N.; Fang, B.; Mott, D.; Yin, J.et al. Nanoengineered PtCo and PtNi Catalysts for Oxygen Reduction Reaction: An Assessment of the Structural and Electrocatalytic Properties. *J. Phys. Chem. C* **2011,** *115*, 1682-1694.

(71) Mayrhofer, K.; Blizanac, B.; Arenz, M.; Stamenkovic, V.; Ross, P.; Markovic, N. The impact of geometric and surface electronic properties of Pt-catalysts on the particle size effect in electrocatalysis. *J. Phys. Chem. B* **2005,** *109*, 14433-14440.

(72) Shao, M.; Peles, A.; Shoemaker, K. Electrocatalysis on Platinum Nanoparticles: Particle Size Effect on Oxygen Reduction Reaction Activity. *Nano Lett.* **2011,** *11*, 3714-3719.

(73) Li, D.; Wang, C.; Strmcnik, D. S.; Tripkovic, D. V.; Sun, X.; Kang, Y.; Chi, M.; Snyder, J. D.; van der Vliet, D.; Tsai, Y.et al. Functional links between Pt single crystal morphology and nanoparticles with different size and shape: the oxygen reduction reaction case. *Energy Environ. Sci.* **2014,** *7*, 4061-4069.

(74) Sheng, W.; Chen, S.; Vescovo, E.; Shao-Horn, Y. Size influence on the oxygen reduction reaction activity and instability of supported Pt nanoparticles. *J. Electrochem. Soc.* **2011,** *159*, B96-B103.

(75) Watanabe, M.; Sei, H.; Stonehart, P. The influence of platinum crystallite size on the electroreduction of oxygen. *J. Electroanal. Chem. Interf. Electrochem.* **1989,** *261*, 375-387.

(76) Nesselberger, M.; Ashton, S.; Meier, J. C.; Katsounaros, I.; Mayrhofer, K. J. J.; Arenz, M. The Particle Size Effect on the Oxygen Reduction Reaction Activity of Pt Catalysts: Influence of Electrolyte and Relation to Single Crystal Models. *J. Am. Chem. Soc.* **2011,** *133*, 17428-17433.

(77) Meier, J. C.; Galeano, C.; Katsounaros, I.; Witte, J.; Bongard, H. J.; Topalov, A. A.; Baldizzone, C.; Mezzavilla, S.; Schüth, F.; Mayrhofer, K. J. Design criteria for stable Pt/C fuel cell catalysts. *Beilstein J. Nanotechnol.* **2014,** *5*, 44.

(78) Holby, E. F.; Sheng, W.; Shao-Horn, Y.; Morgan, D. Pt nanoparticle stability in PEM fuel cells: influence of particle size distribution and crossover hydrogen. *Energy Environ. Sci.* **2009,** *2*, 865-871.

(79) Shao-Horn, Y.; Sheng, W.; Chen, S.; Ferreira, P.; Holby, E.; Morgan, D. Instability of supported platinum nanoparticles in low-temperature fuel cells. *Top. Catal.* **2007,** *46*, 285-305.

(80) Wang, C.; van der Vliet, D.; Chang, K.-C.; You, H.; Strmcnik, D.; Schlueter, J. A.; Markovic, N. M.; Stamenkovic, V. R. Monodisperse Pt3Co Nanoparticles as a Catalyst for the Oxygen Reduction Reaction: Size-Dependent Activity. *J. Phys. Chem. C* **2009,** *113*, 19365-19368.

(81) Choi, S. I.; Xie, S.; Shao, M.; Lu, N.; Guerrero, S.; Odell, J. H.; Park, J.; Wang, J.; Kim, M. J.; Xia, Y. Controlling the size and composition of nanosized Pt–Ni octahedra to optimize their catalytic activities toward the oxygen reduction reaction. *ChemSusChem* **2014,** *7*, 1476-1483.

(82)   Gan, L.; Rudi, S.; Cui, C.; Heggen, M.; Strasser, P. Size-Controlled Synthesis of Sub-10 nm PtNi3 Alloy Nanoparticles and their Unusual Volcano-Shaped Size Effect on ORR Electrocatalysis. *Small* **2016,** *12*, 3189-3196.

(83)   Wang, C.; Chi, M.; Li, D.; van der Vliet, D.; Wang, G.; Lin, Q.; Mitchell, J. F.; More, K. L.; Markovic, N. M.; Stamenkovic, V. R. Synthesis of homogeneous Pt-bimetallic nanoparticles as highly efficient electrocatalysts. *ACS Catal.* **2011,** *1*, 1355-1359.

(84)   Wang, C.; Chi, M.; Wang, G.; Van der Vliet, D.; Li, D.; More, K.; Wang, H. H.; Schlueter, J. A.; Markovic, N. M.; Stamenkovic, V. R. Correlation Between Surface Chemistry and Electrocatalytic Properties of Monodisperse PtxNi1-x Nanoparticles. *Adv. Funct. Mater.* **2011,** *21*, 147-152.

(85)   Cui, C.; Gan, L.; Neumann, M.; Heggen, M.; Cuenya, B. R.; Strasser, P. Carbon monoxide-assisted size confinement of bimetallic alloy nanoparticles. *J. Am. Chem. Soc.* **2014,** *136*, 4813-4816.

(86)   Hernandez-Fernandez, P.; Masini, F.; McCarthy, D. N.; Strebel, C. E.; Friebel, D.; Deiana, D.; Malacrida, P.; Nierhoff, A.; Bodin, A.; Wise, A. M.et al. Mass-selected nanoparticles of PtxY as model catalysts for oxygen electroreduction. *Nat. Chem.* **2014,** *6*, 732-738.

(87)   Velázquez-Palenzuela, A.; Masini, F.; Pedersen, A. F.; Escudero-Escribano, M.; Deiana, D.; Malacrida, P.; Hansen, T. W.; Friebel, D.; Nilsson, A.; Stephens, I. E. The enhanced activity of mass-selected PtxGd nanoparticles for oxygen electroreduction. *J. Catal.* **2015,** *328*, 297-307.

(88)   Brandiele, R.; Durante, C.; Grądzka, E.; Rizzi, G.; Zheng, J.; Badocco, D.; Centomo, P.; Pastore, P.; Granozzi, G.; Gennaro, A. One step forward to a scalable synthesis of platinum–yttrium alloy nanoparticles on mesoporous carbon for the oxygen reduction reaction. *J. Mater. Chem. A* **2016,** *4*, 12232-12240.

(89)   Roy, C.; Knudsen, B. P.; Pedersen, C. M.; Velázquez-Palenzuela, A.; Christensen, L. H.; Damsgaard, C. D.; Stephens, I. E. L.; Chorkendorff, I. Scalable Synthesis of Carbon-Supported Platinum–Lanthanide and −Rare-Earth Alloys for Oxygen Reduction. *ACS Catal.* **2018,** *8*, 2071-2080.

(90)   Choi, S. I.; Choi, R.; Han, S. W.; Park, J. T. Synthesis and characterization of Pt9Co nanocubes with high activity for oxygen reduction. *Chem. Commun.* **2010,** *46*, 4950-4952.

(91)   Kang, Y. J.; Murray, C. B. Synthesis and Electrocatalytic Properties of Cubic Mn-Pt Nanocrystals (Nanocubes). *J. Am. Chem. Soc.* **2010,** *132*, 7568-7569.

(92)   Wu, Y.; Cai, S.; Wang, D.; He, W.; Li, Y. Syntheses of water-soluble octahedral, truncated octahedral, and cubic Pt–Ni nanocrystals and their structure–activity study in model hydrogenation reactions. *J. Am. Chem. Soc.* **2012,** *134*, 8975-8981.

(93)   Xu, D.; Liu, Z. P.; Yang, H. Z.; Liu, Q. S.; Zhang, J.; Fang, J. Y.; Zou, S. Z.; Sun, K. Solution-Based Evolution and Enhanced Methanol Oxidation Activity of Monodisperse Platinum-Copper Nanocubes. *Angew. Chem., Int. Ed.* **2009,** *48*, 4217-4221.

(94)   Yang, H. Z.; Zhang, J.; Sun, K.; Zou, S. Z.; Fang, J. Y. Enhancing by Weakening: Electrooxidation of Methanol on Pt3Co and Pt Nanocubes. *Angew. Chem., Int. Ed.* **2010,** *49*, 6848-6851.

(95)   Yin, A. X.; Min, X. Q.; Zhang, Y. W.; Yan, C. H. Shape-Selective Synthesis and Facet-Dependent Enhanced Electrocatalytic Activity and Durability of Monodisperse Sub-10 nm Pt-Pd Tetrahedrons and Cubes. *J. Am. Chem. Soc.* **2011,** *133*, 3816-3819.

(96)   Zhang, J.; Yang, H. Z.; Yang, K. K.; Fang, J.; Zou, S. Z.; Luo, Z. P.; Wang, H.; Bae, I. T.; Jung, D. Y. Monodisperse Pt3Fe Nanocubes: Synthesis, Characterization, Self-Assembly, and Electrocatalytic Activity. *Adv. Funct. Mater.* **2010,** *20*, 3727-3733.

(97)   Choi, S.-I.; Xie, S.; Shao, M.; Odell, J. H.; Lu, N.; Peng, H.-C.; Protsailo, L.; Guerrero, S.; Park, J.; Xia, X. Synthesis and characterization of 9 nm Pt–Ni octahedra with a record high activity of 3.3 A/mgPt for the oxygen reduction reaction. *Nano Lett.* **2013,** *13*, 3420-3425.

(98)   Chou, S.-W.; Lai, Y.-R.; Yang, Y. Y.; Tang, C.-Y.; Hayashi, M.; Chen, H.-C.; Chen, H.-L.; Chou, P.-T. Uniform size and composition tuning of PtNi octahedra for systematic studies of oxygen reduction reactions. *J. Catal.* **2014,** *309*, 343-350.

(99)   Cui, C.; Gan, L.; Li, H.-H.; Yu, S.-H.; Heggen, M.; Strasser, P. Octahedral PtNi nanoparticle catalysts: exceptional oxygen reduction activity by tuning the alloy particle surface composition. *Nano Lett.* **2012,** *12*, 5885-5889.

(100)   Huang, X.; Zhao, Z.; Cao, L.; Chen, Y.; Zhu, E.; Lin, Z.; Li, M.; Yan, A.; Zettl, A.; Wang, Y. M. High-performance transition metal–doped Pt3Ni octahedra for oxygen reduction reaction. *Science* **2015,** *348*, 1230-1234.

(101)   Huang, X. Q.; Li, Y. J.; Li, Y. J.; Zhou, H. L.; Duan, X. F.; Huang, Y. Synthesis of PtPd Bimetal Nanocrystals with Controllable Shape, Composition, and Their Tunable Catalytic Properties. *Nano Lett.* **2012,** *12*, 4265-4270.

(102) Wu, J. B.; Zhang, J. L.; Peng, Z. M.; Yang, S. C.; Wagner, F. T.; Yang, H. Truncated Octahedral Pt3Ni Oxygen Reduction Reaction Electrocatalysts. *J. Am. Chem. Soc.* **2010**, *132*, 4984-4985.

(103) Zhang, J.; Yang, H. Z.; Fang, J. Y.; Zou, S. Z. Synthesis and Oxygen Reduction Activity of Shape-Controlled Pt3Ni Nanopolyhedra. *Nano Lett.* **2010,** *10*, 638-644.

(104) Wu, J.; Gross, A.; Yang, H. Shape and composition-controlled platinum alloy nanocrystals using carbon monoxide as reducing agent. *Nano Lett.* **2011,** *11*, 798-802.

(105) Wu, J. B.; Qi, L.; You, H. J.; Gross, A.; Li, J.; Yang, H. Icosahedral Platinum Alloy Nanocrystals with Enhanced Electrocatalytic Activities. *J. Am. Chem. Soc.* **2012,** *134*, 11880-11883.

(106) Beermann, V.; Gocyla, M.; Kühl, S.; Padgett, E.; Schmies, H.; Goerlin, M.; Erini, N.; Shviro, M.; Heggen, M.; Dunin-Borkowski, R. E. Tuning the Electrocatalytic Oxygen Reduction Reaction Activity and Stability of Shape-Controlled Pt–Ni Nanoparticles by Thermal Annealing− Elucidating the Surface Atomic Structural and Compositional Changes. *J. Am. Chem. Soc.* **2017,** *139*, 16536-16547.

(107) Lim, J.; Shin, H.; Kim, M.; Lee, H.; Lee, K.-S.; Kwon, Y.; Song, D.; Oh, S.; Kim, H.; Cho, E. Ga–Doped Pt–Ni Octahedral Nanoparticles as a Highly Active and Durable Electrocatalyst for Oxygen Reduction Reaction. *Nano Lett.* **2018,** *18*, 2450-2458.

(108) Zhang, C.; Hwang, S. Y.; Trout, A.; Peng, Z. Solid-state chemistry-enabled scalable production of octahedral Pt–Ni alloy electrocatalyst for oxygen reduction reaction. *J. Am. Chem. Soc.* **2014,** *136*, 7805-7808.

(109) Kongkanand, A.; Mathias, M. F. The Priority and Challenge of High-Power Performance of Low-Platinum Proton-Exchange Membrane Fuel Cells. *J. Phys. Chem. Lett.* **2016,** *7*, 1127-1137.

(110) Carpenter, M. K.; Moylan, T. E.; Kukreja, R. S.; Atwan, M. H.; Tessema, M. M. Solvothermal synthesis of platinum alloy nanoparticles for oxygen reduction electrocatalysis. *J. Am. Chem. Soc.* **2012,** *134*, 8535-8542.

(111) Wu, J.; Yang, H. Study of the durability of faceted Pt3Ni oxygen–reduction electrocatalysts. *ChemCatChem* **2012,** *4*, 1572-1577.

(112) Erini, N.; Beermann, V.; Gocyla, M.; Gliech, M.; Heggen, M.; Dunin-Borkowski, R. E.; Strasser, P. The Effect of Surface Site Ensembles on the Activity and Selectivity of Ethanol Electrooxidation by Octahedral PtNiRh Nanoparticles. *Angew. Chem., Int. Ed.* **2017,** *129*, 6633-6638.

(113) Albiter, A.; Espinosa-Medina, M.; Gonzalez-Rodriguez, J.; Perez, R. Effect of Mo, Ga and Fe on the corrosion resistance of nanocrystalline NiAl alloy in acidic media. *Int. J. Hydrogen Energy* **2005,** *30*, 1311-1315.

(114) Sun, S. H.; Zhang, G. X.; Geng, D. S.; Chen, Y. G.; Li, R. Y.; Cai, M.; Sun, X. L. A Highly Durable Platinum Nanocatalyst for Proton Exchange Membrane Fuel Cells: Multiarmed Starlike Nanowire Single Crystal. *Angew. Chem., Int. Ed.* **2011,** *50*, 422-426.

(115) Koenigsmann, C.; Santulli, A. C.; Gong, K. P.; Vukmirovic, M. B.; Zhou, W. P.; Sutter, E.; Wong, S. S.; Adzic, R. R. Enhanced Electrocatalytic Performance of Processed, Ultrathin, Supported Pd-Pt Core-Shell Nanowire Catalysts for the Oxygen Reduction Reaction. *J. Am. Chem. Soc.* **2011,** *133*, 9783-9795.

(116) Niu, Z. Q.; Wang, D. S.; Yu, R.; Peng, Q.; Li, Y. D. Highly branched Pt-Ni nanocrystals enclosed by stepped surface for methanol oxidation. *Chem. Sci.* **2012,** *3*, 1925-1929.

(117) Van Der Vliet, D. F.; Wang, C.; Tripkovic, D.; Strmcnik, D.; Zhang, X. F.; Debe, M. K.; Atanasoski, R. T.; Markovic, N. M.; Stamenkovic, V. R. Mesostructured thin films as electrocatalysts with tunable composition and surface morphology. *Nat. Mater.* **2012,** *11*, 1051-1058.

(118) Tamaki, T.; Kuroki, H.; Ogura, S.; Fuchigami, T.; Kitamoto, Y.; Yamaguchi, T. Connected nanoparticle catalysts possessing a porous, hollow capsule structure as carbon-free electrocatalysts for oxygen reduction in polymer electrolyte fuel cells. *Energy Environ. Sci.* **2015,** *8*, 3545-3549.

(119) Liang, H. W.; Cao, X.; Zhou, F.; Cui, C. H.; Zhang, W. J.; Yu, S. H. A Free-Standing Pt-Nanowire Membrane as a Highly Stable Electrocatalyst for the Oxygen Reduction Reaction. *Adv. Mater.* **2011,** *23*, 1467-1471.

(120) Chen, Z.; Waje, M.; Li, W.; Yan, Y. Supportless Pt and PtPd nanotubes as electrocatalysts for oxygen-reduction reactions. *Angew. Chem., Int. Ed.* **2007,** *119*, 4138-4141.

(121) Wang, W.; Lv, F.; Lei, B.; Wan, S.; Luo, M.; Guo, S. Tuning Nanowires and Nanotubes for Efficient Fuel-Cell Electrocatalysis. *Adv. Mater.* **2016,** *28*, 10117-10141.

(122) Wittkopf, J. A.; Zheng, J.; Yan, Y. High-performance dealloyed PtCu/CuNW oxygen reduction reaction catalyst for proton exchange membrane fuel cells. *ACS Catal.* **2014,** *4*, 3145-3151.

(123) Kanady, J. S.; Leidinger, P.; Haas, A.; Titlbach, S.; Schunk, S.; Schierle-Arndt, K.; Crumlin, E. J.; Wu, C. H.; Alivisatos, A. P. Synthesis of Pt3Y and Other Early–Late Intermetallic Nanoparticles by Way of a Molten Reducing Agent. *J. Am. Chem. Soc.* **2017,** *139*, 5672-5675.

(124)   Shekhar, M.; Wang, J.; Lee, W.-S.; Williams, W. D.; Kim, S. M.; Stach, E. A.; Miller, J. T.; Delgass, W. N.; Ribeiro, F. H. Size and Support Effects for the Water–Gas Shift Catalysis over Gold Nanoparticles Supported on Model Al2O3 and TiO2. *J. Am. Chem. Soc.* **2012,** *134*, 4700-4708.

(125)   Alia, S. M.; Ngo, C.; Shulda, S.; Ha, M.-A.; Dameron, A. A.; Weker, J. N.; Neyerlin, K. C.; Kocha, S. S.; Pylypenko, S.; Pivovar, B. S. Exceptional Oxygen Reduction Reaction Activity and Durability of Platinum–Nickel Nanowires through Synthesis and Post-Treatment Optimization. *ACS Omega* **2017,** *2*, 1408-1418.

(126)   Alia, S. M.; Larsen, B. A.; Pylypenko, S.; Cullen, D. A.; Diercks, D. R.; Neyerlin, K. C.; Kocha, S. S.; Pivovar, B. S. Platinum-coated nickel nanowires as oxygen-reducing electrocatalysts. *ACS Catal.* **2014,** *4*, 1114-1119.

(127)   Xia, B. Y.; Wu, H. B.; Li, N.; Yan, Y.; Lou, X. W. D.; Wang, X. One-Pot Synthesis of Pt–Co Alloy Nanowire Assemblies with Tunable Composition and Enhanced Electrocatalytic Properties. *Angew. Chem., Int. Ed.* **2015**, *54*, 3797-3801.

(128)   Liu, Q. S.; Yan, Z.; Henderson, N. L.; Bauer, J. C.; Goodman, D. W.; Batteas, J. D.; Schaak, R. E. Synthesis of CuPt Nanorod Catalysts with Tunable Lengths. *J. Am. Chem. Soc.* **2009,** *131*, 5720-5721.

(129)   Xia, B. Y.; Wu, H. B.; Yan, Y.; Lou, X. W.; Wang, X. Ultrathin and Ultralong Single-Crystal Platinum Nanowire Assemblies with Highly Stable Electrocatalytic Activity. *J. Am. Chem. Soc.* **2013,** *135*, 9480-9485.

(130)   Guo, S.; Li, D.; Zhu, H.; Zhang, S.; Markovic, N. M.; Stamenkovic, V. R.; Sun, S. FePt and CoPt nanowires as efficient catalysts for the oxygen reduction reaction. *Angew. Chem., Int. Ed.* **2013,** *125*, 3549-3552.

(131)   Bu, L.; Ding, J.; Guo, S.; Zhang, X.; Su, D.; Zhu, X.; Yao, J.; Guo, J.; Lu, G.; Huang, X. A general method for multimetallic platinum alloy nanowires as highly active and stable oxygen reduction catalysts. *Adv. Mater.* **2015,** *27*, 7204-7212.

(132)   Bu, L.; Guo, S.; Zhang, X.; Shen, X.; Su, D.; Lu, G.; Zhu, X.; Yao, J.; Guo, J.; Huang, X. Surface engineering of hierarchical platinum-cobalt nanowires for efficient electrocatalysis. *Nat. Commun.* **2016,** *7*, 11850.

(133)   Li, M.; Zhao, Z.; Cheng, T.; Fortunelli, A.; Chen, C.-Y.; Yu, R.; Zhang, Q.; Gu, L.; Merinov, B. V.; Lin, Z. Ultrafine jagged platinum nanowires enable ultrahigh mass activity for the oxygen reduction reaction. *Science* **2016,** *354*, 1414-1419.

(134)   Wang, D. L.; Xin, H. L. L.; Hovden, R.; Wang, H. S.; Yu, Y. C.; Muller, D. A.; DiSalvo, F. J.; Abruna, H. D. Structurally ordered intermetallic platinum-cobalt core-shell nanoparticles with enhanced activity and stability as oxygen reduction electrocatalysts. *Nat. Mater.* **2013,** *12*, 81-87.

(135)   Bu, L.; Zhang, N.; Guo, S.; Zhang, X.; Li, J.; Yao, J.; Wu, T.; Lu, G.; Ma, J.-Y.; Su, D. Biaxially strained PtPb/Pt core/shell nanoplate boosts oxygen reduction catalysis. *Science* **2016,** *354*, 1410-1414.

(136)   Liu, L.; Corma, A. Metal Catalysts for Heterogeneous Catalysis: From Single Atoms to Nanoclusters and Nanoparticles. *Chem. Rev.* **2018,** *118*, 4981-5079.

(137)   Maligal-Ganesh, R. V.; Xiao, C.; Goh, T. W.; Wang, L.-L.; Gustafson, J.; Pei, Y.; Qi, Z.; Johnson, D. D.; Zhang, S.; Tao, F.et al. A Ship-in-a-Bottle Strategy To Synthesize Encapsulated Intermetallic Nanoparticle Catalysts: Exemplified for Furfural Hydrogenation. *ACS Catal.* **2016,** *6*, 1754-1763.

(138)   Chung, D. Y.; Jun, S. W.; Yoon, G.; Kwon, S. G.; Shin, D. Y.; Seo, P.; Yoo, J. M.; Shin, H.; Chung, Y.-H.; Kim, H. Highly durable and active PtFe nanocatalyst for electrochemical oxygen reduction reaction. *J. Am. Chem. Soc.* **2015,** *137*, 15478-15485.

(139)   Chen, H.; Wang, D.; Yu, Y.; Newton, K. A.; Muller, D. A.; Abruña, H. c.; DiSalvo, F. J. A surfactant-free strategy for synthesizing and processing intermetallic platinum-based nanoparticle catalysts. *J. Am. Chem. Soc.* **2012,** *134*, 18453-18459.

(140)   He, C.; Zhao, N. One-step solid-phase synthesis of ultrasmall homogeneous face-centered tetragonal FePt nanoparticles encapsulated in thin carbon shells. *J. Mater. Chem.* **2012,** *22*, 1297-1304.

(141)   Wang, D.; Yu, Y.; Xin, H. L.; Hovden, R.; Ercius, P.; Mundy, J. A.; Chen, H.; Richard, J. H.; Muller, D. A.; DiSalvo, F. J.et al. Tuning Oxygen Reduction Reaction Activity via Controllable Dealloying: A Model Study of Ordered Cu3Pt/C Intermetallic Nanocatalysts. *Nano Lett.* **2012,** *12*, 5230-5238.

(142)   Zou, L.; Li, J.; Yuan, T.; Zhou, Y.; Li, X.; Yang, H. Structural transformation of carbon-supported Pt 3 Cr nanoparticles from a disordered to an ordered phase as a durable oxygen reduction electrocatalyst. *Nanoscale* **2014,** *6*, 10686-10692.

(143)   Ghosh, T.; Leonard, B. M.; Zhou, Q.; DiSalvo, F. J. Pt Alloy and Intermetallic Phases with V, Cr, Mn, Ni, and Cu: Synthesis As Nanomaterials and Possible Applications As Fuel Cell Catalysts. *Chem. Mater.* **2010,** *22*, 2190-2202.

(144)   Bu, L.; Shao, Q.; E, B.; Guo, J.; Yao, J.; Huang, X. PtPb/PtNi Intermetallic Core/Atomic Layer Shell Octahedra for Efficient Oxygen Reduction Electrocatalysis. *J. Am. Chem. Soc.* **2017,** *139*, 9576-9582.

(145)   Ghosh, T.; Vukmirovic, M. B.; DiSalvo, F. J.; Adzic, R. R. Intermetallics as Novel Supports for Pt Monolayer O2 Reduction Electrocatalysts: Potential for Significantly Improving Properties. *J. Am. Chem. Soc.* **2010,** *132*, 906-907.

(146)   Wang, C.; Chi, M.; Li, D.; Strmcnik, D.; Van der Vliet, D.; Wang, G.; Komanicky, V.; Chang, K.-C.; Paulikas, A. P.; Tripkovic, D. Design and synthesis of bimetallic electrocatalyst with multilayered Pt-skin surfaces. *J. Am. Chem. Soc.* **2011,** *133*, 14396-14403.

(147)   Chen, S.; Ferreira, P. J.; Sheng, W.; Yabuuchi, N.; Allard, L. F.; Shao-Horn, Y. Enhanced Activity for Oxygen Reduction Reaction on "Pt3Co" Nanoparticles: Direct Evidence of Percolated and Sandwich-Segregation Structures. *J. Am. Chem. Soc.* **2008,** *130*, 13818-13819.

(148)   Chen, S.; Sheng, W.; Yabuuchi, N.; Ferreira, P. J.; Allard, L. F.; Shao-Horn, Y. Origin of Oxygen Reduction Reaction Activity on "Pt3Co" Nanoparticles: Atomically Resolved Chemical Compositions and Structures. *J. Phys. Chem. C* **2009,** *113*, 1109-1125.

(149)   Malheiro, A. R.; Perez, J.; Santiago, E. I.; Villullas, H. M. The Extent on the Nanoscale of Pt-Skin Effects on Oxygen Reduction and Its Influence on Fuel Cell Power. *J. Phys. Chem. C* **2010,** *114*, 20267-20271.

(150)   van der Vliet, D. F.; Wang, C.; Li, D.; Paulikas, A. P.; Greeley, J.; Rankin, R. B.; Strmcnik, D.; Tripkovic, D.; Markovic, N. M.; Stamenkovic, V. R. Unique electrochemical adsorption properties of Pt-Skin Surfaces. *Angew. Chem., Int. Ed.* **2012,** *124*, 3193-3196.

(151)   Ahmadi, M.; Behafarid, F.; Cui, C.; Strasser, P.; Cuenya, B. R. Long-Range Segregation Phenomena in Shape-Selected Bimetallic Nanoparticles: Chemical State Effects. *ACS Nano* **2013,** *7*, 9195-9204.

(152)   Kang, Y.; Snyder, J.; Chi, M.; Li, D.; More, K. L.; Markovic, N. M.; Stamenkovic, V. R. Multimetallic Core/Interlayer/Shell Nanostructures as Advanced Electrocatalysts. *Nano Lett.* **2014,** *14*, 6361-6367.

(153)   Heggen, M.; Oezaslan, M.; Houben, L.; Strasser, P. Formation and Analysis of Core–Shell Fine Structures in Pt Bimetallic Nanoparticle Fuel Cell Electrocatalysts. *J. Phys. Chem. C* **2012,** *116*, 19073-19083.

(154)   Sasaki, K.; Naohara, H.; Cai, Y.; Choi, Y. M.; Liu, P.; Vukmirovic, M. B.; Wang, J. X.; Adzic, R. R. Core-Protected Platinum Monolayer Shell High-Stability Electrocatalysts for Fuel-Cell Cathodes. *Angew. Chem., Int. Ed.* **2010,** *49*, 8602-8607.

(155)   Wang, G. W.; Huang, B.; Xiao, L.; Ren, Z. D.; Chen, H.; Wang, D. L.; Abruna, H. D.; Lu, J. T.; Zhuang, L. Pt Skin on AuCu Intermetallic Substrate: A Strategy to Maximize Pt Utilization for Fuel Cells. *J. Am. Chem. Soc.* **2014,** *136*, 9643-9649.

(156)   Xiong, Y.; Yang, Y.; DiSalvo, F. J.; Abruña, H. D. Pt-Decorated Composition-Tunable Pd-Fe@ Pd/C Core-Shell Nanoparticles with Enhanced Electrocatalytic Activity towards the Oxygen Reduction Reaction. *J. Am. Chem. Soc.* **2018,** *140,* 7248-7255.

(157)   Wang, C.; Sang, X.; Gamler, J. T. L.; Chen, D. P.; Unocic, R. R.; Skrabalak, S. E. Facet-Dependent Deposition of Highly Strained Alloyed Shells on Intermetallic Nanoparticles for Enhanced Electrocatalysis. *Nano Lett.* **2017,** *17*, 5526-5532.

(158)   Kuttiyiel, K. A.; Sasaki, K.; Su, D.; Wu, L. J.; Zhu, Y. M.; Adzic, R. R. Gold-promoted structurally ordered intermetallic palladium cobalt nanoparticles for the oxygen reduction reaction. *Nat. Commun.* **2014,** *5,* 5185.

(159)   Yang, J.; Yang, J.; Ying, J. Y. Morphology and Lateral Strain Control of Pt Nanoparticles via Core–Shell Construction Using Alloy AgPd Core Toward Oxygen Reduction Reaction. *ACS Nano* **2012**, *6*, 9373-9382.

(160)   Sasaki, K.; Naohara, H.; Choi, Y.; Cai, Y.; Chen, W.-F.; Liu, P.; Adzic, R. R. Highly stable Pt monolayer on PdAu nanoparticle electrocatalysts for the oxygen reduction reaction. *Nat. Commun.* **2012,** *3*, 1115.

(161)   Hunt, S. T.; Milina, M.; Alba-Rubio, A. C.; Hendon, C. H.; Dumesic, J. A.; Román-Leshkov, Y. Self-assembly of noble metal monolayers on transition metal carbide nanoparticle catalysts. *Science* **2016,** *352*, 974-978.

(162)   Kuttiyiel, K. A.; Sasaki, K.; Choi, Y. M.; Su, D.; Liu, P.; Adzic, R. R. Nitride Stabilized PtNi Core-Shell Nanocatalyst for high Oxygen Reduction Activity. *Nano Lett.* **2012,** *12*, 6266-6271.

(163)   Tian, X. L.; Luo, J. M.; Nan, H. X.; Zou, H. B.; Chen, R.; Shu, T.; Li, X. H.; Li, Y. W.; Song, H. Y.; Liao, S. J.et al. Transition Metal Nitride Coated with Atomic Layers of Pt as a Low-Cost, Highly Stable Electrocatalyst for the Oxygen Reduction Reaction. *J. Am. Chem. Soc.* **2016,** *138*, 1575-1583.

(164)   Davies, J.; Hayden, B.; Offin, L. Stabilising Oxide Core—Platinum Shell Catalysts for the Oxygen Reduction Reaction. *Electrochim. Acta* **2017,** *248*, 470-477.

(165)   Xia, X.; Xie, S.; Liu, M.; Peng, H.-C.; Lu, N.; Wang, J.; Kim, M. J.; Xia, Y. On the role of surface diffusion in determining the shape or morphology of noble-metal nanocrystals. *Proc. Natl. Acad. Sci. U.S.A.* **2013**, *110*, 6669-6673.

(166) Niu, Z.; Cui, F.; Yu, Y.; Becknell, N.; Sun, Y.; Khanarian, G.; Kim, D.; Dou, L.; Dehestani, A.; Schierle-Arndt, K.et al. Ultrathin Epitaxial Cu@Au Core–Shell Nanowires for Stable Transparent Conductors. *J. Am. Chem. Soc.* **2017,** *139,* 7348-7354.

(167) Gilroy, K. D.; Yang, X.; Xie, S.; Zhao, M.; Qin, D.; Xia, Y. Shape-Controlled Synthesis of Colloidal Metal Nanocrystals by Replicating the Surface Atomic Structure on the Seed. *Adv. Mater.* **2018,** *30,* 1706312.

(168) Li, X.; Iocozzia, J.; Chen, Y.; Zhao, S.; Cui, X.; Wang, W.; Yu, H.; Lin, S.; Lin, Z. Functional Nanoparticles Enabled by Block Copolymer Templates: from Precision Synthesis of Block Copolymers to Properties and Applications of Nanoparticles. *Angew. Chem., Int. Ed.* **2018,** *57,* 2046-2070.

(169) Pang, X. C.; He, Y. J.; Jung, J. H.; Lin, Z. Q. 1D nanocrystals with precisely controlled dimensions, compositions, and architectures. *Science* **2016,** *353,* 1268-1272.

(170) Xie, S.; Choi, S.-I.; Lu, N.; Roling, L. T.; Herron, J. A.; Zhang, L.; Park, J.; Wang, J.; Kim, M. J.; Xie, Z.et al. Atomic Layer-by-Layer Deposition of Pt on Pd Nanocubes for Catalysts with Enhanced Activity and Durability toward Oxygen Reduction. *Nano Lett.* **2014,** *14,* 3570-3576.

(171) Habas, S. E.; Lee, H.; Radmilovic, V.; Somorjai, G. A.; Yang, P. Shaping binary metal nanocrystals through epitaxial seeded growth. *Nat. Mater.* **2007,** *6,* 692-697.

(172) Park, J.; Zhang, L.; Choi, S.-I.; Roling, L. T.; Lu, N.; Herron, J. A.; Xie, S.; Wang, J.; Kim, M. J.; Mavrikakis, M.et al. Atomic Layer-by-Layer Deposition of Platinum on Palladium Octahedra for Enhanced Catalysts toward the Oxygen Reduction Reaction. *ACS Nano* **2015,** *9,* 2635-2647.

(173) Wang, X.; Vara, M.; Luo, M.; Huang, H.; Ruditskiy, A.; Park, J.; Bao, S.; Liu, J.; Howe, J.; Chi, M. Pd@ Pt core–shell concave decahedra: a class of catalysts for the oxygen reduction reaction with enhanced activity and durability. *J. Am. Chem. Soc.* **2015,** *137,* 15036-15042.

(174) Chi, M.; Wang, C.; Lei, Y.; Wang, G.; Li, D.; More, K. L.; Lupini, A.; Allard, L. F.; Markovic, N. M.; Stamenkovic, V. R. Surface faceting and elemental diffusion behaviour at atomic scale for alloy nanoparticles during in situ annealing. *Nat. Commun.* **2015,** *6,* 8925.

(175) Wang, X.; Luo, M.; Huang, H.; Chi, M.; Howe, J.; Xie, Z.; Xia, Y. Facile Synthesis of Pt–Pd Alloy Nanocages and Pt Nanorings by Templating with Pd Nanoplates. *ChemNanoMat* **2016,** *2,* 1086-1091.

(176) Park, J.; Liu, J.; Peng, H. C.; Figueroa-Cosme, L.; Miao, S.; Choi, S. I.; Bao, S.; Yang, X.; Xia, Y. Coating Pt–Ni octahedra with ultrathin Pt shells to enhance the durability without compromising the activity toward oxygen reduction. *ChemSusChem* **2016,** *9,* 2209-2215.

(177) Gao, P.; Li, S.; Bu, X.; Dang, S.; Liu, Z.; Wang, H.; Zhong, L.; Qiu, M.; Yang, C.; Cai, J.et al. Direct conversion of CO2 into liquid fuels with high selectivity over a bifunctional catalyst. *Nat. Chem.* **2017,** *9,* 1019-1024.

(178) Zhao, X.; Chen, S.; Fang, Z.; Ding, J.; Sang, W.; Wang, Y.; Zhao, J.; Peng, Z.; Zeng, J. Octahedral Pd@ Pt1. 8Ni Core-Shell Nanocrystals with Ultrathin PtNi Alloy Shells as Active Catalysts for Oxygen Reduction Reaction. *J. Am. Chem. Soc.* **2015,** *137,* 2804-2807.

(179) Jiang, K.; Siahrostami, S.; Akey, A. J.; Li, Y.; Lu, Z.; Lattimer, J.; Hu, Y.; Stokes, C.; Gangishetty, M.; Chen, G.et al. Transition-Metal Single Atoms in a Graphene Shell as Active Centers for Highly Efficient Artificial Photosynthesis. *Chem* **2017,** *3,* 950-960.

(180) Xin, H. L.; Mundy, J. A.; Liu, Z.; Cabezas, R.; Hovden, R.; Kourkoutis, L. F.; Zhang, J.; Subramanian, N. P.; Makharia, R.; Wagner, F. T. Atomic-resolution spectroscopic imaging of ensembles of nanocatalyst particles across the life of a fuel cell. *Nano Lett.* **2011,** *12,* 490-497.

(181) Gan, L.; Cui, C.; Rudi, S.; Strasser, P. Core–shell and nanoporous particle architectures and their effect on the activity and stability of Pt ORR electrocatalysts. *Top. Catal.* **2014,** *57,* 236-244.

(182) Kühl, S.; Strasser, P. Oxygen electrocatalysis on dealloyed Pt nanocatalysts. *Top. Catal.* **2016,** *59,* 1628-1637.

(183) Strasser, P.; Kühl, S. Dealloyed Pt-based core-shell oxygen reduction electrocatalysts. *Nano Energy* **2016,** *29,* 166-177.

(184) Oezaslan, M.; Hasche, F.; Strasser, P. Pt-based core–shell catalyst architectures for oxygen fuel cell electrodes. *J. Phys. Chem. Lett.* **2013,** *4,* 3273-3291.

(185) Koh, S.; Strasser, P. Electrocatalysis on bimetallic surfaces: modifying catalytic reactivity for oxygen reduction by voltammetric surface dealloying. *J. Am. Chem. Soc.* **2007,** *129,* 12624-12625.

(186) Strasser, P.; Koh, S.; Anniyev, T.; Greeley, J.; More, K.; Yu, C.; Liu, Z.; Kaya, S.; Nordlund, D.; Ogasawara, H. Lattice-strain control of the activity in dealloyed core–shell fuel cell catalysts. *Nat. Chem.* **2010,** *2,* 454-460.

(187) Mani, P.; Srivastava, R.; Strasser, P. Dealloyed Pt− Cu core− shell nanoparticle electrocatalysts for use in PEM fuel cell cathodes. *J. Phys. Chem. C* **2008,** *112,* 2770-2778.

(188)	Hasché, F.; Oezaslan, M.; Strasser, P. Activity, stability, and degradation mechanisms of dealloyed PtCu3 and PtCo3 nanoparticle fuel cell catalysts. *ChemCatChem* **2011,** *3,* 1805-1813.

(189)	Mani, P.; Srivastava, R.; Strasser, P. Dealloyed binary PtM3 (M= Cu, Co, Ni) and ternary PtNi3M (M= Cu, Co, Fe, Cr) electrocatalysts for the oxygen reduction reaction: Performance in polymer electrolyte membrane fuel cells. *J. Power Sources* **2011,** *196,* 666-673.

(190)	Gan, L.; Heggen, M.; Rudi, S.; Strasser, P. Core–Shell Compositional Fine Structures of Dealloyed Pt x Ni1– x Nanoparticles and Their Impact on Oxygen Reduction Catalysis. *Nano Lett.* **2012,** *12,* 5423-5430.

(191)	Gan, L.; Heggen, M.; O'Malley, R.; Theobald, B.; Strasser, P. Understanding and controlling nanoporosity formation for improving the stability of bimetallic fuel cell catalysts. *Nano Lett.* **2013,** *13,* 1131-1138.

(192)	Han, B.; Carlton, C. E.; Kongkanand, A.; Kukreja, R. S.; Theobald, B. R.; Gan, L.; O'Malley, R.; Strasser, P.; Wagner, F. T.; Shao-Horn, Y. Record activity and stability of dealloyed bimetallic catalysts for proton exchange membrane fuel cells. *Energy Environ. Sci.* **2015,** *8,* 258-266.

(193)	Zhang, J.; Vukmirovic, M. B.; Xu, Y.; Mavrikakis, M.; Adzic, R. R. Controlling the catalytic activity of platinum-monolayer electrocatalysts for oxygen reduction with different substrates. *Angew. Chem., Int. Ed.* **2005,** *117,* 2170-2173.

(194)	Wang, J. X.; Inada, H.; Wu, L.; Zhu, Y.; Choi, Y.; Liu, P.; Zhou, W.-P.; Adzic, R. R. Oxygen Reduction on Well-Defined Core−Shell Nanocatalysts: Particle Size, Facet, and Pt Shell Thickness Effects. *J. Am. Chem. Soc.* **2009,** *131,* 17298-17302.

(195)	Zhou, W.-P.; Yang, X.; Vukmirovic, M. B.; Koel, B. E.; Jiao, J.; Peng, G.; Mavrikakis, M.; Adzic, R. R. Improving electrocatalysts for O2 reduction by fine-tuning the Pt− support interaction: Pt monolayer on the surfaces of a Pd3Fe (111) single-crystal alloy. *J. Am. Chem. Soc.* **2009,** *131,* 12755-12762.

(196)	Kuttiyiel, K. A.; Sasaki, K.; Su, D.; Vukmirovic, M. B.; Marinkovic, N. S.; Adzic, R. R. Pt monolayer on Au-stabilized PdNi core–shell nanoparticles for oxygen reduction reaction. *Electrochim. Acta* **2013,** *110,* 267-272.

(197)	Shao, M.; Smith, B. H.; Guerrero, S.; Protsailo, L.; Su, D.; Kaneko, K.; Odell, J. H.; Humbert, M. P.; Sasaki, K.; Marzullo, J. Core–shell catalysts consisting of nanoporous cores for oxygen reduction reaction. *Phys. Chem. Chem. Phys.* **2013,** *15,* 15078-15090.

(198)	Gong, K.; Choi, Y.; Vukmirovic, M. B.; Liu, P.; Ma, C.; Su, D.; Adzic, R. R. Tetrahedral palladium nanocrystals: a new support for platinum monolayer electrocatalysts with high activity and stability in the oxygen reduction reaction. *Z. Phys. Chem. (Muenchen, Ger.)* **2012,** *226,* 1025-1038.

(199)	Yang, L.; Vukmirovic, M. B.; Su, D.; Sasaki, K.; Herron, J. A.; Mavrikakis, M.; Liao, S.; Adzic, R. R. Tuning the catalytic activity of Ru@ Pt core–shell nanoparticles for the oxygen reduction reaction by varying the shell thickness. *J. Phys. Chem. C* **2013,** *117,* 1748-1753.

(200)	Chen, C.; Kang, Y. J.; Huo, Z. Y.; Zhu, Z. W.; Huang, W. Y.; Xin, H. L. L.; Snyder, J. D.; Li, D. G.; Herron, J. A.; Mavrikakis, M.et al. Highly Crystalline Multimetallic Nanoframes with Three-Dimensional Electrocatalytic Surfaces. *Science* **2014,** *343,* 1339-1343.

(201)	Zhang, L.; Roling, L. T.; Wang, X.; Vara, M.; Chi, M.; Liu, J.; Choi, S.-I.; Park, J.; Herron, J. A.; Xie, Z.et al. Platinum-based nanocages with subnanometer-thick walls and well-defined, controllable facets. *Science* **2015,** *349,* 412-416.

(202)	Sen, S.; Liu, D.; Palmore, G. T. R. Electrochemical Reduction of CO2 at Copper Nanofoams. *ACS Catal.* **2014,** *4,* 3091-3095.

(203)	Boo, H.; Park, S.; Ku, B.; Kim, Y.; Park, J. H.; Kim, H. C.; Chung, T. D. Ionic strength-controlled virtual area of mesoporous platinum electrode. *J. Am. Chem. Soc.* **2004,** *126,* 4524-4525.

(204)	Bae, J. H.; Han, J.-H.; Chung, T. D. Electrochemistry at nanoporous interfaces: new opportunity for electrocatalysis. *Phys. Chem. Chem. Phys.* **2012,** *14,* 448-463.

(205)	Kibsgaard, J.; Gorlin, Y.; Chen, Z.; Jaramillo, T. F. Meso-structured platinum thin films: active and stable electrocatalysts for the oxygen reduction reaction. *J. Am. Chem. Soc.* **2012,** *134,* 7758-7765.

(206)	Attard, G. S.; Bartlett, P. N.; Coleman, N. R.; Elliott, J. M.; Owen, J. R.; Wang, J. H. Mesoporous platinum films from lyotropic liquid crystalline phases. *Science* **1997,** *278,* 838-840.

(207)	Attard, G. S.; Corker, J. M.; Göltner, C. G.; Henke, S.; Templer, R. H. Liquid-Crystal Templates for Nanostructured Metals. *Angew. Chem., Int. Ed. EngI.* **1997,** *36,* 1315-1317.

(208)	Yamauchi, Y.; Takai, A.; Komatsu, M.; Sawada, M.; Ohsuna, T.; Kuroda, K. Vapor infiltration of a reducing agent for facile synthesis of mesoporous Pt and Pt-based alloys and its application for the preparation of mesoporous Pt microrods in anodic porous membranes. *Chem. Mater.* **2007,** *20,* 1004-1011.

(209) Yamauchi, Y.; Tonegawa, A.; Komatsu, M.; Wang, H.; Wang, L.; Nemoto, Y.; Suzuki, N.; Kuroda, K. Electrochemical Synthesis of Mesoporous Pt–Au Binary Alloys with Tunable Compositions for Enhancement of Electrochemical Performance. *J. Am. Chem. Soc.* **2012**, *134*, 5100-5109.

(210) Wang, H.; Jeong, H. Y.; Imura, M.; Wang, L.; Radhakrishnan, L.; Fujita, N.; Castle, T.; Terasaki, O.; Yamauchi, Y. Shape-and size-controlled synthesis in hard templates: sophisticated chemical reduction for mesoporous monocrystalline platinum nanoparticles. *J. Am. Chem. Soc.* **2011**, *133*, 14526-14529.

(211) Kim, H. Y.; Cho, S.; Sa, Y. J.; Hwang, S. M.; Park, G. G.; Shin, T. J.; Jeong, H. Y.; Yim, S. D.; Joo, S. H. Self-Supported Mesostructured Pt-Based Bimetallic Nanospheres Containing an Intermetallic Phase as Ultrastable Oxygen Reduction Electrocatalysts. *Small* **2016**, *12*, 5347-5353.

(212) Li, J.; Yin, H.-M.; Li, X.-B.; Okunishi, E.; Shen, Y.-L.; He, J.; Tang, Z.-K.; Wang, W.-X.; Yücelen, E.; Li, C. Surface evolution of a Pt–Pd–Au electrocatalyst for stable oxygen reduction. *Nat. Energy* **2017**, *2*, 17111.

(213) Zhao, M.; Wang, X.; Yang, X.; Gilroy, K. D.; Qin, D.; Xia, Y. Hollow Metal Nanocrystals with Ultrathin, Porous Walls and Well-Controlled Surface Structures. *Adv. Mater.* **2018**, 1801956.

(214) Yang, X.; Roling, L. T.; Vara, M.; Elnabawy, A. O.; Zhao, M.; Hood, Z. D.; Bao, S.; Mavrikakis, M.; Xia, Y. Synthesis and Characterization of Pt–Ag Alloy Nanocages with Enhanced Activity and Durability toward Oxygen Reduction. *Nano Lett.* **2016**, *16*, 6644-6649.

(215) Wang, X.; Figueroa-Cosme, L.; Yang, X.; Luo, M.; Liu, J.; Xie, Z.; Xia, Y. Pt-based icosahedral nanocages: using a combination of {111} facets, twin defects, and ultrathin walls to greatly enhance their activity toward oxygen reduction. *Nano Lett.* **2016**, *16*, 1467-1471.

(216) Huang, H.; Ruditskiy, A.; Choi, S.-I.; Zhang, L.; Liu, J.; Ye, Z.; Xia, Y. One-Pot Synthesis of Penta-twinned Palladium Nanowires and Their Enhanced Electrocatalytic Properties. *ACS Appl. Mater. Interfaces* **2017**, *9*, 31203-31212.

(217) Cui, C.; Gan, L.; Heggen, M.; Rudi, S.; Strasser, P. Compositional segregation in shaped Pt alloy nanoparticles and their structural behaviour during electrocatalysis. *Nat. Mater.* **2013**, *12*, 765-771.

(218) Gan, L.; Cui, C.; Heggen, M.; Dionigi, F.; Rudi, S.; Strasser, P. Element-specific anisotropic growth of shaped platinum alloy nanocrystals. *Science* **2014**, *346*, 1502-1506.

(219) Nagao, A.; Higashimine, K.; Huaman, J. L. C.; Iwamoto, T.; Matsumoto, T.; Yoshinori, I.; Maenosono, S.; Miyamura, H.; Jeyadevan, B. Formation of Pt decorated Ni-Pt Nanocubes Through Low Temperature Atomic Diffusion-Time-resolved Elemental Analysis of Nanoparticle Formation. *Nanoscale* **2015**, *7*, 9927-9934.

(220) Wang, D. S.; Zhao, P.; Li, Y. D. General preparation for Pt-based alloy nanoporous nanoparticles as potential nanocatalysts. *Sci. Rep.* **2011**, *1,* 37.

(221) Snyder, J.; McCue, I.; Livi, K.; Erlebacher, J. Structure/Processing/Properties Relationships in Nanoporous Nanoparticles As Applied to Catalysis of the Cathodic Oxygen Reduction Reaction. *J. Am. Chem. Soc.* **2012**, *134*, 8633-8645.

(222) Zhu, E.; Li, Y.; Chiu, C.-Y.; Huang, X.; Li, M.; Zhao, Z.; Liu, Y.; Duan, X.; Huang, Y. In situ development of highly concave and composition-confined PtNi octahedra with high oxygen reduction reaction activity and durability. *Nano Res.* **2016**, *9*, 149-157.

(223) Wu, Y.; Wang, D.; Niu, Z.; Chen, P.; Zhou, G.; Li, Y. A strategy for designing a concave Pt–Ni alloy through controllable chemical etching. *Angew. Chem., Int. Ed.* **2012**, *124*, 12692-12696.

(224) Oh, A.; Baik, H.; Choi, D. S.; Cheon, J. Y.; Kim, B.; Kim, H.; Kwon, S. J.; Joo, S. H.; Jung, Y.; Lee, K. Skeletal Octahedral Nanoframe with Cartesian Coordinates via Geometrically Precise Nanoscale Phase Segregation in a Pt@Ni Core–Shell Nanocrystal. *ACS Nano* **2015**, *9*, 2856-2867.

(225) Becknell, N.; Zheng, C.; Chen, C.; Yu, Y.; Yang, P. Synthesis of PtCo 3 polyhedral nanoparticles and evolution to Pt 3 Co nanoframes. *Surf. Sci.* **2016**, *648*, 328-332.

(226) Nosheen, F.; Zhang, Z. C.; Zhuang, J.; Wang, X. One-pot fabrication of single-crystalline octahedral Pt-Cu nanoframes and their enhanced electrocatalytic activity. *Nanoscale* **2013**, *5*, 3660-3663.

(227) Xia, B. Y.; Wu, H. B.; Wang, X.; Lou, X. W. One-Pot Synthesis of Cubic PtCu3 Nanocages with Enhanced Electrocatalytic Activity for the Methanol Oxidation Reaction. *J. Am. Chem. Soc.* **2012**, *134*, 13934-13937.

(228) Han, L.; Liu, H.; Cui, P. L.; Peng, Z. J.; Zhang, S. J.; Yang, J. Alloy Cu3Pt nanoframes through the structure evolution in Cu-Pt nanoparticles with a core-shell construction. *Scientific Reports* **2014**, *4*, 6414.

(229) Jia, Y. Y.; Jiang, Y. Q.; Zhang, J. W.; Zhang, L.; Chen, Q. L.; Xie, Z. X.; Zheng, L. S. Unique Excavated Rhombic Dodecahedral PtCu3 Alloy Nanocrystals Constructed with Ultrathin Nanosheets of High-Energy {110} Facets. *J. Am. Chem. Soc.* **2014**, *136*, 3748-3751.

(230) Tang, M.; Luo, S.; Wang, K.; Du, H.; Sriphathoorat, R.; Shen, P. Simultaneous formation of trimetallic Pt-Ni-Cu excavated rhombic dodecahedrons with enhanced catalytic performance for the methanol oxidation reaction. *Nano Res.*, **2018**, *11*, 4786-4795.

(231) Zhang, Z.-P.; Zhu, W.; Yan, C.-H.; Zhang, Y. Selective Synthesis of Rhodium-based Nanoframe Catalysts by Chemical Etching of 3d Metals. *Chem. Commun.* **2015,** *51,* 3997-4000.

(232) Xie, S.; Lu, N.; Xie, Z.; Wang, J.; Kim, M. J.; Xia, Y. Synthesis of Pd-Rh Core–Frame Concave Nanocubes and Their Conversion to Rh Cubic Nanoframes by Selective Etching of the Pd Cores. *Angew. Chem., Int. Ed.* **2012,** *51,* 10266-10270.

(233) McEachran, M.; Keogh, D.; Pietrobon, B.; Cathcart, N.; Gourevich, I.; Coombs, N.; Kitaev, V. Ultrathin gold nanoframes through surfactant-free templating of faceted pentagonal silver nanoparticles. *J. Am. Chem. Soc.* **2011,** *133,* 8066-8069.

(234) Becknell, N.; Kang, Y.; Chen, C.; Resasco, J.; Kornienko, N.; Guo, J.; Markovic, N. M.; Somorjai, G. A.; Stamenkovic, V. R.; Yang, P. Atomic structure of Pt3Ni nanoframe electrocatalysts by in situ X-ray absorption spectroscopy. *J. Am. Chem. Soc.* **2015,** *137,* 15817-15824.

(235) Niu, Z.; Becknell, N.; Yu, Y.; Kim, D.; Chen, C.; Kornienko, N.; Somorjai, G. A.; Yang, P. Anisotropic phase segregation and migration of Pt in nanocrystals en route to nanoframe catalysts. *Nat. Mater.* **2016,** *15,* 1188-1194.

(236) Vitos, L.; Ruban, A.; Skriver, H. L.; Kollar, J. The surface energy of metals. *Surf. Sci.* **1998,** *411,* 186-202.

(237) Becknell, N.; Son, Y.; Kim, D.; Li, D.; Yu, Y.; Niu, Z.; Lei, T.; Sneed, B. T.; More, K. L.; Markovic, N. M.et al. Control of Architecture in Rhombic Dodecahedral Pt–Ni Nanoframe Electrocatalysts. *J. Am. Chem. Soc.* **2017,** *139,* 11678-11681.

(238) Durst, J.; Lopez-Haro, M.; Dubau, L.; Chatenet, M.; Soldo-Olivier, Y.; Guétaz, L.; Bayle-Guillemaud, P.; Maillard, F. d. r. Reversibility of Pt-skin and Pt-skeleton nanostructures in acidic media. *J. Phys. Chem. Lett.* **2014,** *5,* 434-439.

(239) Rudi, S.; Teschner, D.; Beermann, V.; Hetaba, W.; Gan, L.; Cui, C.; Gliech, M.; Schlögl, R.; Strasser, P. pH-Induced versus Oxygen-Induced Surface Enrichment and Segregation Effects in Pt–Ni Alloy Nanoparticle Fuel Cell Catalysts. *ACS Catal.* **2017,** *7,* 6376-6384.

(240) Bezerra, C. W.; Zhang, L.; Liu, H.; Lee, K.; Marques, A. L.; Marques, E. P.; Wang, H.; Zhang, J. A review of heat-treatment effects on activity and stability of PEM fuel cell catalysts for oxygen reduction reaction. *J. Power Sources* **2007,** *173,* 891-908.

(241) Cui, C.; Ahmadi, M.; Behafarid, F.; Gan, L.; Neumann, M.; Heggen, M.; Cuenya, B. R.; Strasser, P. Shape-selected bimetallic nanoparticle electrocatalysts: evolution of their atomic-scale structure, chemical composition, and electrochemical reactivity under various chemical environments. *Faraday Discuss.* **2013,** *162,* 91-112.

(242) Gan, L.; Heggen, M.; Cui, C.; Strasser, P. Thermal facet healing of concave octahedral Pt–Ni nanoparticles imaged in situ at the atomic scale: implications for the rational synthesis of durable high-performance ORR electrocatalysts. *ACS Catal.* **2015,** *6,* 692-695.

(243) Lopes, P. P.; Strmcnik, D.; Tripkovic, D.; Connell, J. G.; Stamenkovic, V.; Markovic, N. M. Relationships between atomic level surface structure and stability/activity of platinum surface atoms in aqueous environments. *ACS Catal.* **2016,** *6,* 2536-2544.

(244) Van Hardeveld, R.; Hartog, F. The statistics of surface atoms and surface sites on metal crystals. *Surf. Sci.* **1969,** *15,* 189-230.

(245) Chen, S.; Niu, Z.; Xie, C.; Gao, M.; Lai, M.; Li, M.; Yang, P. Effects of Catalyst Processing on the Activity and Stability of Pt–Ni Nanoframe Electrocatalysts. *ACS Nano* **2018,** *12,* 8697-9705.

(246) Gatalo, M.; Jovanovič, P.; Polymeros, G.; Grote, J.-P.; Pavlišič, A.; Ruiz-Zepeda, F.; Šelih, V. S.; Šala, M.; Hočevar, S.; Bele, M. Positive effect of surface doping with Au on the stability of Pt-Based electrocatalysts. *ACS Catal.* **2016,** *6,* 1630-1634.

(247) Zhang, J.; Sasaki, K.; Sutter, E.; Adzic, R. Stabilization of platinum oxygen-reduction electrocatalysts using gold clusters. *Science* **2007,** *315,* 220-222.

(248) Kuhl, K. P.; Cave, E. R.; Abram, D. N.; Jaramillo, T. F. New insights into the electrochemical reduction of carbon dioxide on metallic copper surfaces. *Energy Environ. Sci.* **2012,** *5,* 7050-7050.

(249) Hori, Y. Electrochemical CO2 Reduction on Metal Electrodes. In: Vayenas C.G., White R.E., Gamboa-Aldeco M.E. (eds) *Modern Aspects of Electrochemistry* **2008,** 42, 89-189 .

(250) Koper, M. T. M. Thermodynamic theory of multi-electron transfer reactions: Implications for electrocatalysis. *J. Electroanal. Chem.* **2011,** *660,* 254-254.

(251) Schouten, K. J. P.; Calle-Vallejo, F.; Koper, M. T. M. A Step Closer to the Electrochemical Production of Liquid Fuels. *Angew. Chem., Int. Ed.* **2014,** *53,* 10858-10860.

(252) Kortlever, R.; Shen, J.; Schouten, K. J. P.; Calle-Vallejo, F.; Koper, M. T. M. Catalysts and Reaction Pathways for the Electrochemical Reduction of Carbon Dioxide. *J. Phys. Chem. Lett.* **2015,** *6,* 4073-4082.

(253) Mistry, H.; Varela, A. S.; Kühl, S.; Strasser, P.; Cuenya, B. R. Nanostructured electrocatalysts with tunable activity and selectivity. *Nat. Rev. Mater.* **2016,** *1*, 16009-16009.

(254) Jitaru, M.; Lowy, D. A.; Toma, M.; Toma, B. C.; Oniciu, L. Electrochemical reduction of carbon dioxide on flat metallic cathodes. *J. Appl. Electrochem.* **1997,** *27*, 875-889.

(255) Chen, Y.; Li, C. W.; Kanan, M. W. Aqueous CO_2 Reduction at Very Low Overpotential on Oxide-Derived Au Nanoparticles. *J. Am. Chem. Soc.* **2012,** *134*, 19969-19972.

(256) Lu, Q.; Rosen, J.; Zhou, Y.; Hutchings, G. S.; Kimmel, Y. C.; Chen, J. G.; Jiao, F. A selective and efficient electrocatalyst for carbon dioxide reduction. *Nat. Commun.* **2014,** *5*, 3242-3242.

(257) Hori, Y.; Murata, A.; Kikuchi, K.; Suzuki, S. Electrochemical reduction of carbon dioxides to carbon monoxide at a gold electrode in aqueous potassium hydrogen carbonate. *J. Chem. Soc., Chem. Commun.* **1987,** *10*, 728-728.

(258) Noda, H.; Ikeda, S.; Yamamoto, A.; Einaga, H.; Ito, K. Kinetics of Electrochemical Reduction of Carbon Dioxide on a Gold Electrode in Phosphate Buffer Solutions. *Bull. Chem. Soc. Jpn.* **1995,** *68*, 1889-1895.

(259) Hatsukade, T.; Kuhl, K. P.; Cave, E. R.; Abram, D. N.; Jaramillo, T. F. Insights into the electrocatalytic reduction of CO_2 on metallic silver surfaces. *Phys. Chem. Chem. Phys.* **2014,** *16*, 13814-13819.

(260) Rosen, J.; Hutchings, G. S.; Lu, Q.; Rivera, S.; Zhou, Y.; Vlachos, D. G.; Jiao, F. Mechanistic Insights into the Electrochemical Reduction of CO_2 to CO on Nanostructured Ag Surfaces. *ACS Catal.* **2015,** *5*, 4293-4299.

(261) Firet, N. J.; Smith, W. A. Probing the Reaction Mechanism of CO2 Electroreduction over Ag Films via Operando Infrared Spectroscopy. *ACS Catal.* **2017,** *7*, 606-612.

(262) Wuttig, A.; Yoon, Y.; Ryu, J.; Surendranath, Y. Bicarbonate Is Not a General Acid in Au-Catalyzed CO_2 Electroreduction. *J. Am. Chem. Soc.* **2017,** *139*, 17109-17113.

(263) Wuttig, A.; Yaguchi, M.; Motobayashi, K.; Osawa, M.; Surendranath, Y. Inhibited proton transfer enhances Au-catalyzed CO2-to-fuels selectivity. *Proc. Natl. Acad. Sci. U. S. A.* **2016,** *113*, E4585-4593.

(264) Lee, C. W.; Cho, N. H.; Yang, K. D.; Nam, K. T. Reaction Mechanisms of the Electrochemical Conversion of Carbon Dioxide to Formic Acid on Tin Oxide Electrodes. *ChemElectroChem* **2017,** *4*, 2130-2136.

(265) Chernyshova, I. V.; Somasundaran, P.; Ponnurangam, S. On the origin of the elusive first intermediate of CO_2 electroreduction. *Proc. Natl. Acad. Sci. U.S.A.* **2018,** *115*, E9261.

(266) Feaster, J. T.; Shi, C.; Cave, E. R.; Hatsukade, T.; Abram, D. N.; Kuhl, K. P.; Hahn, C.; Nørskov, J. K.; Jaramillo, T. F. Understanding Selectivity for the Electrochemical Reduction of Carbon Dioxide to Formic Acid and Carbon Monoxide on Metal Electrodes. *ACS Catal.* **2017,** *7*, 4822-4827.

(267) Yoo, J. S.; Christensen, R.; Vegge, T.; Nørskov, J. K.; Studt, F. Theoretical Insight into the Trends that Guide the Electrochemical Reduction of Carbon Dioxide to Formic Acid. *ChemSusChem* **2016,** *9*, 358-363.

(268) Chen, Y.; Kanan, M. W. Tin oxide dependence of the CO_2 reduction efficiency on tin electrodes and enhanced activity for tin/tin oxide thin-film catalysts. *J. Am. Chem. Soc.* **2012,** *134*, 1986-1989.

(269) Dutta, A.; Kuzume, A.; Rahaman, M.; Vesztergom, S.; Broekmann, P. Monitoring the Chemical State of Catalysts for CO2 Electroreduction: An In Operando Study. *ACS Catal.* **2015,** *5*, 7498-7502.

(270) Baruch, M. F.; Pander, J. E.; White, J. L.; Bocarsly, A. B. Mechanistic Insights into the Reduction of CO_2 on Tin Electrodes using in Situ ATR-IR Spectroscopy. *ACS Catal.* **2015,** *5*, 3148-3156.

(271) Detweiler, Z. M.; White, J. L.; Bernasek, S. L.; Bocarsly, A. B. Anodized Indium Metal Electrodes for Enhanced Carbon Dioxide Reduction in Aqueous Electrolyte. *Langmuir* **2014,** *30*, 7593-7600.

(272) Pander, J. E.; Baruch, M. F.; Bocarsly, A. B. Probing the Mechanism of Aqueous CO_2 Reduction on Post-Transition-Metal Electrodes using ATR-IR Spectroelectrochemistry. *ACS Catal.* **2016,** *6*, 7824-7833.

(273) Lee, C. H.; Kanan, M. W. Controlling H + vs CO_2 Reduction Selectivity on Pb Electrodes. *ACS Catal.* **2015,** *5*, 465-469.

(274) Min, X.; Kanan, M. W. Pd-Catalyzed Electrohydrogenation of Carbon Dioxide to Formate: High Mass Activity at Low Overpotential and Identification of the Deactivation Pathway. *J. Am. Chem. Soc.* **2015,** *137*, 4701-4708.

(275) Peterson, A. A.; Abild-Pedersen, F.; Studt, F.; Rossmeisl, J.; Nørskov, J. K. How copper catalyzes the electroreduction of carbon dioxide into hydrocarbon fuels. *Energy Environ. Sci.* **2010,** *3*, 1311-1311.

(276) Nie, X.; Esopi, M. R.; Janik, M. J.; Asthagiri, A. Selectivity of CO_2 Reduction on Copper Electrodes: The Role of the Kinetics of Elementary Steps. *Angew. Chem., Int. Ed.* **2013,** *52*, 2459-2462.

(277) Cheng, T.; Xiao, H.; Goddard, W. A. Full atomistic reaction mechanism with kinetics for CO reduction on Cu(100) from ab initio molecular dynamics free-energy calculations at 298 K. *Proc. Natl. Acad. Sci. U.S.A.* **2017,** *114*, 1795-1800.

(278)   Cheng, T.; Xiao, H.; Goddard, W. A. Free-Energy Barriers and Reaction Mechanisms for the Electrochemical Reduction of CO on the Cu(100) Surface, Including Multiple Layers of Explicit Solvent at pH 0. *J. Phys. Chem. Lett.* **2015,** *6,* 4767-4773.

(279)   Kuhl, K. P.; Hatsukade, T.; Cave, E. R.; Abram, D. N.; Kibsgaard, J.; Jaramillo, T. F. Electrocatalytic Conversion of Carbon Dioxide to Methane and Methanol on Transition Metal Surfaces. *J. Am. Chem. Soc.* **2014,** *136,* 14107-14113.

(280)   Hori, Y.; Kikuchi, K.; Suzuki, S. PRODUCTION OF CO AND CH 4 IN ELECTROCHEMICAL REDUCTION OF CO 2 AT METAL ELECTRODES IN AQUEOUS HYDROGENCARBONATE SOLUTION. *Chem. Lett.* **1985,** *14,* 1695-1698.

(281)   Cook, R. L. Evidence for Formaldehyde, Formic Acid, and Acetaldehyde as Possible Intermediates during Electrochemical Carbon Dioxide Reduction at Copper. *J. Electrochem. Soc.* **1989,** *136,* 1982-1982.

(282)   DeWulf, D. W. Electrochemical and Surface Studies of Carbon Dioxide Reduction to Methane and Ethylene at Copper Electrodes in Aqueous Solutions. *J. Electrochem. Soc.* **1989,** *136,* 1686-1686.

(283)   Schouten, K. J. P.; Kwon, Y.; van der Ham, C. J. M.; Qin, Z.; Koper, M. T. M. A new mechanism for the selectivity to C1 and C2 species in the electrochemical reduction of carbon dioxide on copper electrodes. *Chem. Sci.* **2011,** *2,* 1902-1902.

(284)   Friebe, P.; Bogdanoff, P.; Alonso-Vante, N.; Tributsch, H. A Real-Time Mass Spectroscopy Study of the (Electro)chemical Factors Affecting CO2Reduction at Copper. *J. Catal.* **1997,** *168,* 374-385.

(285)   Cook, R. L. On the Electrochemical Reduction of Carbon Dioxide at In Situ Electrodeposited Copper. *J. Electrochem. Soc.* **1988,** *135,* 1320-1320.

(286)   Hori, Y.; Takahashi, R.; Yoshinami, Y.; Murata, A. Electrochemical Reduction of CO at a Copper Electrode. *J. Phys. Chem. B* **1997,** *101,* 7075-7081.

(287)   Gattrell, M.; Gupta, N.; Co, A. A review of the aqueous electrochemical reduction of CO2 to hydrocarbons at copper. *J. Electroanal. Chem.* **2006,** *594,* 1-19.

(288)   Schouten, K. J. P.; Qin, Z.; Pérez Gallent, E.; Koper, M. T. M. Two Pathways for the Formation of Ethylene in CO Reduction on Single-Crystal Copper Electrodes. *J. Am. Chem. Soc.* **2012,** *134,* 9864-9867.

(289)   Schouten, K. J. P.; Pérez Gallent, E.; Koper, M. T. M. Structure Sensitivity of the Electrochemical Reduction of Carbon Monoxide on Copper Single Crystals. *ACS Catal.* **2013,** *3,* 1292-1295.

(290)   Calle-Vallejo, F.; Koper, M. T. M. Theoretical Considerations on the Electroreduction of CO to C 2 Species on Cu(100) Electrodes. *Angew. Chem., Int. Ed.* **2013,** *52,* 7282-7285.

(291)   Ou, L.; Long, W.; Chen, Y.; Jin, J. New reduction mechanism of CO dimer by hydrogenation to C2H4 on a Cu(100) surface: theoretical insight into the kinetics of the elementary steps. *RSC Adv.* **2015,** *5,* 96281-96289.

(292)   Garza, A. J.; Bell, A. T.; Head-Gordon, M. Mechanism of CO 2 Reduction at Copper Surfaces: Pathways to C 2 Products. *ACS Catal.* **2018,** *8,* 1490-1499.

(293)   Goodpaster, J. D.; Bell, A. T.; Head-Gordon, M. Identification of Possible Pathways for C-C Bond Formation during Electrochemical Reduction of CO2: New Theoretical Insights from an Improved Electrochemical Model. *J. Phys. Chem. Lett.* **2016,** *7,* 1471-1477.

(294)   Pérez-Gallent, E.; Figueiredo, M. C.; Calle-Vallejo, F.; Koper, M. T. M. Spectroscopic Observation of a Hydrogenated CO Dimer Intermediate During CO Reduction on Cu(100) Electrodes. *Angew. Chem., Int. Ed.* **2017,** *56,* 3621-3624.

(295)   Zhu, S.; Jiang, B.; Cai, W.-B.; Shao, M. Direct Observation on Reaction Intermediates and the Role of Bicarbonate Anions in CO 2 Electrochemical Reduction Reaction on Cu Surfaces. *J. Am. Chem. Soc.* **2017,** *139,* 15664-15667.

(296)   Dunwell, M.; Lu, Q.; Heyes, J. M.; Rosen, J.; Chen, J. G.; Yan, Y.; Jiao, F.; Xu, B. The Central Role of Bicarbonate in the Electrochemical Reduction of Carbon Dioxide on Gold. *J. Am. Chem. Soc.* **2017,** *139,* 3774-3783.

(297)   Gupta, N.; Gattrell, M.; MacDougall, B. Calculation for the cathode surface concentrations in the electrochemical reduction of CO2in KHCO3solutions. *J. Appl. Electrochem.* **2006,** *36,* 161-172.

(298)   Varela, A. S.; Kroschel, M.; Reier, T.; Strasser, P. Controlling the selectivity of CO2 electroreduction on copper: The effect of the electrolyte concentration and the importance of the local pH. *Catal. Today* **2016,** *260,* 8-13.

(299)   Ma, M.; Djanashvili, K.; Smith, W. A. Controllable Hydrocarbon Formation from the Electrochemical Reduction of CO2 over Cu Nanowire Arrays. *Angew. Chem., Int. Ed.* **2016,** *55,* 6680-6684.

(300)   Roberts, F. S.; Kuhl, K. P.; Nilsson, A. Electroreduction of Carbon Monoxide Over a Copper Nanocube Catalyst: Surface Structure and pH Dependence on Selectivity. *ChemCatChem* **2016,** *8,* 1119-1124.

(301) Dinh, C.-T.; Burdyny, T.; Kibria, M. G.; Seifitokaldani, A.; Gabardo, C. M.; García de Arquer, F. P.; Kiani, A.; Edwards, J. P.; De Luna, P.; Bushuyev, O. S.et al. CO2 electroreduction to ethylene via hydroxide-mediated copper catalysis at an abrupt interface. *Science* **2018**, *360*, 783-787.

(302) Lum, Y.; Yue, B.; Lobaccaro, P.; Bell, A. T.; Ager, J. W. Optimizing C–C Coupling on Oxide-Derived Copper Catalysts for Electrochemical CO2 Reduction. *J. Phys. Chem. C* **2017**, *121*, 14191-14203.

(303) Schouten, K. J. P.; Pérez Gallent, E.; Koper, M. T. M. The influence of pH on the reduction of CO and CO2 to hydrocarbons on copper electrodes. *J. Electroanal. Chem.* **2014**, *716*, 53-57.

(304) Murata, A.; Hori, Y., Product selectivity affected by cationic species in electrochemical reduction of CO2 and CO at a Cu electrode. *Bull. Chem. Soc. Jpn.* **1991**, *64*, 123-127.

(305) Kyriacou, G. Z.; Anagnostopoulos, A. K. Influence CO2 partial pressure and the supporting electrolyte cation on the product distribution in CO2 electroreduction. *J. Appl. Electrochem.* **1993**, *23*, 483-486.

(306) Singh, M. R.; Kwon, Y.; Lum, Y.; Ager, J. W.; Bell, A. T. Hydrolysis of Electrolyte Cations Enhances the Electrochemical Reduction of CO 2 over Ag and Cu. *J. Am. Chem. Soc.* **2016**, *138*, 13006-13012.

(307) Ayemoba, O.; Cuesta, A. Spectroscopic Evidence of Size-Dependent Buffering of Interfacial pH by Cation Hydrolysis during CO 2 Electroreduction. *ACS Appl. Mater. Interfaces* **2017**, *9*, 27377-27382.

(308) Akhade, S. A.; McCrum, I. T.; Janik, M. J. The Impact of Specifically Adsorbed Ions on the Copper-Catalyzed Electroreduction of CO 2. *J. Electrochem. Soc.* **2016**, *163*, F477-F484.

(309) Chen, L. D.; Urushihara, M.; Chan, K.; Nørskov, J. K. Electric Field Effects in Electrochemical CO2Reduction. *ACS Catal.* **2016**, *6*, 7133-7139.

(310) Resasco, J.; Chen, L. D.; Clark, E.; Tsai, C.; Hahn, C.; Jaramillo, T. F.; Chan, K.; Bell, A. T. Promoter Effects of Alkali Metal Cations on the Electrochemical Reduction of Carbon Dioxide. *J. Am. Chem. Soc.* **2017**, *139*, 11277-11287.

(311) Kas, R.; Kortlever, R.; Yılmaz, H.; Koper, M. T. M.; Mul, G. Manipulating the Hydrocarbon Selectivity of Copper Nanoparticles in CO 2 Electroreduction by Process Conditions. *ChemElectroChem* **2015**, *2*, 354-358.

(312) Lobaccaro, P.; Singh, M. R.; Clark, E. L.; Kwon, Y.; Bell, A. T.; Ager, J. W. Effects of temperature and gas–liquid mass transfer on the operation of small electrochemical cells for the quantitative evaluation of CO$_2$ reduction electrocatalysts. *Phys. Chem. Chem. Phys.* **2016**, *18*, 26777-26785.

(313) Hori, Y.; Konishi, H.; Futamura, T.; Murata, A.; Koga, O.; Sakurai, H.; Oguma, K. "Deactivation of copper electrode" in electrochemical reduction of CO2. *Electrochim. Acta* **2005**, *50*, 5354-5369.

(314) Wuttig, A.; Surendranath, Y. Impurity Ion Complexation Enhances Carbon Dioxide Reduction Catalysis. *ACS Catal.* **2015**, *5*, 4479-4484.

(315) Lum, Y.; Kwon, Y.; Lobaccaro, P.; Chen, L.; Clark, E. L.; Bell, A. T.; Ager, J. W. Trace Levels of Copper in Carbon Materials Show Significant Electrochemical CO2 Reduction Activity. *ACS Catal.* **2016**, *6*, 202-209.

(316) Kyriacou, G.; Anagnostopoulos, A. Electroreduction of CO2 on differently prepared copper electrodes. *J. Electroanal. Chem.* **1992**, *322*, 233-246.

(317) Francke, R.; Schille, B.; Roemelt, M. Homogeneously Catalyzed Electroreduction of Carbon Dioxide—Methods, Mechanisms, and Catalysts. *Chem. Rev.* **2018**, *118*, 4631-4701.

(318) Bagger, A.; Ju, W.; Varela, A. S.; Strasser, P.; Rossmeisl, J. Electrochemical CO2 Reduction: A Classification Problem. *ChemPhysChem* **2017**, *04510*, 3266-3273.

(319) Peterson, A. A.; Nørskov, J. K. Activity Descriptors for CO 2 Electroreduction to Methane on Transition-Metal Catalysts. *J. Phys. Chem. Lett.* **2012**, *3*, 251-258.

(320) Shi, C.; Hansen, H. a.; Lausche, A. C.; Nørskov, J. K. Trends in electrochemical CO2 reduction activity for open and close-packed metal surfaces. *Phys. Chem. Chem. Phys.* **2014**, *16*, 4720-4727.

(321) Hansen, H. A.; Varley, J. B.; Peterson, A. A.; Nørskov, J. K. Understanding Trends in the Electrocatalytic Activity of Metals and Enzymes for CO 2 Reduction to CO. *J. Phys. Chem. Lett.* **2013**, *4*, 388-392.

(322) Zhang, S.; Kang, P.; Ubnoske, S.; Brennaman, M. K.; Song, N.; House, R. L.; Glass, J. T.; Meyer, T. J. Polyethylenimine-Enhanced Electrocatalytic Reduction of CO$_2$ to Formate at Nitrogen-Doped Carbon Nanomaterials. *J. Am. Chem. Soc.* **2014**, *136*, 7845-7848.

(323) Duan, X.; Xu, J.; Wei, Z.; Ma, J.; Guo, S.; Wang, S.; Liu, H.; Dou, S. Metal-Free Carbon Materials for CO$_2$ Electrochemical Reduction. *Adv. Mater.* **2017**, *1701784*, 1701784-1701784.

(324) Wu, J.; Ma, S.; Sun, J.; Gold, J. I.; Tiwary, C.; Kim, B.; Zhu, L.; Chopra, N.; Odeh, I. N.; Vajtai, R.et al. A metal-free electrocatalyst for carbon dioxide reduction to multi-carbon hydrocarbons and oxygenates. *Nat. Commun.* **2016**, *7*, 13869-13869.

(325) Varela, A. S.; Ranjbar Sahraie, N.; Steinberg, J.; Ju, W.; Oh, H.-S.; Strasser, P. Metal-Doped Nitrogenated Carbon as an Efficient Catalyst for Direct CO 2 Electroreduction to CO and Hydrocarbons. *Angew. Chem., Int. Ed.* **2015**, *54*, 10758-10762.

(326) Zou, X.; Liu, M.; Wu, J.; Ajayan, P. M.; Li, J.; Liu, B.; Yakobson, B. I. How Nitrogen-Doped Graphene Quantum Dots Catalyze Electroreduction of CO 2 to Hydrocarbons and Oxygenates. *ACS Catal.* **2017,** *7*, 6245-6250.

(327) Yang, H. B.; Hung, S.-F.; Liu, S.; Yuan, K.; Miao, S.; Zhang, L.; Huang, X.; Wang, H.-Y.; Cai, W.; Chen, R.et al. Atomically dispersed Ni(i) as the active site for electrochemical CO2 reduction. *Nat. Energy* **2018,** *3*, 140-147.

(328) Back, S.; Yeom, M. S.; Jung, Y. Active Sites of Au and Ag Nanoparticle Catalysts for CO 2 Electroreduction to CO. *ACS Catal.* **2015,** *5*, 5089-5096.

(329) Zhu, W.; Michalsky, R.; Metin, Ö.; Lv, H.; Guo, S.; Wright, C. J.; Sun, X.; Peterson, A. a.; Sun, S. Monodisperse Au Nanoparticles for Selective Electrocatalytic Reduction of CO 2 to CO. *J. Am. Chem. Soc.* **2013,** *135*, 16833-16836.

(330) Mistry, H.; Reske, R.; Zeng, Z.; Zhao, Z.-J.; Greeley, J.; Strasser, P.; Cuenya, B. R. Exceptional Size-Dependent Activity Enhancement in the Electroreduction of CO 2 over Au Nanoparticles. *J. Am. Chem. Soc.* **2014,** *136*, 16473-16476.

(331) Zhu, W.; Zhang, Y.-J.; Zhang, H.; Lv, H.; Li, Q.; Michalsky, R.; Peterson, A. a.; Sun, S. Active and Selective Conversion of CO 2 to CO on Ultrathin Au Nanowires. *J. Am. Chem. Soc.* **2014,** *136*, 16132-16135.

(332) Lee, H.-E.; Yang, K. D.; Yoon, S. M.; Ahn, H.-Y.; Lee, Y. Y.; Chang, H.; Jeong, D. H.; Lee, Y.-S.; Kim, M. Y.; Nam, K. T. Concave Rhombic Dodecahedral Au Nanocatalyst with Multiple High-Index Facets for CO 2 Reduction. *ACS Nano* **2015,** *9*, 8384-8393.

(333) Kauffman, D. R.; Alfonso, D.; Matranga, C.; Qian, H.; Jin, R. Experimental and computational investigation of Au25 clusters and CO2: a unique interaction and enhanced electrocatalytic activity. *J. Am. Chem. Soc.* **2012,** *134*, 10237-10243.

(334) Kauffman, D. R.; Alfonso, D.; Matranga, C.; Ohodnicki, P.; Deng, X.; Siva, R. C.; Zeng, C.; Jin, R. Probing active site chemistry with differently charged Au25q nanoclusters (q = −1, 0, +1). *Chem. Sci.* **2014,** *5*, 3151-3157.

(335) Kauffman, D. R.; Thakkar, J.; Siva, R.; Matranga, C.; Ohodnicki, P. R.; Zeng, C.; Jin, R. Efficient Electrochemical CO 2 Conversion Powered by Renewable Energy. *ACS Appl. Mater. Interfaces* **2015,** *7*, 15626-15632.

(336) Alfonso, D. R.; Kauffman, D.; Matranga, C. Active sites of ligand-protected Au25 nanoparticle catalysts for CO2 electroreduction to CO. *The Journal of Chemical Physics* **2016,** *144*, 184705-184705.

(337) Zhao, S.; Austin, N.; Li, M.; Song, Y.; House, S. D.; Bernhard, S.; Yang, J. C.; Mpourmpakis, G.; Jin, R. Influence of Atomic-Level Morphology on Catalysis: The Case of Sphere and Rod-Like Gold Nanoclusters for CO2 Electroreduction. *ACS Catal.* **2018,** *8*, 4996-5001.

(338) Salehi-Khojin, A.; Jhong, H. R. M.; Rosen, B. A.; Zhu, W.; Ma, S.; Kenis, P. J. A.; Masel, R. I. Nanoparticle silver catalysts that show enhanced activity for carbon dioxide electrolysis. *J. Phys. Chem. C* **2013,** *117*, 1627-1632.

(339) Liu, S.; Tao, H.; Zeng, L.; Liu, Q.; Xu, Z.; Liu, Q.; Luo, J. L. Shape-Dependent Electrocatalytic Reduction of CO2to CO on Triangular Silver Nanoplates. *J. Am. Chem. Soc.* **2017,** *139*, 2160-2163.

(340) Andrews, E.; Katla, S.; Kumar, C.; Patterson, M.; Sprunger, P.; Flake, J. Electrocatalytic Reduction of CO2 at Au Nanoparticle Electrodes: Effects of Interfacial Chemistry on Reduction Behavior. *J. Electrochem. Soc.* **2015,** *162*, F1373-F1378.

(341) Kim, C.; Jeon, H. S.; Eom, T.; Jee, M. S.; Kim, H.; Friend, C. M.; Min, B. K.; Hwang, Y. J. Achieving Selective and Efficient Electrocatalytic Activity for CO2 Reduction Using Immobilized Silver Nanoparticles. *J. Am. Chem. Soc.* **2015,** *137*, 13844-13850.

(342) Cao, Z.; Kim, D.; Hong, D.; Yu, Y.; Xu, J.; Lin, S.; Wen, X.; Nichols, E. M.; Jeong, K.; Reimer, J. A.et al. A Molecular Surface Functionalization Approach to Tuning Nanoparticle Electrocatalysts for Carbon Dioxide Reduction. *J. Am. Chem. Soc.* **2016,** *138*, 8120-8125.

(343) Fang, Y.; Flake, J. C. Electrochemical Reduction of CO 2 at Functionalized Au Electrodes. *J. Am. Chem. Soc.* **2017,** *139*, 3399-3405.

(344) Wang, Z.; Wu, L.; Sun, K.; Chen, T.; Jiang, Z.; Cheng, T.; Goddard, W. A. Surface Ligand Promotion of Carbon Dioxide Reduction through Stabilizing Chemisorbed Reactive Intermediates. *J. Phys. Chem. Lett.* **2018,** *9*, 3057-3061.

113

(345) Gao, D.; Zhang, Y.; Zhou, Z.; Cai, F.; Zhao, X.; Huang, W.; Li, Y.; Zhu, J.; Liu, P.; Yang, F.et al. Enhancing CO 2 Electroreduction with the Metal–Oxide Interface. *J. Am. Chem. Soc.* **2017,** *139,* 5652-5655.

(346) Rogers, C.; Perkins, W. S.; Veber, G.; Williams, T. E.; Cloke, R. R.; Fischer, F. R. Synergistic Enhancement of Electrocatalytic CO 2 Reduction with Gold Nanoparticles Embedded in Functional Graphene Nanoribbon Composite Electrodes. *J. Am. Chem. Soc.* **2017,** *139,* 4052-4061.

(347) Kim, J.-H.; Woo, H.; Choi, J.; Jung, H.-W.; Kim, Y.-T. CO 2 Electroreduction on Au/TiC: Enhanced Activity Due to Metal–Support Interaction. *ACS Catal.* **2017,** *7,* 2101-2106.

(348) Ma, S.; Lan, Y.; Perez, G. M. J.; Moniri, S.; Kenis, P. J. A. Silver supported on titania as an active catalyst for electrochemical carbon dioxide reduction. *ChemSusChem* **2014,** *7,* 866-874.

(349) Mistry, H.; Choi, Y.-W.; Bagger, A.; Scholten, F.; Bonifacio, C. S.; Sinev, I.; Divins, N. J.; Zegkinoglou, I.; Jeon, H. S.; Kisslinger, K.et al. Enhanced Carbon Dioxide Electroreduction to Carbon Monoxide over Defect-Rich Plasma-Activated Silver Catalysts. *Angew. Chem., Int. Ed.* **2017,** *56,* 11394-11398.

(350) Ma, M.; Trześniewski, B. J.; Xie, J.; Smith, W. A. Selective and Efficient Reduction of Carbon Dioxide to Carbon Monoxide on Oxide-Derived Nanostructured Silver Electrocatalysts. *Angew. Chem., Int. Ed.* **2016,** *55,* 9748-9752.

(351) Feng, X.; Jiang, K.; Fan, S.; Kanan, M. W. Grain-Boundary-Dependent CO 2 Electroreduction Activity. *J. Am. Chem. Soc.* **2015,** *137,* 4606-4609.

(352) Mariano, R. G.; McKelvey, K.; White, H. S.; Kanan, M. W. Selective increase in CO 2 electroreduction activity at grain-boundary surface terminations. *Science* **2017,** *358,* 1187-1192.

(353) Kim, K. S.; Kim, W. J.; Lim, H. K.; Lee, E. K.; Kim, H. Tuned Chemical Bonding Ability of Au at Grain Boundaries for Enhanced Electrochemical CO2Reduction. *ACS Catal.* **2016,** *6,* 4443-4448.

(354) Dong, C.; Fu, J.; Liu, H.; Ling, T.; Yang, J.; Qiao, S. Z.; Du, X. W. Tuning the selectivity and activity of Au catalysts for carbon dioxide electroreduction via grain boundary engineering: a DFT study. *J. Mater. Chem. A* **2017,** *5,* 7184-7190.

(355) Jee, M. S.; Kim, H.; Jeon, H. S.; Min, B. K.; Hwang, Y. J.; Chae, K. H. Stable surface oxygen on nanostructured silver for efficient CO2 electroreduction. *Catal. Today* **2017,** *288,* 48-53.

(356) Jiang, K.; Kharel, P.; Peng, Y.; Gangishetty, M. K.; Lin, H. Y. G.; Stavitski, E.; Attenkofer, K.; Wang, H. Silver Nanoparticles with Surface-Bonded Oxygen for Highly Selective CO2Reduction. *ACS Sustainable Chem. Eng.* **2017,** *5,* 8529-8534.

(357) Yoon, Y.; Hall, A. S.; Surendranath, Y. Tuning of Silver Catalyst Mesostructure Promotes Selective Carbon Dioxide Conversion into Fuels. *Angew. Chem., Int. Ed.* **2016,** *55,* 15282-15286.

(358) Hall, A. S.; Yoon, Y.; Wuttig, A.; Surendranath, Y. Mesostructure-Induced Selectivity in CO 2 Reduction Catalysis. *J. Am. Chem. Soc.* **2015,** *137,* 14834-14837.

(359) Hsieh, Y.-C.; Senanayake, S. D.; Zhang, Y.; Xu, W.; Polyansky, D. E. Effect of Chloride Anions on the Synthesis and Enhanced Catalytic Activity of Silver Nanocoral Electrodes for CO 2 Electroreduction. *ACS Catal.* **2015,** *5,* 5349-5356.

(360) Liu, M.; Pang, Y.; Zhang, B.; De Luna, P.; Voznyy, O.; Xu, J.; Zheng, X.; Dinh, C. T.; Fan, F.; Cao, C.et al. Enhanced electrocatalytic CO2 reduction via field-induced reagent concentration. *Nature* **2016,** *537,* 382-386.

(361) Burdyny, T.; Graham, P. J.; Pang, Y.; Dinh, C.-T.; Liu, M.; Sargent, E. H.; Sinton, D. Nanomorphology-Enhanced Gas-Evolution Intensifies CO2 Reduction Electrochemistry. *ACS Sustain. Chem. Eng.* **2017,** *5,* 4031-4040.

(362) Kapusta, S. The Electroreduction of Carbon Dioxide and Formic Acid on Tin and Indium Electrodes. *J. Electrochem. Soc.* **1983,** *130,* 607-607.

(363) Zhang, S.; Kang, P.; Meyer, T. J. Nanostructured Tin Catalysts for Selective Electrochemical Reduction of Carbon Dioxide to Formate. *J. Am. Chem. Soc.* **2014,** *136,* 1734-1737.

(364) Liang, C.; Kim, B.; Yang, S.; Yang, L.; Francisco Woellner, C.; Li, Z.; Vajtai, R.; Yang, W.; Wu, J.; Kenis, P. J. A.et al. High efficiency electrochemical reduction of CO2 beyond the two-electron transfer pathway on grain boundary rich ultra-small SnO2nanoparticles. *J. Mater. Chem. A* **2018,** *6,* 10313-10319.

(365) Li, F.; Chen, L.; Knowles, G. P.; MacFarlane, D. R.; Zhang, J. Hierarchical Mesoporous SnO 2 Nanosheets on Carbon Cloth: A Robust and Flexible Electrocatalyst for CO 2 Reduction with High Efficiency and Selectivity. *Angew. Chem., Int. Ed.* **2017,** *56,* 505-509.

(366) Kumar, B.; Atla, V.; Brian, J. P.; Kumari, S.; Nguyen, T. Q.; Sunkara, M.; Spurgeon, J. M. Reduced SnO 2 Porous Nanowires with a High Density of Grain Boundaries as Catalysts for Efficient Electrochemical CO 2 -into-HCOOH Conversion. *Angew. Chem., Int. Ed.* **2017,** *129,* 3699-3703.

(367) He, J.; Liu, X.; Liu, H.; Zhao, Z.; Ding, Y.; Luo, J. Highly selective electrocatalytic reduction of CO2to formate over Tin(IV) sulfide monolayers. *J. Catal.* **2018**, *364*, 125-130.

(368) Zheng, X.; De Luna, P.; García de Arquer, F. P.; Zhang, B.; Becknell, N.; Ross, M. B.; Li, Y.; Banis, M. N.; Li, Y.; Liu, M.et al. Sulfur-Modulated Tin Sites Enable Highly Selective Electrochemical Reduction of CO 2 to Formate. *Joule* **2017**, *1*, 794-805.

(369) Fan, L.; Xia, Z.; Xu, M.; Lu, Y.; Li, Z. 1D SnO 2 with Wire-in-Tube Architectures for Highly Selective Electrochemical Reduction of CO 2 to C 1 Products. *Adv. Funct. Mater.* **2018**, *28*, 1706289-1706289.

(370) Liu, Y.; Fan, M.; Zhang, X.; Zhang, Q.; Guay, D.; Qiao, J. Design and engineering of urchin-like nanostructured SnO2catalysts via controlled facial hydrothermal synthesis for efficient electro-reduction of CO2. *Electrochim. Acta* **2017**, *248*, 123-132.

(371) Li, Y.; Qiao, J.; Zhang, X.; Lei, T.; Girma, A.; Liu, Y.; Zhang, J. Rational Design and Synthesis of SnO x Electrocatalysts with Coralline Structure for Highly Improved Aqueous CO 2 Reduction to Formate. *ChemElectroChem* **2016**, *3*, 1618-1628.

(372) Li, F.; Chen, L.; Xue, M.; Williams, T.; Zhang, Y.; MacFarlane, D. R.; Zhang, J. Towards a better Sn: Efficient electrocatalytic reduction of CO2to formate by Sn/SnS2derived from SnS2nanosheets. *Nano Energy* **2017**, *31*, 270-277.

(373) Lei, F.; Liu, W.; Sun, Y.; Xu, J.; Liu, K.; Liang, L.; Yao, T.; Pan, B.; Wei, S.; Xie, Y. Metallic tin quantum sheets confined in graphene toward high-efficiency carbon dioxide electroreduction. *Nat. Commun.* **2016**, *7*, 12697-12697.

(374) Zhang, Y.; Chen, L.; Li, F.; Easton, C. D.; Li, J.; Bond, A. M.; Zhang, J. Direct Detection of Electron Transfer Reactions Underpinning the Tin-Catalyzed Electrochemical Reduction of CO2using Fourier-Transformed ac Voltammetry. *ACS Catal.* **2017**, *7*, 4846-4853.

(375) Zhang, H.; Ma, Y.; Quan, F.; Huang, J.; Jia, F.; Zhang, L. Selective electro-reduction of CO2to formate on nanostructured Bi from reduction of BiOCl nanosheets. *Electrochem. Commun.* **2014**, *46*, 63-66.

(376) Lv, W.; Bei, J.; Zhang, R.; Wang, W.; Kong, F.; Wang, L.; Wang, W. Bi 2 O 2 CO 3 Nanosheets as Electrocatalysts for Selective Reduction of CO 2 to Formate at Low Overpotential. *ACS Omega* **2017**, *2*, 2561-2567.

(377) Koh, J. H.; Won, D. H.; Eom, T.; Kim, N.-K.; Jung, K. D.; Kim, H.; Hwang, Y. J.; Min, B. K. Facile CO 2 Electro-Reduction to Formate via Oxygen Bidentate Intermediate Stabilized by High-Index Planes of Bi Dendrite Catalyst. *ACS Catal.* **2017**, *7*, 5071-5077.

(378) Su, P.; Xu, W.; Qiu, Y.; Zhang, T.; Li, X.; Zhang, H. Ultrathin Bismuth nanosheets as highly efficient electrocatalyst for CO2 reduction. *ChemSusChem* **2018**, *11*, 848-853.

(379) Jiang, J.; Zhao, K.; Xiao, X.; Zhang, L. Synthesis and facet-dependent photoreactivity of BiOCl single-crystalline nanosheets. *J. Am. Chem. Soc.* **2012**, *134*, 4473-4476.

(380) Lee, C. W.; Hong, J. S.; Yang, K. D.; Jin, K.; Lee, J. H.; Ahn, H.-Y.; Seo, H.; Sung, N.-E.; Nam, K. T. Selective Electrochemical Production of Formate from Carbon Dioxide with Bismuth-Based Catalysts in an Aqueous Electrolyte. *ACS Catal.* **2018**, *8*, 931-937.

(381) Zhong, H.; Qiu, Y.; Zhang, T.; Li, X.; Zhang, H.; Chen, X. Bismuth nanodendrites as a high performance electrocatalyst for selective conversion of CO 2 to formate. *J. Mater. Chem. A* **2016**, *4*, 13746-13753.

(382) Kim, S.; Dong, W. J.; Gim, S.; Sohn, W.; Park, J. Y.; Yoo, C. J.; Jang, H. W.; Lee, J.-L. Shape-controlled bismuth nanoflakes as highly selective catalysts for electrochemical carbon dioxide reduction to formate. *Nano Energy* **2017**, *39*, 44-52.

(383) Back, S.; Kim, J.-H.; Kim, Y.-T.; Jung, Y. On the mechanism of high product selectivity for HCOOH using Pb in CO 2 electroreduction. *Phys. Chem. Chem. Phys.* **2016**, *18*, 9652-9657.

(384) Podlovchenko, B. I.; Kolyadko, E. A.; Lu, S. Electroreduction of carbon dioxide on palladium electrodes at potentials higher than the reversible hydrogen potential. *J. Electroanal. Chem.* **1994**, *373*, 185-187.

(385) Sheng, W.; Kattel, S.; Yao, S.; Yan, B.; Liang, Z.; Hawxhurst, C. J.; Wu, Q.; Chen, J. G. Electrochemical reduction of CO 2 to synthesis gas with controlled CO/H 2 ratios. *Energy Environ. Sci.* **2017**, *10*, 1180-1185.

(386) Gao, D.; Zhou, H.; Cai, F.; Wang, J.; Wang, G.; Bao, X. Pd-Containing Nanostructures for Electrochemical CO 2 Reduction Reaction. *ACS Catal.* **2018**, *8*, 1510-1519.

(387) Gao, D.; Zhou, H.; Cai, F.; Wang, D.; Hu, Y.; Jiang, B.; Cai, W.-B.; Chen, X.; Si, R.; Yang, F.et al. Switchable CO2 electroreduction via engineering active phases of Pd nanoparticles. *Nano Res.* **2017**, *10*, 2181-2191.

(388) Rahaman, M.; Dutta, A.; Broekmann, P. Size-Dependent Activity of Palladium Nanoparticles: Efficient Conversion of CO 2 into Formate at Low Overpotentials. *ChemSusChem* **2017**, *10*, 1733-1741.

(389) Klinkova, A.; Luna, P. D.; Dinh, C.-T.; Voznyy, O.; Larin, E. M.; Kumacheva, E.; Sargent, E. H. Rational Design of Efficient Palladium Catalysts for Electroreduction of Carbon Dioxide to Formate. *ACS Catal.* **2016,** *6*, 8115-8120.

(390) Gao, D.; Zhou, H.; Wang, J.; Miao, S.; Yang, F.; Wang, G.; Wang, J.; Bao, X. Size-Dependent Electrocatalytic Reduction of CO 2 over Pd Nanoparticles. *J. Am. Chem. Soc.* **2015,** *137*, 4288-4291.

(391) Huang, H.; Jia, H.; Liu, Z.; Gao, P.; Zhao, J.; Luo, Z.; Yang, J.; Zeng, J. Understanding of Strain Effects in the Electrochemical Reduction of CO 2 : Using Pd Nanostructures as an Ideal Platform. *Angew. Chem., Int. Ed.* **2017,** *56*, 3594-3598.

(392) Jiang, B.; Zhang, X.-G.; Jiang, K.; Wu, D.-Y.; Cai, W.-B. Boosting Formate Production in Electrocatalytic CO 2 Reduction over Wide Potential Window on Pd Surfaces. *J. Am. Chem. Soc.* **2018,** *140*, 2880-2889.

(393) Zhou, F.; Li, H.; Fournier, M.; MacFarlane, D. R. Electrocatalytic CO2Reduction to Formate at Low Overpotentials on Electrodeposited Pd Films: Stabilized Performance by Suppression of CO Formation. *ChemSusChem* **2017,** *10*, 1509-1516.

(394) Montoya, J. H.; Peterson, A. A.; Nørskov, J. K. Insights into C□C Coupling in CO 2 Electroreduction on Copper Electrodes. *ChemCatChem* **2013,** *5*, 737-742.

(395) Montoya, J. H.; Shi, C.; Chan, K.; Nørskov, J. K. Theoretical Insights into a CO Dimerization Mechanism in CO 2 Electroreduction. *J. Phys. Chem. Lett.* **2015,** *6*, 2032-2037.

(396) Manthiram, K.; Beberwyck, B. J.; Alivisatos, A. P. Enhanced Electrochemical Methanation of Carbon Dioxide with a Dispersible Nanoscale Copper Catalyst. *J. Am. Chem. Soc.* **2014,** *136*, 13319-13325.

(397) Li, Y.; Cui, F.; Ross, M. B.; Kim, D.; Sun, Y.; Yang, P. Structure-Sensitive CO 2 Electroreduction to Hydrocarbons on Ultrathin 5-fold Twinned Copper Nanowires. *Nano Lett.* **2017,** *17*, 1312-1317.

(398) Hori, Y.; Takahashi, I.; Koga, O.; Hoshi, N. Selective formation of C2 compounds from electrochemical reduction of CO2 at a series of copper single crystal electrodes. *J. Phys. Chem. B* **2002,** *106*, 15-17.

(399) Hori, Y.; Takahashi, I.; Koga, O.; Hoshi, N. Electrochemical reduction of carbon dioxide at various series of copper single crystal electrodes. *J. Mol. Catal. A: Chem.* **2003,** *199*, 39-47.

(400) Luo, W.; Nie, X.; Janik, M. J.; Asthagiri, A. Facet Dependence of CO2 Reduction Paths on Cu Electrodes. *ACS Catal.* **2016,** *6*, 219-229.

(401) Huang, Y.; Handoko, A. D.; Hirunsit, P.; Yeo, B. S. Electrochemical Reduction of CO2 Using Copper Single-Crystal Surfaces: Effects of CO* Coverage on the Selective Formation of Ethylene. *ACS Catal.* **2017,** *7*, 1749-1756.

(402) Pérez-Gallent, E.; Marcandalli, G.; Figueiredo, M. C.; Calle-Vallejo, F.; Koper, M. T. M. Structure- and Potential-Dependent Cation Effects on CO Reduction at Copper Single-Crystal Electrodes. *J. Am. Chem. Soc.* **2017,** *139*, 16412-16419.

(403) Roberts, F. S.; Kuhl, K. P.; Nilsson, A. High Selectivity for Ethylene from Carbon Dioxide Reduction over Copper Nanocube Electrocatalysts. *Angew. Chem., Int. Ed.* **2015,** *54*, 5179-5182.

(404) Kwon, Y.; Lum, Y.; Clark, E. L.; Ager, J. W.; Bell, A. T. CO 2 Electroreduction with Enhanced Ethylene and Ethanol Selectivity by Nanostructuring Polycrystalline Copper. *ChemElectroChem* **2016,** *3*, 1012-1019.

(405) Chen, C. S.; Handoko, A. D.; Wan, J. H.; Ma, L.; Ren, D.; Yeo, B. S. Stable and selective electrochemical reduction of carbon dioxide to ethylene on copper mesocrystals. *Catal. Sci. Technol.* **2015,** *5*, 161-168.

(406) Fields, M.; Hong, X.; Nørskov, J. K.; Chan, K. Role of Subsurface Oxygen on Cu Surfaces for CO2 Electrochemical Reduction. *J. Phys. Chem. C* **2018,** *122*, 16209-16215.

(407) Li, C. W.; Kanan, M. W. CO 2 Reduction at Low Overpotential on Cu Electrodes Resulting from the Reduction of Thick Cu 2 O Films. *J. Am. Chem. Soc.* **2012,** *134*, 7231-7234.

(408) Li, C. W.; Ciston, J.; Kanan, M. W. Electroreduction of carbon monoxide to liquid fuel on oxide-derived nanocrystalline copper. *Nature* **2014,** *508*, 504-507.

(409) Feng, X.; Jiang, K.; Fan, S.; Kanan, M. W. A Direct Grain-Boundary-Activity Correlation for CO Electroreduction on Cu Nanoparticles. *ACS Central Science* **2016,** *2*, 169-174.

(410) Mistry, H.; Varela, A. S.; Bonifacio, C. S.; Zegkinoglou, I.; Sinev, I.; Choi, Y.-W.; Kisslinger, K.; Stach, E. A.; Yang, J. C.; Strasser, P.et al. Highly selective plasma-activated copper catalysts for carbon dioxide reduction to ethylene. *Nat. Commun.* **2016,** *7*, 12123-12123.

(411) Handoko, A. D.; Ong, C. W.; Huang, Y.; Lee, Z. G.; Lin, L.; Panetti, G. B.; Yeo, B. S. Mechanistic Insights into the Selective Electroreduction of Carbon Dioxide to Ethylene on Cu 2 O-Derived Copper Catalysts. *J. Phys. Chem. C* **2016,** *120*, 20058-20067.

(412) Handoko, A. D.; Chan, K. W.; Yeo, B. S. –CH 3 Mediated Pathway for the Electroreduction of CO 2 to Ethane and Ethanol on Thick Oxide-Derived Copper Catalysts at Low Overpotentials. *ACS Energy Lett.* **2017,** *2*, 2103-2109.

(413)   Ren, D.; Deng, Y.; Handoko, A. D.; Chen, C. S.; Malkhandi, S.; Yeo, B. S. Selective Electrochemical Reduction of Carbon Dioxide to Ethylene and Ethanol on Copper(I) Oxide Catalysts. *ACS Catal.* **2015**, *5*, 2814-2821.

(414)   Chen, C. S.; Wan, J. H.; Yeo, B. S. Electrochemical Reduction of Carbon Dioxide to Ethane Using Nanostructured Cu 2 O-Derived Copper Catalyst and Palladium(II) Chloride. *J. Phys. Chem. C* **2015**, *119*, 26875-26882.

(415)   Lee, S.; Kim, D.; Lee, J. Electrocatalytic Production of C3-C4 Compounds by Conversion of CO 2 on a Chloride-Induced Bi-Phasic Cu 2 O-Cu Catalyst. *Angew. Chem., Int. Ed.* **2015**, *54*, 14701-14705.

(416)   Kim, D.; Lee, S.; Ocon, J. D.; Jeong, B.; Lee, J. K.; Lee, J. Insights into an autonomously formed oxygen-evacuated Cu 2 O electrode for the selective production of C 2 H 4 from CO 2. *Phys. Chem. Chem. Phys.* **2015**, *17*, 824-830.

(417)   Verdaguer-Casadevall, A.; Li, C. W.; Johansson, T. P.; Scott, S. B.; McKeown, J. T.; Kumar, M.; Stephens, I. E. L.; Kanan, M. W.; Chorkendorff, I. Probing the active surface sites for CO reduction on oxide-derived copper electrocatalysts. *J. Am. Chem. Soc.* **2015**, *137*, 9808-9811.

(418)   Cavalca, F.; Ferragut, R.; Aghion, S.; Eilert, A.; Diaz-Morales, O.; Liu, C.; Koh, A. L.; Hansen, T. W.; Pettersson, L. G. M.; Nilsson, A. Nature and Distribution of Stable Subsurface Oxygen in Copper Electrodes During Electrochemical CO 2 Reduction. *J. Phys. Chem. C* **2017**, *121*, 25003-25009.

(419)   Eilert, A.; Cavalca, F.; Roberts, F. S.; Osterwalder, J.; Liu, C.; Favaro, M.; Crumlin, E. J.; Ogasawara, H.; Friebel, D.; Pettersson, L. G. M.et al. Subsurface Oxygen in Oxide-Derived Copper Electrocatalysts for Carbon Dioxide Reduction. *J. Phys. Chem. Lett.* **2017**, *8*, 285-290.

(420)   Liu, C.; Lourenço, M. P.; Hedström, S.; Cavalca, F.; Diaz-Morales, O.; Duarte, H. A.; Nilsson, A.; Pettersson, L. G. M. Stability and effects of subsurface oxygen in oxide-derived Cu catalyst for CO2reduction. *J. Phys. Chem. C* **2017**, *121*, 25010-25017.

(421)   Favaro, M.; Xiao, H.; Cheng, T.; Goddard, W. A.; Yano, J.; Crumlin, E. J. Subsurface oxide plays a critical role in CO 2 activation by Cu(111) surfaces to form chemisorbed CO2 , the first step in reduction of CO2. *Proc. Natl. Acad. Sci. U.S.A.* **2017**, *114*, 6706-6711.

(422)   Xiao, H.; Goddard, W. A.; Cheng, T.; Liu, Y. Cu metal embedded in oxidized matrix catalyst to promote CO 2 activation and CO dimerization for electrochemical reduction of CO 2. *Proc. Natl. Acad. Sci. U.S.A.* **2017**, *114*, 6685-6688.

(423)   De Luna, P.; Quintero-Bermudez, R.; Dinh, C.-T.; Ross, M. B.; Bushuyev, O. S.; Todorović, P.; Regier, T.; Kelley, S. O.; Yang, P.; Sargent, E. H. Catalyst electro-redeposition controls morphology and oxidation state for selective carbon dioxide reduction. *Nat. Catal.* **2018**, *1*, 103-110.

(424)   Liang, Z.-Q.; Zhuang, T.-T.; Seifitokaldani, A.; Li, J.; Huang, C.-W.; Tan, C.-S.; Li, Y.; De Luna, P.; Dinh, C. T.; Hu, Y.et al. Copper-on-nitride enhances the stable electrosynthesis of multi-carbon products from CO2. *Nat. Commun.* **2018**, *9*, 3828.

(425)   Eilert, A.; Roberts, F. S.; Friebel, D.; Nilsson, A. Formation of Copper Catalysts for CO 2 Reduction with High Ethylene/Methane Product Ratio Investigated with In Situ X-ray Absorption Spectroscopy. *J. Phys. Chem. Lett.* **2016**, *7*, 1466-1470.

(426)   Lum, Y.; Yue, B.; Lobaccaro, P.; Bell, A. T.; Ager, J. W. Optimizing C-C Coupling on Oxide-Derived Copper Catalysts for Electrochemical CO2Reduction. *J. Phys. Chem. C* **2017**, *121*, 14191-14203.

(427)   Dinh, C.-T.; Burdyny, T.; Kibria, M. G.; Seifitokaldani, A.; Gabardo, C. M.; García de Arquer, F. P.; Kiani, A.; Edwards, J. P.; De Luna, P.; Bushuyev, O. S.et al. CO₂ electroreduction to ethylene via hydroxide-mediated copper catalysis at an abrupt interface. *Science* **2018**, *360*, 783-787.

(428)   Lum, Y.; Ager, J. W. Stability of Residual Oxides in Oxide-Derived Copper Catalysts for Electrochemical CO2Reduction Investigated with18O Labeling. *Angew. Chem., Int. Ed.* **2018**, *57*, 551-554.

(429)   Loiudice, A.; Lobaccaro, P.; Kamali, E. A.; Thao, T.; Huang, B. H.; Ager, J. W.; Buonsanti, R. Tailoring Copper Nanocrystals towards C 2 Products in Electrochemical CO 2 Reduction. *Angew. Chem., Int. Ed.* **2016**, *55*, 5789-5792.

(430)   Dutta, A.; Rahaman, M.; Luedi, N. C.; Mohos, M.; Broekmann, P. Morphology Matters: Tuning the Product Distribution of CO 2 Electroreduction on Oxide-Derived Cu Foam Catalysts. *ACS Catal.* **2016**, *6*, 3804-3814.

(431)   Rahaman, M.; Dutta, A.; Zanetti, A.; Broekmann, P. Electrochemical Reduction of CO2into Multicarbon Alcohols on Activated Cu Mesh Catalysts: An Identical Location (IL) Study. *ACS Catal.* **2017**, *7*, 7946-7956.

(432)   Dutta, A.; Rahaman, M.; Mohos, M.; Zanetti, A.; Broekmann, P. Electrochemical CO2Conversion Using Skeleton (Sponge) Type of Cu Catalysts. *ACS Catal.* **2017**, *7*, 5431-5437.

(433) Reller, C.; Krause, R.; Volkova, E.; Schmid, B.; Neubauer, S.; Rucki, A.; Schuster, M.; Schmid, G. Selective Electroreduction of CO 2 toward Ethylene on Nano Dendritic Copper Catalysts at High Current Density. *Adv. Energy Mater.* **2017**, *7*, 1602114.

(434) Gunathunge, C. M.; Li, X.; Li, J.; Hicks, R. P.; Ovalle, V. J.; Waegele, M. M. Spectroscopic Observation of Reversible Surface Reconstruction of Copper Electrodes under CO 2 Reduction. *J. Phys. Chem. C* **2017**, *121*, 12337-12344.

(435) Kim, Y.-G.; Javier, A.; Baricuatro, J. H.; Torelli, D.; Cummins, K. D.; Tsang, C. F.; Hemminger, J. C.; Soriaga, M. P. Surface reconstruction of pure-Cu single-crystal electrodes under CO-reduction potentials in alkaline solutions: A study by seriatim ECSTM-DEMS. *J. Electroanal. Chem.* **2016**, *780*, 290-295.

(436) Kim, D.; Kley, C. S.; Li, Y.; Yang, P. Copper nanoparticle ensembles for selective electroreduction of CO_2 to C_2–C_3 products. *Proc. Natl. Acad. Sci. U.S.A.* **2017**, *114*, 10560-10565.

(437) Hahn, C.; Hatsukade, T.; Kim, Y.-G.; Vailionis, A.; Baricuatro, J. H.; Higgins, D. C.; Nitopi, S. A.; Soriaga, M. P.; Jaramillo, T. F. Engineering Cu surfaces for the electrocatalytic conversion of CO 2 : Controlling selectivity toward oxygenates and hydrocarbons. *Proc. Natl. Acad. Sci. U.S.A.* **2017**, *114*, 5918-5923.

(438) Kim, Y.-G.; Javier, A.; Baricuatro, J. H.; Soriaga, M. P. Regulating the Product Distribution of CO Reduction by the Atomic-Level Structural Modification of the Cu Electrode Surface. *Electrocatalysis* **2016**, *7*, 391-399.

(439) Ren, D.; Wong, N. T.; Handoko, A. D.; Huang, Y.; Yeo, B. S. Mechanistic Insights into the Enhanced Activity and Stability of Agglomerated Cu Nanocrystals for the Electrochemical Reduction of Carbon Dioxide to n -Propanol. *J. Phys. Chem. Lett.* **2016**, *7*, 20-24.

(440) Song, Y.; Peng, R.; Hensley, D. K.; Bonnesen, P. V.; Liang, L.; Wu, Z.; Meyer, H. M.; Chi, M.; Ma, C.; Sumpter, B. G.et al. High-Selectivity Electrochemical Conversion of CO 2 to Ethanol using a Copper Nanoparticle/N-Doped Graphene Electrode. *ChemistrySelect* **2016**, *1*, 6055-6061.

(441) Deng, Y.; Huang, Y.; Ren, D.; Handoko, A. D.; Seh, Z. W.; Hirunsit, P.; Yeo, B. S. On the Role of Sulfur for the Selective Electrochemical Reduction of CO2 to Formate on CuSx Catalysts. *ACS Appl. Mater. Interfaces* **2018**, *10*, 28572-28581.

(442) Zhuang, T.-T.; Liang, Z.-Q.; Seifitokaldani, A.; Li, Y.; De Luna, P.; Burdyny, T.; Che, F.; Meng, F.; Min, Y.; Quintero-Bermudez, R.et al. Steering post-C–C coupling selectivity enables high efficiency electroreduction of carbon dioxide to multi-carbon alcohols. *Nat. Catal.* **2018,** *1*, 421-428.

(443) Yang, K. D.; Ko, W. R.; Lee, J. H.; Kim, S. J.; Lee, H.; Lee, M. H.; Nam, K. T. Morphology-Directed Selective Production of Ethylene or Ethane from CO 2 on a Cu Mesopore Electrode. *Angew. Chem., Int. Ed.* **2017**, *56*, 796-800.

(444) Summers, D. P.; Leach, S.; Frese, K. W. The electrochemical reduction of aqueous carbon dioxide to methanol at molybdenum electrodes with low overpotentials. *J. Electroanal. Chem. Interf. Electrochem.* **1986**, *205*, 219-232.

(445) Won, D. H.; Shin, H.; Koh, J.; Chung, J.; Lee, H. S.; Kim, H.; Woo, S. I. Highly Efficient, Selective, and Stable CO2Electroreduction on a Hexagonal Zn Catalyst. *Angew. Chem., Int. Ed.* **2016,** *55*, 9297-9300.

(446) Asadi, M.; Kumar, B.; Behranginia, A.; Rosen, B. A.; Baskin, A.; Repnin, N.; Pisasale, D.; Phillips, P.; Zhu, W.; Haasch, R.et al. Robust carbon dioxide reduction on molybdenum disulphide edges. *Nat. Commun.* **2014,** *5*, 1-8.

(447) Asadi, M.; Kim, K.; Liu, C.; Addepalli, A. V.; Abbasi, P.; Yasaei, P.; Phillips, P.; Behranginia, A.; Cerrato, J. M.; Haasch, R.et al. Nanostructured transition metal dichalcogenide electrocatalysts for CO 2 reduction in ionic liquid. *Science* **2016**, *353*, 467-470.

(448) Abbasi, P.; Asadi, M.; Liu, C.; Sharifi-Asl, S.; Sayahpour, B.; Behranginia, A.; Zapol, P.; Shahbazian-Yassar, R.; Curtiss, L. A.; Salehi-Khojin, A. Tailoring the Edge Structure of Molybdenum Disulfide toward Electrocatalytic Reduction of Carbon Dioxide. *ACS Nano* **2017,** *11*, 453-460.

(449) Gao, S.; Lin, Y.; Jiao, X.; Sun, Y.; Luo, Q.; Zhang, W.; Li, D.; Yang, J.; Xie, Y. Partially oxidized atomic cobalt layers for carbon dioxide electroreduction to liquid fuel. *Nature* **2016**, *529*, 68-71.

(450) Gao, S.; Jiao, X.; Sun, Z.; Zhang, W.; Sun, Y.; Wang, C.; Hu, Q.; Zu, X.; Yang, F.; Yang, S.et al. Ultrathin Co 3 O 4 Layers Realizing Optimized CO 2 Electroreduction to Formate. *Angew. Chem., Int. Ed.* **2016,** *55*, 698-702.

(451) Gao, S.; Sun, Z.; Liu, W.; Jiao, X.; Zu, X.; Hu, Q.; Sun, Y.; Yao, T.; Zhang, W.; Wei, S.et al. Atomic layer confined vacancies for atomic-level insights into carbon dioxide electroreduction. *Nat. Commun.* **2017**, *8*, 14503-14503.

(452) He, J.; Johnson, N. J.; Huang, A.; Berlinguette, C. Electrocatalytic Alloys for CO2 Reduction. *ChemSusChem* **2017**, *11*, 48-57.

(453) Kim, D.; Resasco, J.; Yu, Y.; Asiri, A. M.; Yang, P. Synergistic geometric and electronic effects for electrochemical reduction of carbon dioxide using gold–copper bimetallic nanoparticles. *Nat. Commun.* **2014,** *5,* 4948.

(454) Ross, M. B.; Dinh, C. T.; Li, Y.; Kim, D.; De Luna, P.; Sargent, E. H.; Yang, P. Tunable Cu Enrichment Enables Designer Syngas Electrosynthesis from CO2. *J. Am. Chem. Soc.* **2017,** *139,* 9359-9363.

(455) Ma, M.; Hansen, H. A.; Valenti, M.; Wang, Z.; Cao, A.; Dong, M.; Smith, W. A. Electrochemical reduction of CO2 on compositionally variant Au-Pt bimetallic thin films. *Nano Energy* **2017,** *42,* 51-57.

(456) Chen, D.; Yao, Q.; Cui, P.; Liu, H.; Xie, J.; Yang, J. Tailoring the Selectivity of Bimetallic Copper–Palladium Nanoalloys for Electrocatalytic Reduction of CO 2 to CO. *ACS Appl. Energy Mater.* **2018,** *1,* 883-890.

(457) Kim, D.; Xie, C.; Becknell, N.; Yu, Y.; Karamad, M.; Chan, K.; Crumlin, E. J.; Nørskov, J. K.; Yang, P. Electrochemical Activation of CO2 through Atomic Ordering Transformations of AuCu Nanoparticles. *J. Am. Chem. Soc.* **2017,** *139,* 8329-8336.

(458) Ma, S.; Sadakiyo, M.; Heima, M.; Luo, R.; Haasch, R. T.; Gold, J. I.; Yamauchi, M.; Kenis, P. J. A. Electroreduction of Carbon Dioxide to Hydrocarbons Using Bimetallic Cu–Pd Catalysts with Different Mixing Patterns. *J. Am. Chem. Soc.* **2017,** *139,* 47-50.

(459) Larrazábal, G. O.; Martín, A. J.; Mitchell, S.; Hauert, R.; Pérez-Ramírez, J. Enhanced Reduction of CO 2 to CO over Cu–In Electrocatalysts: Catalyst Evolution Is the Key. *ACS Catal.* **2016,** *6,* 6265-6274.

(460) Larrazábal, G. O.; Shinagawa, T.; Martín, A. J.; Pérez-Ramírez, J. Microfabricated electrodes unravel the role of interfaces in multicomponent copper-based CO2 reduction catalysts. *Nat. Commun.* **2018,** *9,* 1477.

(461) Bai, X.; Chen, W.; Zhao, C.; Li, S.; Song, Y.; Ge, R.; Wei, W.; Sun, Y. Exclusive Formation of Formic Acid from CO2 Electroreduction by a Tunable Pd-Sn Alloy. *Angew. Chem., Int. Ed.* **2017,** *56,* 12219-12223.

(462) Luc, W.; Collins, C.; Wang, S.; Xin, H.; He, K.; Kang, Y.; Jiao, F. Ag–Sn Bimetallic Catalyst with a Core–Shell Structure for CO 2 Reduction. *J. Am. Chem. Soc.* **2017,** *139,* 1885-1893.

(463) Li, Q.; Fu, J.; Zhu, W.; Chen, Z.; Shen, B.; Wu, L.; Xi, Z.; Wang, T.; Lu, G.; Zhu, J.-j.et al. Tuning Sn-Catalysis for Electrochemical Reduction of CO 2 to CO via the Core/Shell Cu/SnO 2 Structure. *J. Am. Chem. Soc.* **2017,** *139,* 4290-4293.

(464) Wen, G.; Lee, D. U.; Ren, B.; Hassan, F. M.; Jiang, G.; Cano, Z. P.; Gostick, J.; Croiset, E.; Bai, Z.; Yang, L.et al. Orbital Interactions in Bi-Sn Bimetallic Electrocatalysts for Highly Selective Electrochemical CO2 Reduction toward Formate Production. *Adv. Energy Mater.* **2018,** *8,* 1802427.

(465) Lee, S.; Park, G.; Lee, J. Importance of Ag-Cu Biphasic Boundaries for Selective Electrochemical Reduction of CO2 to Ethanol. *ACS Catal.* **2017,** *7,* 8594-8604.

(466) Clark, E. L.; Hahn, C.; Jaramillo, T. F.; Bell, A. T. Electrochemical CO2 Reduction over Compressively Strained CuAg Surface Alloys with Enhanced Multi-Carbon Oxygenate Selectivity. *J. Am. Chem. Soc.* **2017,** *139,* 15848-15857.

(467) Lum, Y.; Ager, J. W. Sequential catalysis controls selectivity in electrochemical CO 2 reduction on Cu. *Energy Environ. Sci.* **2018,** *11,* 2935-2944.

(468) Theaker, N.; Strain, J. M.; Kumar, B.; Brian, J. P.; Kumari, S.; Spurgeon, J. M. Heterogeneously catalyzed two-step cascade electrochemical reduction of CO2 to ethanol. *Electrochim. Acta* **2018,** *274,* 1-8.

(469) Wang, Y.; Wang, D.; Dares, C. J.; Marquard, S. L.; Sheridan, M. V.; Meyer, T. J. CO 2 reduction to acetate in mixtures of ultrasmall (Cu) n ,(Ag) m bimetallic nanoparticles. *Proc. Natl. Acad. Sci. U.S.A.* **2018,** *115,* 278-283.

(470) Torelli, D. A.; Francis, S. A.; Crompton, J. C.; Javier, A.; Thompson, J. R.; Brunschwig, B. S.; Soriaga, M. P.; Lewis, N. S. Nickel–Gallium-Catalyzed Electrochemical Reduction of CO 2 to Highly Reduced Products at Low Overpotentials. *ACS Catal.* **2016,** *6,* 2100-2104.

(471) Kerfeld, C. A.; Aussignargues, C.; Zarzycki, J.; Cai, F.; Sutter, M. Bacterial microcompartments. *Nat. Rev. Microbiol.* **2018,** *16,* 277.

(472) Turmo, A.; Gonzalez-Esquer, C. R.; Kerfeld, C. A. Carboxysomes: metabolic modules for CO2 fixation. *FEMS Microbiol. Lett.* **2017,** *364,* fnx176.

(473) Cannon, G. C.; Heinhorst, S.; Kerfeld, C. A. Carboxysomal carbonic anhydrases: Structure and role in microbial CO2 fixation. *Biochimica et Biophysica Acta (BBA) - Proteins and Proteomics* **2010,** *1804,* 382-392.

(474) Rae, B. D.; Long, B. M.; Badger, M. R.; Price, G. D. Functions, Compositions, and Evolution of the Two Types of Carboxysomes: Polyhedral Microcompartments That Facilitate CO<sub>2</sub> Fixation in Cyanobacteria and Some Proteobacteria. *Microbiol. Mol. Biol. Rev.* **2013,** *77,* 357-359.

(475)   Erbilgin, O.; McDonald, K. L.; Kerfeld, C. A. Characterization of a Planctomycetal Organelle: a Novel Bacterial Microcompartment for the Aerobic Degradation of Plant Saccharides. *Appl. Environ. Microbiol.* **2014,** *80,* 2193.

(476)   Petit, E.; LaTouf, W. G.; Coppi, M. V.; Warnick, T. A.; Currie, D.; Romashko, I.; Deshpande, S.; Haas, K.; Alvelo-Maurosa, J. G.; Wardman, C.et al. Involvement of a Bacterial Microcompartment in the Metabolism of Fucose and Rhamnose by Clostridium phytofermentans. *PLoS ONE* **2013,** *8,* e54337.

(477)   Climent, M. J.; Corma, A.; Iborra, S. Heterogeneous Catalysts for the One-Pot Synthesis of Chemicals and Fine Chemicals. *Chem. Rev.* **2011,** *111,* 1072-1133.

(478)   José Climent, M.; Corma, A.; Iborra, S. Homogeneous and heterogeneous catalysts for multicomponent reactions. *RSC Adv.* **2012,** *2,* 16-58.

(479)   Robert, C.; Thomas, C. M. Tandem catalysis: a new approach to polymers. *Chem. Soc. Rev.* **2013,** *42,* 9392-9402.

(480)   Lohr, T. L.; Marks, T. J. Orthogonal tandem catalysis. *Nat. Chem.* **2015,** *7,* 477.

(481)   Wasilke, J.-C.; Obrey, S. J.; Baker, R. T.; Bazan, G. C. Concurrent Tandem Catalysis. *Chem. Rev.* **2005,** *105,* 1001-1020.

(482)   Green, I. X.; Tang, W.; Neurock, M.; Yates, J. T. Spectroscopic Observation of Dual Catalytic Sites During Oxidation of CO on a Au/TiO2 Catalyst. *Science* **2011,** *333,* 736.

(483)   Schauermann, S.; Nilius, N.; Shaikhutdinov, S.; Freund, H.-J. Nanoparticles for Heterogeneous Catalysis: New Mechanistic Insights. *Acc. Chem. Res.* **2013,** *46,* 1673-1681.

(484)   Yu, W.; Porosoff, M. D.; Chen, J. G. Review of Pt-Based Bimetallic Catalysis: From Model Surfaces to Supported Catalysts. *Chem. Rev.* **2012,** *112,* 5780-5817.

(485)   Bratlie, K. M.; Lee, H.; Komvopoulos, K.; Yang, P.; Somorjai, G. A. Platinum Nanoparticle Shape Effects on Benzene Hydrogenation Selectivity. *Nano Lett.* **2007,** *7,* 3097-3101.

(486)   Li, Y.; Wang, T.; Wu, C.; Lv, Y.; Tsubaki, N. Gasoline-Range Hydrocarbon Synthesis over Cobalt-Based Fischer–Tropsch Catalysts Supported on SiO2/HZSM-5. *Energy Fuels* **2008,** *22,* 1897-1901.

(487)   Zhou, W.; Cheng, K.; Kang, J.; Zhou, C.; Subramanian, V.; Zhang, Q.; Wang, Y. New horizon in C1 chemistry: breaking the selectivity limitation in transformation of syngas and hydrogenation of CO2 into hydrocarbon chemicals and fuels. *Chem. Soc. Rev.* **2019,** *48,* 3193-3228.

(488)   Yamada, Y.; Tsung, C.-K.; Huang, W.; Huo, Z.; Habas, S. E.; Soejima, T.; Aliaga, C. E.; Somorjai, G. A.; Yang, P. Nanocrystal bilayer for tandem catalysis. *Nat. Chem.* **2011,** *3,* 372.

(489)   Jiao, F.; Li, J.; Pan, X.; Xiao, J.; Li, H.; Ma, H.; Wei, M.; Pan, Y.; Zhou, Z.; Li, M.et al. Selective conversion of syngas to light olefins. *Science* **2016,** *351,* 1065-1068.

(490)   Tao, F.; Grass, M. E.; Zhang, Y.; Butcher, D. R.; Renzas, J. R.; Liu, Z.; Chung, J. Y.; Mun, B. S.; Salmeron, M.; Somorjai, G. A. Reaction-Driven Restructuring of Rh-Pd and Pt-Pd Core-Shell Nanoparticles. *Science* **2008,** *322,* 932-934.

(491)   Henzie, J.; Grünwald, M.; Widmer-Cooper, A.; Geissler, P. L.; Yang, P. Self-assembly of uniform polyhedral silver nanocrystals into densest packings and exotic superlattices. *Nat. Mater.* **2011,** *11,* 131-137.

(492)   Matsumoto, R.; Takasaki, M.; Tsukiyama, K.; Oaki, Y.; Imai, H. Layer-by-Layer Manipulation of Heterogeneous Rectangular Nanoblocks: Brick Work for Multilayered Structures with Specific Heterojunction. *Inorg. Chem.* **2018,** *57,* 11655-11661.

(493)   Zhang, B.; Qin, Y. Interface Tailoring of Heterogeneous Catalysts by Atomic Layer Deposition. *ACS Catal.* **2018,** *8,* 10064-10081.

(494)   Resasco, J.; Dasgupta, N. P.; Rosell, J. R.; Guo, J.; Yang, P. Uniform Doping of Metal Oxide Nanowires Using Solid State Diffusion. *J. Am. Chem. Soc.* **2014,** *136,* 10521-10526.

(495)   Dasgupta, N. P.; Liu, C.; Andrews, S.; Prinz, F. B.; Yang, P. Atomic Layer Deposition of Platinum Catalysts on Nanowire Surfaces for Photoelectrochemical Water Reduction. *J. Am. Chem. Soc.* **2013,** *135,* 12932-12935.

(496)   O'Neill, B. J.; Jackson, D. H. K.; Lee, J.; Canlas, C.; Stair, P. C.; Marshall, C. L.; Elam, J. W.; Kuech, T. F.; Dumesic, J. A.; Huber, G. W. Catalyst Design with Atomic Layer Deposition. *ACS Catal.* **2015,** *5,* 1804-1825.

(497)   Lei, Y.; Lee, S.; Low, K.-B.; Marshall, C. L.; Elam, J. W. Combining Electronic and Geometric Effects of ZnO-Promoted Pt Nanocatalysts for Aqueous Phase Reforming of 1-Propanol. *ACS Catal.* **2016,** *6,* 3457-3460.

(498)   Alba-Rubio, A. C.; O'Neill, B. J.; Shi, F.; Akatay, C.; Canlas, C.; Li, T.; Winans, R.; Elam, J. W.; Stach, E. A.; Voyles, P. M.et al. Pore Structure and Bifunctional Catalyst Activity of Overlayers Applied by Atomic Layer Deposition on Copper Nanoparticles. *ACS Catal.* **2014,** *4,* 1554-1557.

(499) Yi, H.; Xia, Y.; Yan, H.; Lu, J. Coating Pd/Al2O3 catalysts with FeOx enhances both activity and selectivity in 1,3-butadiene hydrogenation. *Chin. J. Catal.* **2017**, *38*, 1581-1587.

(500) Hu, Q.; Wang, S.; Gao, Z.; Li, Y.; Zhang, Q.; Xiang, Q.; Qin, Y. The precise decoration of Pt nanoparticles with Fe oxide by atomic layer deposition for the selective hydrogenation of cinnamaldehyde. *Appl. Catal., B* **2017**, *218*, 591-599.

(501) Ge, H.; Zhang, B.; Gu, X.; Liang, H.; Yang, H.; Gao, Z.; Wang, J.; Qin, Y. A Tandem Catalyst with Multiple Metal Oxide Interfaces Produced by Atomic Layer Deposition. *Angew. Chem., Int. Ed.* **2016**, *55*, 7081-7085.

(502) Zhang, J.; Yu, Z.; Gao, Z.; Ge, H.; Zhao, S.; Chen, C.; Chen, S.; Tong, X.; Wang, M.; Zheng, Z.et al. Porous TiO2 Nanotubes with Spatially Separated Platinum and CoOx Cocatalysts Produced by Atomic Layer Deposition for Photocatalytic Hydrogen Production. *Angew. Chem., Int. Ed.* **2016**, *56*, 816-820.

(503) Tan, C.; Chen, J.; Wu, X.-J.; Zhang, H. Epitaxial growth of hybrid nanostructures. *Nat. Rev. Mater.* **2018**, *3*, 17089.

(504) Liu, X.; Iocozzia, J.; Wang, Y.; Cui, X.; Chen, Y.; Zhao, S.; Li, Z.; Lin, Z. Noble metal–metal oxide nanohybrids with tailored nanostructures for efficient solar energy conversion, photocatalysis and environmental remediation. *Energy Environ. Sci.* **2017**, *10*, 402-434.

(505) Damato, T. C.; de Oliveira, C. C. S.; Ando, R. A.; Camargo, P. H. C. A Facile Approach to TiO2 Colloidal Spheres Decorated with Au Nanoparticles Displaying Well-Defined Sizes and Uniform Dispersion. *Langmuir* **2013**, *29*, 1642-1649.

(506) Wang, J.; Ando, R. A.; Camargo, P. H. C. Controlling the Selectivity of the Surface Plasmon Resonance Mediated Oxidation of p-Aminothiophenol on Au Nanoparticles by Charge Transfer from UV-excited TiO2. *Angew. Chem., Int. Ed.* **2015**, *54*, 6909-6912.

(507) Enterkin, J. A.; Poeppelmeier, K. R.; Marks, L. D. Oriented Catalytic Platinum Nanoparticles on High Surface Area Strontium Titanate Nanocuboids. *Nano Lett.* **2011**, *11*, 993-997.

(508) Wang, L.; Ge, J.; Wang, A.; Deng, M.; Wang, X.; Bai, S.; Li, R.; Jiang, J.; Zhang, Q.; Luo, Y.et al. Designing p-Type Semiconductor–Metal Hybrid Structures for Improved Photocatalysis. *Angew. Chem., Int. Ed.* **2014**, *53*, 5107-5111.

(509) Gao, Y.; Wang, W.; Chang, S.; Huang, W. Morphology Effect of CeO2 Support in the Preparation, Metal–Support Interaction, and Catalytic Performance of Pt/CeO2 Catalysts. *ChemCatChem* **2013**, *5*, 3610-3620.

(510) Lin, F.; Hoang, D. T.; Tsung, C.-K.; Huang, W.; Lo, S. H.-Y.; Wood, J. B.; Wang, H.; Tang, J.; Yang, P. Catalytic properties of Pt cluster-decorated CeO2 nanostructures. *Nano Res.* **2011**, *4*, 61-71.

(511) Yu, H.; Chen, M.; Rice, P. M.; Wang, S. X.; White, R. L.; Sun, S. Dumbbell-like Bifunctional Au−Fe3O4 Nanoparticles. *Nano Lett.* **2005**, *5*, 379-382.

(512) Wu, B.; Zhang, H.; Chen, C.; Lin, S.; Zheng, N. Interfacial activation of catalytically inert Au (6.7 nm)-Fe3O4 dumbbell nanoparticles for CO oxidation. *Nano Res.* **2009**, *2*, 975-983.

(513) Wang, C.; Yin, H.; Dai, S.; Sun, S. A General Approach to Noble Metal−Metal Oxide Dumbbell Nanoparticles and Their Catalytic Application for CO Oxidation. *Chem. Mater.* **2010**, *22*, 3277-3282.

(514) Seh, Z. W.; Liu, S.; Low, M.; Zhang, S.-Y.; Liu, Z.; Mlayah, A.; Han, M.-Y. Janus Au-TiO2 Photocatalysts with Strong Localization of Plasmonic Near-Fields for Efficient Visible-Light Hydrogen Generation. *Adv. Mater.* **2012**, *24*, 2310-2314.

(515) Gu, H.; Yang, Z.; Gao, J.; Chang, C. K.; Xu, B. Heterodimers of Nanoparticles: Formation at a Liquid−Liquid Interface and Particle-Specific Surface Modification by Functional Molecules. *J. Am. Chem. Soc.* **2005**, *127*, 34-35.

(516) Herring, N. P.; AbouZeid, K.; Mohamed, M. B.; Pinsk, J.; El-Shall, M. S. Formation Mechanisms of Gold–Zinc Oxide Hexagonal Nanopyramids by Heterogeneous Nucleation using Microwave Synthesis. *Langmuir* **2011**, *27*, 15146-15154.

(517) Li, P.; Wei, Z.; Wu, T.; Peng, Q.; Li, Y. Au−ZnO Hybrid Nanopyramids and Their Photocatalytic Properties. *J. Am. Chem. Soc.* **2011**, *133*, 5660-5663.

(518) Tahir, M. N.; Natalio, F.; Cambaz, M. A.; Panthöfer, M.; Branscheid, R.; Kolb, U.; Tremel, W. Controlled synthesis of linear and branched Au@ZnO hybrid nanocrystals and their photocatalytic properties. *Nanoscale* **2013**, *5*, 9944-9949.

(519) Chen, Y.; Zeng, D.; Zhang, K.; Lu, A.; Wang, L.; Peng, D.-L. Au–ZnO hybrid nanoflowers, nanomultipods and nanopyramids: one-pot reaction synthesis and photocatalytic properties. *Nanoscale* **2014**, *6*, 874-881.

(520) Yao, K. X.; Liu, X.; Zhao, L.; Zeng, H. C.; Han, Y. Site-specific growth of Au particles on ZnO nanopyramids under ultraviolet illumination. *Nanoscale* **2011**, *3*, 4195-4200.

121

(521) Bradley, M. J.; Biacchi, A. J.; Schaak, R. E. Chemical Transformation of Pt–Fe3O4 Colloidal Hybrid Nanoparticles into PtPb–Fe3O4 and Pt3Sn–Fe3O4 Heterodimers and (PtPb–Fe3O4)n Nanoflowers. *Chem. Mater.* **2013,** *25*, 1886-1892.

(522) Wang, C.; Daimon, H.; Sun, S. Dumbbell-like Pt−Fe3O4 Nanoparticles and Their Enhanced Catalysis for Oxygen Reduction Reaction. *Nano Lett.* **2009,** *9*, 1493-1496.

(523) Seh, Z. W.; Liu, S.; Zhang, S.-Y.; Bharathi, M. S.; Ramanarayan, H.; Low, M.; Shah, K. W.; Zhang, Y.-W.; Han, M.-Y. Anisotropic Growth of Titania onto Various Gold Nanostructures: Synthesis, Theoretical Understanding, and Optimization for Catalysis. **2011,** *50*, 10140-10143.

(524) Casavola, M.; Grillo, V.; Carlino, E.; Giannini, C.; Gozzo, F.; Fernandez Pinel, E.; Garcia, M. A.; Manna, L.; Cingolani, R.; Cozzoli, P. D. Topologically Controlled Growth of Magnetic-Metal-Functionalized Semiconductor Oxide Nanorods. *Nano Lett.* **2007,** *7*, 1386-1395.

(525) George, C.; Genovese, A.; Casu, A.; Prato, M.; Povia, M.; Manna, L.; Montanari, T. CO Oxidation on Colloidal Au0.80Pd0.20–FexOy Dumbbell Nanocrystals. *Nano Lett.* **2013,** *13*, 752-757.

(526) Rai, P.; Majhi, S. M.; Yu, Y.-T.; Lee, J.-H. Noble metal@metal oxide semiconductor core@shell nano-architectures as a new platform for gas sensor applications. *RSC Adv.* **2015,** *5*, 76229-76248.

(527) Li, J.-F.; Zhang, Y.-J.; Ding, S.-Y.; Panneerselvam, R.; Tian, Z.-Q. Core–Shell Nanoparticle-Enhanced Raman Spectroscopy. *Chem. Rev.* **2017,** *117*, 5002-5069.

(528) Joo, S. H.; Park, J. Y.; Tsung, C.-K.; Yamada, Y.; Yang, P.; Somorjai, G. A. Thermally stable Pt/mesoporous silica core–shell nanocatalysts for high-temperature reactions. *Nat. Mater.* **2008,** *8*, 126.

(529) Ma, W.-F.; Zhang, Y.; Li, L.-L.; You, L.-J.; Zhang, P.; Zhang, Y.-T.; Li, J.-M.; Yu, M.; Guo, J.; Lu, H.-J.et al. Tailor-Made Magnetic Fe3O4@mTiO2 Microspheres with a Tunable Mesoporous Anatase Shell for Highly Selective and Effective Enrichment of Phosphopeptides. *ACS Nano* **2012,** *6*, 3179-3188.

(530) Kim, J.; Kim, H. S.; Lee, N.; Kim, T.; Kim, H.; Yu, T.; Song, I. C.; Moon, W. K.; Hyeon, T. Multifunctional Uniform Nanoparticles Composed of a Magnetite Nanocrystal Core and a Mesoporous Silica Shell for Magnetic Resonance and Fluorescence Imaging and for Drug Delivery. *Angew. Chem., Int. Ed.* **2008,** *120*, 8566-8569.

(531) Goel, S.; Zones, S. I.; Iglesia, E. Encapsulation of Metal Clusters within MFI via Interzeolite Transformations and Direct Hydrothermal Syntheses and Catalytic Consequences of Their Confinement. *J. Am. Chem. Soc.* **2014,** *136*, 15280-15290.

(532) Cho, H. J.; Kim, D.; Li, J.; Su, D.; Xu, B. Zeolite-Encapsulated Pt Nanoparticles for Tandem Catalysis. *J. Am. Chem. Soc.* **2018,** *140*, 13514-13520.

(533) Ryoo, R.; Cho, S. J.; Pak, C.; Kim, J. G.; Ihm, S. K.; Lee, J. Y. Application of the xenon-adsorption method for the study of metal cluster formation and growth on Y zeolite. *J. Am. Chem. Soc.* **1992,** *114*, 76-82.

(534) Fierro-Gonzalez, J. C.; Hao, Y.; Gates, B. C. Gold Nanoclusters Entrapped in the α-Cages of Y Zeolites: Structural Characterization by X-ray Absorption Spectroscopy. *J. Phys. Chem. C* **2007,** *111*, 6645-6651.

(535) Uzun, A.; Gates, B. C. Real-Time Characterization of Formation and Breakup of Iridium Clusters in Highly Dealuminated Zeolite Y. *Angew. Chem., Int. Ed.* **2008,** *47*, 9245-9248.

(536) Liu, L.; Díaz, U.; Arenal, R.; Agostini, G.; Concepción, P.; Corma, A. Generation of subnanometric platinum with high stability during transformation of a 2D zeolite into 3D. *Nat. Mater.* **2016,** *16*, 132.

(537) Choi, M.; Wu, Z.; Iglesia, E. Mercaptosilane-Assisted Synthesis of Metal Clusters within Zeolites and Catalytic Consequences of Encapsulation. *J. Am. Chem. Soc.* **2010,** *132*, 9129-9137.

(538) Wang, N.; Sun, Q.; Bai, R.; Li, X.; Guo, G.; Yu, J. In Situ Confinement of Ultrasmall Pd Clusters within Nanosized Silicalite-1 Zeolite for Highly Efficient Catalysis of Hydrogen Generation. *J. Am. Chem. Soc.* **2016,** *138*, 7484-7487.

(539) Moliner, M.; Gabay, J. E.; Kliewer, C. E.; Carr, R. T.; Guzman, J.; Casty, G. L.; Serna, P.; Corma, A. Reversible Transformation of Pt Nanoparticles into Single Atoms inside High-Silica Chabazite Zeolite. *J. Am. Chem. Soc.* **2016,** *138*, 15743-15750.

(540) Bao, J.; He, J.; Zhang, Y.; Yoneyama, Y.; Tsubaki, N. A Core/Shell Catalyst Produces a Spatially Confined Effect and Shape Selectivity in a Consecutive Reaction. *Angew. Chem., Int. Ed.* **2007,** *47*, 353-356.

(541) Xiao, W.; Lei, W.; Gong, M.; Xin, H. L.; Wang, D. Recent Advances of Structurally Ordered Intermetallic Nanoparticles for Electrocatalysis. *ACS Catal.* **2018,** *8*, 3237-3256.

(542) Pan, X.; Fan, Z.; Chen, W.; Ding, Y.; Luo, H.; Bao, X. Enhanced ethanol production inside carbon-nanotube reactors containing catalytic particles. *Nat. Mater.* **2007,** *6*, 507-511.

(543) Su, J.; Xie, C.; Chen, C.; Yu, Y.; Kennedy, G.; Somorjai, G. A.; Yang, P. Insights into the Mechanism of Tandem Alkene Hydroformylation over a Nanostructured Catalyst with Multiple Interfaces. *J. Am. Chem. Soc.* **2016,** *138*, 11568-11574.

(544) Xie, C.; Chen, C.; Yu, Y.; Su, J.; Li, Y.; Somorjai, G. A.; Yang, P. Tandem Catalysis for CO2 Hydrogenation to C2–C4 Hydrocarbons. *Nano Lett.* **2017,** *17*, 3798-3802.

(545) Evans, D.; Osborn, J. A.; Wilkinson, G. Hydroformylation of alkenes by use of rhodium complex catalysts. *J. Chem. Soc. A* **1968**, 3133-3142.

(546) Gao, R.; Tan, C. D.; Baker, R. T. K. Ethylene hydroformylation on graphite nanofiber supported rhodium catalysts. *Catal. Today* **2001,** *65*, 19-29.

(547) Hanaoka, T.; Arakawa, H.; Matsuzaki, T.; Sugi, Y.; Kanno, K.; Abe, Y. Ethylene hydroformylation and carbon monoxide hydrogenation over modified and unmodified silica supported rhodium catalysts. *Catal. Today* **2000,** *58*, 271-280.

(548) Dharmidhikari, S.; Abraham, M. A. Rhodium supported on activated carbon as a heterogeneous catalyst for hydroformylation of propylene in supercritical carbon dioxide. *J. Supercrit.l Fluid.* **2000,** *18*, 1-10.

(549) Naito, S.; Tanimoto, M. Effect of sodium cation addition on the hydroformylation of propene over silica-supported Group VIII metal catalysts. *J. Chem. Soc., Chem. Commun.* **1989**, *18*, 1403-1404.

(550) Arai, H.; Tominaga, H. Hydroformylation and hydrogenation of olefins over rhodium zeolite catalyst. *J. Catal.* **1982,** *75*, 188-189.

(551) Takahashi, N.; Kobayashi, M. Comparison of ethylene with propylene hydroformylation over a Rh-Y zeolite catalyst under atmospheric pressure. *J. Catal.* **1984,** *85*, 89-97.

(552) Iglesia, E. Design, synthesis, and use of cobalt-based Fischer-Tropsch synthesis catalysts. *Appl. Catal., A* **1997,** *161*, 59-78.

(553) Schulz, H. Short history and present trends of Fischer–Tropsch synthesis. *Appl. Catal., A* **1999,** *186*, 3-12.

(554) Henrici-Olivé, G.; Olivé, S. The Fischer-Tropsch Synthesis: Molecular Weight Distribution of Primary Products and Reaction Mechanism. **1976,** *15*, 136-141.

(555) Sun, B.; Qiao, M.; Fan, K.; Ulrich, J.; Tao, F. Fischer–Tropsch Synthesis over Molecular Sieve Supported Catalysts. *ChemCatChem* **2011,** *3*, 542-550.

(556) Corma, A.; Díaz-Cabañas, M. J.; Martínez-Triguero, J.; Rey, F.; Rius, J. A large-cavity zeolite with wide pore windows and potential as an oil refining catalyst. *Nature* **2002,** *418*, 514-517.

(557) Primo, A.; Garcia, H. Zeolites as catalysts in oil refining. *Chem. Soc. Rev.* **2014,** *43*, 7548-7561.

(558) Li, J.; He, Y.; Tan, L.; Zhang, P.; Peng, X.; Oruganti, A.; Yang, G.; Abe, H.; Wang, Y.; Tsubaki, N. Integrated tuneable synthesis of liquid fuels via Fischer–Tropsch technology. *Nat. Catal.* **2018,** *1*, 787-793.

(559) Zhong, L.; Yu, F.; An, Y.; Zhao, Y.; Sun, Y.; Li, Z.; Lin, T.; Lin, Y.; Qi, X.; Dai, Y.et al. Cobalt carbide nanoprisms for direct production of lower olefins from syngas. *Nature* **2016,** *538*, 84-87.

(560) Cheng, K.; Gu, B.; Liu, X.; Kang, J.; Zhang, Q.; Wang, Y. Direct and Highly Selective Conversion of Synthesis Gas into Lower Olefins: Design of a Bifunctional Catalyst Combining Methanol Synthesis and Carbon–Carbon Coupling. *Angew. Chem., Int. Ed.* **2016,** *55*, 4725-4728.

(561) Zecevic, J.; Vanbutsele, G.; de Jong, K. P.; Martens, J. A. Nanoscale intimacy in bifunctional catalysts for selective conversion of hydrocarbons. *Nature* **2015,** *528*, 245-248.

(562) Duyckaerts, N.; Bartsch, M.; Trotuş, I.-T.; Pfänder, N.; Lorke, A.; Schüth, F.; Prieto, G. Intermediate Product Regulation in Tandem Solid Catalysts with Multimodal Porosity for High-Yield Synthetic Fuel Production. *Angew. Chem., Int. Ed.* **2017,** *56*, 11480-11484.

(563) Wang, W.; Wang, S.; Ma, X.; Gong, J. Recent advances in catalytic hydrogenation of carbon dioxide. *Chem. Soc. Rev.* **2011,** *40*, 3703-3727.

(564) Kim, S. S.; Lee, H. H.; Hong, S. C. A study on the effect of support's reducibility on the reverse water-gas shift reaction over Pt catalysts. *Appl. Catal., A* **2012,** *423-424*, 100-107.

(565) Goguet, A.; Meunier, F. C.; Tibiletti, D.; Breen, J. P.; Burch, R. Spectrokinetic Investigation of Reverse Water-Gas-Shift Reaction Intermediates over a Pt/CeO2 Catalyst. *J. Phys. Chem. B* **2004,** *108*, 20240-20246.

(566) Tada, S.; Shimizu, T.; Kameyama, H.; Haneda, T.; Kikuchi, R. Ni/CeO2 catalysts with high CO2 methanation activity and high CH4 selectivity at low temperatures. *Int. J. Hydrogen Energy* **2012,** *37*, 5527-5531.

(567) Kattel, S.; Yu, W.; Yang, X.; Yan, B.; Huang, Y.; Wan, W.; Liu, P.; Chen, J. G. CO2 Hydrogenation over Oxide-Supported PtCo Catalysts: The Role of the Oxide Support in Determining the Product Selectivity. *Angew. Chem., Int. Ed.* **2016,** *55*, 7968-7973.

(568) Graciani, J.; Mudiyanselage, K.; Xu, F.; Baber, A. E.; Evans, J.; Senanayake, S. D.; Stacchiola, D. J.; Liu, P.; Hrbek, J.; Sanz, J. F.et al. Highly active copper-ceria and copper-ceria-titania catalysts for methanol synthesis from CO2. *Science* **2014,** *345*, 546-550.

(569) Behrens, M.; Studt, F.; Kasatkin, I.; Kühl, S.; Hävecker, M.; Abild-Pedersen, F.; Zander, S.; Girgsdies, F.; Kurr, P.; Kniep, B.-L.et al. The Active Site of Methanol Synthesis over Cu/ZnO/Al2O3 Industrial Catalysts. *Science* **2012,** *336*, 893-897.

(570)   Martin, O.; Martín, A. J.; Mondelli, C.; Mitchell, S.; Segawa, T. F.; Hauert, R.; Drouilly, C.; Curulla-Ferré, D.; Pérez-Ramírez, J. Indium Oxide as a Superior Catalyst for Methanol Synthesis by CO2 Hydrogenation. *Angew. Chem., Int. Ed.* **2016,** *55*, 6261-6265.

(571)   Hao, C.; Wang, S.; Li, M.; Kang, L.; Ma, X. Hydrogenation of CO2 to formic acid on supported ruthenium catalysts. *Catal. Today* **2011,** *160*, 184-190.

(572)   Yang, H.; Zhang, C.; Gao, P.; Wang, H.; Li, X.; Zhong, L.; Wei, W.; Sun, Y. A review of the catalytic hydrogenation of carbon dioxide into value-added hydrocarbons. *Catal. Sci. Technol.* **2017,** *7*, 4580-4598.

(573)   Wei, J.; Yao, R.; Ge, Q.; Wen, Z.; Ji, X.; Fang, C.; Zhang, J.; Xu, H.; Sun, J. Catalytic Hydrogenation of CO2 to Isoparaffins over Fe-Based Multifunctional Catalysts. *ACS Catal.* **2018,** *8*, 9958-9967.

(574)   Wei, J.; Ge, Q.; Yao, R.; Wen, Z.; Fang, C.; Guo, L.; Xu, H.; Sun, J. Directly converting CO2 into a gasoline fuel. *Nat. Commun.* **2017,** *8*, 15174.

(575)   Porosoff, M. D.; Yan, B.; Chen, J. G. Catalytic reduction of CO2 by H2 for synthesis of CO, methanol and hydrocarbons: challenges and opportunities. *Energy Environ. Sci.* **2016,** *9*, 62-73.

(576)   Li, W.; Wang, H.; Jiang, X.; Zhu, J.; Liu, Z.; Guo, X.; Song, C. A short review of recent advances in CO2 hydrogenation to hydrocarbons over heterogeneous catalysts. *RSC Adv.* **2018,** *8*, 7651-7669.

(577)   Stöcker, M. Methanol-to-hydrocarbons: catalytic materials and their behavior1Dedicated to my wife Wencke Ophaug.1. *Microporous Mesoporous Mater.* **1999,** *29*, 3-48.

(578)   Olsbye, U.; Svelle, S.; Bjørgen, M.; Beato, P.; Janssens, T. V. W.; Joensen, F.; Bordiga, S.; Lillerud, K. P. Conversion of Methanol to Hydrocarbons: How Zeolite Cavity and Pore Size Controls Product Selectivity. *Angew. Chem., Int. Ed.* **2012,** *51*, 5810-5831.

(579)   Li, Z.; Wang, J.; Qu, Y.; Liu, H.; Tang, C.; Miao, S.; Feng, Z.; An, H.; Li, C. Highly Selective Conversion of Carbon Dioxide to Lower Olefins. *ACS Catal.* **2017,** *7*, 8544-8548.

(580)   Ni, Y.; Chen, Z.; Fu, Y.; Liu, Y.; Zhu, W.; Liu, Z. Selective conversion of CO2 and H2 into aromatics. *Nat. Commun.* **2018,** *9*, 3457.

(581)   Li, Z.; Qu, Y.; Wang, J.; Liu, H.; Li, M.; Miao, S.; Li, C. Highly Selective Conversion of Carbon Dioxide to Aromatics over Tandem Catalysts. *Joule* **2019,** *3*, 570-583.

(582)   Zahran, E. M.; Bedford, N. M.; Nguyen, M. A.; Chang, Y.-J.; Guiton, B. S.; Naik, R. R.; Bachas, L. G.; Knecht, M. R. Light-Activated Tandem Catalysis Driven by Multicomponent Nanomaterials. *J. Am. Chem. Soc.* **2014,** *136*, 32-35.

(583)   Rudroff, F.; Mihovilovic, M. D.; Gröger, H.; Snajdrova, R.; Iding, H.; Bornscheuer, U. T. Opportunities and challenges for combining chemo- and biocatalysis. *Nat. Catal.* **2018,** *1*, 12-22.

(584)   Wang, Y.; Zhao, H. Tandem Reactions Combining Biocatalysts and Chemical Catalysts for Asymmetric Synthesis. *Catalysts* **2016,** *6*, 194.

(585)   Kim, D.; Sakimoto, K. K.; Hong, D.; Yang, P. Artificial Photosynthesis for Sustainable Fuel and Chemical Production. *Angew. Chem., Int. Ed.* **2015,** *54*, 3259-3266.

(586)   Sakimoto, K. K.; Kornienko, N.; Cestellos-Blanco, S.; Lim, J.; Liu, C.; Yang, P. Physical Biology of the Materials–Microorganism Interface. *J. Am. Chem. Soc.* **2018,** *140*, 1978-1985.

(587)   Morales-Guio, C. G.; Cave, E. R.; Nitopi, S. A.; Feaster, J. T.; Wang, L.; Kuhl, K. P.; Jackson, A.; Johnson, N. C.; Abram, D. N.; Hatsukade, T.et al. Improved CO2 reduction activity towards C2+ alcohols on a tandem gold on copper electrocatalyst. *Nat. Catal.* **2018,** *1*, 764-771.

(588)   Sakimoto, K. K.; Wong, A. B.; Yang, P. Self-photosensitization of nonphotosynthetic bacteria for solar-to-chemical production. *Science* **2016,** *351*, 74-77.

(589)   Sakimoto, K. K.; Zhang, S. J.; Yang, P. Cysteine–Cystine Photoregeneration for Oxygenic Photosynthesis of Acetic Acid from CO2 by a Tandem Inorganic–Biological Hybrid System. *Nano Lett.* **2016,** *16*, 5883-5887.

Insert Table of Contents artwork here